Functionele respiratoire beeldvorming: een blik in de zwarte doos

Functional Respiratory Imaging: Opening the Black Box

Cedric Van Holsbeke

Promotoren: prof. dr. ir. P. Verdonck, prof. dr. W. De Backer
Proefschrift ingediend tot het behalen van de graad van
Doctor in de Ingenieurswetenschappen: Biomedische Ingenieurstechnieken

Vakgroep Elektronica en Informatiesystemen
Voorzitter: prof. dr. ir. J. Van Campenhout
Faculteit Ingenieurswetenschappen en Architectuur
Academiejaar 2013 - 2014

UNIVERSITEIT GENT

ISBN 978-90-8578-641-2
NUR 954
Wettelijk depot: D/2013/10.500/74

Preface and acknowledgments

This thesis would not have been possible without the support of several people. First and for all, I would like to thank my promoters, Prof. dr. ir. Pascal Verdonck and Prof. dr. Wilfried De Backer. Pascal introduced me to the world of *aerodynamic*s and the possible applications in medicine. Without him I would never have started a PhD in the first place. Wilfried has broadened my scientific vision and gave me insights in the clinical problems that pulmonologists are dealing with every day.

Special thanks go to my colleagues dr. ir. Wim Vos and dr. ir. Jan De Backer as they have made me a better engineer during these four years. Our numerous pleasant *face to face* discussions, combined with a close follow up of the latest *technologic*al advancements, resulted in a thesis that I am proud of!

I also want to express my gratitude to the members of my PhD committee as their input helped me to give this work the final *touch* it deserves.

To my coworkers from FluidDA, Ghent University and Antwerp University Hospital: Annemie, Benjamin, Caroline, Frédéric, Glenn, Heidi, Kirti, Kris, Laurence, Lieve, Marijke, Mathias, Peter, Rita, Rodrigo, Samir, Sarika, Sneha, Stijn, Tom, Vanita, Walter and many others. I want to thank you *one more time* because I really enjoyed working with you!

Most importantly, I want to thank the people closest to me. My parents, Marc and Anne-Marie, have given me all the opportunities in life, have always motivated me to explore and exploit my full potential and are still giving me great advice! Thanks to them, I became the person that I am now and I think they were *doin' it right*. I am also grateful to my godfather and godmother, Sabin and Marijke, as they initiated my interest in computer technology, first leading to multiple *short circuit*s in *motherboard*s, but finally leading to this thesis.

While family does not change, other relationships often do. That is why I am so happy that this is the third thesis in which I can praise my girlfriend Lisa. There is *something about us* that makes us a unique couple. The past seven years have been amazing and I hope that a wonderful future lies ahead of us, including several trips *around the world*!

The combination of a full-time job and a PhD is not straightforward. Especially during the last few months, I spent most of the weekends behind my computer screen. I hereby promise to all my friends that I will make up for the lost time, *harder, better, faster, stronger*!

Ghent, August 2013
Cedric Van Holsbeke

Table of Contents

III Effects of inhalation medication

IV Novel applications

List of Figures

List of Tables

Nomenclature

Abbreviations

3D	Three-dimensional
ACT	Asthma control test
ASL	Airway surface liquid
ATS	American thoracic society
AZLI	Aztreonam lysine
BC	Black carbon
BDP/F	Extrafine beclomethasone/formoterol
CBCT	Cone beam computed tomography
CF	Cystic fibrosis
CF-CT score	Cystic fibrosis computed tomography score
CFC	Chlorofluorocarbons
CFD	Computational fluid dynamics
COPD	Chronic obstructive pulmonary disease
CPD	Coherent point drift algorithm
CRP	Chronic respiratory patients
CT	Computed tomography
DNS	Direct numerical simulation
DPI	Dry powder inhaler
ERS	European respiratory society
F	Female
FRC	Functional residual capacity

FRI	Functional respiratory imaging
FSI	Fluid structure interaction
FVM	Finite volume method
GINA	Global Initiative for Asthma
GOLD	Global Initiative for Chronic Obstructive Lung Disease
HFA	Hydrofluoroalkane
HRCT	High resolution computed tomography
HU	Hounsfield unit
IALD	Internal airflow lobar distribution
ICC	Intraclass correlation coefficient
ICS	Inhaled corticosteroids
LABA	Long acting beta 2 agonist
LES	Large eddy simulation
M	Male
MCP	Maximal comfortable protrusion
MDI	Metered dose inhaler
MIC	Minimal inhibitory concentration
MIC90	MIC to inhibit the growth of 90% of bacterial strains
MP	Maximal protrusion
MR	Mandibular repositioning
MRA	Mandibular repositioning appliance
MRI	Magnetic resonance imaging
OSA	Obstructive sleep apnea-hypopnea syndrome
Pa	Pseudomonas aeruginosa
PRO	Patient reported outcome
RANS	Reynolds averaged Navier-Stokes
RV	Residual volume

SABA	Short acting beta 2 agonist	
SD	Standard deviation	
SGRQ	Saint George's respiratory questionnaire	
SPECT	Single-Photon Emission Computed Tomography	
SVC	Slow vital capacities	
TLC	Total lung capacity	
UA	Upper airway	

Greek symbols

α	Density ratio ρ/ρ_p	$[-]$
β	Width of the Gaussian kernel	$[-]$
Δ	Change in parameter	$[-]$
ϵ	Turbulent dissipation rate	$[m^2/s^3]$
Γ	Diffusion coefficient	$[-]$
λ	General parameter	$[-]$
μ	Dynamic viscosity	[Pas]
∇	Del operator	$[-]$
ν	Kinematic viscosity	$[m^2/s]$
ν_T	Kinematic turbulent viscosity	$[m^2/s]$
Ω	Solid angle	$[-]$
ω	Specific dissipation rate	[1/s]
ϕ	A dummy physical quantity	$[-]$
ρ	Fluid density	$[kg/m^3]$
ρ_p	Particle density	$[kg/m^3]$
τ	Shear stress tensor	$[N/m^2]$
τ_p	Particle response time	[s]
θ	Angle between two vectors	[rad]

Variables

<SaO2>	Mean oxygen saturation	[%]
$\dot{m}$	Mass flow rate through the upper airway	[kg/s]
$\vec{N}$	Normal vector	[−]
$\vec{P}$	Point	[−]
a	Acceleration vector	[m/s^2]
d_h	Hydraulic diameter	[m]
E	Total energy	[J]
F	External force vector	[N]
f	Drag factor	[−]
F_D	Drag force	[N]
F_x	Additional acceleration forces	[N]
G	Affinity matrix	[−]
g	Gravitation vector	[m/s^2]
g_i	Gravity in a certain direction x_i	[m/s^2]
H_0	Null hypothesis	[−]
k	Turbulent kinetic energy	[m^2/s^2]
k_H	Heat conduction coefficient	[W/mK]
L	Length of the upper airway	[mm]
m	Mass	[kg]
n	Number of data points	[−]
n_p	Amount of points	[−]
p	Pressure	[Pa]
$Pos_{S_{min}}$	The position of S_{min}, measured from hard palate	[mm]
$ptot$	Total Pressure	[Pa]
R	Upper airway resistance	[Pas/kg or kPas/L]
r_{res}	Resistance based radius	[m]
r_s	Spearman rank correlation coefficient	[−]

Re	Reynolds number	$[-]$
Re_{crit}	Critical Reynolds number	$[-]$
S	Surface	$[-]$
$S_{avg_{bottom}}$	S_{avg} between epiglottis and larynx	[mm^2]
$S_{avg_{central}}$	S_{avg} between the end of uvula and epiglottis	[mm^2]
$S_{avg_{top}}$	S_{avg} between hard palate and the end of uvula	[mm^2]
S_{avg}	Average cross-sectional area of the upper airway	[mm^2]
S_i	Source term	$[-]$
S_{min}	Minimal cross-sectional area of the upper airway	[mm^2]
S_{min}/S_{avg}	Concavity of the upper airway	$[-]$
S_{surf}	Surface area	[m^2]
T	Temperature	[K]
t	Time	[s]
U	Fluid velocity vector	[m/s]
u_i	Fluid velocity in a certain direction x_i	[m/s]
V_{air}	Volume of the upper airway	[mm^3]
v_i	Particle velocity in a certain direction x_i	[m/s]
V_{tot}	Total volume	[m^3]
x	Cartesian coordinate in x-direction	[m]
y	Cartesian coordinate in y-direction	[m]
z	Cartesian coordinate in z-direction	[m]
AD	Aerodynamic diameter	[µm]
AHI	Apnea-hypopnea index	$[-]$
AM	Angulus mandibulae	[°]
BMI	Body mass index	[kg/m^2]
d_1	Maximum Ferret's diameter	[µm]
d_2	Minimum Ferret's diameter	[µm]

dp	Average particle diameter	[µm]
eNO	Exhaled nitric oxide	[ppb]
FEV1	Forced expiratory volume in one-second	[L or $\%$]
FEV1/FVC	Tiffeneau index	[$\%$]
FVC	Forced vital capacity	[L]
iRaw	Imaging airway resistance	[kPas/L]
iVaw	Imaging airway volume	[cm^3]
MMAD	Mean mass aerodynamic diameter	[µm]
MMD	Mass median diameter	[µm]
oAHI	Obstructive Apnea-Hypopnea index	[$-$]
OAI	Obstructive apnea index	[$-$]
ODI	Oxygen desaturation index	[$-$]
PEF	Peak expiratory flow	[L/s]
Raw	Airway resistance	[kPas/L]
RDI	Respiratory disturbance index	[$-$]
SaO2 nadir	Lowest level of oxygen saturation	[$\%$]
sRaw	Specific airway resistance	[kPas]
VC	Vital capacity	[$\%$]

Nederlandstalige samenvatting –Summary in Dutch–

In de pneumologie bestaan er verschillende kwantitatieve meetinstrumenten om de clinici te helpen met hun diagnose. Het probleem met deze traditionele technieken is dat ze weinig gevoelig zijn in het detecteren van veranderingen en dat de variatie tussen de verschillende metingen heel hoog is. Dit heeft als gevolg dat de ontwikkeling van medicatie voor luchtwegziektes duurder is dan de geneesmiddelenontwikkeling in andere takken van de geneeskunde. Er zijn namelijk grootschalige onderzoeken, in meerdere centra, in een groot aantal patiënten, gedurende een lange periode nodig om het effect van een nieuw product te kunnen aantonen. Deze kosten beperken de innovatie, wat resulteert in een onvervulde behoefte aan gevoelige kwantificeerbare parameters in farmacologische ontwikkeling en klinische praktijk.

De reden hiervoor is dat de traditionele technieken de patiënt aanschouwen als een zwarte doos. In dit proefschrift wordt functionele respiratoire beeldvorming (FRI) voorgesteld als een instrument om "een blik in de zwarte doos" te werpen. FRI is een methode waarbij patiënt specifieke medische beelden worden gecombineerd met numerieke stromingsberekeningen. Dit opent de mogelijkheid om lokale informatie over de anatomie en functionaliteit van de luchtwegen te genereren. Op die manier kunnen lokale waarden van luchtweg volume, diameter en weerstand worden gemeten en vergeleken. De uitspraak "een blik in de zwarte doos" verwijst naar deze lokale informatie, maar verwijst ook naar de mogelijkheden van FRI in verschillende ziektebeelden en in verschillende wetenschappelijke domeinen binnen en buiten de geneeskunde.

Het eerste deel van dit proefschrift handelt over de mogelijkheden van FRI bij de evaluatie en behandeling van het obstructieve slaapapneusyndroom (OSA). Er is aangetoond dat FRI de effecten van een behandeling op de morfologie en functionaliteit van de bovenste luchtwegen kan kwantificeren en dat deze effecten kunnen worden voorspeld. Bij pediatrische OSA patiënten is er geconstateerd dat FRI parameters sterker gecorreleerd zijn met de ernst van OSA dan de klinische scores die abnormaliteiten in de bovenste luchtweg quantificeren.

Het tweede deel behandelt de depositie van geïnhaleerde medicatie. FRI is in staat

om het belang van de patiënt specifieke anatomie aan te tonen wanneer men de effectieve medicatiedosis in de longen wilt simuleren. FRI analyses tonen ook aan dat er een grote inter- en intra-individuele variabiliteit zit in de morfologie en functionaliteit van bovenste luchtwegen. Deze bevindingen onderstrepen het belang van het gebruik van zoveel mogelijk patiënt specifieke informatie wanneer men de depositie van deeltjes wil simuleren. FRI is ook bruikbaar gebleken in het patiënt specifiek optimaliseren van een behandeling met een geïnhaleerde antibioticum bij patiënten met mucoviscidose.

In het derde deel wordt FRI gebruikt om de effecten van inhalatie medicatie bij patiënten met astma en chronische obstructieve longziekte (COPD) te evalueren. FRI blijkt erg gevoelig te zijn om wijzigingen in de lokale luchtweg morfologie en functionaliteit op te merken. Zowel bij astma als bij COPD patiënten blijken FRI gegenereerde parameters 3 à 6 maal gevoeliger te zijn in het opmerken van drugs geïnduceerde veranderingen dan de traditionele testen. Verder is er een verhoogde specificiteit waargenomen en zijn er, in tegenstelling tot de traditionele testen, correlaties gevonden tussen veranderingen in FRI parameters en veranderingen in het subjectieve gevoel van patiënten.

Het vierde deel is erop gericht om FRI te gebruiken buiten de klinische studies, door het verkennen van nieuwe toepassingsgebieden. Er is aangetoond dat FRI kan helpen om het gedrag van fijn stof in de longen te begrijpen door uitgebreide fysisch-chemische analyses van vervuilde lucht te combineren met patiënt specifieke simulaties. Het potentieel van FRI in het personaliseren van respiratoire behandelingen is ook bestudeerd. Twee patiënten met een idiopathische unilaterale verlamming van het middenrif werden anders behandeld ondanks het feit dat beiden soortgelijke anatomische en fysiologische afwijkingen vertoonden op radiologisch onderzoek. FRI toonde aan dat er problemen waren met de ventilatie en geneesmiddelafgifte bij een patiënt, terwijl dit niet het geval was bij de andere patiënt, resulterend in respectievelijk een chirurgische en conservatieve benadering.

FRI bevindt zich nog in een vroege ontwikkelingsfase en is niet zo goed gevalideerd in vergelijking met de traditionele testen. In dit proefschrift wordt echter aangetoond dat FRI een meerwaarde kan betekenen in verschillende onderzoeksdomeinen binnen de pneumologie en in de klinische praktijk.

De hoge sensitiviteit en specificiteit van FRI maken de techniek heel geschikt als een instrument om een beter inzicht te krijgen in de fysiologische werkingsmechanismen van een bepaald medisch apparaat of geneesmiddel. Dit kan helpen om beslissingen te nemen vroeg in het ontwikkelingsproces van dit apparaat of geneesmiddel. Het gebruik van FRI in kleinschalige klinische fase IIa studies maakt het mogelijk om het risico te verschuiven van de zeer dure fase III studies naar de goedkopere fase II studies. FRI is ook een interessante technologie voor nichemarkten met onvervulde behoeften, zoals mensen die een ingrijpende operatie moeten ondergaan of die lijden aan zeldzame ziekten. Het probleem met deze zeldzame ziekten is dat

sommigen onder hen zo zeldzaam zijn dat het bijna onmogelijk is om grootschalige studies uit te voeren. De kans is hier dan ook groot dat de traditionele technieken niet gevoelig genoeg zijn om mogelijke effecten te detecteren. Dit opent de mogelijkheid om FRI te gebruiken als een surrogaat eindpunt. Een andere uitdaging die kan worden aangepakt met behulp van FRI is de kwestie van de bio-equivalentie. FRI kan worden gebruikt om zowel de effectieve longdepositie als het effect van het originele en generieke geneesmiddel beoordelen. Op die manier kan er bepaald worden of de twee producten vergelijkbare effecten induceren. Gepersonaliseerde geneeskunde is een ander domein waarin FRI een toegevoegde waarde kan hebben. FRI maakt het mogelijk om patiënt specifieke inzichten te creëren waardoor de juiste behandeling aan de juiste patiënt kan worden gegeven. FRI kan ook helpen om de gezondheidseffecten van luchtverontreiniging te begrijpen in een multidisciplinaire aanpak. De fysisch-chemische karakterisering van luchtvervuiling kan worden gebruikt als randvoorwaarde voor FRI, dat op zijn beurt invoergegevens kan generen voor algoritmes die de gezondheidseffecten modelleren. Wanneer dit gecombineerd wordt met klinische studies kunnen er nieuwe inzichten verkregen worden in de mechanismen en effecten van fijn stof.

Verder onderzoek is nodig om de mogelijkheden van FRI in de toekomst uit te breiden. Een eerste nuttige onderzoekslijn is het zoeken naar correlaties tussen depositie van medicatie en de effecten op de luchtwegen. Dit zou een verbinding kunnen maken tussen het tweede en het derde deel van dit proefschrift. Het is ook interessant om te zoeken naar drempelwaarden voor veranderingen in FRI parameters die klinisch relevant zijn zodat FRI kan gebruikt worden om klinische conclusies te trekken. Een laatste lijn van onderzoek voor de nabije toekomst is de mogelijkheden van FRI te bekijken bij het fenotyperen van patiënten. Een nieuw systeem van pathologieclassificatie zou kunnen leiden tot een betere behandeling van de patiënt.

De lezers van dit proefschrift zullen opmerken dat dit onderzoek eerder vanuit een klinisch oogpunt dan vanuit een technisch oogpunt is aangepakt. Terwijl veel onderzoek in de biomedische ingenieurswereld gericht is naar de creatie van heel ingewikkelde wiskundige modellen in geïdealiseerde geometrieën of kleine cross-sectionele patiënten datasets, streeft de auteur van deze thesis ernaar om eenvoudige, klinisch relevante en schaalbare modellen te ontwerpen die gemakkelijk te begrijpen zijn en kunnen gebruikt worden in een normale klinische setting in grote longitudinale studies. Hoewel beide benaderingen hun voor- en nadelen hebben, mag men niet vergeten dat biomedische ingenieurs in dienst moeten staan van de patiënt. Als een model in staat is om een patiënt te helpen, dan is het een zinvol model. Als toevoegingen aan het model leiden tot een betere levenskwaliteit voor de patiënt, dan is het een beter model. Dit proefschrift laat zien dat ingenieurswetenschappen en geneeskunde niet hoeven te botsen. De schrijver gelooft dat multidisciplinaire teams bestaande uit artsen, ingenieurs en (levens-) wetenschappers de toekomst zijn van de geneeskunde en hoopt dat deze thesis een goede stap in die richting is.

Summary in English

In respiratory medicine, several quantitative measurement tools exist that assist the clinicians in their diagnosis. The problem with these traditional techniques is that they lack sensitivity to detect changes and that the variation between different measurements is very high. The result is that the development of respiratory drugs is the most expensive of all drug development because large multicenter studies in a high number of patients over a long period of time are needed in order to asses the effect of a new compound. This limits innovation, resulting in an unmet need for sensitive quantifiable outcome parameters in pharmacological development and clinical respiratory practice.

The main reason is that the traditional techniques are based on a black box approach. In this thesis, functional respiratory imaging (FRI) is proposed as a tool to "open the black box". FRI is a workflow where patient specific medical images are combined with computational fluid dynamics in order to give local information of anatomy and functionality in the respiratory system. In this way, local measures of airway volume, diameter and resistance can be assessed and compared. The statement "opening the black box" refers to this local information, but also refers to the possibilities in different pathologies and different fields of application.

The first part of this thesis deals with FRI in the evaluation and treatment of the obstructive sleep apnea syndrome (OSA). It is shown that FRI is able to quantify the effects on upper airway morphology and functionality due to a treatment and that these effects can be predicted from baseline measurements. In pediatric OSA patients it is found that baseline measured FRI parameters are better correlated with OSA severity than clinical scores of upper airway patency.

The second part deals with deposition of inhaled medication. FRI is able to capture the importance of patient specific features in having a significant impact in the effective lung dose and therefore the treatment efficacy. Furthermore, FRI analyses show that there is a large inter- and intra-subject variation in upper airway morphology and functionality, stating the importance of using as much subject specific information as possible when simulating particle deposition. FRI is also shown to be useful in optimizing inhaled antibiotic treatment on a patient specific base in cystic fibrosis patients.

In the third part, FRI is used to evaluate the effects of inhalation medication in asthma and chronic obstructive pulmonary disease (COPD) patients. FRI is found to be very sensitive in picking up changes in local airway morphology and functionality. In both asthma and COPD patients, FRI parameters are three to six-fold more sensitive in picking up drug-induced changes as compared to traditional

tests. Furthermore, an increased specificity is observed and, unlike the traditional tests, correlations were found between changes in FRI parameters and changes in patient feeling.

The fourth part aims to bring FRI outside the clinical trials, exploring different fields of application. It is shown that FRI can help to understand the behaviour of airborne particles in the lungs by combining detailed physical-chemical analyses of particulate pollution with patient specific particle simulations. The potential of FRI in personalizing respiratory treatment was also revealed. In two patients with an idiopathic unilateral diaphragmatic paralysis, a different treatment approach was chosen despite both having similar anatomical and physiological abnormalities on radiological examination. FRI showed impairments in ventilation and drug delivery in one patient, while this was not the case in the other patient, resulting in a surgical and conservative approach respectively.

While FRI is still in its early development phase and is not so well validated when compared to the traditional tests, this thesis shows that FRI can have an added value in multiple research domains within pulmonology and in everyday clinical practice.

The high sensitivity and specificity of FRI make it very well suited as a tool to assess the mode of action in order to reach go/no go decisions early in the development process of a device or drug. Using FRI in small-scale clinical phase IIa trials can significantly de-risk the very expensive phase III trials. FRI is also an interesting technology for niche markets with high unmet needs, like people who undergo major surgery or who suffer from orphan diseases. The problem with these rare diseases is that some of them are so rare that it is almost impossible to perform large-scale studies. Chances are real that traditional techniques are not sensitive enough to detect possible effects in these studies, opening the possibility of FRI as a surrogate endpoint. Another challenge that can be tackled using FRI is the question of bioequivalence. FRI can be used to assess the effective lung deposition and effect of both original and generic compound, making it possible to determine if the two products induce similar effects. Personalized medicine is another domain where FRI can have an added value. FRI can generate patient specific insights, making it possible to deliver the right treatment to the right patient. FRI can also help to understand the health effects of air pollution in a multidisciplinary approach. Physical-chemical characterization of air pollution measurements can be used as input data for FRI, which can on his turn generate input data for health-effect modelling algorithms. Combining this approach with clinical trials can result in a better understanding of the mechanics and clinical effects of air pollution.

Further research is needed in order to expand the possibilities of FRI in the future. A first research line that comes to mind is to search for correlations between drug deposition and effect size, making a link between the second and the third part of this thesis. It would also be interesting to search for threshold values for changes in FRI parameters that indicate clinical significance. In that way, FRI can be used to draw clinical conclusions. A last line of research for the near future is the power of FRI in phenotyping patients. A new system of pathology classification could lead to better patient treatment.

The readers of this thesis will notice that the research approach is more from a clinical than from an engineering point of view. While a lot of research in biomedical engineering is targeted towards the creation of very complicated mathematical models in idealised geometries or small cross-sectional patient datasets, the author of this thesis strives to design simple, clinically relevant and scalable models that are easy to understand and that can be used in a normal clinical setting in large longitudinal studies. Although both top-down and bottom-up approaches have their advantages and disadvantages, one should not forget that biomedical engineering is not only about the algorithm but about the patient. If a model is able to help a patient, then it is a useful model. If adding some complexity to the model leads to a better quality of life for the patient, then it is a better model. This thesis shows that engineering and medicine do not have to clash. The author believes that multidisciplinary teams consisting of doctors, engineers and (life) scientists are the future of medicine and hopes that this thesis is a good step forward in that direction.

1 Introduction

Breathing is one of the most elementary functions of the human body as it supplies our cells with oxygen and removes excess carbon dioxide. Without this gas exchange, the various metabolic processes in our body would stop functioning and our organs would shut down. Before this gas exchange occurs, the inhaled air flows through several anatomical regions that are grouped under the term respiratory system.

The upper airway is defined as the part of the respiratory system lying outside of the thorax (extrathoracic region) [2]. Its main respiratory function is to clean, heat and moisten the incoming air [16]. The anatomy of the upper respiratory tract is shown in figure 1.1.

In order to perform its function in the most optimal way, the preferred entrance of incoming air is the nose. The hairs in the nasal vestibule regions filter the large airborne particles after which the various sinuses and conchae cleanse, humidify and heat the air [2]. After passing the pharyngeal regions, the trachea leads the air to the lower airways and lung. In between, the epiglottis prevents swallowed objects from entering the downstream respiratory system [2]. Furthermore, the cough reflexes of the upper airway protect the lungs from the inhalation of foreign material and clear secretions from them [16].

The lower airways and lung are defined as the part of the respiratory system lying inside of the thorax (intrathoracic region). The lower airways consist of the trachea, different bronchi and bronchioles that lead the air to the lungs where the gas exchange takes place in the alveoli. The anatomy of the lower respiratory tract is shown in figure 1.2.

The lung consists of five lobes. The left lung is subdivided into upper and lower lobes by the oblique fissure whereas the right lung is partitioned into upper,

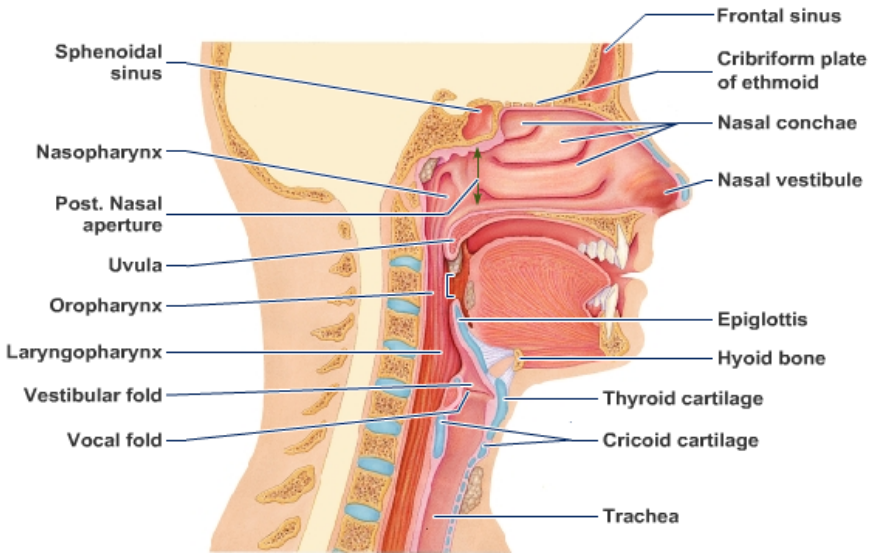

Figure 1.1: The anatomy of the upper airway [12]

middle and lower lobes by the oblique and horizontal fissures. All these lobes contain a number of segments separated from one another by connective tissue septa [12].

As the respiratory system is directly connected to the outside world, it is very prone to infections and sensitive to pollution. These external factors can induce respiratory diseases or worsen the symptoms of underlying pathologies.

In respiratory medicine, several quantitative measurement tools exist that assist the clinicians in their diagnosis. Most of these techniques aim to quantify the state of the airways, alveoli and lung tissue by measurements of flow, volume or pressure.

Small airway diseases are mostly assessed using pulmonary function tests (PFT). One of the most important outcome parameters that can be obtained by PFT is the forced expiratory volume in 1 second (FEV1). To obtain this value, the subject has to blow out as hard as possible in a device that measures the exhaled flow. The total volume of air that has been exhaled at the end of the first second is defined as FEV1.

Sleep-related breathing disorders such as the obstructive sleep apnea syndrome (OSA) are mostly evaluated by letting the patient sleep in a sleep lab environment. During the sleep, a polysomnography study is performed, resulting in real-time signals of respiratory airflow, respiratory effort and blood gasses. These signals are then analyzed and scored by a clinician, resulting in outcome parameters such as the apnea-hypopnea index (AHI). AHI is defined as the sum of all occurring complete cessations (apnea) and partial obstructions (hypopnea) of breathing during the night, expressed on an hourly basis.

The problem with these traditional techniques is that they measure the prop-

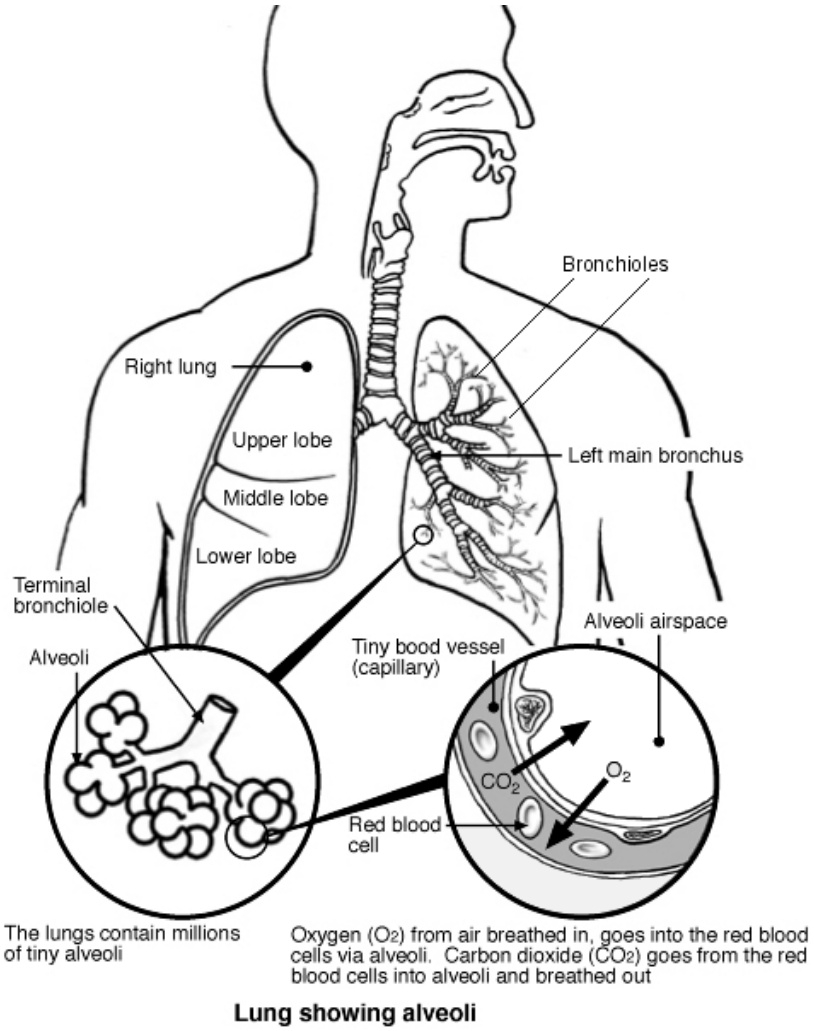

Figure 1.2: The anatomy of the lower respiratory tract [15]

erties of the whole (respiratory) system of the subject. At first sight, this can be considered as a very strong asset but it also has some drawbacks. Using these techniques, subjects are reduced to "black boxes". When abnormalities are detected in one of the parameters, the clinical cause cannot be localized. Also, the amount of information that is included in these parameters is so large, that a lot of sensitivity is lost. The human body is so powerful that it can keep its functionality intact even when a disease is already in an advanced state. These internal compensating mechanisms are also incorporated in the traditional techniques, making them not sensitive to detect changes.

An even larger problem is the variability within the same test. As FEV1 measurements need an effort from the subject, this results in day-to-day variability. The recent UPLIFT trial in 6000 chronic obstructive pulmonary disease (COPD) patients showed that there is between-test variability of 0.141 ± 0.138 L and that changes are only considered clinically important if they are higher than 0.323 L [10]. As a moderate COPD patient has an FEV1 in the order of 1.5 – 2 L, these variations can be considered important. Night-to-night variations in the AHI value equal or higher than 10 events per hour are observed in the majority of OSA patients while the cut-off value for being diagnosed with OSA is set at 5 events per hour [4]. As both tests are used to classify patients by disease severity, the possibility exist that patients are wrongly categorized. This can result in the patient not receiving the optimal therapy.

The development of respiratory drugs is the most expensive of all drug development cycles with development costs of more than a billion dollars per product [1]. Due to the lack of sensitivity and the variability of the traditional tests, large multicenter studies in a high number of patients over a long period of time are needed in order to asses the effect of a new compound. Even in these studies, there is no guarantee that the results will be satisfying. Very large trials such as ISOLDE [6], TRISTAN [7] and TORCH [8] showed that it is very difficult to detect changes using classic PFT and that only weak correlations exist between PFT values and the patient's condition.

This results in only a limited number of large companies who want to invest in these therapies. Companies with more limited resources often invest in therapeutic areas with a higher return on investment. This limits innovation from which the patient will be the victim.

It can be concluded that there is an unmet need for sensitive quantifiable outcome parameters in pharmacological development and clinical respiratory practice.

Medical imaging techniques have the capabilities to "open the black box" and provide regional information of airway structure and function. More and more researchers understand the usefulness of medical imaging in research and clinical practice. Work by Martonen and Longest provided important insights into aerosol deposition characteristics by combining medical imaging with advanced analysis methods [3, 11, 13, 19]. Most of the research in that domain was however performed in generalized or idealized airway geometries. Although these studies provided useful information about general mechanisms, they lacked the possibility to give information about the behavior in an individual subject. This is especially important

when dealing with diseased subjects as most pathologies are so heterogeneous, that a one size fits all model does not work. At that point, the step towards subject specific models needs to be taken. This approach has already proven to be valuable as the COPDgene cohort, based on patient specific computed tomography scans, has yielded interesting results on the airway and blood vessel structure in relation to smoking [17], exacerbations [18] and healthy lungs [20].

Despite increasing evidence of the added value of medical imaging in clinical trails and clinical practice, the overall quantitative usage of imaging tools is low. One of the reasons is that most of these techniques are not as quantitative as they should be. In most cases, data have to be interpreted by a human, introducing variation in the process. Another reason is that a lot of the outcome parameters are so complex that it is difficult to relate them to the human physiology. However, the main reason is that a lot of these techniques require a specialized infrastructure that is not readily available in most clinical centers [9, 14]. In this thesis, functional respiratory imaging (FRI) is proposed as a tool to counter the issues of the present techniques. FRI is a workflow where patient specific medical images are combined with computational algorithms in order to give local information of anatomy and functionality in the respiratory system. This technique has the advantages that minimal user interpretation is required, that the resulting outcome parameters directly relate to human physiology and that the necessary equipment is present in most clinical centers. A detailed description of FRI can be found in chapter 2.

FRI has already been the subject of research in the past. The PhD thesis of Dr. Jan De Backer elaborated on the usefulness of medical imaging in the field of respiratory medicine and gave first insights on how functionality is added to these images by performing flow simulations using computational fluid dynamics. It was shown that these techniques can be used to gain a better understanding of biomechanical principles and that it opened the possibilities of evaluating treatment effects. This work can be considered as the basis for FRI. In the PhD thesis of Dr. Wim Vos it was shown that FRI outcome parameters can be obtained through a repeatable, high quality workflow. Furthermore, it was shown that correlations exist between traditional techniques and FRI and that FRI can have an added value for both patient and clinician.

The goal of this thesis is to explore the real power of FRI in “opening the black box”. At the end, it has to be clear where FRI can help to meet some of the needs in pharmacological development and clinical respiratory practice. Furthermore, the first steps towards personalized medicine will be set and it will be explored how FRI can be used in non-medical domains. To achieve this, the following approach will be taken:

- More advantage will be taken of the regional measurement possibilities of FRI. The region of interest will be split into distinct anatomical regions and local analyses will be performed
- Where previous FRI research focused on adult asthma, COPD and sleep apnea patients, this thesis wants to explore the possibilities in more vulnerable groups with higher unmet needs such as pediatric patients with cystic fibrosis

- Previous work all happened in clinical trail settings. In this thesis, the technology will be brought into environmental science and clinical practice.

The statement "opening the black box" refers thus not only to the regional information, but also refers to the possibilities in different pathologies and different fields of application. To accomplish this, this thesis is divided into four major parts.

The first part deals with FRI in the evaluation and treatment of OSA. OSA is characterized by a repeated collapse of the upper airway during sleep. To overcome this abnormal situation, the respiratory reflexes will activate the upper airway muscles in order to restore the airflow to the lungs. These so-called arousals disturb the patient's sleep, causing comorbidities such as a constant feeling of tiredness, depression and vascular diseases. Chapter 3 describes a large scale cross-sectional retrospective study in adult OSA patients where the effects of mandibular protrusion on upper airway geometry and functionality are investigated. It is also inspected which baseline characteristics determine these effects and if they are in line with clinical findings. The goal of chapter 4 is to search for correlations between FRI parameters and OSA severity in pediatric OSA patients. Furthermore, it is examined if FRI can predict the effect of treatment outcome.

The second part deals with deposition of inhaled medication. As the response of a patient to a certain inhaled drug is driven both by the receptiveness of the body to that drug as by the amount of the drug reaching the lung, it is important to have insights in these mechanics on a patient specific base. Chapter 5 describes how FRI can be used to assess the lung deposited fraction of a respiratory compound. As upper airway morphology is considered important when assessing the effective lung dose, it is investigated if FRI can capture the influence of these patient specific features. A lot of drug deposition modeling is performed in vitro, using casts of generalized upper airways. These casts are based on scans in a supine position while inhaled medication is mostly administered in an upright position. Chapter 6 describes a prospective open cross-over study that tries to quantify the differences in airway morphology and functionality between supine and upright position in healthy volunteers. Cystic fibrosis is a genetic disorder that has an effect on the composition of the mucus in the airways. The mucus becomes more viscous, leading to decreased mucus clearance resulting in bacterial infections. Inhaled antibiotics have become popular treatments to counter these infections. The problem with antibiotics is that the delivered dose has to be high enough to kill the bacteria. Too low local concentrations result in suboptimal eradication of the bacteria and contribute to the development of antibiotic resistance. In chapter 7, FRI is used to increase the understanding of deposition mechanisms in diseased airways of pediatric cystic fibrosis patients.

In the third part, FRI is used to evaluate the effects of inhalation medication in asthma and COPD patients. Asthma and COPD are both chronic inflammatory diseases that involve the small airways and cause airflow limitation. The nature of inflammation and the anatomical sites that are involved are different: while asthma affects only the airways, COPD affects both the airways and lung parenchyma [5]. In chapter 8, the acute effects of administering a budesonide/formoterol combination

in COPD patients are examined. This placebo controlled crossover study aims to demonstrate the higher sensitivity of FRI compared to the classic lung function parameters in detecting changes due to the medication. It is also assessed if FRI has a higher specificity when it comes to distinguishing between product and placebo. In chapter 9, it is examined how FRI can be used to evaluate the effects of transferring asthma patients from the standard fine particle treatment to an extra fine particle treatment. The goal is to show that switching patients to a different product can lead to additional, clinically relevant, long-term beneficial effects that are best observed using FRI.

The fourth part aims to bring FRI a step further, outside the clinical trails. It is known that air pollution has an associated increase in morbidity and mortality. The behavior of individual airborne particles in the human lung is however not yet understood. Current research is mostly based on generalized casts or computer models obtained from morphometric analysis of the lungs. In chapter 10, it is determined how the composition of individual particles, obtained with micro-analytical techniques, can be combined with patient specific simulations of particle deposition in the airways. When performing clinical trails, most results are obtained using statistical analysis. However, it is not because a treatment works for the mean of the population, that it will work for an individual patient. Chapter 11 aims to be a first step in using FRI as a tool for personalized medicine. This chapter tries to demonstrate the clinical value of FRI in describing a new clinical presentation of the anatomical and physiological abnormalities in two subjects with an idiopathic unilateral diaphragmatic paralysis. It is examined how FRI can help the clinician in his decision process.

As large amounts of data are processed in this thesis, a lot of work is put in improving the scalability of FRI by designing robust automation algorithms and by reducing the turnaround time of the simulations. At the beginning of each individual chapter, the contributions of the author and main challenges in engineering that are tackled in that chapter are given. Some of these are explained in detail in chapter 12, including some advanced algorithms that can possibly be used in future work. The thesis ends with chapter 13 where the conclusions that can be drawn from this work are listed. The strengths en weaknesses of FRI are described and the future research directions are pointed out.

References

[1] Christopher P. Adams and Van V. Brantner. Estimating the cost of new drug development: Is it really $802 million? *Health Affairs*, 25(2):420–428, March 2006. PMID: 16522582.

[2] I. Edward Alcamo. *Anatomy Coloring Workbook, Second Edition*. The Princeton Review, 2003.

[3] Gabriela Apiou-Sbirlea, Ira M. Katz, and Ted B. Martonen. The effects of simulated airway diseases and affected flow distributions on aerosol deposition. *Respiratory Care*, 55(6):707–718, June 2010. PMID: 20507653.

[4] Lia Rita Azeredo Bittencourt, Deborah Suchecki, Sergio Tufik, Clóvis Peres, Sônia Maria Togeiro, Maurício Da Cunha Bagnato, and Luiz Eduardo Nery. The variability of the apnoea–hypopnoea index. *Journal of Sleep Research*, 10(3):245–251, 2001.

[5] A. S. Buist. Similarities and differences between asthma and chronic obstructive pulmonary disease: treatment and early outcomes. *European Respiratory Journal*, 21(39 suppl):30s–35s, January 2003. PMID: 12572699.

[6] P S Burge. Randomised, double blind, placebo controlled study of fluticasone propionate in patients with moderate to severe chronic obstructive pulmonary disease: the ISOLDE trial. *BMJ*, 320(7245):1297–1303, May 2000.

[7] Peter Calverley, Romain Pauwels, Jørgen Vestbo, Paul Jones, Neil Pride, Amund Gulsvik, Julie Anderson, and Claire Maden. Combined salmeterol and fluticasone in the treatment of chronic obstructive pulmonary disease: a randomised controlled trial. *The Lancet*, 361(9356):449–456, February 2003.

[8] Peter M.A. Calverley, Julie A. Anderson, Bartolome Celli, Gary T. Ferguson, Christine Jenkins, Paul W. Jones, Julie C. Yates, and Jørgen Vestbo. Salmeterol and fluticasone propionate and survival in chronic obstructive pulmonary disease. *New England Journal of Medicine*, 356(8):775–789, 2007. PMID: 17314337.

[9] Sean Fain, Mark L. Schiebler, David G. McCormack, and Grace Parraga. Imaging of lung function using hyperpolarized helium-3 magnetic resonance imaging: Review of current and emerging translational methods and applications. *Journal of Magnetic Resonance Imaging*, 32(6):1398–1408, 2010.

[10] W. Janssens, Y. Liu, D. Liu, S. Kesten, D.P. Tashkin, B.R. Celli, and M. Decramer. Quality and reproducibility of spirometry in COPD patients in a randomized trial (UPLIFT®). *Respiratory Medicine*.

[11] P. Worth Longest and Samir Vinchurkar. Effects of mesh style and grid convergence on particle deposition in bifurcating airway models with comparisons

to experimental data. *Medical Engineering & Physics*, 29(3):350–366, April 2007.

[12] Elaine Marieb and Katja Hoehn. *Anatomy and physiology: International edition*. Pearson Education (US), [S.l.], 3th edition, April 2007.

[13] T.b. Martonen, J.d. Schroeter, and J.s. Fleming. 3D in silico modeling of the human respiratory system for inhaled drug delivery and imaging analysis. *Journal of Pharmaceutical Sciences*, 96(3):603–617, 2007.

[14] Yoshiharu Ohno, Hisanobu Koyama, Takeshi Yoshikawa, Keiko Matsumoto, Nobukazu Aoyama, Yumiko Onishi, Daisuke Takenaka, Sumiaki Matsumoto, Yoshihiro Nishimura, and Kazuro Sugimura. Comparison of capability of dynamic o2-enhanced MRI and quantitative thin-section MDCT to assess COPD in smokers. *European Journal of Radiology*, 81(5):1068–1075, May 2012.

[15] Patient UK (n.d.). The lungs and respiratory tract.

[16] Rj Pierce and Cj Worsnop. Upper airway function and dysfunction in respiration. *Clinical and Experimental Pharmacology and Physiology*, 26(1):1–10, 1999.

[17] George R. Washko, Gary M. Hunninghake, Isis E. Fernandez, Mizuki Nishino, Yuka Okajima, Tsuneo Yamashiro, James C. Ross, Raúl San José Estépar, David A. Lynch, John M. Brehm, Katherine P. Andriole, Alejandro A. Diaz, Ramin Khorasani, Katherine D'Aco, Frank C. Sciurba, Edwin K. Silverman, Hiroto Hatabu, and Ivan O. Rosas. Lung volumes and emphysema in smokers with interstitial lung abnormalities. *New England Journal of Medicine*, 364(10):897–906, 2011. PMID: 21388308.

[18] J. Michael Wells, George R. Washko, MeiLan K. Han, Naseer Abbas, Hrudaya Nath, A. James Mamary, Elizabeth Regan, William C. Bailey, Fernando J. Martinez, Elizabeth Westfall, Terri H. Beaty, Douglas Curran-Everett, Jeffrey L. Curtis, John E. Hokanson, David A. Lynch, Barry J. Make, James D. Crapo, Edwin K. Silverman, Russell P. Bowler, and Mark T. Dransfield. Pulmonary arterial enlargement and acute exacerbations of COPD. *New England Journal of Medicine*, 367(10):913–921, 2012. PMID: 22938715.

[19] P. Worth Longest and Samir Vinchurkar. Validating CFD predictions of respiratory aerosol deposition: Effects of upstream transition and turbulence. *Journal of Biomechanics*, 40(2):305–316, 2007.

[20] Jordan Alexander Zach, John D. Jr Newell, Joyce Schroeder, James R. Murphy, Douglas Curran-Everett, Eric A. Hoffman, Philip M. Westgate, MeiLan K. Han, Edwin K. Silverman, James D. Crapo, David A. Lynch, and on behalf of the COPDGene Investigators. Quantitative computed tomography of the lungs and airways in healthy nonsmoking adults. *Investigative Radiology October 2012*, 47(10):596–602, 2012.

2
Functional respiratory imaging

Functional respiratory imaging (FRI) is the process of extracting patient specific physiological data of the respiratory system from medical images. The purpose of FRI is to assess the influence of a certain biological or mechanical process on the respiratory system of a certain subject.

The medical images that are used as input data for FRI can originate from a variety of imaging techniques (Figure 2.1). These techniques can be divided in two large groups:

- Anatomical imaging techniques such as radiography, computed tomography (CT), cone beam computed tomography (CBCT) and magnetic resonance imaging (MRI)

- Functional imaging techniques such as ultrasonography, scintigraphy, positron emission tomography, single-photon emission computed tomography and hyperpolarized gas MRI

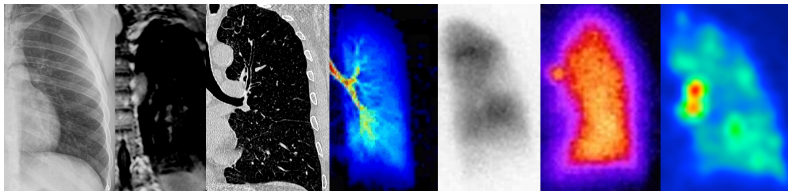

Figure 2.1: Images of the respiratory tract obtained from different imaging modalities (radiography [4], MRI [1], CT, helium MRI [8], scintigraphy [10], PET [11], SPECT [5])

In this thesis, the techniques from the first group are used as input data. Although it seems contradictory to extract *functional* data from *anatomical* images, a lot of information can be obtained when making the images in an intelligent way and combining them with computational techniques. The main building blocks of the FRI workflow are: medical imaging, image processing and computational fluid dynamics.

2.1 Medical imaging

To be able to start the FRI workflow, the medical images must satisfy some conditions. It is important that the images have a high quality and that they are taken at the right moment. Furthermore, the risks for the patient has to be as low as reasonably achievable and it has to be possible to obtain the images in a normal clinical setting.

In this thesis, CT is used as primary imaging modality (Figure 2.2). With CT, cross-sectional images (slices) are made by rotating an X-ray source and detector around a subject as shown in figure 2.3.

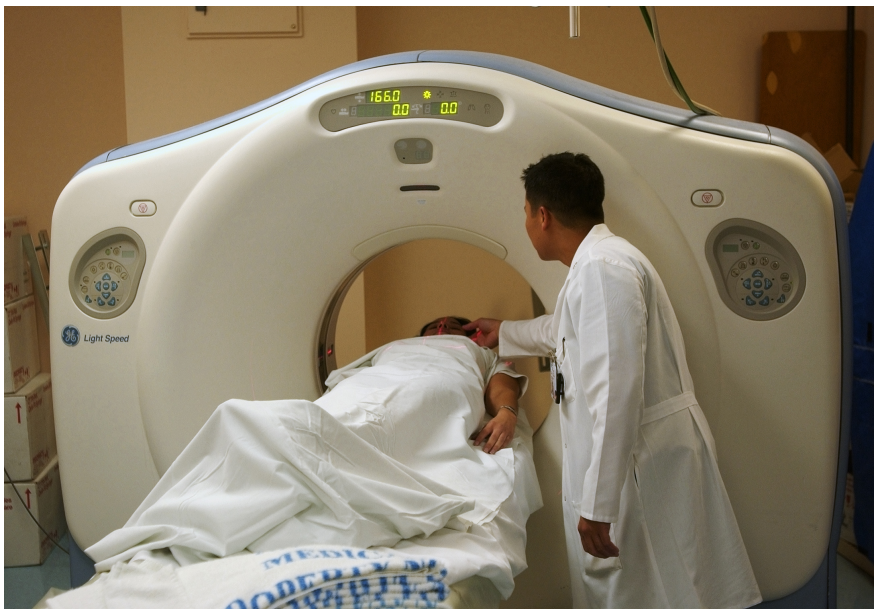

Figure 2.2: A patient inside a CT-scanner [12]

The source sends out a beam of X-rays with known intensity and the detector measures the radiation intensity on the opposite side. The difference between these two values is the mean attenuation of the signal due to the line of tissue between the source and detector. When rotating the source and detector, it is possible to get the attenuation values (measured in Hounsfield units) for all the pixels in a cross-section

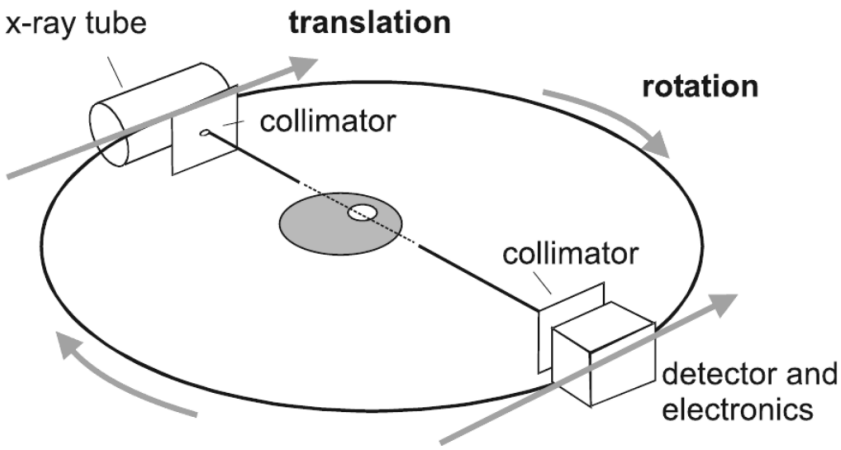

Figure 2.3: Principles of computed tomography [9]

of the subject. As different tissues have different attenuation properties, it is now possible create an anatomical cross-sectional image by applying a tomographic reconstruction algorithm to the signal. When performing helical rotations, it is even possible to get three-dimensional images. In order to improve the speed and accuracy of CT scanners, modern CT scanners use fan beam X-ray sources and multiple detector rows that make it possible to scan multiple slices at the same time (Figure 2.4).

A variation of CT that is used in chapter 6 is CBCT. In this type of scanner, the X-ray beam is conical shaped and the detector is able to perform two-dimensional measurements. This makes it possible to construct three-dimensional images using a single rotation.

Because air functions as a natural contrast agent, CT has the highest signal to noise ratio and spatial resolution of all pulmonary imaging tools. On top of that, the acquisition time is very short, allowing the whole lungs to be imaged during breath hold to rule out motion artifacts. Furthermore, this technique allows analyzing the region of interest in three dimensions. The disadvantage is that CT produces ionizing radiation, possibly resulting in adverse health effects for the patient. However, due to the high signal to noise ratio when imaging air, the radiation dose needed for FRI is much lower as compared to conventional CT scans [3]. With today's technology, it is possible to perform a thorax scan with an effective radiation dose for a patient of around 2 mSv. The next generation CT scanners will be using more advanced iterative imaging reconstruction algorithms and it is expected that the effective dose will be reduced to the level of a normal chest radiography. As children are more sensitive to radiation than adults, they were scanned with adapted protocols in order to decrease the dose even more.

Even more important than the quality of the image is the moment at which it is taken. This is a prerequisite for extracting functional data and also allows

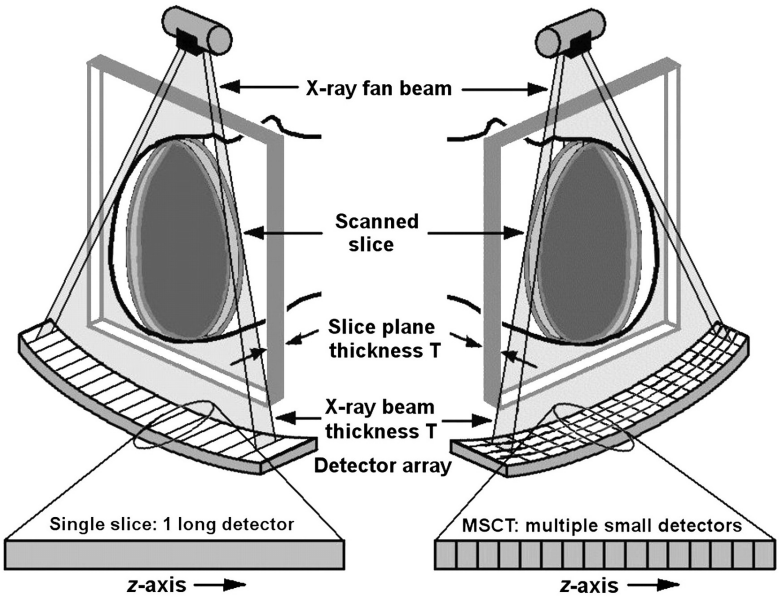

Figure 2.4: Computed tomography with multiple detectors [7]

comparing a pre and post situation. The moment is here defined as the lung level or the moment during the breathing cycle. For upper airway geometries this moment was set depending on the purpose, as the image has to give an optimal representation of the process one wants to investigate. Since obstructive sleep apnea is an expiratory phenomenon, it was hypothesized that the end inspiratory geometry is the main driver for collapsibility. Since inhalation medication is mostly taken during a slow inhalation, the scan was also taken during that maneuver. For the lower airways, the CT images were taken during breath hold at two distinct lung levels: at the end of a normal exhalation (functional respiratory capacity or FRC) and at maximal inspiration (total lung capacity or TLC). In this way, functional information is generated as it is now possible to assess how airway geometry and lobar volumes change over the breathing cycle. In order to scan (diseased) subjects at breath hold, the acquisition time needs to be as low as possible. In general, any scanner that is able to scan the whole lung in around 6 s with a voxel size of around 0.6 mm can generate high quality input data for FRI. Most modern 64-slice CT scanners fulfil these requirements.

As it is necessary to scan at the correct moment, the breathing signal has to be monitored while the patient is on the table. Using a pneumotach device, it is possible to get a real time measurement of the breathing pattern and lung levels. In this way, it is guaranteed that the images are taken at the moment that was predefined for the study.

The only devices that are needed to create the correct input data for FRI

analyses are a modern CT scanner and a pneumotach device. Since these devices are available in most clinical settings, FRI is not limited to academic research but is applicable in clinical trails and medical practice.

2.2 Image processing

After the acquisition of the medical images, the regions of interest are extracted using segmentation algorithms. A combination of automatic algorithms and manual correction is used to correctly select the voxels. The automatic airway segmentation algorithm that is used in this thesis is a proprietary algorithm based on the work of Tschirren et al. [13]. Although this approach is not ideal due to possible variability in the manual part, it is the only possibility at this moment. The results that were presented at the fourth international workshop on pulmonary image analysis in Toronto after a segmentation challenge showed that human interaction is still necessary when segmenting airways and lobes [2]. The biggest challenge is the automatic detection of fissure lines that are needed to make a distinction between the lobes as these are easily lost due to the noise in the images (Figure 2.5). An internal sensitivity study showed that the influences of the manual interventions are quite small when people are well trained (a maximal difference of less than 3 %). With this workflow, it is possible to segment down to bronchi with a diameter of about 1 – 2 mm. To obtain the most patient specific information, the lower airways are extracted at TLC level as the larger airway lumen allows segmenting more airway generations.

After the segmentation, the extracted voxels are converted to a triangulated three-dimensional model (Figure 2.6) on which anatomical measurements can be performed. Furthermore, this model can be post-processed by labeling the correct anatomical regions and defining inlets and outlets for the computational fluid dynamics simulations.

2.3 Computational fluid dynamics

Computational fluid dynamics (CFD) is a computer simulation technique that allows to determine the behavior of a flow in a model [6]. In this method, flow is described by the Navier-Stokes equations and is numerically solved on a computational grid (the mesh). This method makes it possible for the system of mathematical equations to be solved iteratively. The result is that flow features such as speed, pressure and density are known everywhere in the model.

The theory around CFD is described in previous work of the author [14] and is given in appendix A. For the integration with FRI, the Navier-Stokes equations can be adapted to be optimal for the study. These adaptations are described in the different chapters.

In most cases, adaptation is a synonym for simplification. CFD can be made very simple and very complicated, depending on the requirements. If one wants

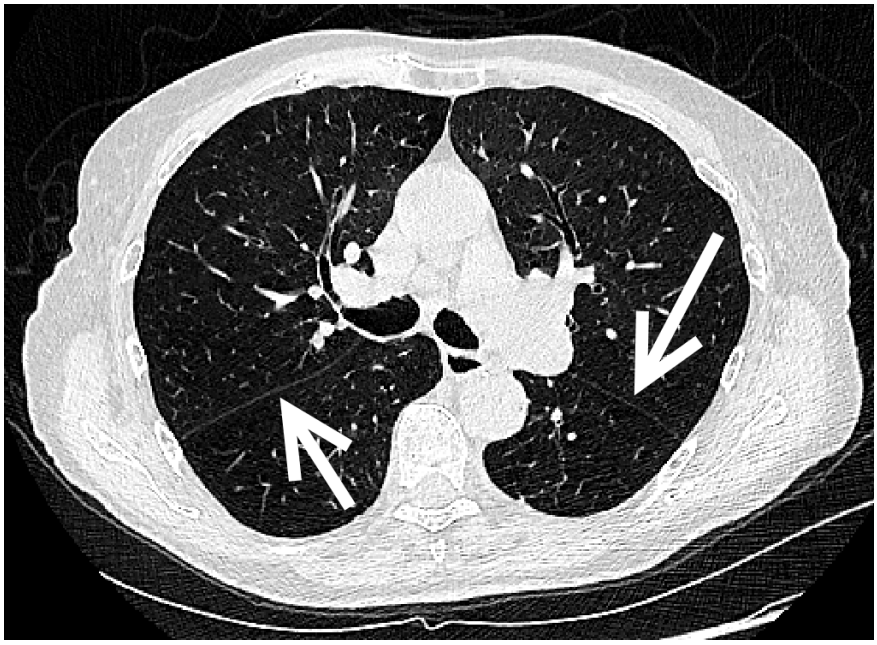

Figure 2.5: Axial CT-slice of the lung. The white arrows indicate the fissure lines

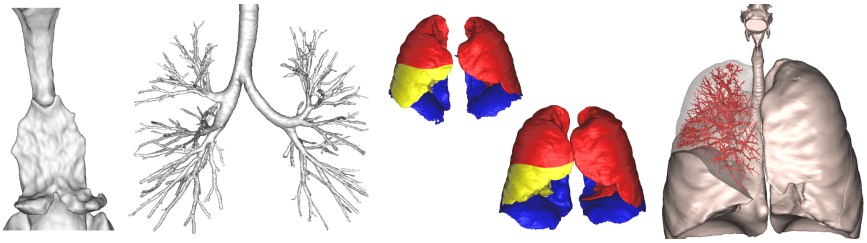

Figure 2.6: Reconstructed models of the upper airway, lower airways, lung lobes and pulmonary blood vessels

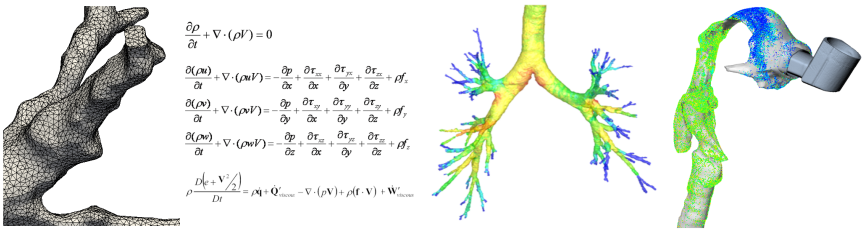

Figure 2.7: A detail of a meshed airway, the Navier-Stokes equations, two results of CFD calculations (pressure contours and particle deposition)

to design a car, it is useful to use very complex models that mimic the reality as good as possible as insights in every vortex can be used to optimize the design. As the car will be produced in mass, every small optimization can have large financial consequences. Furthermore, the computational grid can be manually optimized for the given geometry and boundary conditions can be defined exactly. If one wants to simulate a patient, it is useful to use models that are as simple as possible for the phenomenon one wants to investigate. As time is critical for making simulations clinically relevant, it is counterproductive to use complex models that do not add any clinical relevance as compared to much simpler models. One of the main reasons is that the numerical precision is not the limiting factor for a correct simulation, but the uncertainties in the boundary conditions are.

The largest problem when simulation biological flows is the correct definition of boundary conditions as it is very difficult to measure these in a patient in a non-invasive way. However, to make the simulations fully patient specific, physiological correct boundary conditions are a must.

Upper airways are the easiest to simulate (Figure 2.8). As there is only one inlet and one outlet, a simple physiological pressure difference or mass flow is sufficient to obtain good results. Although the possibility exists that upstream and downstream regions have an effect on the exact results, these will be very small making it difficult to justify the taking of additional scans to obtain more information about these regions. Also, upper airway simulations are mostly performed to simulate changes in upper airway functionality before and after an intervention that only affects that region.

When simulating lower airways, things become more complicated. A normal airway branch consists of one inlet and multiple outlets that are connected to different anatomical regions (the lobes) in the lung. While the boundary conditions at the inlet are straightforward (a physiological pressure or a mass flow) and are easy to measure, the boundary conditions at the outlets are unknown. The problem is that these conditions need to reflect the impedances of the downstream regions, which are not visible on the CT-scanner due to resolution limitations. However, as scans are taken at FRC and at TLC, some functional information concerning the downstream bronchial resistances and alveolar stiffness can be extracted. Although it is not possible to extract all individual features, it is possible to segment the envelop of the lobe. When segmenting the different lobes at the two levels, it is possible to compare the volumes. The volume difference between TLC and FRC of a certain lobe is then a measure for the flow that goes to that lobe. As it is known which outlet goes to which lobe, it is possible to define the flow that goes through that outlet. This is defined as the internal airflow lobar distribution (Figure 2.9). As outflow conditions are numerically not stable in these irregular geometries and as the flow per lobe is known but not the flow per outlet, an iterative algorithm is used that calculates the under pressures that are needed to obtain that flow.

The main advantage of this method is that it is fully patient specific, even incorporating the dynamics of diseased anatomical areas.

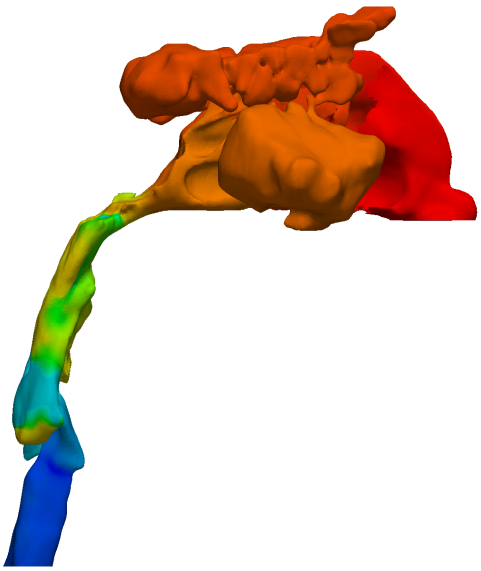

Figure 2.8: Pressure values from an inspiratory flow simulation in an upper airway. The under pressure at the larynx (blue) drives the air at atmospheric pressure (red) from the nostrils to the downstream regions, resulting in a pressure drop over the upper airway

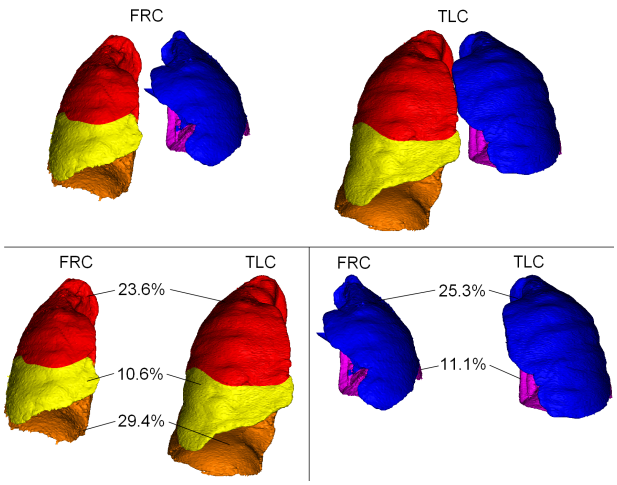

Figure 2.9: Lobes at FRC and TLC and the resulting internal airflow lobar distribution

2.4 Clinical relevance

In the previous sections, statements are made about the clinically relevant results that can be obtained with FRI. However, how are the clinically relevant outcome parameters defined? A clinically relevant parameter is a parameter that can be linked to the wellbeing of the patient. One of the problems in biomedical engineering is that clinicians and engineers have a different expertise and that communication between them can be confusing. As the clinician is in the end responsible for the patient, he will not make any decision based on data where he has no confidence in.

That is why the engineers have to provide the clinician with parameters that can be directly translated to the physiological status of the respiratory system. It is therefore not useful to provide him with local measures of turbulent kinetic energy if one wants to test if a certain inhalation compound has an effect in a patient suffering from asthma. More useful parameters are the changes in volume and resistance as it easy to see how these parameters correspond to lung function. When providing these parameters on a lobar level, the clinician can have more insight into the heterogeneity of the disease and the mode of action.

Especially these local insights make FRI so valuable. The human body adapts so well to new situations that traditional pulmonary function tests, which generate global outcome parameters covering the whole respiratory system, are not able to detect lung diseases in an early stage. In this way, the possibility exists that irreversible damage has occurred before any test has given an indication. That also emphasizes the importance of time. The goal of FRI is become a technique that is more sensitive than the traditional techniques, but with a speed that is similar.

References

[1] Keyoumars Ashkan and Adrian T. H. Casey. Pulmonary apex schwannoma. *Journal of Neurology, Neurosurgery & Psychiatry*, 63(6):719–719, December 1997.

[2] Reinhard Beichel, Atilla Kiraly, Jan-Martin Kuhnigk, Jamie McClelland, Kensaku Mori, Eva van Rikxoort, Simon Rit, Marleen de Bruijne, Bram van Ginneken, and Sven Kabus. *The Fourth International Workshop on Pulmonary Image Analysis*. CreateSpace Independent Publishing Platform, August 2011.

[3] P.M. Boiselle, G. Dippolito, J. Copeland, H. Kang, M. Ahmed, D. Weeks, E. Halpern, and S.N. Goldberg. Multiplanar and 3D imaging of the central airways: comparison of image quality and radiation dose of single-detector row CT and multi-detector row CT at differing tube currents in dogs. *Radiology*, 228(1):107–111, July 2003.

[4] Mike Cadogan. Life in the fast lane medical education blog: Quiz radiology 008, November 2009.

[5] Jan W De Backer, Wim G Vos, Samir C Vinchurkar, Rita Claes, Anton Drollmann, Denis Wulfrank, Paul M Parizel, Paul Germonpré, and Wilfried De Backer. Validation of computational fluid dynamics in CT-based airway models with SPECT/CT. *Radiology*, 257(3):854–862, December 2010. PMID: 21084417.

[6] Ludovic de Rochefort, Laurence Vial, Redouane Fodil, Xavier Maitre, Bruno Louis, Daniel Isabey, Georges Caillibotte, Marc Thiriet, Jacques Bittoun, Emmanuel Durand, and Gabriela Sbirlea-Apiou. In vitro validation of computational fluid dynamic simulation in human proximal airways with hyperpolarized 3He magnetic resonance phase-contrast velocimetry. *J Appl Physiol*, 102(5):2012–2023, May 2007.

[7] Lee W. Goldman. Principles of CT: multislice CT. *Journal of Nuclear Medicine Technology*, 36(2):57–68, June 2008. PMID: 18483143.

[8] R. E. Jacob, S. W. Morgan, B. Saam, and J. C. Leawoods. Wall relaxation of ^{3}He in spin-exchange cells. *Physical Review Letters*, 87(14):143004, September 2001.

[9] Willi A. Kalender. *Computed Tomography: Fundamentals, System Technology, Image Quality, Applications*. John Wiley & Sons, July 2011.

[10] Caroline McCann, Deepa Gopalan, Karen Sheares, and Nicholas Screaton. Imaging in pulmonary hypertension, part 1: clinical perspectives, classification, imaging techniques and imaging algorithm. *Postgraduate Medical Journal*, January 2012.

[11] University of Rhode Island. Biomedical engineering medical image database: Positron emission tomography.

[12] U. S. Navy photo by Chief Warrant Officer 4 Seth Rossman. English: National naval medical center, bethesda, md., (aug. 19, 2003) – hospital corpsman 2nd class roy puerto, right, of olangapo city, philippines, demonstrates the operation of the CT scan machine at the national naval medical center in bethesda, maryland. U.S. navy photo by chief warrant officer 4 seth rossman. (RELEASED), August 2003.

[13] J. Tschirren, T. Yavarna, and J. M. Reinhardt. Airway Segmentation Framework for Clinical Environments. In M. Brown, M. de Bruijne, B. van Ginneken, A. Kiraly, J.-M. Kuhnigk, C. Lorenz, J. R. McClelland, K. Mori, A. Reeves, and J. M. Reinhardt, editors, *Second International Workshop on Pulmonary Image Analysis*, page 227, London, UK, 2009.

[14] Cedric Van Holsbeke. *Numerical Modeling of Patient-Specific Airways*. Master thesis, Ghent University, Ghent, 2009.

Part I

Obstructive sleep apnea syndrome

3

Anatomical and functional changes in the upper airways of sleep apnea patients due to mandibular repositioning: A large scale study

Journal of Biomechanics 2011; 44: 442 – 449

Cedric Van Holsbeke, Jan De Backer, Wim Vos, Pascal Verdonck, Peter Van Ransbeeck, Tom Claessens, Marc Braem, Olivier Vanderveken and Wilfried De Backer

3.1 Abstract

The obstructive sleep apnea-hypopnea syndrome (OSA) is a sleep related breathing disorder. A popular treatment is the use of a mandibular repositioning appliance (MRA) which advances the mandibula during the sleep and decreases the collapsibility of the upper airway. The success rate of such a device is, however, limited and very variable within a population of patients. Previous studies using computational fluid dynamics have shown that there is a decrease in upper airway resistance in patients who improve clinically due to an MRA. In this article, correlations between patient specific anatomical and functional parameters are studied to examine how MRA induced biomechanical changes will have an impact on the upper airway resistance. Low-dose computed tomography (CT) scans are made from 143 patients suffering from OSA. A baseline scan and a scan after mandibular repositioning

(MR) are performed in order to study variations in parameters. It is found that MR using a simulation bite is able to induce resistance changes by changing the pharyngeal lumen. The change in minimal cross-sectional area is the best parameter to predict the change in upper airway resistance. Looking at baseline values, the ideal patients for MR induced resistance decrease seem to be women with short airways, high initial resistance and no baseline occlusion.

3.2 Contributions of the author

The author of this thesis was the principal researcher in this study. He performed the segmentation of the airways, investigated the meshing strategy and determined the setup of the computational fluid dynamics simulations. He was involved in the choice of outcome parameters, and performed all measurements manually. Furthermore, he was responsible for all statistical analyses and the interpretation of the results. The main challenge in this study was to extract and combine the large amounts of data, originating from different sources and having different file structures.

3.3 Introduction

The obstructive sleep apnea-hypopnea syndrome (OSA) is a sleep related breathing disorder that is characterized by repeated partial or complete closure of the pharynx [1]. To overcome this abnormal situation, the respiratory reflexes will activate the upper airway muscles in order to restore the flow to the lungs. These so-called arousals disturb the patient's sleep, causing excessive sleepiness at daytime [12]. The physiologic consequences of these episodes of airway collapse are repetitive bursts of sympathetic activity, hypoxia, hypercapnia, increased left ventricular afterload, and acute hypertension [5]. This pathology is often associated with increased risk of cardiovascular co-morbidity [29]. The golden standard in assessing the severity of OSA is the Apnea Hypopnea Index (AHI), which is the sum of all occurring respiratory events during the night, expressed on a hourly basis. This value can be measured by performing polysomnography in a sleep clinic [12, 19].

Previous studies showed that anatomical markers are not able to differentiate healthy individuals from OSA patients [35]. However, within the population of OSA patients, several of these do correlate with the severity of the pathology. The size of the pharyngeal airway lumen has been measured using different imaging techniques [7, 20, 28, 34, 36, 38]. Correlations are found between OSA severity and velopharyngeal airway size, minimal cross-sectional area [36], minimal posterior airway space [25, 30], reduced minimum palatal airway widths [17], airway volume and several other parameters describing the narrowness of the pharyngeal airway [34]. It is thought that these parameters can help to select the ideal treatment on a patient specific basis.

One of the possible treatments for OSA is the use of a mandibular repositioning

appliance (MRA). This device repositions the mandibula during the sleep and decreases the collapsibility of the upper airway. The major drawback of this treatment is that the success rate is limited and very variable within a population of patients [32]. A technique to predict the patient specific success would be of significant clinical importance [8]. Previous studies have shown that functional respiratory imaging, by means of computational fluid dynamics, can predict the efficiency of the MRA treatment. The percentage change in upper airway resistance correlates very well with a change in AHI [10, 11, 34].

In this study, relationships between patient specific anatomical and functional parameters will be studied. In this way, it is possible to examine how the mandibular repositioning (MR) induced biomechanical changes will have an impact on the upper airway resistance. The hypothesis is that these insights can help future clinical research.

3.4 Methods

3.4.1 Patient data

Low-dose computed tomography (CT) scans are made from 143 patients suffering from OSA, lying on their back. Patients are selected as possible candidates for MRA treatment after standard ENT clinical examination and standard polysomnography. The patients are then referred to the dental sleep professional for a clinical and radiological dental examination. Patients with active temporo-mandibular disfunction are excluded from the study as well as patients suffering from untreated caries and periodontal disease, edentulous patients and those having an insufficient number of remaining teeth. If no further contraindications for MRA treatment are present, the patients are included [26, 32]. A baseline scan and a scan with the mandibula in an advanced position using a prefabricated bite registration are performed so variations in parameters before and after MR can be studied. The registration bites used in this study can be seen in Figure 3.1 and are prepared by a dental technician and fitted as well as adjusted intraorally by the dentist titrating mandibular advancement to the maximal comfortable protrusion (MCP).

This position differs from the maximal protrusion (MP) in that the MP is an extreme protrusion where no other movements in lateral and/or cranio-caudal direction is possible anymore. The MCP is determined by having the patient in the MP from which the mandible is gently moved backwards, retruded, until the patient does not experience any more the constraints of the MP [6]. This procedure is repeated three times and the MCP is taken as the average of these measurements. The advantage of this procedure is furthermore that one does not start with an arbitrary position of, e.g. 50% of the MP, but with an individually determined position. This will furthermore increase the patients therapy compliance.

Institutional review board approval is obtained and all patients signed an informed consent.

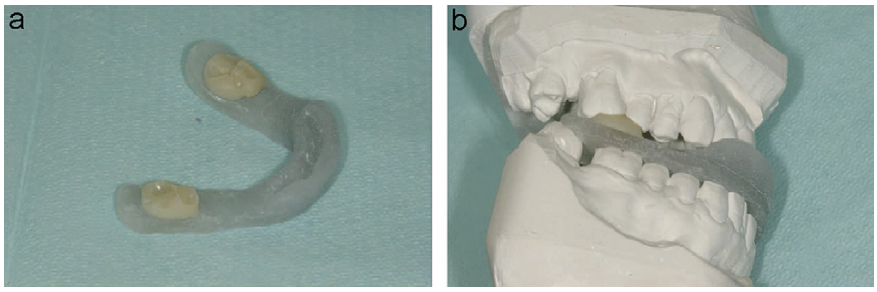

Figure 3.1: Registration bite as used in this study: (a) Registration bite, (b) Placed in an in situ model

3.4.2 Computational domain and grid

The CT-images of a patient are loaded into Mimics (Materialise, Leuven, Belgium) and are ordered in a way that correct sagittal, transverse and coronal views are reconstructed. On these reconstructed views, the region of interest is defined in a mask. A mask is defined as a part of the image where the gray values lie in a specified interval of Hounsfield units (HU). For upper airways, a range of HU between -1024 and -400 is seen to give very good results while a range between 226 and 3071 is used for the skull [16, 39]. The masks are extracted from the images and patient specific 3D reconstructions of the upper airway (the region behind the tongue, from the hard palate to the vocal cords, as seen in Figure 3.2(a) and skull are obtained.

To prepare the segmented upper airway for CFD calculations, a computational grid is created using TGrid 4.0.16 (Ansys, Lebanon, USA). A sensitivity study showed that a computational grid between 500,000 and 1,000,000 tetrahedral cells is sufficient for reaching mesh convergence.

3.4.3 Physical models and boundary conditions

Computations are done with a commercial Navier-Stokes solver (Fluent 6.3.26, Ansys, Lebanon, USA). As the air velocity in the upper airways is smaller than a Mach number of 0.2, the compressibility of air can be neglected [4]. Also, the flow in the upper airways is considered adiabatic. The Navier-Stokes equations are now given by the continuity (Equation 3.1) and momentum (Equation 3.2) equations for an incompressible flow with constant dynamic viscosity [2, 31, 33].

$$\nabla \cdot U = 0 \tag{3.1}$$

$$\rho \left(\frac{\partial U}{\partial t} + U \cdot \nabla U \right) = -\nabla p + \mu \nabla^2 U \tag{3.2}$$

In this equation, U is the velocity vector, ρ is the density, t is the time, p is the pressure and μ is the dynamic viscosity. The values for ρ and μ are taken

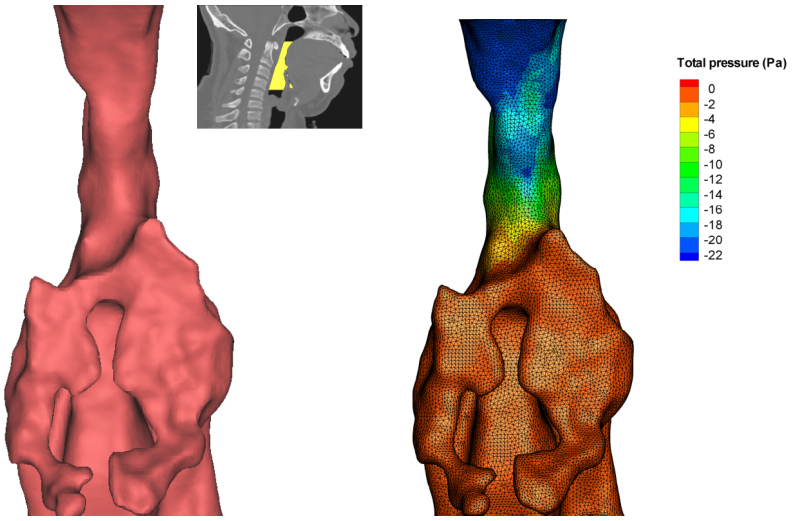

(a) Location of the upper airway (b) Computational grid and pressure drop

Figure 3.2: Three-dimensional upper airway model

for air at 15 °C. Flow simulations are performed by solving Equation 3.1 and Equation 3.2 numerically. The pressure-based solver is used with a node-based Green-Gauss gradient treatment as it achieves higher accuracy in unstructured tetrahedral grids compared to the cell-based gradient evaluation. Second-order discretization schemes are used for the pressure and momentum equations. The pressure-velocity coupling is solved using the SIMPLE scheme.

In order to enable proper comparison between the models the applied pressures at the in- and outlet are equal for all models. The steady boundary conditions are chosen, so that a laminar approach is possible. At the inlet, a total pressure of 0 Pa is set and at the outlet, a static pressure of -20 Pa is applied. Pressure boundary conditions are chosen for realistic inter-patient comparison as a constriction of the upper airway will not change the static pressure difference between atmosphere and lungs, but will restrict the airflow.

3.4.4 Outcome parameters

3.4.4.1 Upper airway morphology

All measurements on the upper airways are done before and after MR. In this way it is possible to detect morphological changes due to the treatment. The anatomical parameters that are measured are:

- The volume of the upper airway (V_{air}).

- The length of the upper airway (L). This is kept constant inter-patient.
- The minimal cross-sectional area of the upper airway (S_{min}).
- The position of the minimal cross-sectional area ($Pos_{S_{min}}$). This is done by measuring the distance between the top of the upper airway and the minimal cross-sectional area. This value is divided by L in order to obtain a parameter that is normalized for the length of the airway.

Starting from these measurements, other parameters are calculated. The mean cross-sectional area of the upper airway is calculated by means of Equation 3.3.

$$S_{avg} = \frac{V_{air}}{L} \tag{3.3}$$

The ratio S_{min}/S_{avg} is calculated as it is to be investigated whether upper airways with a rather uniform area distribution react differently from airways which are more concave and thus have a lower S_{min}/S_{avg}.

3.4.4.2 Skull morphology

To determine if the morphology of the skull has an influence on the MR, the angulus mandibulae (AM) is measured. Therefore, two construction lines are created. One line connects the midpoint of the arc formed by the AM with the center of the condylus. The other line contains the same midpoint and acts as a tangent line to the lower part of the mandibula. The angle between both lines is considered the AM as seen in Figure 3.3 [11].

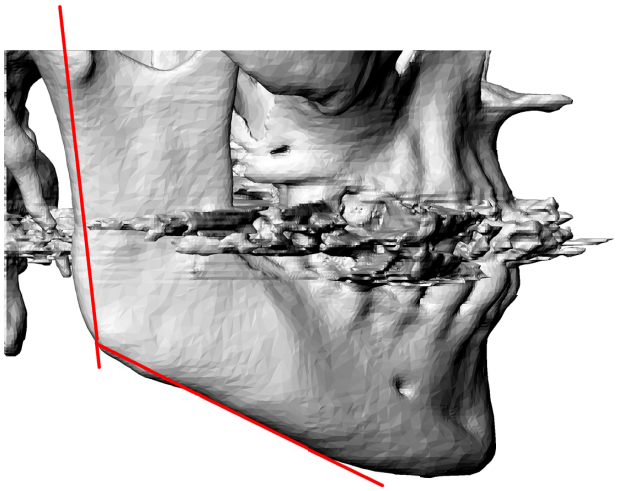

Figure 3.3: Angulus mandibulae

3.4.4.3 Functional parameters

The airway resistance R is given by Equation 3.4 [21, 23].

$$R = \frac{\Delta p}{\dot{m}} \tag{3.4}$$

In this equation, Δp is the total pressure drop and $\dot{m}$ is the mass flow rate in the upper airway. The resistance can be converted to a resistance-based radius r_{res} by combining the Poiseuille equation, given as Equation 3.5, with Equation 3.4.

$$\Delta p = \frac{8\mu L\dot{m}}{\pi\rho r_{res}^4} \tag{3.5}$$

$$\Leftrightarrow r_{res} = \sqrt[4]{\frac{8\mu L}{\pi\rho R}} \tag{3.6}$$

This parameter, given by Equation 3.6, is an approximation as the Poiseuille equation is only valid for straight, rigid tubes [3, 37]. However, r_{res} is calculated for statistical purposes as R can become infinite. Finally, it is investigated if men and women respond differently to the MR treatment.

3.4.5 Statistics

The data are tested for normality by using the Shapiro-Wilk W Test. It is found that none of the measured parameters and none of the calculated evolutions due to the treatment are normally distributed. Therefore, non-parametric techniques are needed to perform correct statistical analysis [27]. Statistical analysis was performed using commercial statistical software (Statistica 7.0, Statsoft). The techniques used in this paper are Spearman rank correlation and Mann-Whitney U-test. The significance level is chosen to be $p < 0.05$.

3.5 Results

3.5.1 Correlations between changes in functional and anatomical parameters

From here on, the symbol Δ is used to define the percentage difference between the parameter before and after MR. Figure 3.4(a) shows that there is a significant inverse correlation between the percent change in upper airway volume and the percent change in upper airway resistance. As L is held constant inter-patient, the exact same result is found when comparing ΔS_{avg}. There is a highly significant inverse correlation between ΔS_{min} and the percent change in resistance, as illustrated in 3.4(b). The resistance also tends to decrease when the airway becomes less concave. Detailed results are found in Table 3.1.

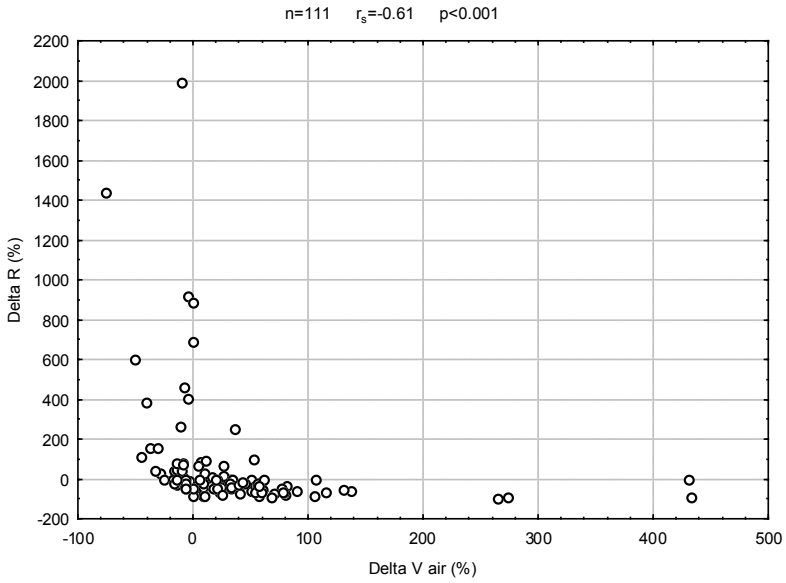

(a) Correlation between change in volume and change in resistance

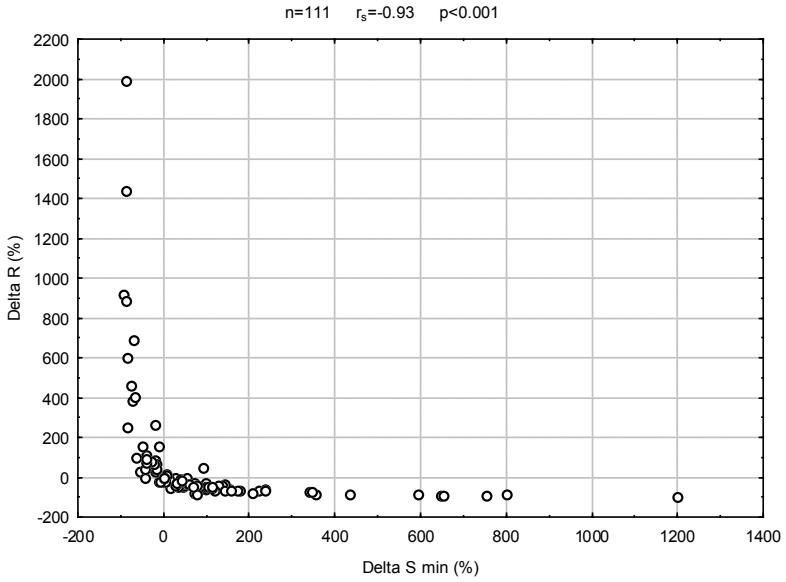

(b) Correlation between change in S_{min} and change in resistance

Figure 3.4: Correlations between changes in functional and anatomical parameters

Parameter1	Parameter2	n	r_s	p
ΔR	ΔV_{air}	111	-0.61	< 0.001
	ΔS_{avg}	111	-0.61	< 0.001
	ΔS_{min}	111	-0.93	< 0.001
	$\Delta S_{min}/S_{avg}$	111	-0.78	< 0.001
Δr_{res}	ΔV_{air}	123	0.56	< 0.001
	ΔS_{avg}	123	0.56	< 0.001
	ΔS_{min}	123	0.94	< 0.001
	$\Delta S_{min}/S_{avg}$	123	0.84	< 0.001

Table 3.1: Correlations between changes in functional and anatomical parameters

3.5.2 Correlations between changes in functional and baseline parameters

There seems to be a significant difference between men and women, as seen in Figure 3.5. In women, resistance tends to decrease while this is not the case in men. The baseline resistance, L and S_{min} can give an indication of the change in resistance, but the correlations are weak. No correlations with AM are found; however, it has to be mentioned that the AM data are missing for some patients as their CT-scan did not include the condylus, making it impossible to perform measurements. Detailed results are found in Table 3.2.

Better correlations between anatomical baseline parameters and resistance changes are found when patients with a baseline occlusion are excluded. Especially baseline L and r_{res} are promising parameters. Detailed results are found in Table 3.2. Also here, the gender differences are visible (see Table 3.3), but the resistance tends to decrease in both sexes. It is discovered that patients with smaller and more concave anatomical structures at baseline tend to occlude more after MR. Especially a smaller S_{min} and a smaller S_{min}/S_{avg} (see Figure 3.6(a)) are risk factors. Also, when S_{min} is closer to the tongue, there is a higher chance of obstruction, as seen in Figure 3.6(b). Detailed results are shown in Table 3.4.

3.6 Discussion

Details of the mode of action of MRAs in the treatment of snoring and OSA remain uncertain. Several studies suggest that the tongue, soft palate, lateral pharyngeal walls and mandibula interact to control airway size. It is thought that mandibular advancement induces complex changes in these structures, resulting in improved airway stability [9]. The goal of this study is to understand the MR induced biomechanical changes, in order to support future clinical research. The strength of this study is the fact that measurements are done on a very large patient data set. In this way, it is possible to confirm or reject hypotheses that were formulated

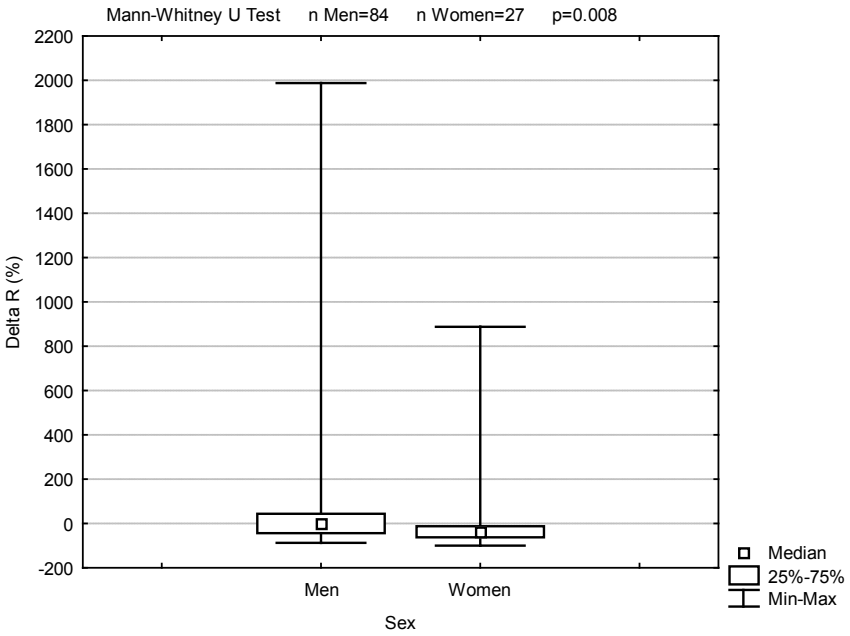

Figure 3.5: Difference between the sexes in change in resistance

Parameter1	Parameter2	All Patients			Patients without baseline collapse		
		n	r_s	p	n	r_s	p
ΔR	V_{air}	111	0.16	NS	96	0.29	0.004
	S_{avg}	111	0.13	NS	96	0.25	0.016
	S_{min}	111	0.20	0.040	96	0.39	< 0.001
	S_{min}/S_{avg}	111	0.18	NS	96	0.37	< 0.001
	L	111	0.15	NS	96	0.22	0.029
	r_{res}	111	0.21	0.029	96	0.41	< 0.001
	AM	100	0.16	NS	86	0.14	NS
Δr_{res}	V_{air}	123	-0.13	NS	108	-0.19	0.048
	S_{avg}	123	-0.10	NS	108	-0.19	0.048
	L	123	-0.21	0.018	108	-0.26	0.006
	r_{res}	123	-0.11	NS	108	-0.20	0.036
	AM	112	-0.09	NS	98	-0.07	NS

Table 3.2: Correlations between changes in functional and baseline parameters

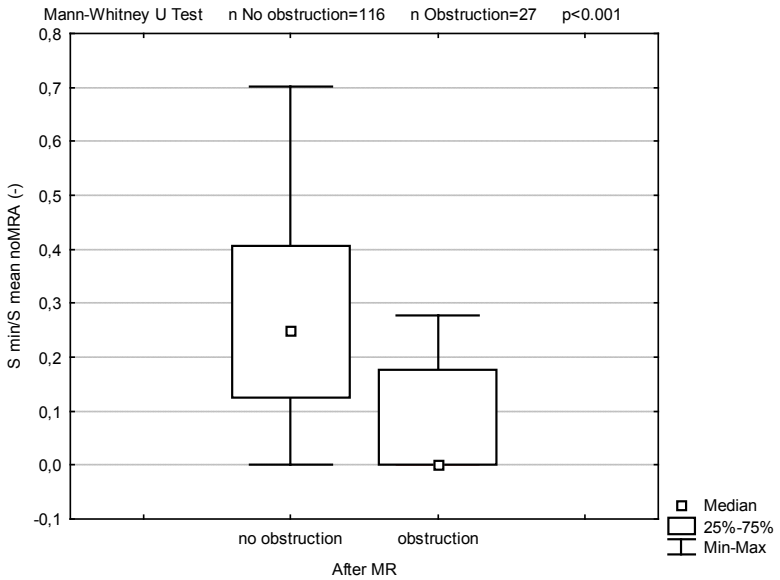

(a) Comparison of baseline S_{min}/S_{avg} in patients without and with MR induced obstruction

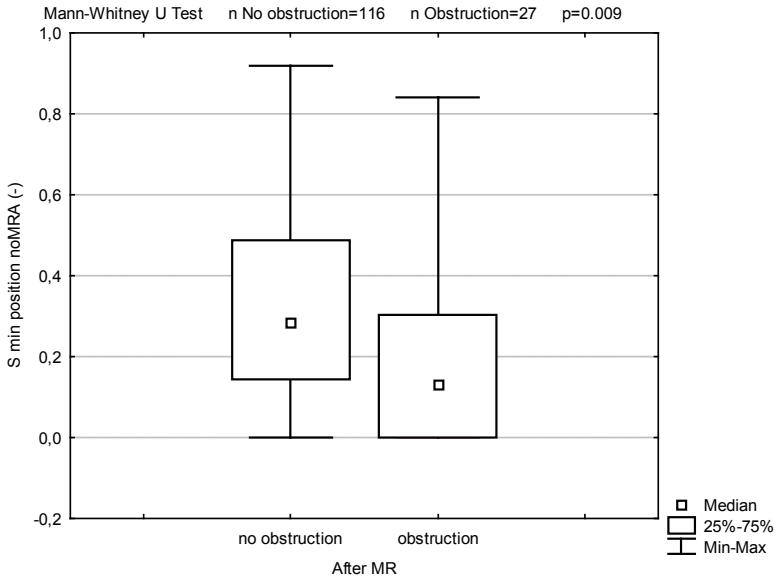

(b) Comparison of baseline $\mathrm{Pos}_{S_{min}}$ in patients without and with MR induced obstruction

Figure 3.6: Correlations between changes in functional and baseline parameters

All patients					
Parameter	nMen	nWomen	Median [quartile] men	Median [quartile] women	p
ΔR (%)	84	27	-0.34 [-45.48/41.41]	-38.08 [-61.08/-11.08]	0.008
Δr_{res} (%)	95	28	0 [-16.88/13.69]	12.55 [2.15/24.62]	0.003
Patients without baseline collapse					
Parameter	nMen	nWomen	Median [quartile] men	Median [quartile] women	p
ΔR (%)	71	25	-19.02 [-52.06/72.97]	-39.17 [-61.08/-20.39]	0.023
Δr_{res} (%)	82	26	0.43 [-26.89/16.86]	12.98 [3.75/26.61]	0.007

Table 3.3: Relationship between sex and the change in resistance

Parameter	n		median		p
	no obstruction	obstruction	no obstruction	obstruction	
V_{air} [mm^3]	116	27	8676.88	5837.18	$<$ 0.001
S_{avg} [mm^2]	116	27	138.12	86.55	0.002
S_{min} [mm^2]	116	27	39.04	0	$<$ 0.001
S_{min}/S_{avg} [-]	116	27	0.25	0	$<$ 0.001
$Pos_{S_{min}}$ [-]	116	27	0.28	0.13	0.009

Table 3.4: Risk factors for an MR induced obstruction

Number	Description
143	The total number of patients
123	Patients where Δr_{res} can be calculated. This excludes patients with $\Delta r_{res} = \pm\infty$
108	The same as above, but also excludes patients with a baseline occlusion
112-98	The same as the above two, but excludes patients where the AM could not be measured (CT-scan did not include the condylus)
111	Patients where ΔR can be calculated. This excludes patients with $\Delta r_{res} = \pm\infty$
96	The same as above, but also excludes patients with a baseline occlusion
100-86	The same as the above two, but excludes patients where the AM could not be measured (CT-scan did not include the condylus)

Table 3.5: Description of the amount of patients

in small-scaled studies. The different subgroups of patients that are used in the statistics are described in Table 3.5.

For this patient dataset, the upper airway resistance decreases in 58.7% of the cases, which is in the same range as the clinical success rate [24, 32]. It is found that the change in the upper airway resistance due to MR is determined by the change in pharyngeal lumen. This confirms the results of De Backer et al. [10] and Vos et al. [34] in small patient populations. However, in 20.3% of the patients, the resistance increases or stays the same while the volume increases. The changes in S_{min} and S_{min}/S_{avg} are better parameters to deal with this effect. In only 3.5% of the patients, the resistance increases or remains unchanged while these parameters increase. Especially a MR induced change in minimal cross-sectional area is a good parameter to predict the change in upper airway resistance. This is a very interesting finding and can be explained by the fact that the MR induces a rotation of the tongue in some patients. This rotation causes a partial or full occlusion of the upper airway and thus an increase in its resistance. The change in minimal cross sectional area is much more sensitive to this rotation than the change in volume, making it a better parameter to predict the resistance change. This strong link between CFD calculated resistance and the minimal cross-sectional area confirms the observations of Yu et al. [40].

It is discovered that baseline parameters can also give some indications about the change in resistance. Women tend to have a larger resistance decrease compared to men, which is confirmed by the clinical results of Marklund et al. [22]. Also, patients with a high initial resistance tend to improve more. However, people with a baseline occlusion or very concave airways have a higher chance of an occlusion while wearing the protrusive bite registration. This is especially true if S_{min} is close to the tongue. This is logical as even a small rotation of the tongue can cause an occlusion in these patients. This confirms clinical observations as an occlusion at baseline indicates that the patient suffers from severe OSA, while MRAs are only suited for patients with mild-to-moderate OSA [18].

No correlations using the angulus mandibulae are found, despite the fact that De Backer et al. [11] found a weak correlation between the AM and ΔV_{air} , making it a promising parameter for this larger scale patient study. A possible explanation is that a baseline value of the skull is only indirectly related to the soft tissue morphology. For future research, it would be interesting to check for correlations between resistance changes and mandibular protrusion. Mandibular protrusion has shown to have an effect on the pharyngeal cross-sectional area [13]. In a study using video endoscopy, the mandibular protrusion resulted in a significant increase in airway diameter, primarily in the oropharyngeal cross-sectional area, in both obese and nonobese subjects [14]. It is thought that protrusion is necessary to make the MRA work because placebo MRAs that do not perform a mandibular protrusion do not decrease AHI [15].

When excluding the patients with a baseline occlusion, better correlations are found. The ideal patients for MR induced resistance decrease seem to be women with short airways and high but finite initial resistance. However, one should take care about interpreting baseline resistance values. Due to the major and minor losses

in the geometry, the resistance will change with changing boundary conditions. The boundary conditions have to be exactly the same for all patients in order to get a resistance value that is only geometry dependent.

In this study, upper airway walls are assumed rigid. On longterm, it should be intriguing to develop a fluid structure interaction model of the upper airway in order to investigate the relationship between structural and flow parameters. In this way, the behavior of the surrounding tissue can be analyzed, opening possibilities to create predictive techniques for a whole range of treatments for OSA. Using rigid walls, the laminar approach is the most appropriate for calculating the geometrical resistance. A sensitivity study showed that there is no difference in resistance when using a turbulence model. The nasal cavity was not segmented as no geometrical changes are expected in this region as a result of mandibular repositioning. Furthermore, one would reduce the sensitivity to pick up change that are specifically induced by the device by including the nasal resistance in the CFD calculations. Another reason to exclude the nasal cavity was to limit radiation exposure as much as possible. Considering the limited influence of this region to describe MR related changes, it was judged to be better not to expose the retina to X-rays.

The largest limitation of this study is that the biomechanical observations cannot be mapped directly to clinical outcome. However, it is thought that the results of this study, using patient specific computer models, can provide an added value for the MR treatment of OSA. The gained biomechanical insights can be used to interpret results from future clinical research.

References

[1] American Academy of Sleep Medicine Task Force. Sleep-related breathing disorders in adults: recommendations for syndrome definition and measurement techniques in clinical research. *Sleep*, 22(5):667–689, August 1999. PMID: 10450601.

[2] John D. Anderson. *Computational Fluid Dynamics*. McGraw-Hill Science/Engineering/Math, 1st edition, February 1995.

[3] Steven J. Barker and Kevin K. Tremper. Pressure losses of endotracheal tubes: Preformed versus straight tubes. *Journal of Clinical Engineering*, 11(5):371–376, 1986.

[4] J. Blazek. *Computational Fluid Dynamics: Principles and Applications*. Elsevier Science, 1st edition, June 2001.

[5] T. Douglas Bradley and John S. Floras. Sleep apnea and heart failure: Part i: Obstructive sleep apnea. *Circulation*, 107(12):1671–1678, April 2003.

[6] M.J. Braem, M. Dieltjens, P.H. Van de Heyning, and O.M. Vanderveken. Mandibular protusive characteristics in patients using a duobloc adjustable mandibular repositioning appliance: preliminary results. San Antonio, Texas, June 2010. Abstract accepted by the American Academy of Dental Sleep Medicine 19th Annual Meeting.

[7] A S L Chan, R W W Lee, V K Srinivasan, M A Darendeliler, R R Grunstein, and P A Cistulli. Nasopharyngoscopic evaluation of oral appliance therapy for obstructive sleep apnoea. *The European Respiratory Journal: Official Journal of the European Society for Clinical Respiratory Physiology*, September 2009.

[8] Andrew Sl Chan and Peter A Cistulli. Oral appliance treatment of obstructive sleep apnea: an update. *Current Opinion in Pulmonary Medicine*, August 2009.

[9] Peter A. Cistulli, Helen Gotsopoulos, Marie Marklund, and Alan A. Lowe. Treatment of snoring and obstructive sleep apnea with mandibular repositioning appliances. *Sleep Medicine Reviews*, 8(6):443–457, December 2004.

[10] J. W. De Backer, W. G. Vos, S. L. Verhulst, and W. De Backer. Novel imaging techniques using computer methods for the evaluation of the upper airway in patients with sleep-disordered breathing: A comprehensive review. *Sleep Medicine Reviews*, 12(6):437–447, December 2008.

[11] J.W. De Backer, O.M. Vanderveken, W.G. Vos, A. Devolder, S.L. Verhulst, J.A. Verbraecken, P.M. Parizel, M.J. Braem, P.H. Van de Heyning, and W.A. De Backer. Functional imaging using computational fluid dynamics to predict treatment success of mandibular advancement devices in sleep-disordered breathing. *Journal of Biomechanics*, 40(16):3708–3714, 2007.

[12] Wilfried De Backer, Paul Germonpré, and Johan Verbraecken. *Handboek longziekten*. Uitgeverij Acco, Brusselsestraat 153, 3000 Leuven (België), 1e dr. edition, 2007.

[13] L. C. Dort, E. Hadjuk, and J. E. Remmers. Mandibular advancement and obstructive sleep apnoea: a method for determining effective mandibular protrusion. *Eur Respir J*, 27(5):1003–1009, May 2006.

[14] KA Ferguson, LL Love, and CF Ryan. Effect of mandibular and tongue protrusion on upper airway size during wakefulness. *Am. J. Respir. Crit. Care Med.*, 155(5):1748–1754, May 1997.

[15] Kathleen A Ferguson, Rosalind Cartwright, Robert Rogers, and Wolfgang Schmidt-Nowara. Oral appliances for snoring and obstructive sleep apnea: a review. *Sleep*, 29(2):244–262, February 2006. PMID: 16494093.

[16] G.R. Ferretti, I. Bricault, and M. Coulomb. Virtual tools for imaging of the thorax. *European Respiratory Journal*, 18(2):381 –392, 2001.

[17] Ama Johal and Clair Conaghan. Maxillary morphology in obstructive sleep apnea: a cephalometric and model study. *The Angle Orthodontist*, 74(5):648–656, October 2004. PMID: 15529500.

[18] Clete A Kushida, Timothy I Morgenthaler, Michael R Littner, Cathy A Alessi, Dennis Bailey, Jack Coleman, Leah Friedman, Max Hirshkowitz, Sheldon Kapen, Milton Kramer, Teofilo Lee-Chiong, Judith Owens, and Jeffrey P Pancer. Practice parameters for the treatment of snoring and obstructive sleep apnea with oral appliances: an update for 2005. *Sleep*, 29(2):240–243, February 2006. PMID: 16494092.

[19] J. o-Dee L. Lattimore, David S. Celermajer, and Ian Wilcox. Obstructive sleep apnea and cardiovascular disease. *Journal of the American College of Cardiology*, 41(9):1429–1437, May 2003.

[20] Hseuh-Yu Li, Ning-Hung Chen, Chao-Ran Wang, Yu-Hsiang Shu, and Pa-Chun Wang. Use of 3-dimensional computed tomography scan to evaluate upper airway patency for patients undergoing sleep-disordered breathing surgery. *Otolaryngology - Head and Neck Surgery*, 129(4):336–342, October 2003.

[21] Elaine Marieb and Katja Hoehn. *Anatomy and physiology: International edition*. Pearson Education (US), [S.l.], 3th edition, April 2007.

[22] Marie Marklund, Hans Stenlund, and Karl A Franklin. Mandibular advancement devices in 630 men and women with obstructive sleep apnea and snoring: tolerability and predictors of treatment success. *Chest*, 125(4):1270–1278, April 2004. PMID: 15078734.

[23] B. Mauroy, M. Filoche, E. R. Weibel, and B. Sapoval. An optimal bronchial tree may be dangerous. *Nature*, 427(6975):633–636, February 2004.

[24] Andrew Ng, Helen Gotsopoulos, Ali M Darendeliler, and Peter A Cistulli. Oral appliance therapy for obstructive sleep apnea. *Treatments in Respiratory Medicine*, 4(6):409–422, 2005. PMID: 16336026.

[25] Hüseyin Özdemir, Remzi Altin, Ayhan Söğüt, Fikret Çınar, Kamran Mahmutyazıcıoğlu, Levent Kart, Lokman Uzun, Halit Davşancı, Sadi Gündoğdu, and Nazan Tomaç. Craniofacial differences according to AHI scores of children with obstructive sleep apnoea syndrome: cephalometric study in 39 patients. *Pediatric Radiology*, 34:393–399, 2004.

[26] Francois-Xavier Petit, Jean-Louis Pepin, Georges Bettega, Hazem Sadek, Bernard Raphael, and Patrick Levy. Mandibular advancement devices: Rate of contraindications in 100 consecutive obstructive sleep apnea patients. *Am. J. Respir. Crit. Care Med.*, 166(3):274–278, August 2002.

[27] Kristina M. Ropella. *Introduction to Statistics for Biomedical Engineers*. Morgan & Claypool Publishers, 2007.

[28] Richard J Schwab, Michael Pasirstein, Robert Pierson, Adonna Mackley, Robert Hachadoorian, Raanan Arens, Greg Maislin, and Allan I Pack. Identification of upper airway anatomic risk factors for obstructive sleep apnea with volumetric MRI. *Am. J. Respir. Crit. Care Med.*, pages 200208–866OC, May 2003.

[29] Bharati Shivalkar, Caroline Van De Heyning, Mieke Kerremans, Diana Rinkevich, Johan Verbraecken, Wilfried De Backer, and Christiaan Vrints. Obstructive sleep apnea syndrome: More insights on structural and functional cardiac alterations, and the effects of treatment with continuous positive airway pressure. *Journal of the American College of Cardiology*, 47(7):1433–1439, April 2006.

[30] V Tangugsorn, O Krogstad, L Espeland, and T Lyberg. Obstructive sleep apnea: a canonical correlation of cephalometric and selected demographic variables in obese and nonobese patients. *The Angle Orthodontist*, 71(1):23–35, February 2001. PMID: 11211294.

[31] John C. Tannehill, Dale Arden Anderson, and Richard H. Pletcher. *Computational Fluid Mechanics and Heat Transfer*. Taylor & Francis, 2nd edition, 1997.

[32] O. M. Vanderveken, A. Devolder, M. Marklund, An N. Boudewyns, M. J. Braem, W. Okkerse, J. A. Verbraecken, K. A. Franklin, W. A. De Backer, and P. H. Van de Heyning. Comparison of a custom-made and a thermoplastic oral appliance for the treatment of mild sleep apnea. *Am. J. Respir. Crit. Care Med.*, 178(2):197–202, July 2008.

[33] H. Versteeg and W. Malalasekra. *An Introduction to Computational Fluid Dynamics: The Finite Volume Method*. Prentice Hall, August 1995.

[34] W. Vos, J. De Backer, A. Devolder, O. Vanderveken, S. Verhulst, R. Salgado, P. Germonpré, B. Partoens, F. Wuyts, P. Parizel, and W. De Backer. Correlation between severity of sleep apnea and upper airway morphology based on advanced anatomical and functional imaging. *Journal of Biomechanics*, 40(10):2207–2213, 2007.

[35] Wim G Vos, Wilfried A De Backer, and Stijn L Verhulst. Correlation between the severity of sleep apnea and upper airway morphology in pediatric and adult patients. *Current Opinion in Allergy and Clinical Immunology*, 10(1):26–33, 2010.

[36] Jennifer H. Walsh, Matthew S. Leigh, Alexandre Paduch, Kathleen J. Maddison, Danielle L. Philippe, Julian J. Armstrong, David D. Sampson, David R. Hillman, and Peter R. Eastwood. Evaluation of pharyngeal shape and size using anatomical optical coherence tomography in individuals with and without obstructive sleep apnoea. *Journal of Sleep Research*, 17(2):230–238, 2008.

[37] Nico Westerhof, Nikos Stergiopulos, and Mark I.M. Noble. *Snapshots of Hemodynamics*, volume 18. Springer US, 2005.

[38] B. Tucker Woodson and Marvin R. Wooten. Comparison of upper-airway evaluations during wakefulness and sleep. *The Laryngoscope*, 104(7):821–828, 1994.

[39] Muhammed Selim Yavuz, Mustafa Cemil Buyukkurt, Sinan Tozoglu, Ilhan Metin Dagsuyu, and Mecit Kantarci. Evaluation of volumetry and density of mandibular symphysis bone grafts by three-dimensional computed tomography. *Dental Traumatology*, 25(5):475–479, 2009.

[40] Chung-Chih Yu, Hung-Da Hsiao, Lung-Cheng Lee, Chih-Min Yao, Ning-Hung Chen, Chau-Jan Wang, and Yu-Ray Chen. Computational fluid dynamic study on obstructive sleep apnea syndrome treated with maxillomandibular advancement. *Journal of Craniofacial Surgery*, 20(2):426–430, 2009.

4

Functional respiratory imaging as a tool to assess upper airway patency in children with obstructive sleep apnea

Sleep Medicine 2013; 14(5): 433 – 439

Cedric Van Holsbeke, Wim Vos, Kim Van Hoorenbeeck, An Boudewyns, Rodrigo Salgado, Pascal Verdonck, Jose Ramet, Jan De Backer, Wilfried De Backer and Stijn Verhulst

4.1 Abstract

Objective: To investigate if anatomical and functional properties of the upper airway using computational 3D-models derived from CT images better predict obstructive sleep apnea (OSA) severity than standard clinical markers.
Methods: Consecutive children with suspected OSA underwent polysomnography, clinical assessment of upper airway patency and a CT scan while being awake. A 3D-reconstruction of the pharyngeal airway was built from these images, and computational fluid dynamics modelling of low inspiratory flow was performed using open source software.
Results: 33 children were included (23 boys, mean age was 6.0 $\pm$ 3.2 years). OSA was diagnosed in 23 patients. Children with OSA had a significantly lower volume of the overlap region between tonsils and adenoids (median volume of 1408 mm compared to 2173 mm; p = 0.04), a lower mean cross-sectional area at

this location (median of 69.3 mm^2 compared to 114.3 mm^2; p = 0.04) and a lower minimal cross-sectional area (median of 17.9 mm^2 compared to 25.9 mm^2; p = 0.05). Various significant correlations were found between several imaging parameters and the severity of OSA, most pronounced for upper airway conductance (r = -0.46; $p < 0.01$) for correlation between upper airway conductance and the apnea hypopnea index. No differences or significant correlations were observed with clinical parameters of upper airway patency. Preliminary data after treatment showed that none of the patients with residual OSA had their smallest cross-sectional area located in segment 3 and this frequency was significantly lower than in their peers whose sleep study normalized (64%; p = 0.05).
Conclusion: Functional respiratory imaging parameters are highly correlated with OSA severity and are a more powerful correlate than clinical scores of upper airway patency. Preliminary data also showed that we could identify differences in the upper airway of those subjects who did not benefit from a local upper airway treatment.

4.2 Contributions of the author

The author of this thesis was the principal technical researcher in this study. He was involved in the study design, scanning protocol and cooperated in the segmentation of the airways. While a commercial computational fluid dynamics (CFD) software package was used in chapter 3, he investigated how these problems could be solved using open source software. He created his own CFD solver based on OpenFOAM and tuned boundary conditions, solver settings and mesh settings to give similar results to the validated commercial software. The complex geometry of the nasal region and the need for automation (see section 12.2) made this a very challenging topic. Furthermore, the author designed algorithms to extract the outcome parameters in an automated way (see section 12.3). He was also involved in the statistical analyses.

4.3 Introduction

Obstructive sleep apnea (OSA) is a prevalent disorder affecting 1 to 4% of the general pediatric population [18]. However, this prevalence is much higher exceeding 50% in children with specific risk factors including obesity and Down syndrome [24, 26]. OSA in children is also associated with significant complications affecting the developing nervous and cardiovascular systems and should therefore be correctly treated [8].

The main anatomical risk factor for pediatric OSA is adenotonsillar hypertrophy but other factors such as craniofacial abnormalities, obesity and alterations in neuromotor tone may also play a role. Second, residual disease after adenotonsillectomy is present in a large proportion of children [6]. Although indices of nocturnal breathing improve in the majority of patients after adenotonsillectomy, there is a

subset of patients who do not significantly improve to have justified surgery. In view of several non-surgical alternatives, one of the challenges in this field will be to closely match the anatomical characteristics of an individual patient with the most appropriate treatment. A meta-analysis showed that the association between a clinical score of tonsillar hypertrophy and the severity of OSA is weak [21]. A number of imaging studies, mainly using magnetic resonance imaging (MRI), have investigated the relation between upper airway structural anatomy and OSA severity [1–5, 12, 14, 23]. Converting these images to three-dimensional (3D) models enables calculation of specific volumes of the upper airway, but also allows the application of computational fluid dynamics (CFD) too. This method can derive additional functional and quantitative properties of the upper airway such as local resistances.

It was shown that these CFD parameters predict the severity of OSA in adult patients as well as a response to treatment [10, 25, 27]. In children, CFD has mainly been used to investigate physiological changes in intra-luminal pressures and resistances during obstruction rather than as a parameter of OSA severity or as a tool for treatment selection [22, 28]. The aim of this study was therefore to evaluate upper airway characteristics by use of ultra low dose computed tomography (CT) and computational fluid dynamics in children with sleep-disordered breathing. Furthermore using preliminary data, we also investigated if these imaging parameters could predict treatment outcome.

4.4 Materials and Methods

4.4.1 Study population

Consecutive children and adolescents between 3 to 16 years referred to the Pediatric Sleep Lab of the Antwerp University Hospital for suspected OSA were included between January 2011 and May 2012. All children had to be free of any acute disease at the moment of sleep screening and subjects with neuromuscular disease or any genetic or craniofacial syndrome were excluded. The Ethical Committee of the Antwerp University Hospital approved this study and informed consent was obtained from the subjects and their parents.

4.4.2 Questionnaire and physical examination

The parents completed a standardized questionnaire regarding sleep and respiratory co-morbidities. Tonsillar size was rated by two authors (A.B. and S.V.) using the Brodsky scale [7]. A score “0” was given in case of tonsillectomy. Tonsillar hypertrophy was scored with tonsil size > 2. Modified Mallampati scale was also assessed [19]. Height and weight were measured according to standardized techniques. Body mass index (BMI) was calculated as weight in kilograms over height in m^2, and was further analyzed as z-scores.

4.4.3 Polysomnography

All subjects underwent polysomnography (Brain RT, OSG, Rumst, Belgium) according to standardized criteria. All tracings were manually scored using the AASM guidelines [15]. OSA was defined if obstructive apnea index (OAI) ≥ 1 or obstructive apnea hypopnea index ≥ 2. Other parameters of interest included mean oxygen saturation (<SaO2>), SaO2 nadir, oxygen desaturation index (ODI) and arousal index.

4.4.4 CT scan

All patients underwent a CT scan to evaluate upper airway geometry. Scanning was performed with patients in supine and neutral position. The scan was performed using a GE LightSpeed 64-slice CT scanner with an average acquisition time between two to five seconds. This resulted in a dataset containing an average of 350 – 400 DICOM images, all images having an in-plane spatial resolution of 0.3 mm and reconstructed with a slice increment of 0.5 mm. Since the main interest was to obtain images discriminating air in the airways from the surrounding soft-tissue, all CT examinations were performed with an adapted low-dose scan protocol. This was achieved using an 80 kV setting, a modulated mA dosage depending on anatomic configuration (less dose in anatomic short-axis and more dose in the long-axis direction) and by limiting the scan range to the strictly minimal anatomic limits.

4.4.5 Upper airway morphology extraction from CT

The acquired DICOM images were processed using a commercial software package (Mimics 15.0, Materialise). Subsequently a segmentation of the upper airway was done using the Hounsfield Unit (HU) of each voxel in the DICOM images as a discriminatory parameter, making a binary distinction between air and solid structures. The HU is a value for the radiodensity of the tissue and reaches from -1024 to 3071. Characteristic values on the Hounsfield scale are -1024 HU and 1000 HU respectively corresponding with air and bone. Segmentation was performed from the nares to the first thoracic vertebra. The segmented region was then converted to a 3D model using a contour interpolation algorithm. Since this model is based on a segmentation of (near) cubic pixels, a staircasing-effect can result. Using an appropriate smoothing algorithm with volume compensation the 3D model was converted to a smooth realistic model without loss of patient specific morphology of the upper airway. This model was then used for detailed analysis of the anatomical parameters, volume meshing and CFD simulation. The following parameters were calculated: effective upper airway volume, minimal and mean cross-sectional area. Effective upper airway volume is defined as the total upper airway volume excluding the regions where there is almost no flow such as the sinuses and the air pockets close to the vocal cords. The upper airway was then divided in the following regions (Figure 4.1): nostril to bottom of inferior turbinate (segment 1), bottom of inferior turbinate to choanae (segment 2), choanae to tip of

uvula (segment 3); uvula to epiglottis (segment 4) and epiglottis to the first thoracic vertebra (segment 5). Volumes of these segments were also calculated and the location of the minimal cross-sectional area was recorded.

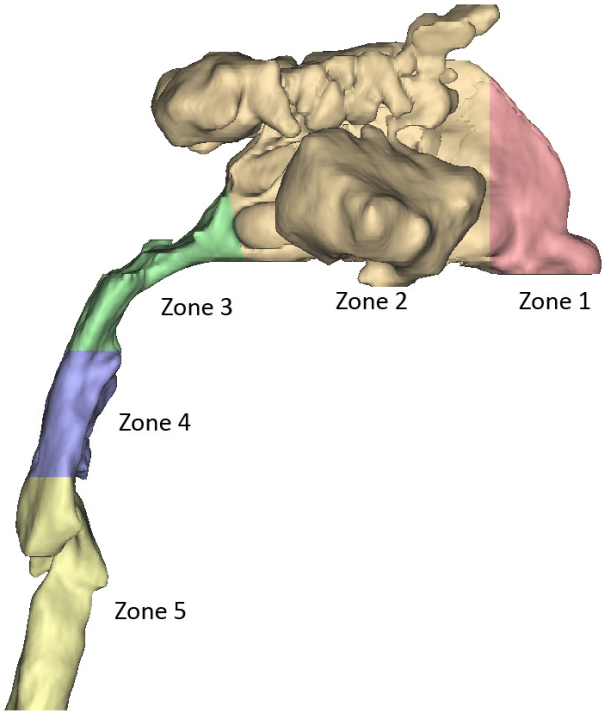

Figure 4.1: Studied regions of the upper airway: nostril to bottom of inferior turbinate (segment 1), bottom of inferior turbinate to choanae (segment 2), choanae to tip of uvula (segment 3), uvula to epiglottis (segment 4), and epiglottis to the first thoracic vertebra (segment 5).

4.4.6 Upper airway characteristics extraction from CFD

The 3D model obtained after segmentation was then divided into discrete cells to form a hexahedral dominant computational domain (SnappyHexMesh 2.0.1, OpenCFD Ltd, UK). The cells volumes were in the order of 1e-14 to 1e-8 m^3. The mesh was not aligned to the axial flow direction and the cells were extra refined near the boundaries. This resulted in a computational grid of the upper airway typically consisting of approximately 800,000 computational cells. This 3D mesh was exported and read into a custom Reynolds Average Navier Stokes CFD solver based on OpenFOAM 2.0.1 (OpenCFD Ltd, UK). Here the following boundary conditions were set to the model:

- a pressure outlet at the outlet surface in the larynx of -20 Pa
- a pressure inlet at the inlet surface at the nostrils of 0 Pa,
- non-impermeable walls (no-slip condition) for the sides of the upper airway.

Pressure based boundary conditions were used as this enables the simulation of the flow demand for the wide range of patient ages and sizes. Second-order discretization schemes were used and the pressure-velocity coupling was solved using the SIMPLE scheme. A steady, laminar simulation of the inspiratory airflow was then performed until convergence of the mass flow rate through the upper airway was achieved. From the outcome of the CFD analysis the resistance of the upper airway was calculated. Some patients expressed an obstruction during the CT-scan. Therefore, this value was transformed to the inverse of the resistance to the fourth power and defined as the conductance.

4.4.7 Statistical analysis

Statistical analysis was performed using IBM SPSS 20.0. Normally distributed data are presented as mean $\pm$ standard deviation (SD) and skewed data as median and range. Consecutive patients referred for possible OSA were classified as normal or OSA based on the results of the sleep study. No individual matching was performed. Groups were compared using Mann-Whitney or chi-square analyses. Spearman correlation analysis was also performed. A multiple regression analysis for the logarithm of oAHI was also performed. All analyses are two-tailed and significance was set as $p < 0.05$.

In view of our hypothesis that CFD analysis of the upper airway would be a more sensitive correlate of the severity of OSA, we based a sample size calculation on the correlation between upper airway conductance and oAHI. The correlation coefficient was set on 0.48 based on preliminary data. Based on this coefficient with alpha set at 0.05 and power at 0.80, the requested sample size was 25 subjects.

4.5 Results

4.5.1 Patient characteristics

33 children were included. There were 23 boys and mean age was 6.0 $\pm$ 3.2 years. Mean BMI z-score was 0.65 $\pm$ 1.50 and 11 children were overweight or obese. Respiratory allergy was diagnosed in 5 patients and asthma in 4 patients. Seven children had a prior history of adenotonsillectomy and 3 had a history of adenoidectomy. OSA was diagnosed in 23 patients (70%). There was no difference in characteristics between subjects with and without OSA except for several polysomnographic characteristics (Table 4.1).

	Normal sleep study	OSA	p
N	10	23	
Age (y)	7.2 ± 3.1	6.5 ± 3.8	0.2
Sex (% males)	60%	74%	0.4
BMI z-score	1.1 ± 1.2	0.8 ± 1.6	0.5
Respiratory Allergy (%)	30%	10%	0.1
Asthma (%)	20%	10%	0.6
Previous Adenotonsillectomy (%)	20%	22%	0.9
Previous Adenoidectomy (%)	20%	4%	0.2
OAI	0.0 (0.0 – 0.1)	0.8 (0.0 – 2.6)	**<0.001**
oAHI	0.6 (0.2 – 1.9)	8.2 (3.7 – 34.0)	**<0.001**
RDI	1.5 (0.8 – 5.0)	14.3 (5.1 – 35.6)	**<0.001**
ODI	0.3 (0.0 – 0.9)	2.8 (0.7 – 5.0)	**<0.001**
<SaO2> (%)	97.0 (96.4 – 98.3)	96.9 (95.8 – 97.8)	0.4
SaO2 nadir (%)	87.0 (82.0 – 92.0)	88.0 (85.0 – 92.0)	0.9
Arousal Index	8.4 (0.5 – 43.6)	18.7 (2.8 – 29.0)	0.1

Table 4.1: Patient and sleep characteristics of subjects with and without OSA

4.5.2 Correlation between imaging parameters and OSA

Children with OSA had a significantly lower volume of segment 3, a lower mean cross-sectional area of segment 3 and a lower minimal cross-sectional area (Table 4.2). Various significant correlations were found between imaging parameters and OSA severity, most pronounced for conductance, followed by the minimal cross-sectional area, mean cross-sectional area of segments 3 and 5, volumes of segments 3 and 5, mean cross-sectional area and effective upper airway volume (Table 4.3 and Figure 4.2). The minimal cross-sectional area was located in segment 3 (overlap region of tonsils and adenoids) in half of the studied patients (52%), followed by segment 5 (30%), segment 2 (9%), segment 1 (6%) and segment 4 (3%).

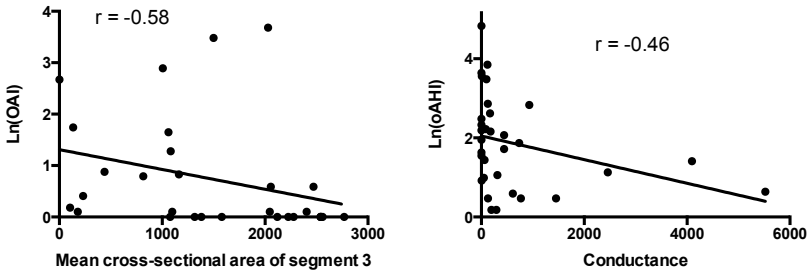

(a) (b)

Figure 4.2: Scatterplot between the mean cross-sectional area of segment 3 and OAI (part a) and conductance and oAHI (OAI and oAHI were log-transformed).

	Normal sleep study	OSA	p
Upper airway volume (mm^3)	29718.6 (13551.2 – 55091.6)	17387.4 (2610.4 – 62025.7)	0.2
Effective upper airway volume (mm^3)	25834.7 (9802.3 – 46853.0)	14717.5 (2447.7 – 52655.3)	0.1
Volume of segment 1 (mm^3)	2438.8 (961.5 – 4278.6)	1966.2 (393.6 – 3810.4)	0.09
Volume of segment 2 (mm^3)	12805.2 (1656.3 – 34553.0)	5343.4 (246.3 – 35710.2)	0.2
Volume of segment 3 (mm^3)	2172.5 (1077.2 – 2769.8)	1407.9 (0.0 – 2699.9)	0.04
Volume of segment 4 (mm^3)	960.6 (289.3 – 2315.2)	1317.9 (0.0 – 3301.0)	0.9
Volume of segment 5 (mm^3)	5539.5 (2297.8 – 7476.8)	3896.5 (2297.8 – 7476.8)	0.1
Mean cross-sectional area (mm^2)	185.5 (75.99 – 320.91)	116.20 (23.31 – 318.35)	0.2
Mean cross-sectional area of segment 1 (mm^2)	130.72 (50.60 – 225.19)	92.28 (20.71 – 200.55)	0.09
Mean cross-sectional area of segment 2 (mm^2)	317.81 (40.40 – 803.56)	171.36 (9.47 – 849.77)	0.1
Mean cross-sectional area of segment 3 (mm^2)	114.34 (56.70 – 145.78)	69.29 (0.00 – 142.10)	0.04
Mean cross-sectional area of segment 4 (mm^2)	151.55 (83.04 – 605.85)	159.90 (0.00 – 287.34)	0.5
Mean cross-sectional area of segment 5 (mm^2)	93.87 (52.22 – 145.00)	72.49 (25.66 – 145.42)	0.2
Minimal cross-sectional area (mm^2)	25.9 (11.2 – 58.0)	17.9 (0.0 – 77.9)	0.05
Conductance [$(L/kPas)^{\frac{1}{4}}$]	301.6 (6.1 – 5521.9)	92.2 (0.0 – 4096.0)	0.2

Table 4.2: Imaging parameters in subjects with and without OSA

	Upper airway volume	Effective upper airway volume	Volume of segment 1	Volume of segment 2	Volume of segment 3	Volume of segment 4	Volume of segment 5	Minimal cross-sectional area
OAI	-0.36*	-0.40*	-0.36*	-0.33	-0.58°	-0.09	-0.51°	-0.45*
oAHI	-0.26	-0.28	-0.25	-0.24	-0.42*	-0.06	-0.41*	-0.37*
RDI	-0.33	-0.35*	-0.30	-0.35*	-0.39*	-0.13	-0.41*	-0.41*
ODI	-0.25	-0.26	-0.23	-0.20	-0.34	-0.13	-0.40*	-0.40*
<SaO2>	-0.00	0.03	0.02	0.05	0.01	-0.02	-0.10	0.23
SaO2 nadir	0.27	0.31	0.22	0.38*	0.29	0.04	0.16	0.34
Arousal index	-0.41*	-0.39*	-0.34	-0.32	-0.31	-0.40*	-0.43*	-0.37*

	Mean cross-sectional area	Mean cross-sectional area of segment 1	Mean cross-sectional area of segment 2	Mean cross-sectional area of segment 3	Mean cross-sectional area of segment 4	Mean cross-sectional area of segment 5	Conductance
OAI	-0.36*	-0.36*	-0.32	-0.58°	-0.04	-0.36*	-0.43*
oAHI	-0.27	-0.25	-0.25	-0.42*	-0.22	-0.35*	-0.46°
RDI	-0.34*	-0.30	-0.36*	-0.39*	-0.16	-0.34*	-0.46°
ODI	-0.28	-0.23	-0.20	-0.34	-0.32	-0.39*	-0.52°
<SaO2>	0.01	0.02	0.09	0.01	-0.01	-0.20	0.32
SaO2 nadir	0.30	0.22	0.37*	0.29	0.04	0.03	0.41*
Arousal index	-0.37*	-0.34*	-0.31	-0.31	-0.30	-0.40*	-0.40*

Table 4.3: Correlation analyses between imaging parameters and OSA severity ($p < 0.05$; °$p < 0.01$)*

4.5.3 Correlation between clinical assessment of upper airway patency and OSA

There was no difference in parameters reflecting the clinical assessment of upper airway patency between subjects with or without OSA (Table 4.4). Spearman correlation analyses between these parameters and OSA severity is presented in Table 4.5. Several trends were observed for Mallampati score that reached statistical significance only with SaO2 nadir.

	Normal sleep study	OSA	p
Mallampati score	2 (1 – 3)	2 (1 – 3)	0.2
Tonsillar size	2 (0 – 3)	3 (0 – 4)	0.6
Tonsillar hypertrophy	20%	48%	0.2

Table 4.4: Clinical assessment of upper airway patency in subjects with or without OSA

	Mallampati	Tonsillar size
OAI	0.34	0.11
oAHI	0.35	0.27
RDI	0.34	0.29
ODI	0.10	0.28
<SaO2>	-0.18	-0.15
SaO2 nadir	-0.39*	-0.28
Arousal index	0.17	-0.08

*Table 4.5: Correlation analyses between clinical parameters of upper airway patency and OSA severity (*p < 0.05)*

4.5.4 Correlation between imaging and clinical assessment of upper airway patency

Tonsillar size significantly correlated with the volume of segment 3 (r = -0.49; p = 0.004), the mean cross sectional area of segments 2 (r = -0.35; p = 0.04) and 3 (r = -0.49; p = 0.004), the minimal cross-sectional area (r = -0.34; p = 0.05) and upper airway conductance (r = -0.50; p = 0.004). No significant correlations were found for Mallampati score.

4.5.5 Correlation analyses for upper airway conductance and minimal cross sectional area

Upper airway conductance was correlated with the volumes of segment 1 (r = 0.68; p < 0.001), segment 2 (r = 0.71; p < 0.001), segment 3 (r = 0.58, p = 0.001) and

segment 5 ($r = 0.45$; $p = 0.009$) and with the mean cross-sectional area ($r = 0.69$; $p < 0.001$), the mean cross-sectional area of segment 1 ($r = 0.68$; $p < 0.001$), 2 ($r = 0.73$; $p < 0.001$) and 3 ($r = 0.58$; $p = 0.001$). The minimal cross-sectional area was correlated with the volumes of segment 1 ($r = 0.68$; $p < 0.001$), segment 2 ($r = 0.59$; $p < 0.001$), segment 3 ($r = 0.67$, $p = 0.001$) and segment 5 ($r = 0.54$; $p = 0.009$), and the mean cross-sectional area ($r = 0.60$; $p < 0.001$), mean cross-sectional of segments 1 ($r = 0.68$; $p < 0.001$), 2 ($r = 0.59$; $p < 0.001$) and 3 ($r = 0.67$; $p < 0.001$). Multiple regression analysis was not possible because of multicollinearity between these parameters.

4.5.6 Final model for oAHI

In multiple regression analysis, only the volume of segment 5 was significantly correlated with oAHI. Volume and mean cross-sectional area of segment 3, the minimal cross-sectional area, upper airway conductance, Mallampati score and tonsil size did not reach sufficient significance to remain in a stepwise model. However, results should be interpreted with caution because of multicollinearity between these parameters.

4.5.7 Post-treatment data

Post-treatment data was available for 15 patients diagnosed with OSA: 8 patients underwent adenotonsillectomy, 2 patients adenoidectomy and 5 patients were treated with montelukast. A control polysomnography showed residual OSA in 4 out of 15 patients. None of the patients with residual OSA had their smallest cross-sectional area located in segment 3 and this frequency was significantly lower than in their peers whose sleep study normalized (percentage of subjects with the smallest cross-sectional area in segment 3 was 64% in this group; $p = 0.05$). There were no other differences between these two groups.

4.6 Discussion

This study investigated upper airway dimensions during wakefulness by means of computational fluid dynamics in children with sleep-disordered breathing. Our study clearly showed that upper airway dimensions are correlated with OSA severity. Furthermore, preliminary data showed that 4 subjects with residual OSA after treatment had their smallest cross-sectional area, prior to surgery, outside of the overlap region between adenoids and tonsils (segment 3) suggesting that imaging could predict the effect of treatment outcome.

Our study agrees with previous imaging studies that children with OSA have smaller airways. In our study, children with OSA had a significantly lower volume and mean cross-sectional area of segment 3 (overlap region between adenoids and tonsils) and a lower minimal cross-sectional area. Second, multiple significant correlations were found between upper airway volume, the minimal cross-sectional

area, mean cross-sectional area, mean cross-sectional area and volumes of segments 1, 2, 3 and 5 and several markers of OSA severity indicating that a smaller upper airway was related to more severe OSA. Fregosi et al. found similar differences and correlations in 18 children with OSA studied by MRI [13]. Similarly, Arens et al. demonstrated a smaller minimal and mean cross-sectional area and a smaller airway volume. Furthermore, the most restricted segment of the airway was the overlap region [2, 3]. Donnelly et al. also observed similar differences in another MRI study [12]. Our study also showed that CFD-based parameters are even stronger correlated with OSA severity. The CFD-calculated conductance expressed the highest correlation coefficient with oAHI, RDI, ODI and SaO2 nadir suggesting that CFD brings additional value to imaging-based upper airway analysis. This finding confirms previous data in adults with OSA [10]. Although we have to note that the volume of segment 5 was the only significant variable in a multiple regression analysis of oAHI. This could indicate that the narrowing or loss of tone of the upper airway extends into the trachea as shown in adults [17] or that there is less tracheal traction on the upper airway. However, this finding should be confirmed in follow-up studies because multiple regression was difficult to perform because of multicollinearity between these variables. CFD has only been applied in a limited number of studies in pediatric OSA. Xu et al. studied the influence of pharyngeal airway shape in children on internal pressure distribution in children with OSA [28]. Another study by Persak et al. applied CFD to estimate pharyngeal airway resistance and compliance in children with and without OSA. They showed that the airways of subjects with OSA were more compliant and that this method could also characterize differences along the pharynx and between OSA subjects. These studies clearly show the additional value of this technique. CFD allows not only for a non-invasive estimation of functional characteristics of the upper airway but also allows for more detailed segmental analyses. 3D-airway reconstruction and/or CFD analysis can identify that part of the airway that is most likely responsible for OSA in an individual patient. Resistance and conductance are ideal CFD endpoints as these incorporate both flow and pressure measurements in a given geometry and thus provide a lot of information in one single number. Furthermore, clinicians are familiar with these terms, giving them more insight in the clinical relevance of CFD. It could be interesting to investigate local flow parameters such as maximum velocity and minimal pressures. However, it is difficult to assess what the influence of these very local effects is in a complex biological system. The results are promising and future studies should use these techniques to predict the effect of adenotonsillectomy for instance prior to the actual surgery. In this prospect, we demonstrated that there was a difference in the location of the smallest cross-sectional area in subjects who did not benefit from local upper airway treatment. This study therefore warrants more and larger scale studies to investigate the usefulness of imaging coupled with CFD in predicting treatment response. Furthermore, these studies should include other subpopulations where other anatomical factors than adenotonsillar hypertrophy and especially neuromotor factors are playing a more dominant role such as Down syndrome, cerebral palsy and obesity.

In spite of the limited applications of CFD in pediatric sleep apnea, CFD has been validated on in vitro models both in children as in adults [9, 11, 16, 28]. Our present study did not include such a validation arm, but there was a significant correlation between the degree of tonsillar hypertrophy and airway conductance. Significant correlations were also observed between the Brodsky scale and the minimal cross-sectional area and the volume of segment 3. In spite of these correlations, there was no significant relation between clinical assessment of upper airway patency and OSA severity. Whether this will still hold in future studies identifying predictors of treatment will need to be confirmed. In this view, it is important to note that more easily obtained techniques could also be of value. For instance, it was demonstrated that parameters obtained from a lateral cephalogram are also valid measures of upper airway dimensions. Clinical assessment of tonsillar size correlated with imaging parameters in this study as well [23]. Therefore, future studies should compare the usefulness of these and other techniques including clinical assessment, plain radiographs, CT or MRI images, CFD, sleep endoscopy, etc.

Limitations of our study include the absence of a control group without symptoms of OSA. However, our aim was to characterize the severity of OSA and differences with a normal control group have been described before. A limited number of patients had a history of upper airway surgery although this percentage was not significantly different between both studied groups. Although this probably reflects the population referred to a pediatric sleep lab for OSA, our study sample cannot be considered as a homogeneous population. Second, we did not use sequential images to characterize the upper airway during inspiration and expiration. It has been shown that the airway of subjects with OSA is more compliant [1, 4]. Our goal was to identify markers that could be obtained from a relatively straightforward protocol in order to use it in large-scale studies to identify predictors of treatment success. We have therefore chosen to obtain cross-sectional images only. Future studies with this goal should also incorporate other clinical parameters related to OSA severity including questionnaire data or more easily obtainable radiographic measures with for instance a lateral neck radiograph. Finally, this study used CT-imaging, which requires radiation. However, we could significantly reduce the radiation dosage due to specific protocols as described previously [20].

In conclusion, this study showed that parameters obtained from 3D reconstruction of CT-images of the upper airway post-processed with CFD are highly correlated with OSA severity and are a more powerful correlate than clinical scores of upper airway patency. Preliminary data also showed that we could identify differences in the upper airway of those subjects who did not benefit from a local upper airway treatment. Future large scale studies, also in subpopulations with other risk factors besides adenotonsillar hypertrophy, are needed to confirm the usefulness of these techniques in predicting treatment response.

References

[1] M. Bret Abbott, Lane F. Donnelly, Bernard J. Dardzinski, Stacy A. Poe, Barbara A. Chini, and Raouf S. Amin. Obstructive sleep apnea: MR imaging volume segmentation analysis. *Radiology*, 232(3):889–895, September 2004.

[2] Raanan Arens, Joseph M. McDonough, Aaron M. Corbin, Nathania K. Rubin, Mary Ellen Carroll, Allan I. Pack, Jianguo Liu, and Jayaram K. Udupa. Upper airway size analysis by magnetic resonance imaging of children with obstructive sleep apnea syndrome. *American Journal of Respiratory and Critical Care Medicine*, 167(1):65–70, January 2003.

[3] Raanan Arens, Joseph M. McDonough, Andrew T. Costarino, Soroosh Mahboubi, Catherine E. Tayag-Kier, Greg Maislin, Richard J. Schwab, and Allan I. Pack. Magnetic resonance imaging of the upper airway structure of children with obstructive sleep apnea syndrome. *American Journal of Respiratory and Critical Care Medicine*, 164(4):698–703, August 2001.

[4] Raanan Arens, Sanghun Sin, Joseph M. McDonough, John M. Palmer, Troy Dominguez, Heiko Meyer, David M. Wootton, and Allan I. Pack. Changes in upper airway size during tidal breathing in children with obstructive sleep apnea syndrome. *American Journal of Respiratory and Critical Care Medicine*, 171(11):1298–1304, June 2005.

[5] Raanan Arens, Sanghun Sin, Kiran Nandalike, Jessica Rieder, Unab I. Khan, Katherine Freeman, Judith Wylie-Rosett, Michael L. Lipton, David M. Wootton, Joseph M. McDonough, and Keivan Shifteh. Upper airway structure and body fat composition in obese children with obstructive sleep apnea syndrome. *American Journal of Respiratory and Critical Care Medicine*, 183(6):782–787, March 2011.

[6] Rakesh Bhattacharjee, Leila Kheirandish-Gozal, Karen Spruyt, Ron B. Mitchell, Jungrak Promchiarak, Narong Simakajornboon, Athanasios G. Kaditis, Deborah Splaingard, Mark Splaingard, Lee J. Brooks, Carole L. Marcus, Sanghun Sin, Raanan Arens, Stijn L. Verhulst, and David Gozal. Adenotonsillectomy outcomes in treatment of obstructive sleep apnea in children a multicenter retrospective study. *American Journal of Respiratory and Critical Care Medicine*, 182(5):676–683, September 2010.

[7] L Brodsky. Modern assessment of tonsils and adenoids. *Pediatric clinics of North America*, 36(6):1551–1569, December 1989.

[8] Oscar Sans Capdevila, Leila Kheirandish-Gozal, Ehab Dayyat, and David Gozal. Pediatric obstructive sleep apnea complications, management, and long-term outcomes. *Proceedings of the American Thoracic Society*, 5(2):274–282, February 2008.

[9] Céline Croce, Redouane Fodil, Marc Durand, Gabriela Sbirlea-Apiou, Georges Caillibotte, Jean-François Papon, Jean-Robert Blondeau, André Coste, Daniel Isabey, and Bruno Louis. In vitro experiments and numerical simulations of airflow in realistic nasal airway geometry. *Annals of Biomedical Engineering*, 34(6):997–1007, June 2006.

[10] J. W. De Backer, O. M. Vanderveken, W. G. Vos, A. Devolder, S. L. Verhulst, J. A. Verbraecken, P. M. Parizel, M. J. Braem, P. H. Van de Heyning, and W. A. De Backer. Functional imaging using computational fluid dynamics to predict treatment success of mandibular advancement devices in sleep-disordered breathing. *Journal of Biomechanics*, 40(16):3708–3714, 2007.

[11] Jan W. De Backer, Wim G. Vos, Stijn L. Verhulst, and Wilfried De Backer. Novel imaging techniques using computer methods for the evaluation of the upper airway in patients with sleep-disordered breathing: A comprehensive review. *Sleep Medicine Reviews*, 12(6):437–447, December 2008.

[12] Lane F. Donnelly, Victoria Surdulescu, Barbara A. Chini, Keith A. Casper, Stacy A. Poe, and Raouf S. Amin. Upper airway motion depicted at cine MR imaging performed during sleep: Comparison between young patients with and those without obstructive sleep apnea. *Radiology*, 227(1):239–245, April 2003.

[13] Ralph F. Fregosi and Stuart F. Quan. MRI of pharyngeal airway in children with sleep-disordered breathing. *Journal of Applied Physiology*, 99(6):2470–2470, 2005.

[14] Ralph F. Fregosi, Stuart F. Quan, Kris L. Kaemingk, Wayne J. Morgan, J. L. Goodwin, Rosaria Cabrera, and Arthur Gmitro. Sleep-disordered breathing, pharyngeal size and soft tissue anatomy in children. *Journal of Applied Physiology*, 95(5):2030–2038, 2003.

[15] Conrad Iber. *The AASM Manual for the Scoring of Sleep and Associated Events: Rules, Terminology and Technical Specifications*. American Academy of Sleep Medicine, 2007.

[16] Soo-Jin Jeong, Woo-Seung Kim, and Sang-Jin Sung. Numerical investigation on the flow characteristics and aerodynamic force of the upper airway of patient with obstructive sleep apnea using computational fluid dynamics. *Medical Engineering & Physics*, 29(6):637–651, July 2007.

[17] I. Katz, N. Zamel, A. S. Slutsky, A. S. Rebuck, and V. Hoffstein. Tracheal hysteresis in sleep apnea. *Journal of Applied Physiology*, 67(4):1349–1353, October 1989.

[18] Julie C. Lumeng and Ronald D. Chervin. Epidemiology of pediatric obstructive sleep apnea. *Proceedings of the American Thoracic Society*, 5(2):242–252, February 2008.

[19] S. Rao Mallampati, Stephen P. Gatt, Laveme D. Gugino, Sukumar P. Desai, Barbara Waraksa, Dubravka Freiberger, and Philip L. Liu. A clinical sign to predict difficult tracheal intubation; a prospective study. *Canadian Anaesthetists' Society Journal*, 32(4):429–434, July 1985.

[20] TH Mulkens, C Broers, S Fieuws, JL Termote, and P Bellnick. Comparison of effective doses for low-dose MDCT and radiographic examination of sinuses in children. *American Journal of Roentgenology*, 184(5):1611–1618, May 2005.

[21] Jennifer Nolan and Scott E. Brietzke. Systematic review of pediatric tonsil size and polysomnogram-measured obstructive sleep apnea severity. *Otolaryngology – Head and Neck Surgery*, 144(6):844–850, June 2011.

[22] Steven C. Persak, Sanghun Sin, Joseph M. McDonough, Raanan Arens, and David M. Wootton. Noninvasive estimation of pharyngeal airway resistance and compliance in children based on volume-gated dynamic MRI and computational fluid dynamics. *Journal of Applied Physiology*, 111(6):1819–1827, December 2011.

[23] Kirsi Pirilä-Parkkinen, Heikki Löppönen, Peter Nieminen, Uolevi Tolonen, Eija Pääkkö, and Pertti Pirttiniemi. Validity of upper airway assessment in children: A clinical, cephalometric, and MRI study. *The Angle Orthodontist*, 81(3):433–439, May 2011.

[24] Dennis Rosen. Management of obstructive sleep apnea associated with down syndrome and other craniofacial dysmorphologies. *Current Opinion in Pulmonary Medicine*, page 1, September 2011.

[25] Cedric Van Holsbeke, Jan De Backer, Wim Vos, Pascal Verdonck, Peter Van Ransbeeck, Tom Claessens, Marc Braem, Olivier Vanderveken, and Wilfried De Backer. Anatomical and functional changes in the upper airways of sleep apnea patients due to mandibular repositioning: A large scale study. *Journal of Biomechanics*, 44(3):442–449, February 2011.

[26] Stijn L. Verhulst, Luc Van Gaal, Wilfried De Backer, and Kristine Desager. The prevalence, anatomical correlates and treatment of sleep-disordered breathing in obese children and adolescents. *Sleep Medicine Reviews*, 12(5):339–346, October 2008.

[27] W. Vos, J. De Backer, A. Devolder, O. Vanderveken, S. Verhulst, R. Salgado, P. Germonpre, B. Partoens, F. Wuyts, P. Parizel, and W. De Backer. Correlation between severity of sleep apnea and upper airway morphology based on advanced anatomical and functional imaging. *Journal of Biomechanics*, 40(10):2207–2213, 2007.

[28] Chun Xu, SangHun Sin, Joseph M. McDonough, Jayaram K. Udupa, Allon Guez, Raanan Arens, and David M. Wootton. Computational fluid dynamics modeling of the upper airway of children with obstructive sleep apnea syndrome in steady flow. *Journal of Biomechanics*, 39(11):2043–2054, 2006.

Part II

Simulation of inhalation medication

5

Lung deposition analysis of inhaled medication: Effect of upper airway morphology and comparison with in vivo data

Inhalation Toxicology 2012; 24: 81 – 88

Samir Vinchurkar, Lieve De Backer, Wim Vos, Cedric Van Holsbeke, Jan De Backer and Wilfried De Backer

5.1 Abstract

Background: Asthma affects 20 million Americans resulting in an economic burden of approximately $18 billion in the US alone [2, 37]. Research studies based on differences in patient specific airway morphology for asthma and the associated effect on deposition of inhaled aerosols are currently not available in the literature. Therefore, the role of morphological variations such as upper airway occlusion is not well documented. Furthermore, no studies were found that compared numerical studies on patient specific lung deposition with in vivo data.
Methods: Functional respiratory imaging based computational fluid dynamics (CFD) of the respiratory airways for five asthmatic subjects is performed in this study using computed tomography (CT) based patient specific airway models and boundary conditions. The CFD simulations were used for obtaining lung deposition

using beclomethasone/formoterol® HFA metered dose inhaler.
Results: The lung deposition obtained using CFD was in excellent agreement with available in vivo data using the same product. Specifically, CFD resulted in 30% lung deposition, whereas in vivo lung deposition was reported to be approximately 31%.
Conclusion: It was concluded that a combination of patient specific airway models and lobar boundary conditions can be used to obtain accurate lung deposition estimates. Additionally, lower lung deposition can be expected for patients with higher extrathoracic resistance. Novel respiratory drug delivery devices need to accommodate population sub-groups based on these morphological and anatomical differences in addition to subject age.

5.2 Contributions of the author

From all studies that are described in this thesis, the author was least involved in this one. However, the author cooperated in the segmentation of the airways, setup of the computational fluid dynamics simulations and post processing of the discrete phase.

5.3 Introduction

Inhalation therapy has become a popular therapeutic technique for diseases such as asthma and chronic obstructive pulmonary disease (COPD). Particle deposition characteristics in respiratory airways are needed to develop and improve systemic and local drug delivery using inhalation medication [15, 24]. Additionally, these studies can be useful to assign risk factors to corresponding particle size groups for inhalation toxicology [5, 26, 39, 50]. Experimental investigations are widely performed to evaluate the particle size groups of interest [40, 43, 44] as well as evaluate pre-clinical dosimetry [14, 31]. Numerical analyses assist in selection of pre-clinical criteria and comparison with in vitro and in vivo data [38, 47]. The advantage of performing numerical studies lies in the fact that models and boundary conditions can be created and modified without much difficulty as compared to in vitro and in vivo studies.

Particularly, computational fluid dynamics (CFD) has been extensively applied to study flow characteristics and particle deposition in idealistic [8, 33], physiologically realistic [7, 17] and patient specific [20, 46] airway models. While the models studied were mathematically detailed to capture the airway morphology, very few studies have considered the actual airway morphology without any modifications [20]. Furthermore, the available studies have related the quantitative effect of specific numerical conditions including inlet velocity profiles and turbulent models on deposition in simple, mathematically detailed and user developed airway models [16, 32, 49]. These results need to be validated using models with a higher degree of morphological accuracy since relatively smaller changes in the

morphology can lead to a significant effect on deposition characteristics in the airways [30, 41].

Recently, De Rochefort et al. [22] performed CFD analysis of patient specific airway models by integrating the airway reconstruction process from in vivo thoracic scans with the velocity field calculation. Volumetric CT based images were used to perform airway segmentation of an ovine and human lung. A significant correlation was shown between the airway flow patterns, and local and global geometrical factors. Kabilan et al. [29] studied flow characteristics in a CT based ovine lung model. The study showed asymmetric and highly vortical flow patterns as compared to idealized bipodial flow [29]. These studies show that airway morphology can significantly affect deposition in the respiratory airways.

It is well known that subjects suffering from asthma are characterized by high airway resistance as compared to normal subjects [1, 3, 27]. Therefore, some studies have modelled the airway structure for asthma by constricting the downstream diameters of smooth pipe models representative of respiratory airways [35]. However, using the complete patient specific airway morphology can play a significant role in respiratory airway deposition [30, 41]. Available studies show that patient specific airway segmentation can be obtained down to the level of the small airways with diameters between 1 and 2 mm which is around the 5th – 9th generation [4]. This information can be applied to analyze the effect of airway morphology on lung dose and identify sub-group populations based on important airway structure parameters, for example the diameter of the trachea, the dimensions of the laryngeal opening etcetera.

Changes in airway morphology can significantly affect local deposition leading to hotspot formations [30]. Additionally, numerical factors including flow conditions, turbulence model and boundary conditions employed can affect the accuracy of numerical calculations. For example, (a) steady state conditions are not entirely representative of actual breathing conditions [28], (b) Initial particle injection time can be a significant factor for dosimetry analysis in airway models [19, 28], (c) Reynolds averaged turbulence models are inadequate to accurately model particle deposition for turbulent conditions [44]. To obtain accurate deposition estimates, the effects of different morphological, numerical and boundary conditions including lobar flow distribution needs to be studied for patient specific airway models.

Very few studies employed anatomical based models for performing deposition in the upper airways [34, 42, 45]. However, no studies were found on variability in upper airway morphology and associated effects on lung dose for a targeted patient-population. The objective of the current study was to assess the effect of upper airway geometry on lung deposition in asthma patients by using a combination of patient specific models as well as boundary conditions. The airway models for asthmatic subjects were derived from high resolution computed tomography (HRCT) images. Subsequently numerical analyses were performed to obtain particle deposition patterns in these models using the inhalation formulation employed in an in vivo study [21]. In this in vivo study, lung deposition of a beclomethasone/formoterol formulation in asthmatic patients was assessed using gamma scintigraphy. With gamma scintigraphy, radioisotopes (here the radioactive technetium labelled

formulation) are inhaled and the emitted gamma radiation is captured by external detectors. In this way two-dimensional images of the location of the radioisotopes in the lungs are obtained. The numerical results obtained in the current study were evaluated against this in vivo data for lung deposition. Special attention was given to the deposition in the upper respiratory tract as this is a determining factor for the dosage effectively delivered to the thoracic region [9, 12].

5.4 Materials and methods

5.4.1 High resolution CT scans

For this study, imaging information of 5 asthmatic patients was retrospectively used. The subjects' age used for the CFD study was 52 $\pm$ 10 years as shown in Table 5.1. The protocol was approved by the ethics committee at the Antwerp University Hospital (Wilrijkstraat 10, Edegem 2650). All patients gave their written informed consent. The HRCT scans were performed at a low dose radiation level using a multi-slice CT scanner with 64 receptors (GE VCT Lightspeed). Scanning of the thoracic region was performed at functional residual capacity (FRC) which is the lung level attained after normal expiration and at total lung capacity (TLC). The scanning region started at the larynx and extended down to the diaphragm. These imaging sequences took between 2 and 8 seconds per scan. The lung volumes were controlled using adapted spirometry during the CT procedure. The radiation dose was reduced by reduction of the tube current and voltage [10, 51]. Additionally, there was an increase in noise factor on further reduction of the radiation dose. Images of the extrathoracic region, ranging from the soft palate down to the larynx, were obtained in a separate scan and fused together with the thoracic region. Total radiation exposure was below 5 mSv per patient. The resulting images had a pixel size of approximately 0.5 mm and a slice thickness of 0.3 mm.

Patient no	Age	sex
1	38	M
2	60	M
3	57	F
4	63	F
5	42	M

Table 5.1: Patient's demographic details

5.4.2 Three-dimensional airway models

The HRCT mages were subsequently used for accurate 3D reconstructions of the airway geometries using a semi-automatic algorithm of the airways up to the point where no distinction could be made between the intra-luminal and alveolar air (5th

– 9th bifurcation). The segmentation and three-dimensional reconstruction was performed with a commercially developed and validated software package (Mimics version 13.1, Materialise nv, Belgium). The segmented airway model was then smoothed with a volume compensation algorithm. A fully developed 3D model is illustrated in Figure 5.1. These models were divided in Parts 1 – 5 as shown in the figure. The Parts 1 – 5 represented the extrathoracic region, the tracheal region, the right lung (right airway region), the left lung (left airway region) and the fraction entering the deep lung region (beyond the segmented airway region), respectively.

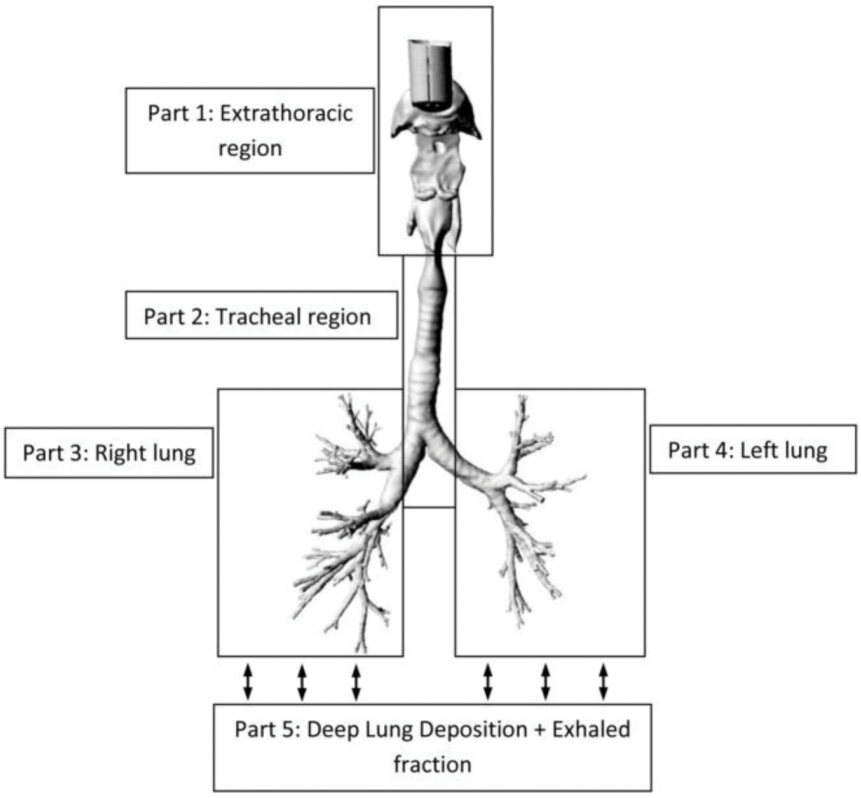

Figure 5.1: Representative patient specific airway model attached with inhaler illustrating division of parts 1 to 5 for obtaining local particle deposition results

5.4.3 Flow simulations

Flow behavior in the airway models could be mathematically described by the Navier-Stokes equations. These governing equations are based on the conservation

of mass and momentums and are given by:

$$\frac{\delta \overline{u}_i}{\delta x_i} = 0 \tag{5.1}$$

$$\frac{\delta \overline{u}_i}{\delta t} + \overline{u}_j \frac{\delta \overline{u}_i}{\delta x_j} = -\frac{1}{\rho}\frac{\delta p}{\delta x_i} + \frac{\delta}{\delta x_j}\left[(\nu + \nu_T)\left(\frac{\delta \overline{u}_i}{\delta x_j} + \frac{\delta \overline{u}_j}{\delta x_i}\right)\right] \tag{5.2}$$

Where u_i is the time-averaged velocity in three coordinate directions, i.e., i = 1, 2, and 3, p is the time-averaged pressure, ρ is the fluid density, ν is the kinematic viscosity, and ν_T is the turbulent viscosity. An important flow feature, especially when considering aerosol interaction, is turbulence. The Large Eddy Simulation technique (LES) is an intermediate approach to model turbulence between the Reynolds Averaged Navier Stokes (RANS) turbulence models wherein the fluctuating part of the flow is ensemble averaged and Direct Numerical Simulation (DNS) wherein the fluctuating part of the flow is fully resolved. The LES technique solves the larger eddies carrying most of the energy, whereas the remaining smaller eddies are modelled using a sub-grid scale model such as a RANS k-ϵ model. LES solutions provide a higher numerical accuracy as compared to the RANS models [11, 13]. Additionally, LES has been shown to provide better solutions for respiratory models due to the nature of the flow separation in such models [36]. Despite the larger computational cost, the LES method has been used in this study. Further details on the turbulent viscosity ν_T for LES with dynamic kinetic energy subgrid scale model can be obtained in the User's manual for Fluent 6.3.

5.4.4 Aerosol transport

For the discrete phase or particle transport, the governing transport equation can be written as:

$$\frac{dv_i}{dt} = \alpha\frac{Du_i}{Dt} + \frac{f}{\tau_p}(u_i - v_i) + g_i(1-\alpha) + f_{i_{lubrification+lift}} \tag{5.3}$$

$$\frac{dx_i}{dt} = v_i(t) \tag{5.4}$$

where v_i and u_i are the components of the particle and local fluid velocity, respectively, and g_i denotes gravity. The drag factor is given by 'f', the response time for particles is denoted by $\tau_p = \rho_p dp^2/18\mu$, and the density ratio $\alpha = \rho/\rho_p \approx 10^{-3}$. Particles are typically initiated at user-specified start and end time. In this study the particles were initiated at two points: At beginning of the inhalation cycle between 0 and 0.3 second (case A) and at the peak of the inhalation cycle between 0.5 to 0.8 seconds (case B). The exact temporal injection time were 0 – 0.3 seconds for actuation 'A' at the beginning of inhalation, and and 0.5 – 0.8 seconds for actuation 'B' at peak of inhalation. The particles were initiated as a solid cone injection with

a half angle of 18 ° approximately which is representative for metered dose inhalers. The particle diameter distribution for the injections in the CFD models was equal to the aerosol size distribution of the formulation used in the study by De Backer et al. [21] in order to allow for proper comparison of the results. The formulation had a mass median aerodynamic diameter of 1.30 ± 0.10 µm with a geometric standard deviation of 1.97 ± 0.12 µm.

5.4.5 Computational grid and boundary conditions

In order to solve the governing equations in the flow domain, hence the respiratory system, a computational grid must be created. For the geometry and the flow rates under consideration a grid size of approximately 6 million cells is required in combination with a time-step of 0.005 s. Further details on grid convergence are reported in a previous study by De Backer et al [18]. This grid was created using a commercial grid generation package (TGrid version 5.0.6, Ansys Inc.). This grid was then imported in a commercial flow solver to perform the numerical simulations (Fluent 6.3, Fluent Inc). Adequate grid convergence studies were performed for the airway models. The inhalation profiles for this study were modelled based on data measured for an asthma patient with a sample inhalation device. Three breathing patterns with average flow rates of 15, 30 and 60 L/min were employed representing sedentary, light and heavy breathing conditions, respectively as shown in Figure 5.2 together with the measured profile. Internal mass flow distributions for individual lobes were based on the volume changes between the FRC and TLC scans. The lobar mass flow distributions are calculated as a ratio of the difference between the total lung capacity (TLC) and functional residual capacity (FRC) volume of an individual lobe to the sum of the differences in TLC and FRC volumes for all lobes. Based on the mass flow distribution, patient specific lobe under-pressures were calculated using an in-house algorithm. These under-pressures were then employed as outlet boundary conditions for CFD simulations. The latter ensured that besides the airway geometry also the internal airflow distribution was patient specific. (Pat. pend. EU 09161455.2 US 61/182.493 [25]).

Finally, the imaging algorithms used in the current study were validated earlier in a separate study which compared the functional respiratory imaging methods applied in the current study with CT and single-photon emission computed tomography (SPECT). It was shown by De Backer et al. [18] that lung ventilation results obtained using functional respiratory imaging based CFD were in good agreement (± 3%) with results obtained using SPECT-CT. Further details on the validation of the imaging and CFD techniques used in the current study are available in De Backer et al [18].

5.5 Results

The CFD simulations yield aerosol deposition patterns in different regions of the airway model. Of particular interest to developers of inhalation medication is the

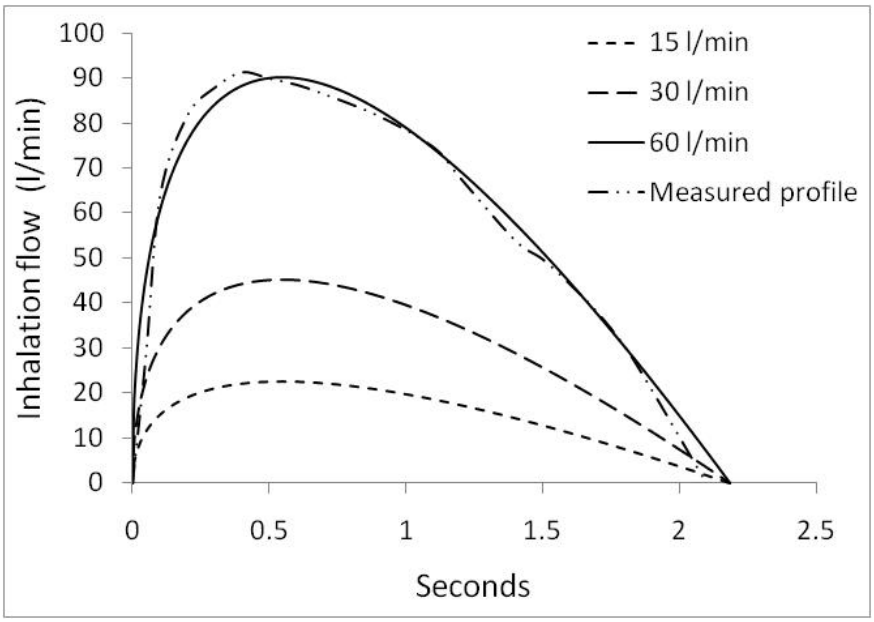

Figure 5.2: Modelled inhalation profile using three flow rates shown together with the measured profile from an asthmatic subject

fraction of the nominal inhaled dose that reaches the thoracic airways (part 3 – 5) as this determines the biological availability of the product to a large extent. The current study showed that for patients 1, 2, 4 and 5 the thoracic or lung deposition for the 30 l/min case was relatively similar with 28.6%, 32.9%, 28.7% and 30.1% respectively when considering the actuation of the inhaled particles at the beginning of the inhalation cycle (case A). Patient 3 however demonstrated a significantly lower fraction of aerosols depositing in the lower airways with only 11.4% of the nominal dose deposited beyond the trachea for case A. On further analyzing all five patients' morphological characteristics it was found that patient 3 was characterized by a narrow laryngopharynx as shown in Figure 5.3. Additionally, a higher upper airway resistance was obtained via CFD simulations for patient 3 as compared to the other patients as illustrated in Table 5.2. Therefore the extrathoracic deposition for patient 3 was significantly higher as compared to other patients. The resistance values show an order of magnitude increase for patient 3 as compared to the other patients. Deposition in the thoracic region was consistently lower for actuation of particles at the peak of the inhalation (case B) for all cases studied due to enhanced extrathoracic deposition caused by increased particle impaction as shown in Figure 5.4. The average lower thoracic deposition for the CFD-based models was 26.3 ± 8.6% for case A and 23.0 ± 7.3% for case B.

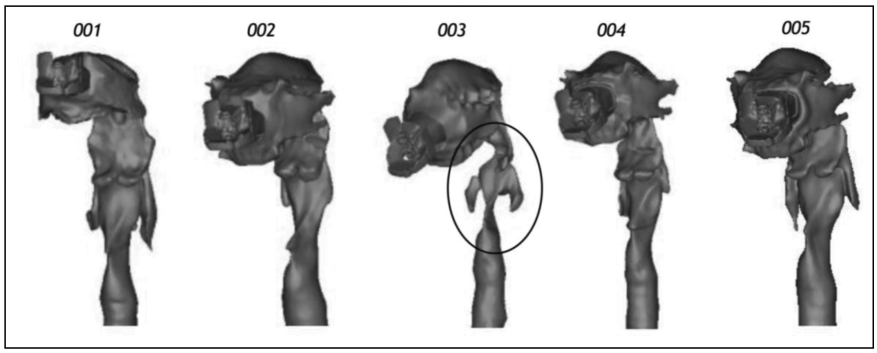

Figure 5.3: Upper airway region for the five asthmatic patients studied showed a partial occlusion for Patient 003 characterized by lower lung dose

Considering all three flow rates including 15, 30 and 60 l/min, the lowest flow rate resulted in the highest thoracic deposition of 28.3 ± 8.3% and 25.4 ± 7.9% for cases A and B, respectively. Due to higher impaction losses in the extrathoracic region, the highest flow rate resulted in the lowest thoracic deposition obtained as 22.9 ± 8.6% and 17.5 ± 7.5% for cases A and B, respectively. Overall, the thoracic deposition was inversely proportional to the inhalation flow rate. Patients with occluded upper airway regions, for example patient 3 in this study, show even higher effect of the flow rate. For this patient the thoracic deposition reduced from approximately 15% for 15 l/min flow rate to approximately 5% for 60 l/min flow rate.

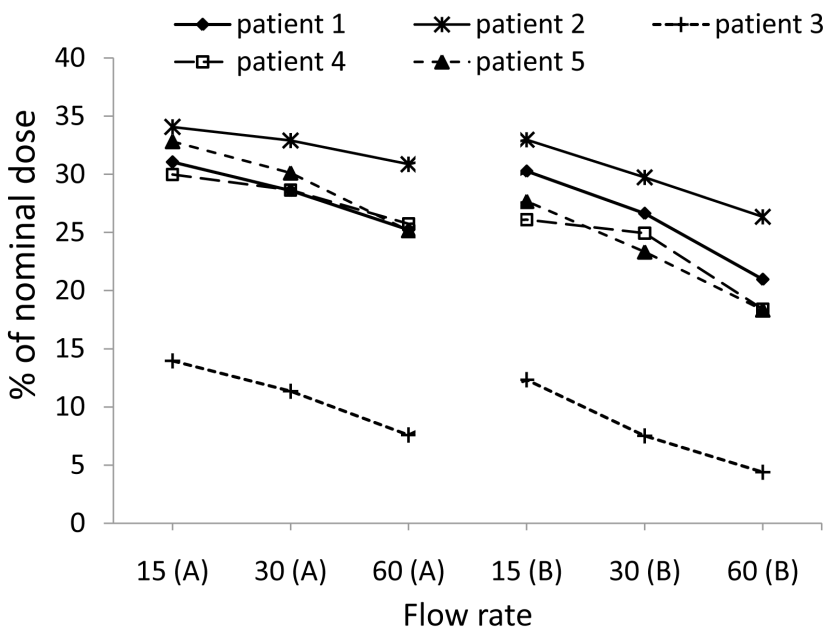

Figure 5.4: Lung deposition obtained in the current study for five asthmatics with actuation at the beginning of inhalation (A) and peak of inhalation (B) shown as a function of the inhalation flow rate

Patient no	Upper airway resistance [Pa/kg/s]
1	91852.2
2	73216.7
3	1561266.7
4	170183.3
5	102004.2

Table 5.2: Upper airway region resistance for the five asthmatic patients analyzed in this study

The comparison of results obtained in the current study using CFD with the in vivo results by De Backer et al. [21] are shown in Figure 5.5 for all patients studied, and excluding patient 3 for the CFD study in the same figure. The in vivo study showed a deposited thoracic fraction of 30.8% on average with a standard deviation of 8.8%. The difference between the average deposition in the CFD models and the in vivo scintigraphy study is therefore 5% where the standard deviations are almost equal. When only considering the deposited thoracic fraction of patients 1, 2, 4 and 5 the average difference between the CFD and in vivo study reduces to approximately 1% as shown in Figure 5.5. The averaged thoracic deposition obtained for these four patients is 30.2% with a standard deviation of 2%.

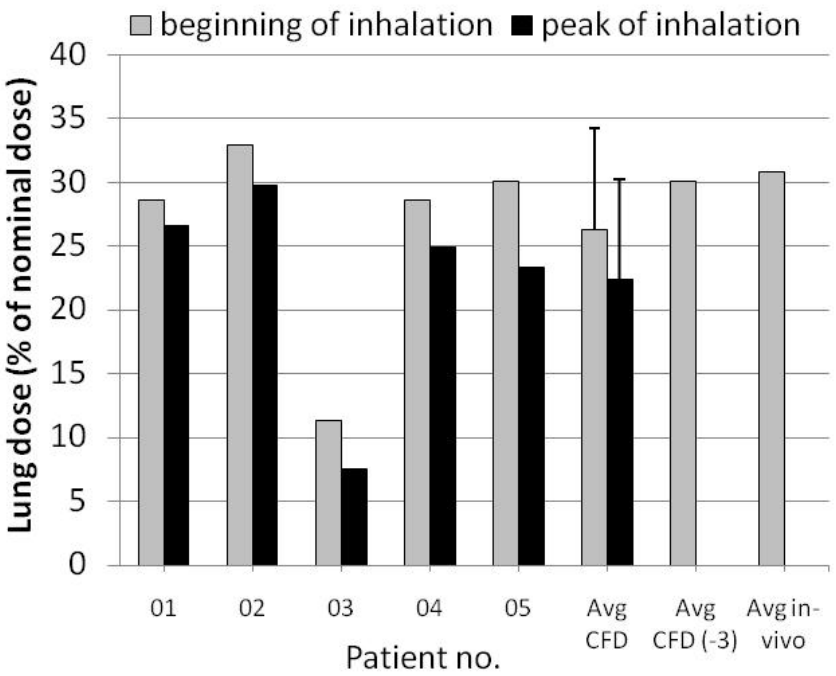

Figure 5.5: Comparison of lung deposition results obtained in the current study using CFD at 30 l/min with the in vivo study performed by De Backer et al. [21]. Exclusion of patient 03 from the CFD analysis (avg CFD (-3)) provides a good comparison with the in vivo data (avg in vivo). The error bars represent standard deviation.

Furthermore, hotspot formations were observed in the upper airway region from the pharynx through the larynx. However, the carinal ridge and subsequent bifurcations showed relatively mild or no hotspot formations as compared to previous studies reporting deposition in pipe lung models [6, 52]. Specifically, even the largest particles with 9 µm diameter resulted in less than 4% of the total deposited particles at the carinal ridge (first bifurcation).

5.6 Discussion

Gamma scintigraphy has been extensively used in the past to assess the deposition location of inhaled drugs. By labeling the drug with a radioactive tracer the location in the respiratory system could be determined afterwards using a non-invasive approach. Although this method could be used to assess the deposited aerosol fraction in the extrathoracic region, the central and peripheral airways, there remain some limitations. The labeling of the product under consideration is not always straightforward and usually time consuming. Furthermore, the scintigraphy test is typically used as an evaluation tool rather than a design tool as it is difficult to repeat the measurements with different parameters. In this regard, the in-silico method could offer a number of advantages to complement the existing tools. Patient specific models could be constructed with minimal patient involvement (e.g., a low dose CT scan at FRC and TLC) and subsequently be used to assess the influence of several parameters on global and local deposition patterns. These parameters can include pharmaceutical and device components such as aerosol size distribution and injection velocities as well as clinical characteristics such as inhalation profiles.

The current study showed a good agreement between the CFD results and in vivo data in terms of thoracic deposition at similar flow rates and inhalation conditions. The same aerosol size distribution was employed for both studies. However, the asthmatic patients included for the CFD study were different than the in vivo study. The results in the current study show that lower inhalation flow rates lead to higher thoracic deposition for all patients considered. Patient 3 showed very low thoracic deposition as compared to the averaged deposition data for the remaining 4 patients since the subject was characterized by a narrow laryngeal region resulting in relatively high upper airway resistance further leading to low thoracic deposition. Additionally, lower thoracic deposition would be expected for patients characterized by a narrow oropharyngeal region accounting to an associated high velocity zone. These airway occlusions resulted in higher particle deposition downstream of the occlusion characterized by impaction as well as upstream of the occlusion due to recirculation zones characterized by dispersion. An example of the downstream deposition is the laryngeal jet region, whereas an example for the upstream deposition is the recirculating region below the uvula adjoining the epiglottis. The overall maximum variability in deposition is obtained to be 26%, which can be highly significant considering that average deposition for asthma inhalation medication is on the order of 30%. The current results present a case study for inter-patient variability in lung dose. More patients with differing morphological features need to be studied for accurate estimation of inter-subject variability. These need to be validated with clinical studies for realistic lung dose variability in asthmatics.

Furthermore, the prevalence of a narrow upper airway in asthmatics should be investigated. Sleep apnea is associated with narrow upper airway regions [48], which occurs on the order of 5% in the population. It was also reported that obesity played a role in sleep apnea particularly in pediatrics. However, a

straightforward relation between obesity and sleep apnea was not demonstrated indicating that further studies were essential to evaluate the effect of obesity on sleep apnea and association with upper airway narrowing. Although upper airway morphological data was not found for asthmatics, obesity and asthma are understood to be interlinked with possibly multiple mechanisms involved [23]. Uncontrolled asthma population needs to be studied for obesity and associated patient specific inhaler performance. Only then can a meaningful correlation be sought between asthma, obesity and upper airway narrowing. There is a possibility that significant uncontrolled asthma population may be receiving lower inhaled medication due to a narrow upper airway, which can be related to obesity or as an inherently existing independent physiological condition. Further studies on asthmatics are needed to evaluate the role of upper airway narrowing independently and concomitant with obesity.

Previous studies [32] report hotspot formations at the carinal ridge and subsequent bifurcations for smooth airway models. However, these were not obtained in the current study since the flow was driven by under-pressure at the lobes instead of a velocity inlet thus leading to smaller stagnation points at the bifurcations resulting in lower impaction. Furthermore, these under-pressures were calculated based on the fraction of air entering the individual lobes. The lobar mass distribution for a patient can be obtained by using lobar volume data for the TLC and FRC as explained in the methods section. It is assumed that these boundary conditions lead to lesser hotspot formation at sites previously reported. Further studies need to be performed to validate these findings.

5.7 Conclusions

This study illustrated that patient specific lung morphology can play a significant role in lung deposition of inhaled medication. The upper airway morphology was the most important factor affecting lung deposition. However, the prevalence of narrow upper airway as an independent physiologic condition and concurrent with obesity need to be studied for additional asthma patients, particularly the uncontrolled population. A good agreement was obtained between imaging based CFD simulations and in vivo data on lung dose for asthmatics. In general, CFD provides an invaluable method to analyze lung dose variability based on patient morphology, device properties, inhalation patterns and aerosol size distribution characteristics. A few examples include patient morphology with narrow upper airway structure, subjects suffering from COPD and asthmatics. Device properties that can be studied include actuation time, jet velocity and spray cone angle. Inhalation patterns together with an aerosol size distribution can be studied for a combination of the other properties to obtain lung dose. These results can be used to identify sub-group populations for targeted drug delivery. Additionally, device design and size distribution can be optimized for specific sub-population groups. CFD can provide a faster and cheaper way to study effect of one or a combination of these characteristics on respiratory dosimetry. However, satisfactory CFD results need to be followed

by in vitro and in vivo tests to validate the results before clinical implementation. Additional asthma patients with narrow upper airways and a spectrum of body mass index need to be included in future studies. These studies can assist in developing novel delivery devices and particle formulation characteristics which can be used in treating uncontrolled asthma and COPD patients.

5.8 Aknowledgements

The authors would like to thank Dr. Marijke De Decker, Ms Caroline Beckers and Ms. Heidi De Laet for assistance in editing this document.

References

[1] Carroll N; Elliot J; Morton A; James A. The structure of large and small airways in nonfatal and fatal asthma. *American Review Of Respiratory Disease*, 147(2):405–410, 2010.

[2] Allergies and Asthma Foundation. The costs of asthma. Technical report, 2000.

[3] S.S An, T.R. Bai, JHT Bates, and J.L. Black. Airway smooth muscle dynamics: a common pathway of airway obstruction in asthma. *European Respiratory Journal*, 29(5):834–860, 2007.

[4] D. Aykac, E.A. Hoffman, G. McLennan, and J.M. Reinhardt. Segmentation and analysis of the human airway tree from three-dimensional x-ray CT images. *Ieee Transactions on Medical Imaging*, 22(8):940–950, 2003.

[5] M.R. Bailey. The new icrp model for the Respiratory-Tract. *Radiation Protection Dosimetry*, 53(1-4):107–114, 1994.

[6] I. Balashazy, T. Heistracher, and W. Hofmann. Air flow and particle deposition patterns in bronchial airway bifurcations: The effect of different CFD models and bifurcation geometries. *Journal of Aerosol Medicine-Deposition Clearance and Effects in the Lung*, 9(3):287–301, 1996.

[7] I. Balashazy, W. Hofmann, and T. Heistracher. Computation of local enhancement factors for the quantification of particle deposition patterns in airway bifurcations. *Journal of Aerosol Science*, 30(2):185–203, February 1999.

[8] I. Balashazy, T.B. Martonen, and W. Hofmann. Fiber deposition in airway bifurcations. *Journal of Aerosol Medicine-Deposition Clearance and Effects in the Lung*, 3(4):243–260, 1990.

[9] W.D. Benett, K.L. Zeman, C.W. Kang, and C.L. Schecter. Extrathoracic deposition of inhaled coarse particles (4.5 mum) in children vs. adults. *Annals of Occupational Hygiene*, 41(1):497–502, 1997.

[10] P.M. Boiselle, G. Dippolito, J. Copeland, H.J. Kang, M. Ahmed, D. Weeks, E. Halpern, and S.N. Goldberg. Multiplanar and 3D imaging of the central airways: Comparison of image quality and radiation dose of single-detector row CT and multi-detector row CT at differing tube currents in dogs. *Radiology*, 228(1):107–111, July 2003.

[11] M. Breuer, N. Jovicic, and K. Mazaev. Comparison of DES, RANS and LES for the separated flow around a flat plate at high incidence. *International Journal for Numerical Methods in Fluids*, 41(4):357–388, February 2003.

[12] T.L. Chan, R.M. Shcrech, and M. Lippmann. Effect of laryngeal jet on particle deposition in the human trachea and upper bronchial airways. *Journal of Aerosol Science*, 11(5-6):447–459, 1980.

[13] Y. Cheng, F.S. Lien, E. Yee, and R. Sinclair. A comparison of large eddy simulations with a standard k-epsilon reynolds-averaged Navier-Stokes model for the prediction of a fully developed turbulent flow over a matrix of cubes. *Journal of Wind Engineering and Industrial Aerodynamics*, 91(11):1301–1328, November 2003.

[14] Y.S. Cheng, H. Irshad, P. Kuehl, T.D. Holmes, R. Sherwood, and C.H. Hobbs. Lung deposition of droplet aerosols in monkeys. *Inhalation Toxicology*, 20(11):1029–1036, 2008.

[15] A Chow, H Tong, P Chattopadhyay, and B Shekunov. Particle engineering for pulmonary drug delivery. *Pharmaceutical Research*, 24(3), 2007.

[16] J.K. Comer, C. Kleinstreuer, S. Hyun, and C.S. Kim. Aerosol transport and deposition in sequentially bifurcating airways. *Journal of Biomechanical Engineering-Transactions of the Asme*, 122(2):152–158, April 2000.

[17] J.K. Comer, C. Kleinstreuer, and Z. Zhang. Flow structures and particle deposition patterns in double-bifurcation airway models. part 1. air flow fields. *Journal of Fluid Mechanics*, 435:25–54, May 2001.

[18] J.W. De Backer, W. Vos, S. Vinchurkar, A Drollmann, R Claes, P. Parizel, P Gemonpre, and W. De Backer. Validation of computational fluid dynamics (CFD) in CT-based airway models using single photon computed tomography (SPECT). *Radiology*, 257:854–862, 2010.

[19] J.W. De Backer, W.G. Vos, P. Burnell, S.L. Verhulst, P. Salmon, Clerck N. De, and Backer W. De. Study of the variability in upper and lower airway morphology in Sprague-Dawley rats using modern micro-CT scan-based segmentation techniques. *Anat.Rec.(Hoboken.)*, 292(5):720–727, May 2009.

[20] J.W. De Backer, W.G. Vos, C.D. Gorle, P. Germonpre, B. Partoens, F.L. Wuyts, P.M. Parizel, and Backer W. De. Flow analyses in the lower airways: patient-specific model and boundary conditions. *Med Eng Phys.*, 30(7):872–879, 2008.

[21] W. De Backer, A. Devolder, G Poli, D Acerbi, R Monno, C Herpich, K Sommerer, T Meyer, and F Mariotti. Lung deposition of BDP/Formoterol HFA pMDI in healthy volunteers, asthmatic and COPD patients. *Journal of Aerosol Medicine and Pulmonary Drug Delivery*, 23(-):10–12, 2010.

[22] L. de Rochefort, L. Vial, R. Fodil, X. Maitre, B. Louis, D. Isabey, G. Caillibotte, M. Thiriet, J. Bittoun, E. Durand, and G. Sbirlea-Apiou. In vitro

validation of computational fluid dynamic simulation in human proximal airways with hyperpolarized he-3 magnetic resonance phase-contrast velocimetry. *Journal of Applied Physiology*, 102(5):2012–2023, May 2007.

[23] J Delgado, P Barranco, and S Quirce. Obesity and asthma. *Journal of investigational allergology & clinical immunology: official organ of the International Association of Asthmology (INTERASMA) and Sociedad Latinoamericana de Alergia e Inmunología*, 18(6):420–425, 2008. PMID: 19123432.

[24] W.H. Finlay. *The mechanics of inhlaed pharmaceutical aerosols*. 2001.

[25] Belgium FluidDA nv. Methods for determining treatments using patient-specific lung models and computer methods, 2010.

[26] ICRP. ICRP publication 66: Human respiratory tract model for radiological protection, 66, January 1995.

[27] Kuwano K; Bosken CH; Pare PD; Bai TR; Wiggs BR; Hogg JC. Small airways dimensions in asthma and in chronic obstructive pulmonary-disease. *American Review Of Respiratory Disease*, 148(5):1220–1225, November 1993.

[28] H.H. Jin, J.R. Fan, M.J. Zeng, and K.F. Cen. Large eddy simulation of inhaled particle deposition within the human upper respiratory tract. *Journal of Aerosol Science*, 38(3):257–268, March 2007.

[29] S. Kabilan, C.L. Lin, and E.A. Hoffman. Characteristics of airflow in a CT-based ovine lung: a numerical study. *Journal of Applied Physiology*, 102(4):1469–1482, April 2007.

[30] J.T. Kelly, B. Asgharian, J.S. Kimbell, and B.A. Wong. Particle deposition in human nasal airway replicas manufactured by different methods. part i: Inertial regime particles. *Aerosol Science and Technology*, 38(11):1063–1071, November 2004.

[31] J.T. Kelly, B. Asgharian, and B.A. Wong. Inertial particle deposition in a monkey nasal mold compared with that in human nasal replicas. *Inhalation Toxicology*, 17(14):823–830, December 2005.

[32] C. Kleinstreuer, Z. Zhang, and Z. Li. Modeling airflow and particle transport/deposition in pulmonary airways. *Respiratory Physiology & Neurobiology*, 163(1-3):128–138, November 2008.

[33] T.C. Lai, Y.S. Morsi, and M. Singh. Numerical characterization of the flow field in a four-generation airway. *Journal of Mechanics in Medicine and Biology*, 8(1):55–74, March 2008.

[34] A Lambert. *Regional deposition of particles in an image-based airway model: Cfd simulation and left-right lung ventilation asymmetr*. PhD thesis, 2010.

[35] P.W. Longest, S. Vinchurkar, and T. Martonen. Transport and deposition of respiratory aerosols in models of childhood asthma. *Journal of Aerosol Science*, 37(10):1234–1257, October 2006.

[36] M. Mihaescu, S. Murugappan, M. Kalra, S. Khosla, and E. Gutmark. Large eddy simulation and Reynolds-Averaged Navier-Stokes modeling of flow in a realistic pharyngeal airway model: An investigation of obstructive sleep apnea. *Journal of Biomechanics*, 41(10):2279–2288, July 2008.

[37] U.S.CDC National Center for Environmental Health (NCEH). Asthma at a glance. Technical report, 1999.

[38] M.J. Oldham, R.F. Phalen, and T. Heistracher. Computational fluid dynamic predictions and experimental results for particle deposition in an airway model. *Aerosol Science and Technology*, 32(1):61–71, January 2000.

[39] R.F. Phalen, R.G. Cuddihy, G.L. Fisher, O.R. Moss, R.B. Schlesinger, D.L. Swift, and H.C. Yeh. Main features of the proposed ncrp Respiratory-Tract model. *Radiation Protection Dosimetry*, 38(1-3):179–184, 1991.

[40] S. Przyborowski. The deposition of aerosol particles of different sizes in regions of the human respiratory tract–a new experimental approach. *Ann.Occup.Hyg.*, 12(1):27–32, January 1969.

[41] R.J. Robinson, M.J. Oldham, R.E. Clinkenbeard, and P. Rai. Experimental and numerical smoke carcinogen deposition in a multi-generation human replica tracheobronchial model. *Annals of Biomedical Engineering*, 34(3):373–383, March 2006.

[42] J Sandeaua, I Katzb, R Fodila, B Louisa, G Apiou-Sbirleab, G Caillibotteb, and D Isabeya. CFD simulation of particle deposition in a reconstructed human oral extrathoracic airway for air and helium-oxygen mixtures. *Journal of Aerosol Science*, 41(3):281–294, 2010.

[43] R.A. Segal, G.M. Kepler, and J.S. Kimbell. Effects of differences in nasal anatomy on airflow distribution: A comparison of four individuals at rest. *Annals of Biomedical Engineering*, 36(11):1870–1882, November 2008.

[44] K.W. Stapleton, E. Guentsch, M.K. Hoskinson, and W.H. Finlay. On the suitability of k-epsilon turbulence modeling for aerosol deposition in the mouth and throat: A comparison with experiment. *Journal of Aerosol Science*, 31(6):739–749, June 2000.

[45] Jonathan Steffens. *Comparison of particle deposition for realistic adult and adolescent upper airway geometries using unsteady computational fluid dynamics*. PhD thesis, 2010.

[46] R.P. Subramaniam, R.B. Richardson, K.T. Morgan, J.S. Kimbell, and R.A. Guilmette. Computational fluid dynamics simulations of inspiratory airflow in the human nose and nasopharynx. *Inhalation Toxicology*, 10(5):473–502, May 1998.

[47] S. Vinchurkar and P.W. Longest. Evaluation of hexahedral, prismatic and hybrid mesh styles for simulating respiratory aerosol dynamics. *Computers & Fluids*, 37(3):317–331, March 2008.

[48] Wim G Vos, Wilfried A De Backer, and Stijn L Verhulst. Correlation between the severity of sleep apnea and upper airway morphology in pediatric and adult patients. *Current opinion in allergy and clinical immunology*, 10(1):26–33, February 2010. PMID: 19996963.

[49] J.X. Xi and P.W. Longest. Effects of oral airway geometry characteristics on the diffusional deposition of inhaled nanoparticles. *Journal of Biomechanical Engineering-Transactions of the Asme*, 130(1), February 2008.

[50] H.C. Yeh, R.G. Cuddihy, R.F. Phalen, and I.Y. Chang. Comparisons of calculated respiratory tract deposition of particles based on the proposed NCRP model and the new ICRP66 model. *Aerosol Science and Technology*, 25(2):134–140, 1996.

[51] J.B. Zhang, I. Hasegawa, D. Feller-Kopman, and P.M. Boiselle. Dynamic expiratory volumetric CT imaging of the central airways: Comparison of standard-dose and low-dose techniques. *Academic Radiology*, 10(7):719–724, July 2003.

[52] Z. Zhang and C. Kleinstreuer. Effect of particle inlet distributions on deposition in a triple bifurcation lung airway model. *Journal of Aerosol Medicine-Deposition Clearance and Effects in the Lung*, 14(1):13–29, 2001.

6

Change in upper airway geometry between upright and supine position during tidal nasal breathing

Journal of Aerosol Medicine and Pulmonary Drug Delivery 2013; Online Ahead of Print: doi:10.1089/jamp.2012.1010

Cedric Van Holsbeke, Stijn Verhulst, Wim Vos, Jan De Backer, Samir Vinchurkar, Pascal Verdonck, Johanna van Doorn, Nasser Nadjmi and Wilfried De Backer

6.1 Abstract

Background: As the upper airway is the most important limiting factor for the deposition of inhalation medication in the lower airways, it is interesting to assess how its morphology varies between different postures. The goal of this study is to compare the upper airway morphology and functionality of healthy volunteers in upright and supine position during tidal nasal breathing and to search for baseline indicators for these changes. This is done by performing three-dimensional measurements on computed tomography (CT) and cone beam computed tomography (CBCT) scans.
Methods: This prospective study was approved by all relevant institutional review boards. All patients gave their signed informed consent. In this study, twenty healthy volunteers (mean age, 62 years; age range, 37 – 78 years; mean body mass index, 29.26; body mass index range 21.63 – 42.17; 16 men, 4 women) underwent

a supine low dose CT scan and an upright CBCT scan of the upper airway. It was examined if the (local) average (S_{avg}) and minimal (S_{min}) cross-sectional area, the position of the latter, the concavity and the airway resistance changed from upright to supine position. If changes were found, baseline parameters were sought that were indicators for these differences.
Results: There were 5 drop-outs due to movement artifacts in the CBCT scans. S_{avg} and S_{min} were respectively 9.76% and 26.90% larger in the CBCT scan than in the CT scan while the resistance decreased with 26.15% in the upright position. The S_{avg} of the region between the hard palate and the bottom of the uvula increased the most (49.85%). In people with a high BMI, this value changed the least. The airway resistance in men decreased more than in women.
Conclusions: This study demonstrated that there are differences in upper airway morphology and functionality between supine and upright position and that there are baseline indicators for these differences.

6.2 Contributions of the author

The author of this thesis was the principal technical researcher in this study. He was involved in the study design and investigated the feasibility. Similar to the study in chapter 4 the computational fluid dynamics simulation were performed using a custom solver based on OpenFOAM and sensitivity studies on meshing and turbulence were performed. While the measurements in chapter 3 were performed manually, the author designed algorithms to extract the outcome parameters in an automated way (see section 12.3). He was responsible for all statistical analyses and the interpretation of the results.

6.3 Introduction

Small airway diseases such as asthma and chronic obstructive pulmonary disease (COPD) are treated with inhaled compounds according to the Global Initiative for Asthma (GINA) and Global Initiative for Chronic Obstructive Lung Disease (GOLD) guidelines [1, 4]. Delivering the drugs to the inflamed airway regions is critical as under-treatment can cause exacerbations [20, 24]. However, simply increasing the dosage to counter this issue can cause systemic side effects [25] and still not guarantee adequate treatment. Computational fluid dynamics (CFD) in patient specific airway models can predict where the particles of an inhaled compound deposit in a certain patient. This technique has been validated and has promise in assessing patient specific treatment [5, 6, 13].

In order to perform the particle simulations correctly, patient specific boundary conditions and airway anatomy are needed. Upper airway morphology is the most important factor in assessing particle deposition in the lower airways [10, 33, 34] and is mostly obtained using computed tomography (CT) or magnetic resonance imaging scans, as these scanners are widely available. The problem with these

scanning techniques is that the images are taken when the subject or patient is in the supine position. Inhaled medication is however mostly administered in an upright position. Posture is thought to be an important determinant of upper airway dimension [12, 29, 36] and can thus have an influence on the CFD results.

Another interesting item is that most oropharyngeal casts and models that are used for in vitro deposition modelling are based on scans in a supine position such as those by McRobbie et al. [19]. A larger insight in posture dependent differences could possibly help them to optimize the throat models currently used by the industry.

A scanning device that has the possibility to scan a subject in an upright position is the cone beam computed tomography (CBCT) scanner. CBCT is nowadays widely used in dentistry and maxillofacial surgery due to its low radiation dose [15], and has already been used to make upper airway models in an upright position [9, 28, 31]. Also, a phantom study has shown that CBCT is a valid technology for accurately quantifying air volumes [35].

As most particle simulations in realistic airway structures are performed on models obtained with a CT scanner [5, 14, 16, 34], it is interesting to assess if there is a possibility that these simulations under- or over-predict the lung deposition. The purpose of this prospective open cross-over study is to quantify the differences in airway morphology and functionality between supine and upright position using CT and CBCT scans of healthy volunteers. The study also investigates which anatomical regions are more prone to possible position dependent changes and if there are baseline morphological or clinical parameters that have an influence on these.

6.4 Materials and Methods

6.4.1 Subject Data

A total of 20 adult healthy volunteers (mean age, 62 years; age range, 37 – 78 years; mean BMI, 29.26; body mass index range 21.63 – 42.17) were included from 18 March 2011 to 29 April 2011. The population consisted of 16 male and 4 female subjects and was divided in three BMI groups. There were 7 subjects with a BMI lower than 25, 6 subjects with a BMI between 25 and 30 and 7 subjects with a BMI higher than 30. The detailed inclusion and exclusion criteria can be found in Table 6.1. Institutional review board approval was obtained, a written informed consent was signed by all subjects and the study was submitted to ClinicalTrials.gov (NCT01594164).

6.4.2 CT and CBCT

All subjects underwent one low-dose CT scan in supine position and one CBCT scan in upright position on the same day. Both scans were taken during tidal nose-breathing to prevent any patient-induced occlusion of the glottis. A pneumotach

Inclusion criteria	• Written informed consent obtained. • Male or female subject aged $\geq$ 18 years. • BMI $<$ 25 kg/m^2 (group 1), BMI $\geq$ 25 kg/m^2 and $<$ 30 kg/m^2 (group 2) and BMI $\geq$ 30 kg/m^2 (group 3). • Female subject of childbearing potential who confirms that a contraception method was used at least two months before scan.
Exclusion criteria	• Subject is under the age of legal consent. • Subject who is pregnant or is breast-feeding. • Subject with a history of surgery of the upper airway. • Subject with a history of any illness that, in opinion of the investigator, might confound the results of the study or poses an additional risk to the subject by participation in the study. • Subject is unlikely to comply with the protocol or unable to understand the nature, scope and possible consequences of the study. • Subject who received any investigational new drug within the last 4 weeks prior to scan. • Subject who has claustrophobia.

Table 6.1: Inclusion and exclusion criteria

device was used to make sure that the subject breathed consistently and to detect if the subject swallowed during the scan. The scanning region started at the beginning of the palatum and extended down to the sternum.

A Lightspeed VCT scanner (GE Healthcare, Milwaukee, Wisconsin) was used to obtain supine images. The images had a pixel size of approximately 0.5 mm^2 and were reconstructed with a slice thickness of 0.3 mm. The scan took around 1 second and was triggered to start at the beginning of the inspiration. The subject received a radiation dose around 0.1 mSv. An i-CAT CBCT scanner (Imaging Sciences International, Hatfield, Pennsylvania) was used for the upright images. The images had a voxel size of approximately 0.4 mm^3. The scan took around 9 seconds and the effective dose was approximately 68 µSv.

Every volunteer in this study was thus exposed to a total radiation dose around 0.2 mSv.

6.4.3 Airway segmentation

Both CT and CBCT scans were loaded into the Mimics 13.1 (Materialise, Leuven, Belgium) software suite. This validated package (Food and Drug Administration, K073468; Conformité Européenne certificate, BE 05/1191.CE.01) allowed to segment the anatomical region of interest and to generate a three-dimensional representation of it. The scans were first resliced so that the central sagittal slice of the hard palate was positioned horizontally. This enabled to take the same region of interest for both CT and CBCT which was important for a correct comparison. The region of interest was chosen as the space of air posterior to the tongue, from the hard palate to the larynx (Figure 6.1) as this region is most prone to airway collapse due to the weight of the surrounding tissue [11]. The segmented region consisted of pixels in a Hounsfield units region between -1024 and -400 [7]. Subsequently, the segmented mask was converted to a three-dimensional object using a contour interpolation algorithm.

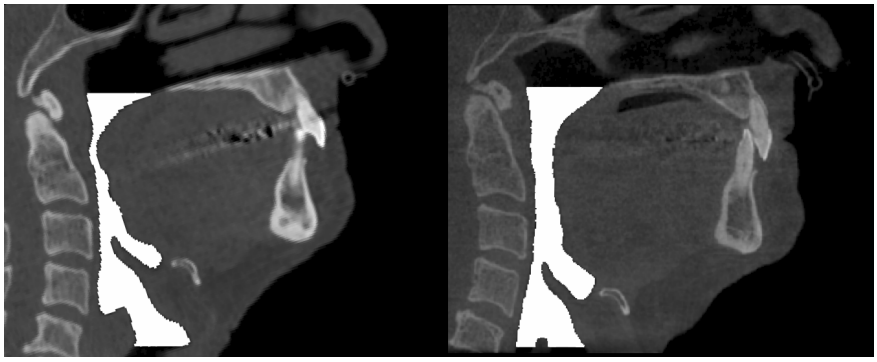

Figure 6.1: Sagittal slice of a CT scan (left) and a CBCT scan (right), taken without contrast material. The region of interest is indicated in white

6.4.4 Computational fluid dynamics

Computational fluid dynamics simulations were performed on the three-dimensional objects in order to generate extra functional data. A hexahedral dominant computational grid was created using SnappyHexMesh 2.0.1 (OpenCFD Ltd, UK). A sensitivity study showed that a computational grid between 300,000 and 1,400,000 cells was sufficient for reaching mesh convergence. This convergence was obtained using differences in mass flow and total pressure drop for increasing mesh refinement levels. The final flow simulations were performed using the mesh size based on a difference of less than 1% between the coarse and fine grids. The computations were performed using a custom made Navier-Stokes solver based on the OpenFOAM 2.0.1 library (OpenCFD Ltd, UK). As the air velocity in the upper airways is smaller than a Mach number of 0.2, an incompressible solver could be used [3]. Also, the flow in the upper airways was considered adiabatic. Second-order discretization schemes were used for the pressure and momentum equations and the pressure-velocity coupling was solved using the SIMPLE scheme. In order to enable proper comparison between the models, the boundary conditions were set equally for all models. At the inlet, a total pressure of 0 Pa was set and at the outlet, a static pressure of -20 Pa was applied. Sensitivity analyses on turbulence showed that no inaccuracies were introduced by employing a laminar flow approach. The mass flow and the total pressure drop were similar between laminar and k-ω SST turbulence boundary conditions (considering 5% turbulence intensity at the inlet) with a maximum difference of less than 1% for the model with the highest Reynolds number. Pressure boundary conditions were chosen for realistic inter-patient comparison as morphology changes in the upper airway will not change the pressure difference between atmosphere and lungs, but will restrict the airflow. The resulting flows were between 6.5 l/min and 50 l/min.

6.4.5 Outcome parameters

All measurements on the upper airways were done on the three-dimensional objects that were extracted from the CT and CBCT scans. In this way it was possible to detect morphological differences. The anatomical parameters that were measured were:

- The average cross-sectional area of the upper airway (S_{avg})
- The minimal cross-sectional area of the upper airway (S_{min})
- The position of S_{min}, measured from the hard palate ($Pos_{S_{min}}$)
- In order to see if the potential differences between CT and CBCT are due to very local movements or due to global movements, the S_{avg} was also measured in three anatomical zones:
  - In the region between the hard palate and the end of the uvula ($S_{avg_{top}}$)
  - In the region between the end of the uvula and the epiglottis ($S_{avg_{central}}$)

– In the region between the epiglottis and the larynx ($S_{avg_{bottom}}$)

The different zones and cross-sectional areas are shown in Figure 6.2. The ratio S_{min}/S_{avg} was defined as the concavity and has been calculated as it was to be investigated whether upper airways with a uniform area distribution react differently from airways which are more concave and thus have a lower S_{min}/S_{avg}.

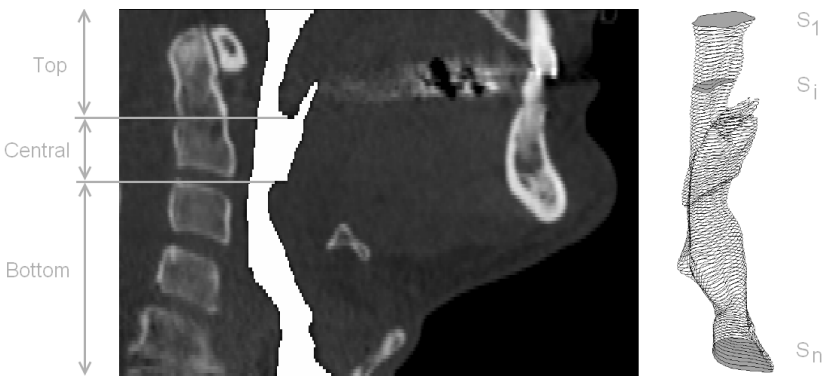

Figure 6.2: The different airway zones and the definition of the cross-sectional areas

From the computational fluid dynamics simulations, the upper airway resistance R was extracted. The resistance was defined as the ratio of the total pressure drop over the upper airway and the mass flow rate through it [17, 18].

Finally, it was investigated if men and women respond differently to the change in posture.

6.4.6 Statistics

The data were tested for normality using the Shapiro-Wilk W Test. Depending on the outcome of these tests, parametric or non-parametric statistical techniques were used. In this study correlations were calculated using the Spearman rank test and differences between CT and CBCT were analyzed using the Wilcoxon Matched Pairs test. Differences between sexes were investigated using the Mann-Whitney U test. Statistical analysis was performed using Statistica 10 (Statsoft, Tulsa, Oklahoma) and the significance level was set at 0.05.

6.5 Results

6.5.1 Drop-outs

From the 20 healthy volunteers that were included, only 15 valid CBCT scans could be analyzed as the rotating gantry of the CBCT touched the shoulders of the

broad-shouldered subjects, causing motion artifacts. These subjects were especially found in the highest BMI group (1 male with a BMI lower than 25, 1 male with a BMI between 25 and 30, 3 males with BMIs above 30).

6.5.2 Differences between CBCT and CT

Values of S_{avg} and S_{min} were significantly larger in the CBCT scan than the same parameters in the CT scan (respectively 9.76% and 26.90%) while the concavity and the $Pos_{S_{min}}$ did not change significantly. A good example can be seen in Figure 6.3. Also, the resistance R was found to be 26.45% smaller in upright posture than when lying down.

When looking more in detail at the diameter distribution, it can be seen that there was a very significant increase (49.85%) in $S_{avg_{top}}$ when the subject changed from supine position to upright position. However, the values of $S_{avg_{central}}$ and $S_{avg_{bottom}}$ were not influenced by this action. Detailed statistical results can be found in Table 6.2.

	Median (Lower/upper quartile)			
Parameter	CT	CBCT	Difference [%]	p-value
S_{avg} [mm^2]	196.55 (126.84/216.91)	216.44 (170.01/378.69)	+9.76	**0.005**
$S_{avg_{top}}$ [mm^2]	135.53 (94.45/202.50)	230.34 (154.35/364.53)	+49.85	$<$ **0.001**
$S_{avg_{central}}$ [mm^2]	178.52 (107.06/248.65)	195.88 (125.22/285.31)	-14.16	0.820
$S_{avg_{bottom}}$ [mm^2]	193.45 (178.66/270.28)	223.32 (192.02/382.69)	+4.25	0.112
S_{min} [mm^2]	57.31 (35.49/84.91)	78.70 (60.66/173.06)	+26.90	**0.027**
$Pos_{S_{min}}$ [mm]	27 (23/57)	41 (24/61)	+6.67	0.177
S_{min}/S_{avg} [-]	0.326 (0.270/0.418)	0.388 (0.336/0.463)	+15.98	0.100
R [kPas/L]	0.084 (0.055/0.116)	0.054 (0.025/0.071)	-26.45	**0.004**

Table 6.2: Differences between CT and CBCT

6.5.3 Indicators for the differences between CBCT and CT

From here on, the symbol Δ is used to define the percentage change between the parameter measured with CBCT and the parameter measured with CT. A positive value means that the CBCT value is larger than the CT value. The significant results in the previous section showed that the median values of ΔS_{avg}, ΔS_{min} and $\Delta S_{avg_{top}}$ are positive, while the median value of ΔR is negative.

BMI was not found to be an indicator for ΔS_{avg}, ΔS_{min} and ΔR. However, it was found that in people with a higher BMI, $\Delta S_{avg_{top}}$ became smaller (Table 6.3). There was an inverse correlation between BMI and $S_{avg_{top}}$ in an upright position (Spearman R: -0.664 p-value: 0.007), but BMI had no relation with $S_{avg_{top}}$ when lying down (Spearman R: -0.282 p-value: 0.308).

There was a significant difference between the sexes for ΔR (Table 6.4). In males, ΔR decreased 42.98% (p-value: 0.006) while this value was not different

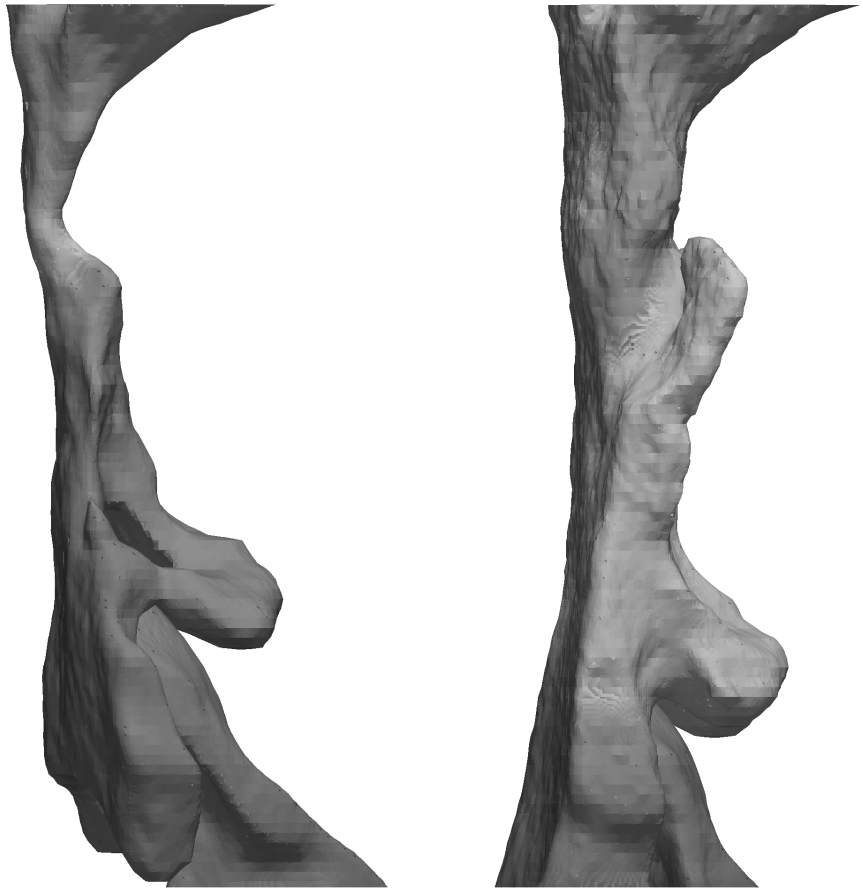

Figure 6.3: These two images show the same upper airway. On the left is the CT scan, on the right is the CBCT scan. It can be seen that the cross-sectional areas are much larger in the CBCT airway scan

Parameters	Spearman R	p-value
BMI & ΔS_{avg}	-0.357	0.191
BMI & $\Delta S_{avg_{top}}$	-0.625	**0.013**
BMI & ΔS_{min}	0.032	0.909
BMI & ΔR	0.111	0.694

Table 6.3: BMI versus difference between CBCT and CT

from zero for women (p-value: 0.715). The closer the upright $Pos_{S_{min}}$ was to the hard palate, the more ΔS_{min} increased and ΔR decreased (Spearman R: 0.611 p-value: 0.016).

Parameters	Mean rank men	Mean rank women	Mann-Whitney U	p-value
Sex & ΔS_{avg}	8.55	6.50	16.00	0.489
Sex & $\Delta S_{avg_{top}}$	7.64	9.00	18.00	0.661
Sex & ΔS_{min}	9.00	5.25	11.00	0.177
Sex & ΔR	6.55	12.00	6.00	**0.040**

Table 6.4: Sex versus difference between CBCT and CT

6.6 Discussion

Particle deposition simulations are mostly performed on airway models that are segmented from CT scans as this technique results in the best visualization of upper and lower airways. As it is possible to decrease the radiation dose for an upper airway scan to 0.1 mSv, the possible negative side effects can be minimized [22]. However, due to the fact that inhalation medication is mostly taken in upright position while the CT scan is taken in supine position, there is a possibility that the simulated geometry will not correspond completely to the real geometry.

The first aim of this study was to compare the upper airway morphology in supine and upright position in order to see if this is the case. This was done by scanning healthy subjects with a CT scanner while lying down and with a CBCT scanner while sitting straight. As both scanning techniques are known to provide good quantitative results when measuring spaces of air, the segmented voxels of both techniques could be compared. We could demonstrate that there is indeed a difference in airway morphology between these postures: the airway becomes significantly smaller and its resistance increases when lying down. This can be explained by the fact that the gravity vectors of the surrounding tissues are aligned perpendicular to the airway walls in this position, increasing the load on the airway muscles. It seems that the tension in the airway muscles does not increase enough to counter the increased load completely, resulting in a smaller airway lumen. The fact that the average airway diameter only decreased in the part posterior to the uvula suggests that, in a population of healthy subjects, this is the region that is most prone to airway collapse. This is supported by previous findings in healthy subjects and sleep apnea patients [2, 11, 32] and is probably due to a posterior displacement of the soft palate and the tongue [21, 30].

The second aim of this study was to find baseline parameters that are indicators for these morphology changes. The closer the position of the minimal cross sectional area to the hard palate when upright, the more the minimal cross sectional area will decrease and the resistance will increase when lying down. This is in line with the fact that the region of collapse is mostly posterior to the uvula.

No correlations were found between the BMI and the global changes in morphological and functional airway parameters. This is an important outcome and implies that in healthy subjects, no large morphological or functional changes occur due to an increased weight of the surrounding tissue. It was even found that in people with a high BMI, there is less area change posterior to the uvula. It can be suspected that in healthy subjects, the airway muscles apply enough force to guarantee a certain airway lumen.

Men and women responded significantly differently to the change in posture. The airway resistance decreases in men while there is no significant change found in women. Although there is a sex imbalance in the included subjects (11 males, 4 females), this is an interesting finding as will be discussed further.

This study had a number of limitations. There were a significant amount of drop-outs in the broad shouldered subjects due to the small diameter of the CBCT rotating gantry that interfered with the region of interest. As this gave some imbalance in the BMI groups, one has to approach the correlations that were found with BMI carefully. The above mentioned sex imbalance is also a limitation. A higher number of women would open the possibility to perform more detailed comparisons. A previous study found no significant differences between CT and CBCT when measuring spaces of air in a phantom [35], so in a static context no differences will be observed due to the different imaging modalities. However, it is known that the upper airway geometry changes during tidal breathing [26] which can introduce movement related errors. As the CT scan only took 1 second and was triggered at the start of the inhalation, the breath induced geometry changes were considered to be very small. However, the long scanning time of the CBCT could have introduced some motion artifacts as the subject performed multiple breaths during the scan. Although there were no visible motion artifacts, the possibility exists that the upright volumes were underestimated as these artifacts would be excluded from the Hounsfield range. As the significant geometrical percentage changes between CBCT and CT were all positive, it is possible that these are underestimated. The effect of the upstream nasal regions were neglected in the CFD simulations. Although this zone was not a part of our region of interest, the exclusion could have had an influence on the results. It was not possible to quantify this influence as the field of view of the CBCT was not large enough to scan both the nasal region and the upper airway in one movement. The skewness of the data had the effect that non-parametric tests were used and no multivariate analyses were performed.

In future studies, it would be interesting to perform this methodology in a population of obstructive sleep apnea (OSA) patients. The first reason is that this would open possibilities to gain insights in the pathology and to help with diagnostics. Another reason is the fact that there are a lot of patients that suffer from both OSA and asthma/COPD [23, 27] and that the conclusions of this study are possibly not valid for them. The most important insight of the current study is that the largest area changes occur at the region posterior to the uvula. As most inhalation compounds are administered through the mouth, it would be interesting to see if the upper airway behavior changes due to mouth breathing. An open mouth

can possibly induce a movement of the uvula, which can influence the local or global airway morphology and functionality. There are plans for a future study where this will be investigated. The insights of the current and future studies can lead to more accurate lung deposition estimates.

The large inter- and intra-subject variation in upper airway morphology shows that there is a need for a subject specific approach when assessing deposition of inhalation medication. Several predictive models exist, as described in a review of Warren H. Finlay and Andrew R. Martin [8], that are very valuable but are based on statistical models en are not able to tell if an individual subject behaves like the fitted deposition curve predicts.

This study demonstrated that there are differences in upper airway morphology and functionality between supine and upright position and that there are baseline indicators for these. The upper airway behavior that was extracted from the CT and CBCT scans is in line with clinical observations and shows the usefulness of these techniques. This is especially true as the large variability within and between the subjects emphasizes the added value of subject specific models.

6.7 Acknowledgements

The authors would like to thank Dr. Marijke De Decker, Ms. Caroline Beckers and Ms. Heidi De Laet for assistance in editing this document.

References

[1] E. D. Bateman, S. S. Hurd, P. J. Barnes, J. Bousquet, J. M. Drazen, M. FitzGerald, P. Gibson, K. Ohta, P. O'Byrne, S. E. Pedersen, E. Pizzichini, S. D. Sullivan, S. E. Wenzel, and H. J. Zar. Global strategy for asthma management and prevention: GINA executive summary. *European Respiratory Journal*, 31(1):143–178, January 2008.

[2] Joanna M. Battagel, Ama Johal, Anne-Marie Smith, and Bhik Kotecha. Postural variation in oropharyngeal dimensions in subjects with sleep disordered breathing: a cephalometric study. *The European Journal of Orthodontics*, 24(3):263–276, January 2002.

[3] J. Blazek. *Computational Fluid Dynamics: Principles and Applications*. Elsevier Science, 1st edition, June 2001.

[4] B. R. Celli, W. MacNee, A. Agusti, A. Anzueto, B. Berg, A. S. Buist, P. M. A. Calverley, N. Chavannes, T. Dillard, B. Fahy, A. Fein, J. Heffner, S. Lareau, P. Meek, F. Martinez, W. McNicholas, J. Muris, E. Austegard, R. Pauwels, S. Rennard, A. Rossi, N. Siafakas, B. Tiep, J. Vestbo, E. Wouters, and R. ZuWallack. Standards for the diagnosis and treatment of patients with COPD: a summary of the ATS/ERS position paper. *European Respiratory Journal*, 23(6):932–946, January 2004.

[5] Jan W. De Backer, Wim G. Vos, Samir C. Vinchurkar, Rita Claes, Anton Drollmann, Denis Wulfrank, Paul M. Parizel, Paul Germonpré, and Wilfried De Backer. Validation of computational fluid dynamics in CT-Based airway models with SPECT/CT. *Radiology*, 257(3):854–862, January 2010.

[6] Ludovic de Rochefort, Laurence Vial, Redouane Fodil, Xavier Maitre, Bruno Louis, Daniel Isabey, Georges Caillibotte, Marc Thiriet, Jacques Bittoun, Emmanuel Durand, and Gabriela Sbirlea-Apiou. In vitro validation of computational fluid dynamic simulation in human proximal airways with hyperpolarized 3He magnetic resonance phase-contrast velocimetry. *J Appl Physiol*, 102(5):2012–2023, 2007.

[7] G. R Ferretti, I. Bricault, and M. Coulomb. Virtual tools for imaging of the thorax. *European Respiratory Journal*, 18(2):381–392, August 2001.

[8] Warren H. Finlay and Andrew R. Martin. Recent advances in predictive understanding of respiratory tract deposition. *Journal of Aerosol Medicine and Pulmonary Drug Delivery*, 21(2):189–206, June 2008.

[9] Dan Grauer, Lucia S.H. Cevidanes, Martin A. Styner, James L. Ackerman, and William R. Proffit. Pharyngeal airway volume and shape from cone-beam computed tomography: Relationship to facial morphology. *American Journal of Orthodontics and Dentofacial Orthopedics*, 136(6):805–814, December 2009.

[10] B Grgic, W.H Finlay, P.K.P Burnell, and A.F Heenan. In vitro intersubject and intrasubject deposition measurements in realistic mouth–throat geometries. *Journal of Aerosol Science*, 35(8):1025–1040, August 2004.

[11] David R. Hillman, Jennifer Walsh, Kathleen Maddison, Peter R. Platt, William J. Noffsinger, and Peter R. Eastwood. Airway collapse or closure via the soft palate as mechanism of obstruction in sedated patients? *Anesthesiology*, 112(2):497, February 2010.

[12] M. A. Jan, I. Marshall, and N. J. Douglas. Effect of posture on upper airway dimensions in normal human. *American Journal of Respiratory and Critical Care Medicine*, 149(1):145–148, January 1994.

[13] S.T. Jayaraju, M. Brouns, C. Lacor, B. Belkassem, and S. Verbanck. Large eddy and detached eddy simulations of fluid flow and particle deposition in a human mouth–throat. *Journal of Aerosol Science*, 39(10):862–875, October 2008.

[14] Andrew R. Lambert, Patrick T. O'shaughnessy, Merryn H. Tawhai, Eric A. Hoffman, and Ching-Long Lin. Regional deposition of particles in an image-based airway model: Large-eddy simulation and left-right lung ventilation asymmetry. *Aerosol Science and Technology*, 45(1):11–25, 2011.

[15] M. Loubele, R. Bogaerts, E. Van Dijck, R. Pauwels, S. Vanheusden, P. Suetens, G. Marchal, G. Sanderink, and R. Jacobs. Comparison between effective radiation dose of CBCT and MSCT scanners for dentomaxillofacial applications. *European Journal of Radiology*, 71(3):461–468, September 2009.

[16] Baoshun Ma and Kenneth R. Lutchen. CFD simulation of aerosol deposition in an anatomically based human Large–Medium airway model. *Annals of Biomedical Engineering*, 37(2):271–285, December 2008.

[17] Elaine Marieb and Katja Hoehn. *Anatomy and physiology: International edition*. Pearson Education (US), [S.l.], 3th edition, April 2007.

[18] B. Mauroy, M. Filoche, E. R. Weibel, and B. Sapoval. An optimal bronchial tree may be dangerous. *Nature*, 427(6975):633–636, February 2004.

[19] Donald W. McRobbie, Susan Pritchard, and Rebecca A. Quest. Studies of the human oropharyngeal airspaces using magnetic resonance imaging. i. validation of a three-dimensional MRI method for producing ex vivo virtual and physical casts of the oropharyngeal airways during inspiration. *Journal of Aerosol Medicine*, 16(4):401–415, December 2003.

[20] Ross M. Miller, Dorothy George, and R. J. Halbert. Improving the management of chronic obstructive pulmonary disease. *Journal for Healthcare Quality*, 27(2):42–47, June 2011.

[21] K. Miyamoto, M. M. Ozbek, A. A. Lowe, and J. A. Fleetham. Effect of body position on tongue posture in awake patients with obstructive sleep apnoea,. *Thorax,*, 52,(3,):255,, March 1997.

[22] Tom Mulkens, Rodrigo Salgado, and Patrick Bellinck. Dose optimization and reduction in CT of the brain and head and neck region. In Denis Tack, Mannudeep K. Kalra, and Pierre Alain Gevenois, editors, *Radiation Dose from Multidetector CT*, Medical Radiology, pages 281–306. Springer Berlin Heidelberg, 2012.

[23] Robert L Owens and Atul Malhotra. Sleep-disordered breathing and COPD: the overlap syndrome. *Respiratory care*, 55(10):1333–1344; discussion 1344–1346, October 2010. PMID: 20875160.

[24] Wark P.A.B. and Gibson P.G. Clinical usefulness of inflammatory markers in asthma. *American Journal of Respiratory Medicine*, 2(1):11–19, 2003.

[25] Dahl Ronald. Systemic side effects of inhaled corticosteroids in patients with asthma. *Respiratory Medicine*, 100(8):1307–1317, August 2006.

[26] R. J. Schwab, W. B. Gefter, A. I. Pack, and E. A. Hoffman. Dynamic imaging of the upper airway during respiration in normal subjects. *Journal of Applied Physiology*, 74(4):1504–1514, January 1993.

[27] Bhavneesh Sharma, Steven Feinsilver, Robert Owens, Atul Malhotra, David McSharry, and Stephen Karbowitz. Obstructive airway disease and obstructive sleep apnea: Effect of pulmonary function. *Lung*, 189(1):37–41, 2011.

[28] Hongjian Shi, William C. Scarfe, and Allan G. Farman. Upper airway segmentation and dimensions estimation from cone-beam CT image datasets. *International Journal of Computer Assisted Radiology and Surgery*, 1(3):177–186, October 2006.

[29] P. Sutthiprapaporn, K. Tanimoto, M. Ohtsuka, T. Nagasaki, Y. Iida, and A. Katsumata. Positional changes of oropharyngeal structures due to gravity in the upright and supine positions. *Dentomaxillofacial Radiology*, 37(3):130–135, March 2008.

[30] Frank J. Trudo, Warren B. Gefter, Kevin C. Welch, Krishanu B. Gupta, Greg Maislin, and Richard J. Schwab. State-related changes in upper airway caliber and surrounding soft-tissue structures in normal subjects. *American Journal of Respiratory and Critical Care Medicine*, 158(4):1259–1270, January 1998.

[31] Hung Hsiag Tso, Janice S. Lee, John C. Huang, Koutaro Maki, David Hatcher, and Arthur J. Miller. Evaluation of the human airway using cone-beam computerized tomography. *Oral Surgery, Oral Medicine, Oral Pathology, Oral Radiology, and Endodontology*, 108(5):768–776, November 2009.

[32] Satoru Tsuiki, Fernanda R. Almeida, Paramvir S. Bhalla, Alan A. Lowe, and John A. Fleetham. Supine-dependent changes in upper airway size in awake obstructive sleep apnea patients. *Sleep and Breathing*, 7(1):43–50, 2003.

[33] S. Verbanck, H.S. Kalsi, M.F. Biddiscombe, V. Agnihotri, B. Belkassem, C. Lacor, and O.S. Usmani. Inspiratory and expiratory aerosol deposition in the upper airway. *Inhalation Toxicology*, 23(2):104–111, February 2011.

[34] Samir Vinchurkar, Lieve De Backer, Wim Vos, Cedric Van Holsbeke, Jan De Backer, and Wilfired De Backer. A case series on lung deposition analysis of inhaled medication using functional imaging based computational fluid dynamics in asthmatic patients: effect of upper airway morphology and comparison with in vivo data. *Inhalation Toxicology*, 24(2):81–88, January 2012.

[35] A. Yamashina, K. Tanimoto, P. Sutthiprapaporn, and Y. Hayakawa. The reliability of computed tomography (CT) values and dimensional measurements of the oropharyngeal region using cone beam CT: comparison with multidetector CT. *Dentomaxillofacial Radiology*, 37(5):245–251, July 2008.

[36] N. Yildirim, M. F Fitzpatrick, K. F Whyte, R. Jalleh, A. J. A Wightman, and N. J Douglas. The effect of posture on upper airway dimensions in normal subjects and in patients with the sleep Apnea/Hypopnea syndrome. *American Journal of Respiratory and Critical Care Medicine*, 144(4):845–847, October 1991.

7

Patient specific evaluation of regional antibiotic concentration levels in a cohort of cystic fibrosis patients

Nature medicine; submitted

Aukje Bos, Cedric Van Holsbeke, Jan De Backer, Mireille van Westreenen, Hettie Janssens, Wim Vos, Harm Tiddens

7.1 Abstract

Small airways disease, related to chronic Pseudomonas aeruginosa (Pa) infection, plays a key role in cystic fibrosis (CF) lung disease. Inhaled antibiotics are the cornerstones of Pa treatment. Unfortunately despite their use, small airways disease progresses and antibiotic-resistant Pa develops, suggesting small airways receive less than the minimal inhibitory concentration. Comprehension of the impact of structural lung changes and breathing profile on local antibiotic concentrations is needed to prevent sub-inhibitory concentrations. We used functional respiratory imaging (FRI) to predict local Aztreonam lysine for inhalation (AZLI) concentrations in CF lungs. FRI was applied to 40 patient-specific chest computed tomography airway models. In most simulated conditions, concentrations were above the minimal inhibitory concentration. However, more diseased lobes were likely to receive less AZLI. Structural lung disease and high tidal volumes greatly reduced small airways concentrations. FRI allows further optimization of anti-Pa

treatment within the small airways.

7.2 Contributions of the author

The author of this thesis was the principal technical researcher in this study. He cooperated in the segmentation and coupling of the different models and determined the optimal boundary conditions and simulation strategy for the particle simulations. This included the generation of lognormal distributions for the aerosol cloud. He automated the complete trajectory from three-dimensional models to computational fluid dynamics results. The main challenge in this chapter was the post-processing of the results. The author programmed the construction of the individual Phalen models and the coupling with their patient specific three-dimensional airway models. He was responsible for the automated extraction of the outcome parameters, semi-automated statistical analyses in the R software environment and cooperated in the interpretation of the results.

7.3 Introduction

Cystic fibrosis (CF) is a severe hereditary and life-threatening disease in the Caucasian population [8], affecting 70,000 patients in the European Union and United States. Life expectancy is restricted to approximately 37 years. The main cause of morbidity and mortality ($>$ 90% of deaths) in CF patients is due to progressive lung disease [42]. An important component in the pathophysiology of CF lung disease is small airways disease which starts early in life [13, 37, 43, 50]. The main pathogen that contributes to lung disease progression in CF is Pseudomonas aeruginosa (Pa) [19, 25, 33]. Inhaled antibiotics play a central role in the eradication and chronic suppressive therapy of Pa infections.

Unfortunately, commonly used therapies to eradicate Pa do not prevent progression of CF lung disease, especially in the small airways. Significant mucus accumulation and wall thickening in the small airways has been found in patients with severe lung disease [43, 50]. Pa has been associated with these changes, mainly in airways smaller than 1 mm in diameter [3]. Hence, further improvement of these anti-Pa therapies is needed. Based on high concentrations of drug in sputum of patients, it has been assumed that inhaled antibiotics result in high concentrations within the airways [24, 27, 35, 44, 59]. However, it is questionable whether concentrations in sputum samples are representative for the concentrations in the small airways. First of all, the overall surface area of the small airways is much larger than that of central airways [43]. As a result, drug bypassing central airways is distributed over a large surface area. Second, sputum originating from the small airways always pass through the central airways before it can be expectorated, taking along the drug deposited in these central airways, what is likely to increase the initial sputum concentration. Unfortunately, very little is known about the concentrations of anti-Pa antibiotics in the small airways because

they are extremely difficult to measure in vivo. The progression of small airways disease in patients with chronic Pa infection despite anti-Pa antibiotics suggests that concentrations of these inhaled antibiotics are perhaps inadequate due to insufficient small airway deposition. To optimize eradication and chronic suppression of Pa with inhaled antibiotics, it is important to obtain local concentrations equal to, or above the minimal inhibitory concentration (MIC). Concentrations below the MIC are thought to result in suboptimal killing of Pa and could contribute to the development of antibiotic resistance [24] and to failure of eradication. When the Pa infection persists, nonmucoid variants are mostly replaced by mucoid forms [8]. These are considered the hallmark of chronic infection [25], as they are to date impossible to eradicate using current therapies. Mucoid Pa are associated with a more rapid decline in lung function and increased treatment burden [33].

To improve inhaled therapy, extensive research has been done to understand the mechanisms of aerosol deposition. It has been established that aerosol deposition is strongly dependent on particle size [12] and airflow. An appropriate airflow is necessary to transport the aerosol to the site of infection. Inhalation technique and factors influencing airflow distribution in the lungs such as structural lung changes and airway obstruction by mucus are known to affect deposition of aerosols [21, 28]. For CF it is known that patients suffering from more severe lung disease have more central airway deposition compared to healthy individuals [28]. This suggests that CF patients might benefit from specific dose adjustments based on their disease severity. Adjusting dose, particle size or inhalation technique to the patient's lung disease status could improve efficiency of aerosol delivery to the site of infection, resulting in more effective treatment. However, to maximize drug delivery to the small airways, the relation between age, structural changes and inspiratory flow profile and antibiotic concentrations in different compartments of the bronchial tree needs to be better understood.

Unfortunately, it is difficult to investigate the simultaneous influence of these factors on deposition in vivo. However, many aspects of aerosol deposition can nowadays be modelled. Functional respiratory imaging (FRI) has been developed to assess the behaviour of inhalation medication in the airways and lungs of a specific patient [15]. This technique has been validated using Single Photon Emission Computed Tomography [16]. So far, this technique has been used to study lung drug deposition in asthma patients [51], and, both in asthma and chronic obstructive pulmonary disease, to assess airflow distribution [15, 16] and the bronchodilating effects of β2-agonists [14, 17, 53]. There are three essential steps in applying FRI to CT data. These steps involve image processing (specifically, segmentation and trimming), three-dimensional image reconstruction and definition of boundary conditions required for simulation of inhalation therapy, such as breathing profile, internal lobar flow distribution and drug characteristics.

FRI can increase our understanding of deposition mechanisms in diseased airways as this technique makes it possible to estimate local measurements of an individual patient. By using patient specific anatomical models obtained from their CT scans, in combination with a flow simulation method, aerosol concentrations in both the central and small airways can be computed. Moreover, by using CT

scans from patients who differ in disease severity, the relationship between airway morphology and airway deposition can be assessed. Additionally, by repeating simulations and changing important variables one at a time, FRI can provide more information on how to optimize small airway aerosol deposition in CF patients with structural lung changes. To our knowledge, patient specific airway models were never used before to estimate local concentrations of inhaled antibiotics in CF patients.

For our current study we aimed to study the relation between structural lung disease and deposition of a recently developed inhaled antibiotic used for suppressive treatment of chronic Pa infections; Aztreonam lysine for inhalation (AZLI). AZLI is a monobactam antibiotic, delivered by the e-Flow® electronic nebuliser [59]. In our study we aimed to use FRI to predict AZLI concentrations in CF lungs. We hypothesized firstly that there is great variation in AZLI concentrations due to differences in airway geometry between subjects and CF lung disease severity. Secondly, we hypothesized that AZLI concentrations in the small airways would be below the MIC for Pa in patients with more severe lung disease. Thirdly, we hypothesized that AZLI concentrations in the small airways could be improved by increasing the dose of AZLI or by modifying the inhalation technique.

7.4 Materials and methods

7.4.1 Study population

We included CF patients who had a volumetric in- and expiratory high resolution CT scans with a slice thickness of 1 mm or less performed as part of their routine annual check up in the Erasmus MC-CF centre (Rotterdam, Netherlands) in the period from 2008 to 2012. Patients were diagnosed as having CF by a positive sweat test and/or genotyping for known CF mutations. For all patients (ages 5 – 17 years), demographic data and pulmonary function tests were collected. Pulmonary function test results were expressed as percentages of predictive values, according to Stanojevic for the forced vital capacity (FVC) and FEV1, and Zapletal for the forced expiratory flow at 75% (FEF75) [46, 58]. Written informed consent for the use of de-identified data was obtained from the parent/guardian and subjects = 12 years prior to inclusion in the study. This retrospective study was approved by the Institutional Review Board of our hospital (MEC-2013-078).

7.4.2 Chest Computed Tomography

For this study 40 consecutive CT scans were included. All CT scan sets were acquired using a 128-slice CT scanner (Somatom Definition Flash, Siemens). Thirty-nine (98%) volumetric CT scans were spirometer controlled (Jaeger AG). For one patient the spirometer was not tolerated and a technician-controlled technique was used.

Before performing the CT scan, a lung function technician trained the study

subjects by practicing the required spirometry manoeuvres in supine position with the children half an hour prior to the CT scan. Children were trained to obtain a breath-hold at maximal inspiration (total lung capacity, TLC) and maximal expiration (residual volume, RV) for 5 – 15 seconds. The inspiratory and expiratory slow vital capacities (SVC) achieved during the training were used as the reference values for the spirometric results during the CT scan. The reference SVC's were performed according to the ATS/ERS criteria [36]. Breathing instructions during the CT scan were given by the same lung function technician. During CT scanning, the lung technician monitored in real time the inspired and expired volumes on the computer screen of the CT-compatible spirometer setup. When the patient obtained the correct TLC (inspiratory scan) or RV (expiratory scan) breath hold level, the lung function technician signalled the CT-technician to start scanning. For the technician-controlled technique the same breathing instructions were given during the CT scan; however, the inspired and expired volumes were not measured using spirometry.

7.4.3 CT settings

Tube voltages of 80 kV (patients $<$ 35 kg) or 110 kV (patients = 35 kg) were used with a 0.6s rotation time. Scanning was done from apex of the lung to base at 1.5 pitch and 6x2 mm collimation. Images were reconstructed with a slice thickness = 1.0 mm, a slice increment = 0.6 mm and kernel B75f. For the inspiratory protocol, a modulating current was used (Siemens) with a reference tube current-time product of 20 mAs for optimal image quality. For expiratory CTs, a tube current fixed at 25mA with an effective tube current-time product of 10 mAs (the typical value for a 5-year-old child) was used producing a lower radiation dose than the inspiratory protocol with sufficient image quality. Total radiation dose was in the order of 0.75 mSv for children below the age of 6 years and 1 mSv in older children.

7.4.4 CT evaluation

To quantify chest CT abnormalities, we used the validated CF-CT scoring system [54]. This scoring method evaluates the 5 lung lobes and the lingula as a sixth lobe for the following components: 1) severity, extent of central and peripheral bronchiectasis; 2) airway wall thickening; 3) central and peripheral mucus plugging; 4) opacities (atelectasis, consolidation, ground glass pattern); 5) cysts and bullae on inspiratory CTs and 6) the pattern and extent of trapped air on expiratory CTs. The maximal possible composite CT score is 207 points and the components scores are expressed as a percentage of this maximal possible score. The component scores for bronchiectasis, airway wall thickening and air trapping were used for analysis. To examine the relation between structural changes in the airways and AZLI concentrations in that area, CF-CT scores were also computed for each of the 5 lobes.

Prior to scoring, all CT scans were de-identified (Myrian®, Intrasense). Next,

scans were scored in random order by an experienced observer, with more than 2 years' experience in scoring, and who was blinded to clinical background. To assess inter-observer agreement, a second observer, with 4 months scoring experience, scored all CT scans. Both observers were initially trained in CF-CT scoring using a standardized instruction module and training sets and started scoring the study CT scans after establishing good intra- and inter-observer agreement. To establish the intra-observer agreement, observer 1 rescored 25 random selected scans after 3 months. CF-CT scores of observer 1 were used for analysis.

7.4.5 Reconstruction of three-dimensional airway models

Based on the inspiratory scan, a semi-automatic algorithm was used to reconstruct patient specific three-dimensional (3D) model of the intra-thoracic region, which we defined arbitrarily as the lower airway. The automatic segmentation could be performed up to the point where no distinction could be made between the intra-luminal and alveolar air. Following automated segmentation of the bronchial tree, the airways were manually checked. Missing branches were added to the bronchial tree and incorrect branches were deleted when necessary; $3.39 \pm 2.51\%$ [0.63 – 10.97] of the branches needed to be manually altered. The respiratory tract was reconstructed down to the level of airways with a diameter of 1 – 2 mm. The segmented airway tree was converted into a 3D model that was smoothed using a volume compensation algorithm. The smoothed model was trimmed perpendicular to the airway centreline at the trachea (using the middle point of the superior side of the sternum as a landmark) and at each terminal bronchus. Remaining noise in this model was then manually removed.

For the upper (extrathoracic) airways, a generic average adult upper airway model was selected and scaled down in such a way that both the anteroposterior and lateral dimension of the scaled model's trachea, at the location of the sternum, matched the average anteroposterior (1.25cm) and lateral (1.19cm) dimension for the 40 patients. The upper airway model was connected with a reverse engineered mouthpiece of the Pari eFlow®. Reverse engineering was done based on a CT scan of the mouthpiece taken on a GE LightSpeed VCT (80 kV, 18.25 mAs, 0.311 mm slice increment, 0.188 mm pixel size, STANDARD reconstruction algorithm). The mouthpiece/upper airway model was trimmed perpendicular to the centreline of the trachea (again using the middle point of the superior side of the sternum as a landmark).

For each of the 40 CT scan sets, the patient specific lower airway model was connected to the selected nebulizer mouthpiece/upper airway model, maximizing the amount of patient specific information. All segmentation and 3D model operations were performed in commercially available validated software packages (Mimics 15.0 and 3-Matic 7.0, Materialise nv, Food and Drug Administration, K073468; ConformitÈ EuropÈenne certificate, BE 05/1191.CE.01).

7.4.6 Meshing

The triangulated, mouthpiece/upper-/lower airway surface models had a maximum triangle edge length of 0.5 mm and a minimum triangle aspect ratio of 0.4. These models were converted to tetrahedral 3D volume meshes using TGrid 14.0 (Ansys Inc). A boundary layer with a growth rate of 1.4 was included in the models. Maximal tetrahedral volume was set to 2 mm^3 and maximal equilateral volume-based skewness to 0.9. Grid convergence demonstrated that a mesh size of 2.9 $\pm$ 0.7M [1.9 – 4.6] cells is appropriate for the study, depending on the size of the patient specific lower airway model. Meshing was done on 1 CPU and meshing time was below 200 s.

7.4.7 Reconstruction of three-dimensional lung lobes

From both the inspiratory and expiratory CT scans, the patient specific lung lobes were extracted using a semi-automated tool that identifies the fissures separating the lung lobes. The internal lobar flow distribution could be calculated based on the lobar volume change from expiration to inspiration. Lung lobe identification has been performed in a commercially available validated software package (Mimics 15.0, Materialise nv, Food and Drug Administration, K073468; Conformité Européenne certificate, BE 05/1191.CE.01).

7.4.8 Breathing profile

The average age of the patient population (11 years) was used to generate a generic breathing profile based on the following parameters: median weight of 11 year old Dutch children is 38 kg (boy: 37 kg, girl 38.5 kg) [47]; tidal volume of 10 mL/kg (380 mL); respiration rate (18 breaths per minute) [55]. The resulting profile had an inspiration/expiration ratio of 1:2 and a sinusoidal shape, see Figure 7.1.

To be able to examine the flow dependency of the simulated results, 2 additional breathing profiles were generated: 1) a high breathing profile, consisting of a higher tidal volume of 14 mL/kg (532 mL) and the respiratory rate of the youngest age (5 years: 22 breaths per minute), and 2) a low breathing profile, consisting of a lower tidal volume of 6 mL/kg (228 mL) and the respiratory rate of oldest age (17 years: 14 breaths per minute). These additional profiles can also be found in Figure 7.1.

7.4.9 Aerosol characteristics

Eleven different trials (Anderson Cascade impactor n = 6, next generation impactor n = 2, and laser diffraction n = 3) studied the diameter distribution of AZLI nebulized via the Pari eFlow® (Gilead data on file). The extremes and the median were selected for use in the FRI simulations: smallest diameter (2.81 $\pm$ 1.47 μm), median diameter (3.18 $\pm$ 1.63 μm) and largest diameter (4.35 $\pm$ 2.05 μm). Furthermore, an in vivo characterization of the eFlow® showed that 35% of the nominal fill volume is either trapped in the mouthpiece or exhaled.

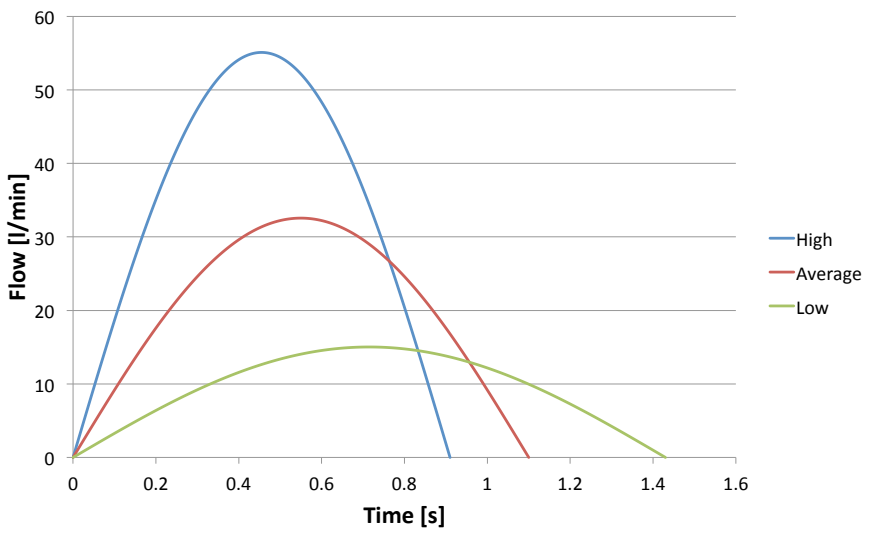

Figure 7.1: Inhalation part of breathing profiles. Small breathing profile: tidal volume of 6 mL/kg (228 mL) and respiration rate of 14 breaths per minute. Average breathing profile: tidal volume of 10 mL/kg (380 mL) and respiration rate of 18 breaths per minute. Large breathing profile: tidal volume of 14 mL/kg (532 mL) and respiration rate of 22 breaths per minute.

7.4.10 Flow simulation

Computational fluid dynamics (CFD) flow simulations were performed in Fluent 14.0 (Ansys Inc). All simulations were transient using a second order time stepping algorithm and a time step of 0.005s. Turbulence was evaluated through large eddy simulations with a turbulent kinetic subgrid model. Aerosol transport was modelled by an implicit Runge-Kutta Lagrangian discrete particle model, with a one-way coupling of the forces from the flow to the particle and taken into account the Saffman lift forces. Particles were considered deposited the moment they hit the airway wall.

The nominal dose of 75 mg AZLI was corrected for the 35% combined inhaler loss and exhaled fraction. Due to the incorporation of the exhaled fraction, only the inhalation was modelled. The boundary condition at the inhaler mouthpiece was represented by the inhalation part of the mean breathing profile in Figure 7.1. The downstream boundary conditions at the terminal bronchi were set such that the percentage of flow exiting the model towards a lobe did match with the internal lobar flow distribution obtained from the expiratory and inspiratory CT data.

To investigate the influence of the inhalation manoeuvre on local concentrations, additional simulations were performed in a subset of the population (2 tallest, 2 smallest, 2 median sized patients). These additional CFD simulations were performed with the altered breathing profiles described in section 7.4.8.

7.4.11 Aerosol deposition analyses

To be able to perform regional analyses, the respiratory tract was subdivided in multiple regions. For the airways with a diameter $>1-2$ mm these regions were obtained from the mouthpiece/upper-/lower airway model, see Figure 7.2. In figure 7.2, the upper airway is divided in two parts: the oral cavity and the pharynx; and the lower airway is divided in a central part and distal parts representing the lung segments. Conducting airways with a diameter $< 1-2$ mm could not be distinguished from the CT images and have been added to the patient specific model by using Phalen's description of the airway tree in infants, children and adolescents [41]. For every simulation, a Phalen model was constructed based on the height of the specific patient.

Regional AZLI deposition was evaluated for both the particles depositing inside the model, in every separate zone indicated in Figure 7.2; as well as for the particles exiting the model at the terminal bronchi, in the small airways represented by the Phalen model on a lobar basis. Once the aerosol entered the Phalen model of a certain lobe, it was assumed that it was distributed homogeneously.

7.4.12 Airway surface liquid

To compute AZLI concentration in the airway surface liquid (ASL) throughout the bronchial tree we used a range of thicknesses based on studies in CF. Three different ASL scenarios were considered: thick ASL (7 μm) [49], thin ASL (3 μm) [48] and

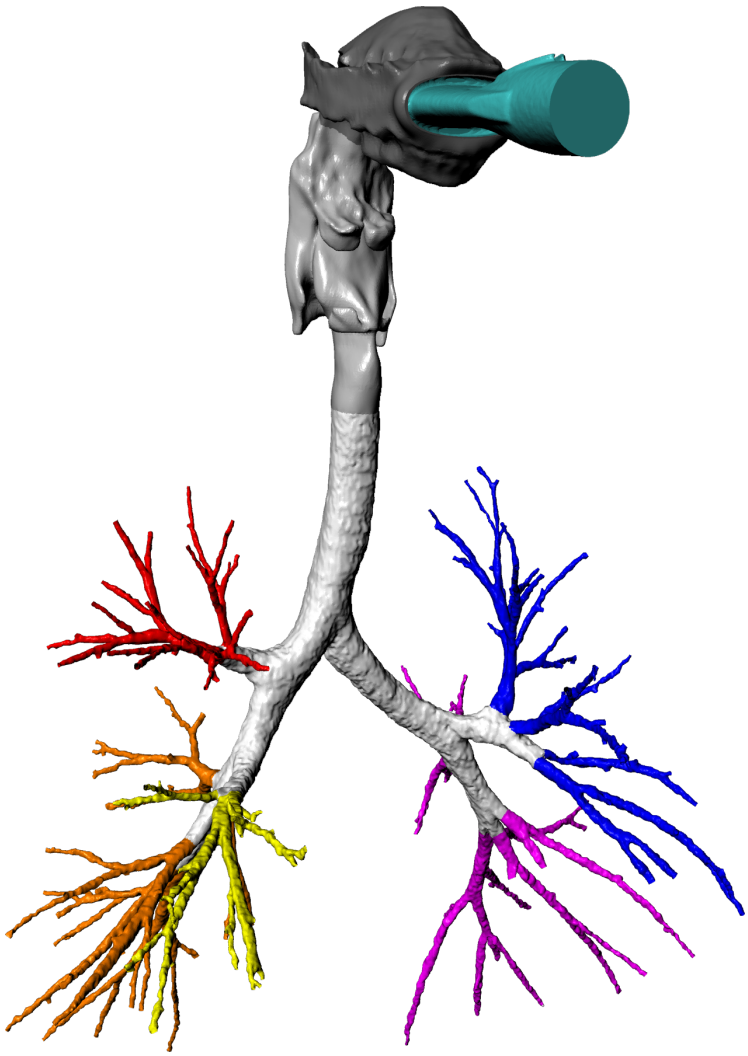

Figure 7.2: Coupled mouthpiece/upper-/lower airway model subdivided in multiple regions. Airways are segmented up to the 5th – 9th generation. The different regions are: mouthpiece (turquoise), mouth (dark grey), upper airway (light grey), central airways (white), distal airways (colored)

the mean ASL (5 µm).

7.4.13 AZLI concentrations

For each reconstructed airway and for each lung lobe, the area was calculated and the CFD simulations provided data on the drug deposition in that region. The regional AZLI concentration was computed as follows: the mass of the deposited drug in an airway was divided by the thickness of the lining fluid multiplied by the surface area of that airway.

Finally, this regional AZLI concentration is expressed relative to the MIC of AZLI required to inhibit the growth of 90% of Pa strains multiplied by 10 (10xMIC90 = 10x128 µg/ml = 1280 µg/ml), since this is the most stringent effective AZLI level reported in literature [27, 40, 44].

7.4.14 Statistical analysis

Inter- and intra-observer agreements of component CF-CT scores were calculated using intraclass correlation coefficients (ICC). Although no universally accepted standards are available for what constitutes good reliability, ICC values between 0.4 and 0.6, 0.6 and 0.8, and = 0.8 are generally considered to represent moderate, good and very good agreement, respectively. Systematic errors in component scores were evaluated using Bland-Altman plots, expressing the differences between two observers as a function of their mean [5].

To establish the correlation between age and disease severity expressed in CF-CT scores and pulmonary function tests, we used Spearman's correlation test. According to Cohen's criteria (1988), correlations between 0.10 and 0.29 are considered weak, between 0.30 and 0.49 moderate and above 0.50 are considered strong.

Differences between multiple groups were investigated using a Kruskal-Wallis test, after which two by two comparisons were made using Mann-Whitney tests. The effect size was noted as r. To search for correlations between parameters that were measured in the different lobes, a generalized estimating equation using an autoregressive covariance matrix was used to account for within-subject correlations. All data are presented as the median (range). Significance level was set at 0.05 and p-values were corrected for multiple testing using Benjamini and Hochberg correction [4]. All statistical computations were performed using the open-source statistical environment R 2.15.3.

7.5 Results

7.5.1 Study population

Forty consecutive inspiratory and expiratory chest CT scans were selected. Baseline characteristics are shown in Table 7.1. Thirty-nine (98%) CT scans were spirometer

controlled, and for 1 CT scan the breathing during the scan was controlled by the technician. There were no significant differences between the sexes for demographics, pulmonary function tests and CF-CT sub scores (Table 7.1), meaning that the dataset did not have to be split in sex groups. ICCs for within-observer agreement ranged from 0.85 (CF-CT air trapping score) to 0.93 (CF-CT bronchiectasis score), whereas between-observer agreement ranged from 0.67 (CF-CT airway wall thickening score) to 0.77 (CF-CT air trapping score).

	Value		**p-value**
N	31		
Male	11	35%	
Age	11.4	(5.8 – 17.3)	0.51
Bronchiectasis score % of max CF-CT score	2.8	(0.0 – 16.0)	0.41
Airway wall thickening score % of max CF-CT score	3.7	(0.0 – 18.5)	0.99
Air trapping score % of max CF-CT score	22.2	(11.1 – 85.2)	0.41
FEV1% pred	93.5	(70.0 – 115.0)	0.1
FVC% pred	104	(78.0 – 127.0)	0.69

Table 7.1: Baseline characteristics: Data are presented as nr. (%) or median (range), unless otherwise indicated. P-values represent differences between the sexes

7.5.2 Correlations

There was a moderate positive correlation between bronchiectasis scores and age (r = 0.481, p = 0.005). Correlations between age and airway wall thickness (r = 0.302, p = 0.087) and air trapping (r = 0.096, p = 0.554) were not significant. Furthermore, there were no significant correlations between age and pulmonary function tests (FVC% pred: r = 0.053, p = 0.885; FEV1% pred: r = -0.024, p = 0.885).

7.5.3 Deposition analyses

Significant differences between the lobes were found for all tested CF-CT sub scores (bronchiectasis score: χ^2 = 24.04, p $<$ 0.001; airway wall thickness: χ^2 = 23.90, p $<$ 0.001; and air trapping: χ^2 = 18.77, p $<$ 0.001). It was found that CF-CT sub scores were generally higher in the right upper lobe than in the other lobes (Table 7.2).

There was a deposition difference of AZLI between the different lobes (Table 7.3). The highest AZLI concentrations were found in the lower lobes. For the lower lobes, AZLI concentrations were always higher than 10xMIC90 independent of the scenario tested. An inverse correlation between AZLI concentration in a lobe and the CF-CT scores was observed, indicating that more diseased lobes received a lower concentration of AZLI (Table 7.4).

When expressing this regional AZLI concentration relative to 10xMIC90,

CF-CT sub score	Lobe	Score (% of total score)	Comparison with other lobes (p-values)				
			RUL	RML	RLL	LUL	LLL
Bronchiectasis	RUL	0 (0 – 33.33)	-	**0.005**	**0.004**	0.058	**0**
	RML	0 (0 – 29.17)	**0.005**	-	1	0.235	0.235
	RLL	0 (0 – 29.17)	**0.004**	1	-	0.235	0.235
	LUL	0 (0 – 18.75)	0.058	0.235	0.235	-	**0.017**
	LLL	0 (0 – 25.00)	**0**	0.235	0.235	**0.017**	-
Airway wall thickness	RUL	11.11 (0 – 27.78)	-	**0.045**	**0.049**	0.472	**0.029**
	RML	0 (0 – 13.89)	**0.045**	-	0.43	**0.034**	0.661
	RLL	0 (0 – 16.67)	**0.049**	0.43	-	**0.023**	0.469
	LUL	2.78 (0 – 16.67)	0.472	**0.034**	**0.023**	-	**0.006**
	LLL	0 (0 – 22.22)	**0.029**	0.661	0.469	**0.006**	-
Air trapping	RUL	11.11 (0 – 50.0)	-	**0.045**	**0.049**	0.472	**0.029**
	RML	11.11 (0 – 33.33)	**0.045**	-	0.43	**0.034**	0.661
	RLL	11.11 (0 – 50.0)	**0.049**	0.43	-	**0.023**	0.469
	LUL	11.11 (0 – 50.0)	0.472	**0.034**	**0.023**	-	**0.006**
	LLL	11.11 (0 – 33.33)	**0.029**	0.661	0.469	**0.006**	-

Table 7.2: Comparison of CF-CT sub scores per lobe: Data are presented as median (range), unless otherwise indicated. P-values in bold represent significant differences. RUL = right upper lobe, RML = right middle lobe. RLL = right lower lobe, LUL = left upper lobe, LLL = left lower lobe.

Lobe	AZLI concentration (µg/ml)	Comparison with other lobes (p-values)				
		RUL	RML	RLL	LUL	LLL
RUL	1332 (888 – 1787)	-	**0.002**	**1.40E-09**	0.156	**2.70E-10**
RML	966 (636 – 1608)	**0.002**	-	**2.70E-10**	**5.60E-06**	**2.70E-10**
RLL	2070 (1387 – 2782)	**1.40E-09**	**2.70E-10**	-	**6.80E-11**	**5.30E-10**
LUL	1391 (468 – 1943)	0.156	**5.60E-06**	**6.80E-11**	-	**3.30E-13**
LLL	2623 (1942 – 3280)	**2.70E-10**	**2.70E-10**	**5.30E-10**	**3.30E-13**	-

Table 7.3: Differences between lobes in AZLI concentrations for the scenario of thick lining fluid with largest aerosol diameter. Data are presented as median (range), unless otherwise indicated. P-values in bold represent significant differences. RUL = right upper lobe, RML = right middle lobe. RLL = right lower lobe, LUL = left upper lobe, LLL = left lower lobe.

ASL	Diameter (µm)	CF-CT score	Estimate	Std.err	Wald	p-value
Thin (3 µm	Smallest (2.9)	Bronchiectasis	-439	115	14.6	**0.00013**
		Airway wall thickness	-466	142	10.7	**0.0011**
		Air trapping	-237.5	85.3	7.76	**0.0053**
	Median (3.18)	Bronchiectasis	-387	108	12.8	**0.00034**
		Airway wall thickness	-421	133	10	**0.0016**
		Air trapping	-229.7	78.5	8.56	**0.0034**
	Largest (4.35)	Bronchiectasis	-278.8	86.5	10.4	**0.0013**
		Airway wall thickness	-316.8	106.2	8.9	**0.0029**
		Air trapping	-190.3	61.4	9.6	**0.0019**
Median (5 µm)	Smallest (2.9)	Bronchiectasis	-263.7	69	14.6	**0.00013**
		Airway wall thickness	-279.6	85.4	10.7	**0.0011**
		Air trapping	-142.5	51.2	7.76	**0.0053**
	Median (3.18)	Bronchiectasis	-232	64.8	12.8	**0.00034**
		Airway wall thickness	-252.7	79.9	10	**0.0016**
		Air trapping	-137.8	47.1	8.56	**0.0034**
	Largest (4.35)	Bronchiectasis	-167.3	51.9	10.4	**0.0013**
		Airway wall thickness	-190.1	63.7	8.9	**0.0029**
		Air trapping	-114.2	36.9	9.6	**0.0019**
Thick (7 µm)	Smallest (2.9)	Bronchiectasis	-188.3	49.3	14.6	**0.00013**
		Airway wall thickness	-199.7	61	10.7	**0.0011**
		Air trapping	-101.8	36.5	7.76	**0.0053**
	Median (3.18)	Bronchiectasis	-165.7	46.3	12.8	**0.00034**
		Airway wall thickness	-180.5	57.1	10	**0.0016**
		Air trapping	-98.5	33.7	8.56	**0.0034**
	Largest (4.35)	Bronchiectasis	-119.5	37.1	10.4	**0.0013**
		Airway wall thickness	-135.8	45.5	8.9	**0.0029**
		Air trapping	-81.6	26.3	9.6	**0.0019**

Table 7.4: Inverse correlation between AZLI concentration in a lobe and the CF-CT scores, shown for the different scenarios and different aerosol diameters. P-values in bold represent significant correlations. ASL = airway surface liquid, Estimate = the estimation of the slope of the linear model, Std.err = the robust standard error estimate, Wald = the Wald statistic (outcome of the Wald test)

differences were observed when using different ASL thicknesses. The combination of the thin lining fluid and smallest diameter of aerosols resulted in AZLI concentrations above 10xMIC90 for all lobes. For the combination of thick lining fluid and largest diameter of aerosols, up to 28% of the lobes received AZLI concentrations below 10xMIC90. The lowest AZLI value that was observed in all the lobes for the tested population was 468.14 µg/ml or 3.66xMIC90. Table 7.5 summarizes the patients and lobes that receive a concentration lower than 10xMIC90 for the different modelling conditions. In figures 7.3 and 7.4, the relative AZLI concentrations in 2 patients are shown for 3 different scenarios. In the central and distal airways, AZLI concentrations 10 – 100x above the threshold of 1280 µg/ml were observed. In the small airways (visualized per lobe in the images), lower concentrations were seen.

ASL	**Diameter (µm)**	**Nr of patients with at least 1 lobe with AZLI < 10xMIC90**	**Nr of lobes with AZLI < 10xMIC90**
Thin (3 µm)	Smallest (2.9)	0	0
	Median (3.18)	0	0
	Largest (4.35)	1 (2.5%)	1 (0.5%)
Median (5 µm)	Smallest (2.9)	1 (2.5%)	1 (0.5%)
	Median (3.18)	3 (7.5%)	3 (1.5%)
	Largest (4.35)	10 (25%)	15 (7.5%)
Thick (7 µm)	Smallest (2.9)	6 (15%)	7 (3.5%)
	Median (3.18)	14 (35%)	19 (9.5%)
	Largest (4.35)	32 (80%)	56 (28%)

Table 7.5: Number of patients and lobes with AZLI <10xMIC90: Data are presented as nr. (%). ASL = airway surface liquid, Nr = number.

Decreasing the tidal volume decreased the deposition in the extrathoracic region. These reductions subsequently resulted in significantly more areas with a concentration above 10xMIC90 in the lungs (Table 7.6).

ASL	**Diameter (µm)**	**% Area with AZLI < 10xMIC90**		
		Low flow	**Average flow**	**High flow**
Thin (3 µm)	Smallest (2.9)	0	0	0
	Median (3.18)	0	0	0
	Largest (4.35)	0	0	0
Median (5 µm)	Smallest (2.9)	0	0	0
	Median (3.18)	0	0	0
	Largest (4.35)	0 (0 – 10.92)	0 (0 – 10.92)	16.51 (0 – 27.37)
Thick (7 µm)	Smallest (2.9)	0 (0 – 10.92)	0 (0 – 10.92)	0 (0 – 10.92)
	Median (3.18)	0 (0 – 10.92)	0 (0 – 10.92)	16.51 (0 – 27.37)
	Largest (4.35)	0 (0 – 10.92)	27.40 (0 – 49.79)	49.40 (27.25 – 49.79)

Table 7.6: Influence of inhalation technique on AZLI concentrations: Data are presented as median (range), unless otherwise indicated. ASL = airway surface liquid.

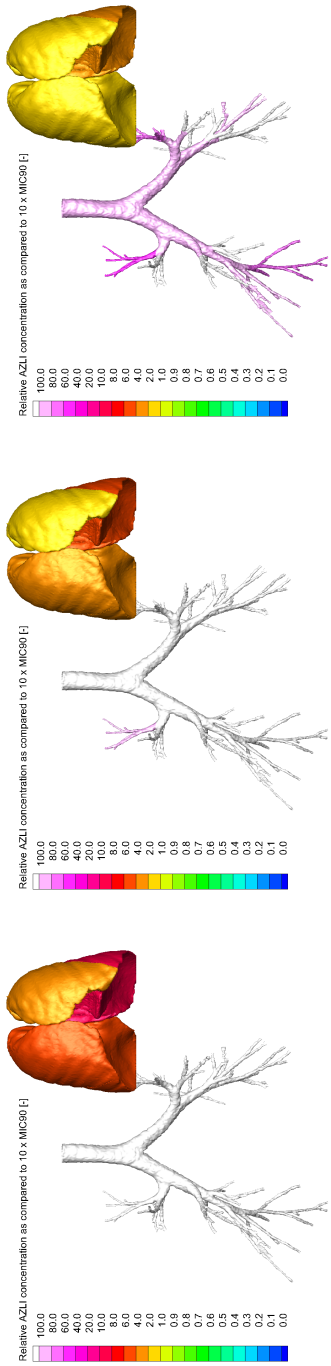

(a) Patient 1 scenario a

(b) Patient 1 scenario b

(c) Patient 1 scenario c

Figure 7.3: Simulations of AZLI deposition in mild CF patient, representing 3 scenarios of varied airway surface liquid thickness (ASL) and aerosol diameter. Severity of CF lung disease was determined by the CF-CT score (% of total CF-CT score). Scenario a = thin ASL with smallest aerosol diameter; scenario b = median ASL with median aerosol diameter; scenario c = thick ASL with largest aerosol diameter. Patient with mild CF lung disease: bronchiectasis 0.0%, airway wall thickening 0.0% and air trapping 11.1%. The patient received concentrations > 10xMIC90 in the central and small airways independent of ASL thickness and aerosol diameter.

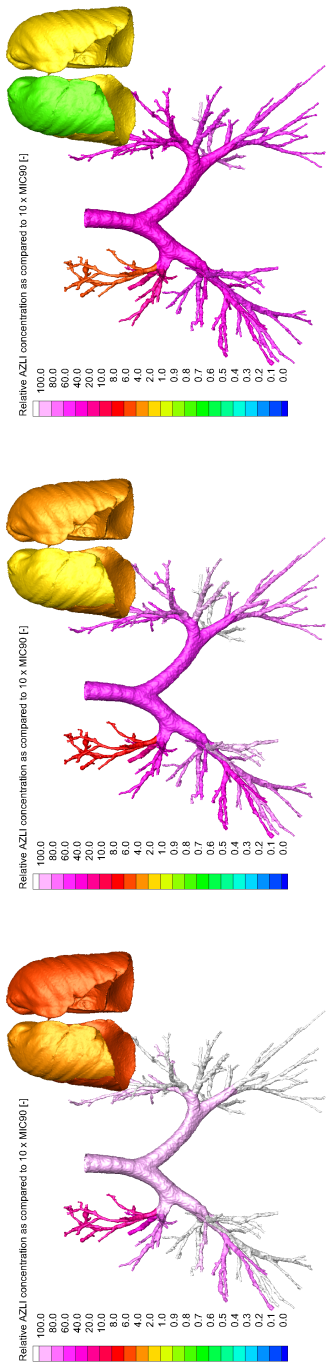

(a) Patient 2 scenario a

(b) Patient 2 scenario b

(c) Patient 2 scenario c

Figure 7.4: Simulations of AZLI deposition in severe CF patient, representing 3 scenarios of varied airway surface liquid thickness (ASL) and aerosol diameter. Severity of CF lung disease was determined by the CF-CT score (% of total CF-CT score). Scenario a = thin ASL with smallest aerosol diameter; scenario b = median ASL with median aerosol diameter; scenario c = thick ASL with largest aerosol diameter. Patient with severe lung disease: bronchiectasis 12.5%, airway wall thickening 11.1% and air trapping 38.9%. The patient received concentrations > 10xMIC90 in the central and small airways in scenario a and b, but AZLI concentrations < 10xMIC90 in the small airways in scenario c (right upper and middle lobes).

7.6 Discussion

This study demonstrates the ability of FRI to give insight in patient specific inhaled antibiotic concentrations throughout the bronchial tree. The most important finding was that the concentrations of the inhaled antibiotic delivered to the airways were highly dependent on patient related factors.

Another important finding of this study was that for the tested inhaled antibiotic (AZLI), effective concentrations above the 10xMIC90 threshold for Pa were observed throughout the lung in most simulated conditions. However, variables, such as particle diameter and lining fluid thickness, had an important impact on the results. Under certain assumptions of these variables, it was shown that the concentration would drop below 10xMIC90 in up to 28% of the lobes. The most critical scenario was the combination of a thick lining fluid and the largest aerosol diameter. However, the lowest observed AZLI concentration in the lobes of the studied population was still above 3xMIC90 for Pa. For this particular patient, an increase of 2.7 times the standard nebulized AZLI dose would have resulted in sufficiently high concentrations in all lobes. In the "best-case" scenario, all lobes received AZLI concentrations above 10xMIC90. The observation that regional low concentrations can exist is of great importance since suboptimal concentrations could result in suboptimal killing and are associated with the development of antibiotic resistance [24].

As in previous studies we observed that the upper lobes were more severely affected relative to the other lobes [31, 56]. The reason for this distribution however is still largely unknown. Our findings suggest that uneven distribution of inhaled drugs could contribute to this inequality. We observed that even in CF patients with relative little structural damage the upper lobes received lower AZLI concentrations than the lower lobes. Furthermore, an inverse correlation between the CF-CT score and the AZLI concentration for a lobe was shown. These findings match deposition studies in CF patients showing that the deposition pattern is more heterogeneous in diseased lungs than in healthy lungs [12, 23, 29]. In addition, it supports previous studies showing that penetration of inhaled drugs in deformed or partial obstructed airways is restricted [23, 29]. These results suggest that upper lobes are more vulnerable to be undertreated and that this effect is stronger once structural damage is present.

With our simulations we showed that lower inhalation flows lead to higher AZLI concentrations in the small airways, due to decreased extrathoracic deposition. This finding is in line with previous studies showing that high flows lead to high extrathoracic and upper airway deposition of drug [12]. Using patient specific airway modelling we were able to study the impact of inhalation flow rate and inhaled volume on local airway drug concentrations in all lobes for individual patients. This information can subsequently be used to set smart nebulisers in such a way that adequate small airways concentrations can be obtained [2]. Or to define the required medication dose for a patient that, independent of the breathing pattern, results in sufficient drug delivery to critical areas of the lung.

FRI could offer a number of advantages to complement available techniques for studying aerosol deposition. First, non-imaging techniques, e.g. pharmacokinetic methods, lack the ability to identify dose deposition into different zones of the lungs [10]. Scintigraphic methods do assess the deposition location of inhaled drugs. However, in these studies the lung is divided into several large regions of interests and aerosol deposition patterns and distribution is compared between these regions [6, 11, 23, 30, 42]. In contrast, FRI enabled us to determine detailed information on aerosol deposition at specific anatomical sites. Second, FRI information allowed us to estimate AZLI concentrations throughout the bronchial tree. In vivo this kind of data are extremely difficult to obtain. To date, great emphasis has been given to sputum concentrations in clinical studies investigating inhaled antibiotics. It is highly likely that these concentrations are primarily reflective of central airway concentrations. The central airway concentrations found in this study were in the range of the fitted sputum concentrations from clinical studies, taking into account that published sputum concentrations were collected at later time points compared to this study (data on file). As suggested by our findings, high concentrations in central airways result in lower concentrations in the small airway compartment, challenging the validity of sputum samples as a useful indicator to explain the failure or success of inhaled antibiotics. Third, our method utilized CT scans that were acquired as part of routine clinical care [32]. Hence, extra clinically relevant information could be extracted from the chest CT beyond lung morphology without the need for additional radiation. Fourth, the model allowed us to study the impact of multiple variables, e.g. particle size distribution, on lung deposition within the same patient. Thus, FRI opens up new pathways to further optimize inhalation therapies even at a personalized level.

To allow modelling of AZLI and estimation of concentrations, several assumptions were made. These assumptions do limit the implementation of our results.

The first assumption was that the antibiotic concentration in the ASL is the most important determinant for effective killing of Pa [7, 9, 57]. To estimate ASL concentrations we had to consider three different scenarios for lining fluid thickness. These scenarios were based on in vitro data of CF bronchial epithelial cultures and covered the complete range of ASL thickness found in CF [48].

While ASL concentration is considered to be a reliable marker of alveolar antibiotic concentration [7, 9, 57], there are several limitations to this assumption. First, we did not take the uptake of drug by alveolar macrophages into consideration as a measure of intracellular penetration in the lungs [45]. Especially in the chronically infected lung, macrophages may play a substantial role in the pharmacodynamics of anti-infective agents. Second, we did take into account binding of AZLI to sputum [45]. Only unbound drug concentrations are considered to be microbiologically active. The significance and the amount of protein binding of AZLI in ASL are unknown and, to our knowledge, have not been studied. In plasma, protein binding for AZLI is around 42 – 56% [34, 52]. Hence, due to sputum binding, estimated concentrations of unbound AZLI could be dramatically lower, increasing the percentage of airways with insufficient ASL concentrations.

Third, we did not account for mucociliary and cough clearance which further reduces AZLI concentrations in the airways within minutes after inhalation [18]. Fourth, the microbiological effect of a β-lactam antibiotic, such as AZLI, is best predicted using function of time above the MIC (T $>$ MIC) [38, 39]. Unfortunately, the half-life of AZLI in the airways is largely unknown. The half-life of AZLI in serum is approximately two hours. Therefore, a prediction of efficacy of AZLI in the airways based on a single time point immediately after inhalation has clear limitations. Thus, even though the concentration of AZLI was well above MIC90 for most simulated conditions immediately after nebulization, concentrations may decrease below MIC90, especially in diseased areas, before a new dose of AZLI is nebulized.

The second assumption was the AZLI concentration that could be considered effective for killing Pa strains. This assumption has limitations as the ideal AZLI concentration for effective killing of Pa in vivo is actually not well defined. First, terms indicating the efficacy level of antibiotics, e.g. MIC and MIC90, are used interchangeably in previous studies [38, 39]. Second, the MIC90 values range between 32 and 128 µg/ml [20, 22, 27, 40, 44]. Third, for AZLI, most susceptible bacteria are killed at concentrations 1 to 4-fold their MIC. However, in some cases an AZLI concentration of 4 to 16-fold the MIC was required to achieve bactericidal killing of Pa [1]. For two other antibiotics, ceftazidime and imipenem, it was shown that mucoid Pa strains required higher antibiotic concentrations as the time-dependent killing pattern for nonmucoid Pa strains changed to concentration-dependent killing [26]. Studies on the efficacy of AZLI mostly use the conservative threshold of 10-fold MIC90, but without clear explanation [20, 22]. This conservative threshold, using 128 µg/ml as MIC90, was also used for our analyses in this manuscript, but no speculations could be made concerning its clinical relevance.

The final limitation of the model is that we did not use patient specific breathing profiles and upper airway models for this study since they were not available. Clearly, this would have improved the precision of the simulations.

In conclusion, it was shown that inhaled antibiotic concentrations in the lung lobes are highly patient specific. Using FRI, we were able to gain insight in the relation between patient specific characteristics such as severity of localized CF lung disease and concentrations of the inhaled antibiotic throughout the lung. This method opens up the possibility of personalizing the medication dose on a patient specific basis.

References

[1] Aztreonam for inhalation solution (NDA 50-814) for improvement of respiratory symptoms in cystic fibrosis patients. FDA Briefing Document NDA 50-814, Anti-Infective Drug Advisory Committee, 2009.

[2] E. M. Bakker, S. Volpi, E. Salonini, E. C. van der Wiel-Kooij, C. J. Sintnicolaas, W. C. Hop, B. M. Assael, P. J. Merkus, and H. A. Tiddens. Improved treatment response to dornase alfa in cystic fibrosis patients using controlled inhalation. *The European respiratory journal : official journal of the European Society for Clinical Respiratory Physiology*, 38(6):1328–1335, December 2011.

[3] R. S. Baltimore, C. D. Christie, and G. J. Smith. Immunohistopathologic localization of pseudomonas aeruginosa in lungs from patients with cystic fibrosis. implications for the pathogenesis of progressive lung deterioration. *The American Review of Respiratory Disease*, 140(6):1650–1661, December 1989.

[4] Y. Benjamini and Y. Hochberg. Controlling the false discovery rate: A practical and powerful approach to multiple testing. *J.R.Statist.Soc.B*, 57(1):189–300, 1995.

[5] J. M. Bland and D. G. Altman. Statistical methods for assessing agreement between two methods of clinical measurement. *Lancet*, 1(8476):307–310, February 1986.

[6] P. Brand, M. Schulte, M. Wencker, C. H. Herpich, G. Klein, K. Hanna, and T. Meyer. Lung deposition of inhaled alpha1-proteinase inhibitor in cystic fibrosis and alpha1-antitrypsin deficiency. *The European respiratory journal : official journal of the European Society for Clinical Respiratory Physiology*, 34(2):354–360, August 2009.

[7] M. Cazzola, F. Blasi, C. Terzano, M. G. Matera, and S. A. Marsico. Delivering antibacterials to the lungs: considerations for optimizing outcomes. *American journal of respiratory medicine : drugs, devices, and other interventions*, 1(4):261–272, 2002.

[8] S. M. Cheer, J. Waugh, and S. Noble. Inhaled tobramycin (TOBI): a review of its use in the management of pseudomonas aeruginosa infections in patients with cystic fibrosis. *Drugs*, 63(22):2501–2520, 2003.

[9] L. M. Chiu and G. W. Amsden. Intrapulmonary pharmacokinetics of antibacterial agents: implications for therapeutics. *American journal of respiratory medicine : drugs, devices, and other interventions*, 1(3):201–209, 2002.

[10] H. Chrystyn. Methods to identify drug deposition in the lungs following inhalation. *British journal of clinical pharmacology*, 51(4):289–299, April 2001.

[11] A. L. Coates, O. Denk, K. Leung, N. Ribeiro, J. Chan, M. Green, S. Martin, M. Charron, M. Edwardes, and M. Keller. Higher tobramycin concentration and vibrating mesh technology can shorten antibiotic treatment time in cystic fibrosis. *Pediatric pulmonology*, 46(4):401–408, April 2011.

[12] C. Darquenne. Aerosol deposition in health and disease. *Journal of aerosol medicine and pulmonary drug delivery*, 25(3):140–147, June 2012.

[13] S. D. Davis and T. Ferkol. Identifying the origins of cystic fibrosis lung disease. *The New England journal of medicine*, 368(21):2026–2028, May 2013.

[14] J. W. De Backer, W. G. Vos, A. Devolder, S. L. Verhulst, P. Germonpre, F. L. Wuyts, P. M. Parizel, and W. A. De Backer. Computational fluid dynamics can detect changes in airway resistance in asthmatics after acute bronchodilation. *Journal of Biomechanics*, 41(1):106–113, 2008.

[15] J. W. De Backer, W. G. Vos, C. D. Gorle, P. Germonpré, B. Partoens, F. L. Wuyts, P. M. Parizel, and W. A. De Backer. Flow analyses in the lower airways: patient-specific model and boundary conditions. *Medical engineering & physics*, 30(7):872–879, September 2008.

[16] J. W. De Backer, Wim G. Vos, Samir C. Vinchurkar, Rita Claes, Anton Drollmann, Denis Wulfrank, Paul M. Parizel, Paul Germonpré, and Wilfried De Backer. Validation of computational fluid dynamics in CT-based airway models with SPECT/CT. *Radiology*, 257(3):854–862, December 2010.

[17] Lieve A. De Backer, Wim Vos, Jan De Backer, Cedric Van Holsbeke, Samir Vinchurkar, and Wilfried De Backer. The acute effect of budesonide/formoterol in COPD: a multi-slice computed tomography and lung function study. *European Respiratory Journal*, 40(2):298–305, August 2012.

[18] S. H. Donaldson, W. D. Bennett, K. L. Zeman, M. R. Knowles, R. Tarran, and R. C. Boucher. Mucus clearance and lung function in cystic fibrosis with hypertonic saline. *The New England journal of medicine*, 354(3):241–250, January 2006.

[19] R. Dopfer, P. Brand, B. Mullinger, T. Hunger, S. Haussermann, T. Meyer, G. Scheuch, and R. Siekmeier. Inhalation of tobramycin in patients with cystic fibrosis: comparison of two methods. *Journal of physiology and pharmacology : an official journal of the Polish Physiological Society*, 58 Suppl 5(Pt 1):141–154, November 2007.

[20] J. S. Elborn and N. R. Henig. Optimal airway antimicrobial therapy for cystic fibrosis: the role of inhaled aztreonam lysine. *Expert opinion on pharmacotherapy*, 11(8):1373–1385, June 2010.

[21] D. E. Geller. The science of aerosol delivery in cystic fibrosis. *Pediatr.Pulmonol.*, 43:S5–S17, July 2008.

[22] R. L. Gibson, G. Z. Retsch-Bogart, C. Oermann, C. Milla, J. Pilewski, C. Daines, R. Ahrens, K. Leon, M. Cohen, S. McNamara, T. L. Callahan, R. Markus, and J. L. Burns. Microbiology, safety, and pharmacokinetics of aztreonam lysinate for inhalation in patients with cystic fibrosis. *Pediatric pulmonology*, 41(7):656–665, July 2006.

[23] M. B. Grotta, E. C. Etchebere, A. F. Ribeiro, J. Romanato, M. A. Ribeiro, and J. D. Ribeiro. Pulmonary deposition of inhaled tobramycin prior to and after respiratory therapy and use of inhaled albuterol in cystic fibrosis patients colonized with pseudomonas aeruginosa. *Jornal brasileiro de pneumologia : publicacao oficial da Sociedade Brasileira de Pneumologia e Tisilogia*, 35(1):35–43, January 2009.

[24] M. A. Hasan and C. F. Lange. Estimating in vivo airway surface liquid concentration in trials of inhaled antibiotics. *Journal of aerosol medicine : the official journal of the International Society for Aerosols in Medicine*, 20(3):282–293, 2007.

[25] H. Heijerman, E. Westerman, S. Conway, D. Touw, G. Doring, and consensus working group. Inhaled medication and inhalation devices for lung disease in patients with cystic fibrosis: A european consensus. *Journal of cystic fibrosis : official journal of the European Cystic Fibrosis Society*, 8(5):295–315, September 2009.

[26] W. Hengzhuang, O. Ciofu, L. Yang, H. Wu, Z. Song, A. Oliver, and N. Hoiby. High beta-lactamase levels change the pharmacodynamics of beta-lactam antibiotics in pseudomonas aeruginosa biofilms. *Antimicrobial Agents and Chemotherapy*, 57(1):196–204, January 2013.

[27] P. King, O. Lomovskaya, D. C. Griffith, J. L. Burns, and M. N. Dudley. In vitro pharmacodynamics of levofloxacin and other aerosolized antibiotics under multiple conditions relevant to chronic pulmonary infection in cystic fibrosis. *Antimicrobial Agents and Chemotherapy*, 54(1):143–148, January 2010.

[28] B. L. Laube. The expanding role of aerosols in systemic drug delivery, gene therapy, and vaccination. *Respiratory care*, 50(9):1161–1176, September 2005.

[29] B. L. Laube, H. M. Janssens, F. H. de Jongh, S. G. Devadason, R. Dhand, P. Diot, M. L. Everard, I. Horvath, P. Navalesi, T. Voshaar, H. Chrystyn, European Respiratory Society, and International Society for Aerosols in Medicine. What the pulmonary specialist should know about the new inhalation therapies. *The European respiratory journal : official journal of the European Society for Clinical Respiratory Physiology*, 37(6):1308–1331, June 2011.

[30] W. Lenney, F. Edenborough, P. Kho, and J. M. Kovarik. Lung deposition of inhaled tobramycin with eFlow rapid/LC plus jet nebuliser in healthy and

cystic fibrosis subjects. *Journal of cystic fibrosis : official journal of the European Cystic Fibrosis Society*, 10(1):9–14, January 2011.

[31] Z. Li, D. B. Sanders, M. J. Rock, M. R. Kosorok, J. Collins, C. G. Green, A. S. Brody, and P. M. Farrell. Regional differences in the evolution of lung disease in children with cystic fibrosis. *Pediatric pulmonology*, 47(7):635–640, July 2012.

[32] M. Loeve, G. P. Krestin, M. Rosenfeld, M. de Bruijne, S. M. Stick, and H. A. Tiddens. Chest computed tomography; a validated surrogate endpoint of cystic fibrosis lung disease? *The European respiratory journal : official journal of the European Society for Clinical Respiratory Physiology*, December 2012.

[33] L. Maiz, R. M. Giron, C. Olveira, E. Quintana, A. Lamas, D. Pastor, R. Canton, and J. Mensa. Inhaled antibiotics for the treatment of chronic bronchopulmonary pseudomonas aeruginosa infection in cystic fibrosis: systematic review of randomised controlled trials. *Expert opinion on pharmacotherapy*, 14(9):1135–1149, June 2013.

[34] H. Mattie. Clinical pharmacokinetics of aztreonam. an update. *Clinical pharmacokinetics*, 26(2):99–106, February 1994.

[35] K. S. McCoy, A. L. Quittner, C. M. Oermann, R. L. Gibson, G. Z. Retsch-Bogart, and A. B. Montgomery. Inhaled aztreonam lysine for chronic airway pseudomonas aeruginosa in cystic fibrosis. *American journal of respiratory and critical care medicine*, 178(9):921–928, November 2008.

[36] M. R. Miller, J. Hankinson, V. Brusasco, F. Burgos, R. Casaburi, A. Coates, R. Crapo, P. Enright, C. P. van der Grinten, P. Gustafsson, R. Jensen, D. C. Johnson, N. MacIntyre, R. McKay, D. Navajas, O. F. Pedersen, R. Pellegrino, G. Viegi, J. Wanger, and ATS/ERS Task Force. Standardisation of spirometry. *The European respiratory journal*, 26(2):319–338, August 2005.

[37] L. S. Mott, J. Park, C. L. Gangell, N. H. de Klerk, P. D. Sly, C. P. Murray, S. M. Stick, and Australian Respiratory Early Surveillance Team for Cystic Fibrosis (AREST CF) Study Group. Distribution of early structural lung changes due to cystic fibrosis detected with chest computed tomography. *The Journal of pediatrics*, 163(1):243–248.e3, July 2013.

[38] J. W. Mouton, M. N. Dudley, O. Cars, H. Derendorf, and G. L. Drusano. Standardization of pharmacokinetic/pharmacodynamic (PK/PD) terminology for anti-infective drugs. *International journal of antimicrobial agents*, 19(4):355–358, April 2002.

[39] J. W. Mouton, M. N. Dudley, O. Cars, H. Derendorf, and G. L. Drusano. Standardization of pharmacokinetic/pharmacodynamic (PK/PD) terminology for anti-infective drugs: an update. *The Journal of antimicrobial chemotherapy*, 55(5):601–607, May 2005.

[40] C. M. Oermann, G. Z. Retsch-Bogart, A. L. Quittner, R. L. Gibson, K. S. McCoy, A. B. Montgomery, and P. J. Cooper. An 18-month study of the safety and efficacy of repeated courses of inhaled aztreonam lysine in cystic fibrosis. *Pediatric pulmonology*, 45(11):1121–1134, November 2010.

[41] R. F. Phalen, M. J. Oldham, M. T. Kleinman, and T. T. Crocker. Tracheobronchial deposition predictions for infants, children and adolescents. *Ann. occup. Hyg.*, 32(Supplement 1):11–21, 1988.

[42] G. Pilcer, J. Goole, B. Van Gansbeke, D. Blocklet, C. Knoop, F. Vanderbist, and K. Amighi. Pharmacoscintigraphic and pharmacokinetic evaluation of tobramycin DPI formulations in cystic fibrosis patients. *European journal of pharmaceutics and biopharmaceutics : official journal of Arbeitsgemeinschaft fur Pharmazeutische Verfahrenstechnik e.V*, 68(2):413–421, February 2008.

[43] F. Ratjen. Cystic fibrosis: the role of the small airways. *Journal of aerosol medicine and pulmonary drug delivery*, 25(5):261–264, October 2012.

[44] G. Z. Retsch-Bogart, A. L. Quittner, R. L. Gibson, C. M. Oermann, K. S. McCoy, A. B. Montgomery, and P. J. Cooper. Efficacy and safety of inhaled aztreonam lysine for airway pseudomonas in cystic fibrosis. *Chest*, 135(5):1223–1232, May 2009.

[45] K. A. Rodvold, L. Yoo, and J. M. George. Penetration of anti-infective agents into pulmonary epithelial lining fluid: focus on antifungal, antitubercular and miscellaneous anti-infective agents. *Clinical pharmacokinetics*, 50(11):689–704, November 2011.

[46] S. Stanojevic, A. Wade, J. Stocks, J. Hankinson, A. L. Coates, H. Pan, M. Rosenthal, M. Corey, P. Lebecque, and T. J. Cole. Reference ranges for spirometry across all ages: a new approach. *American journal of respiratory and critical care medicine*, 177(3):253–260, February 2008.

[47] H. Talma. *Groeidiagrammen 2010: handleiding bij het meten en wegen van kinderen en het invullen van groeidiagrammen.* [S.I.] : TNO innovation for life, 2nd edition, 2011.

[48] R. Tarran, B. Button, and R. C. Boucher. Regulation of normal and cystic fibrosis airway surface liquid volume by phasic shear stress. *Annual Review of Physiology*, 68:543–561, 2006.

[49] R. Tarran, B. Button, M. Picher, A. M. Paradiso, C. M. Ribeiro, E. R. Lazarowski, L. Zhang, P. L. Collins, R. J. Pickles, J. J. Fredberg, and R. C. Boucher. Normal and cystic fibrosis airway surface liquid homeostasis. the effects of phasic shear stress and viral infections. *The Journal of biological chemistry*, 280(42):35751–35759, October 2005.

[50] H. A. Tiddens, S. H. Donaldson, M. Rosenfeld, and P. D. Pare. Cystic fibrosis lung disease starts in the small airways: can we treat it more effectively? *Pediatric pulmonology*, 45(2):107–117, February 2010.

[51] S. Vinchurkar, L. D. De Backer, W. Vos, C. S. Van Holsbeke, J. W. De Backer, and W. A. De Backer. A case series on lung deposition analysis of inhaled medication using functional imaging based computational fluid dynamics in asthmatic patients: effect of upper airway morphology and comparison with in vivo data. *Inhalation toxicology*, 24(2):81–88, 2012.

[52] A. A. Vinks, R. N. van Rossem, R. A. Mathot, H. G. Heijerman, and J. W. Mouton. Pharmacokinetics of aztreonam in healthy subjects and patients with cystic fibrosis and evaluation of dose-exposure relationships using monte carlo simulation. *Antimicrobial Agents and Chemotherapy*, 51(9):3049–3055, September 2007.

[53] Wim Vos, Jan De Backer, Gianluigi Poli, Annick De Volder, Liesbet Ghys, Cedric Van Holsbeke, Samir Vinchurkar, Lieve De Backer, and Wilfried De Backer. Novel functional imaging of changes in small airways of patients treated with extrafine Beclomethasone/Formoterol. *Respiration*, 2013.

[54] C. E. Wainwright, S. Vidmar, D. S. Armstrong, C. A. Byrnes, J. B. Carlin, J. Cheney, P. J. Cooper, K. Grimwood, M. Moodie, C. F. Robertson, H. A. Tiddens, and ACFBAL Study Investigators. Effect of bronchoalveolar lavage-directed therapy on pseudomonas aeruginosa infection and structural lung injury in children with cystic fibrosis: a randomized trial. *JAMA : the journal of the American Medical Association*, 306(2):163–171, July 2011.

[55] L. A. Wallis, M. Healy, M. B. Undy, and I. Maconochie. Age related reference ranges for respiration rate and heart rate from 4 to 16 years. *Archives of Disease in Childhood*, 90(11):1117–1121, November 2005.

[56] D. Willner, M. R. Haynes, M. Furlan, N. Hanson, B. Kirby, Y. W. Lim, P. B. Rainey, R. Schmieder, M. Youle, D. Conrad, and F. Rohwer. Case studies of the spatial heterogeneity of DNA viruses in the cystic fibrosis lung. *American journal of respiratory cell and molecular biology*, 46(2):127–131, February 2012.

[57] K. Yamazaki, S. Ogura, A. Ishizaka, T. Oh-hara, and M. Nishimura. Bronchoscopic microsampling method for measuring drug concentration in epithelial lining fluid. *American journal of respiratory and critical care medicine*, 168(11):1304–1307, December 2003.

[58] A. Zapletal, J. Naidr, and P. Pohunek. A brief description of methods for studying pulmonary function in children and adolescents. *Ceskoslovenska pediatrie*, 47(9):520–523, September 1992.

[59] K. Zeitler, B. Salvas, V. Stevens, and J. Brown. Aztreonam lysine for inhalation: new formulation of an old antibiotic. *American Journal of Health-System Pharmacy : AJHP : Official Journal of the American Society of Health-System Pharmacists*, 69(2):107–115, January 2012.

Part III

Effects of inhalation medication

8

The acute effect of budesonide/formoterol in COPD: a multi-slice computed tomography and lung function study

European Respiratory Journal 2011; 40:298 – 305

Lieve De Backer, Wim Vos, Jan De Backer, Cedric Van Holsbeke, Samir Vinchurkar and Wilfried De Backer

8.1 Abstract

The Global Initiative for Chronic Obstructive Lung Disease (GOLD) classification of chronic obstructive pulmonary disease (COPD) does not always match with other clinical disease descriptors such as exacerbation frequency and quality of life, indicating that forced expiratory volume in 1 s (FEV1) is not a perfect descriptor of the disease. The aim of this study was to find out whether changes in airway geometry after inhalation of the most commonly used inhalation therapy in severe COPD can more adequately be described with an image-based approach than with spirometry. 10 COPD GOLD stage III patients were assessed in a double-blind crossover study. Airway volumes were analysed using segmentation of high resolution computed tomography (HRCT) images; airway resistance was determined using computational fluid dynamics (CFD). Distal airway volume signif-

icantly increased (p = 0.011) in patients 4 h after receiving a budesonide/formoterol combination from 9.6 ± 4.67 cm^3 to 10.14 ± 4.81 cm^3. Also CFD-determined airway resistance significantly decreased (p = 0.047) from 0.051 ± 0.021 kPas/L to 0.043 ± 0.019 kPas/L. None of the lung function parameters showed a significant change. Only functional residual capacity (FRC) showed a trend to decline (p = 0.056). Only the image-based parameters were able to predict the visit at which the combination product was administered. This study showed that imaging is a sensitive, complementary tool to describe changes in airway structure.

8.2 Contributions of the author

The author of this thesis was involved in the design of the double-blind crossover study. He determined the imaging and computational fluid dynamics strategy in order to perform the longitudinal comparisons in the most optimal way and cooperated in the generation of the three-dimensional models. The author designed algorithms to extract the outcome parameters and perform the comparisons in an automated way, including the conversion from blinded to unblinded results. He was involved in the statistical analyses and sample size calculation.

8.3 Introduction

Chronic obstructive pulmonary disease (COPD) is characterised by chronic airway inflammation (bronchitis) and the destruction of lung parenchyma in combination with the loss of vascular structures (emphysema). A hallmark of COPD is the relatively irreversible nature of the airway constriction. In clinical practice, patients are diagnosed with COPD if the decrease in forced expiratory volume in 1 s (FEV1) is not fully reversible after the administration of bronchodilating products and when the ratio between the FEV1 and the forced vital capacity (FVC) remains below 70%. It is, however, possible that a substantial degree of reversibility of bronchoconstriction in COPD can be detected. This reversibility of bronchoconstriction tends to vary over time and with disease severity as well as with the method and product of treatment [5, 25]. It would be interesting to predict this response and categorise patients according to bronchodilating capacity. FEV1 represents the whole of the bronchial tree, so cannot show local bronchodilation, which can be important for the medication to be effective. As COPD is such a heterogeneous disease, bronchodilating capacity is only part of the patient assessment. The severity of COPD is defined by the Global Initiative for Chronic Obstructive Lung Disease (GOLD) guidelines [24] consisting of four categories. Patients are subdivided into these groups based on their post-bronchodilator FEV1 value. Even though FEV1 remains the primary outcome parameter to describe respiratory diseases in clinical studies and practice, only weak correlations have been found between this parameter and patient-reported outcomes such as the St George's Respiratory Questionnaire (SGRQ) [16–20]. The FEV1-based categorisation can still be improved [16]. Today,

the standard treatment of COPD includes inhaled corticosteroids (ICS) and short- (SABA) and long- (LABA) acting β2-agonists. However, the inherent black-box approach of the spirometry parameters in combination with the above-mentioned weak clinical correlations often causes difficult and very costly development and registration processes for new compounds targeted at treating COPD [1]. Even in very large clinical trials the beneficial effect of therapies on FEV1 or even survival is difficult to demonstrate [4, 7, 8]. Given the increasing prevalence of COPD [23], the need for new outcome parameters that more adequately describe the influence of inhalation medication on the respiratory system becomes apparent. These outcome parameters should ideally facilitate development of novel effective therapies that relieve the burden primarily on the patient but also on the social healthcare structure. Within the field of COPD, imaging and in particular high resolution computed tomography (HRCT), has emerged as a complementary tool to spirometry and body plethysmography, predominantly to assess the extent of emphysema [13, 15, 22]. The severity of emphysema is typically correlated with a decrease in local Hounsfield units (HU), indicating a destruction of pulmonary lung tissue. Recent developments have extended the use of HRCT scans by adding more functionality to the static images by means of airway segmentation and computational fluid dynamics (CFD) [21]. Patient specific assessments of the airway volume and airflow in the respiratory system can be obtained by solving mathematical flow equations within the segmented airway structures [12]. Several studies have indicated the possible applications of this method and have validated the approach through comparison with in vitro and in vivo data [10, 11]. The current study used the same approach where patient specific computer models are constructed based on HRCT images using segmentation principles and flow parameters are derived using CFD. The aim of the present study was to find out whether in GOLD stage III COPD patients, treated with inhalation of routinely used inhalation therapy or placebo, changes in airway structure and function are more adequately described with this new imaging technology than with spirometric data. Fixed combinations were chosen as the study medication to reflect the real-life situation. We also performed a sample size calculation to calculate the number of patients in clinical trials needed when using more sensitive, image-based outcome parameters.

8.4 Materials en Methods

8.4.1 Ethics

The study was conducted according to all ethical principles. Approval from the ethical committee was obtained and all patients gave their informed consent (EudraCT 2009-016502-16, PML_DOC_0905_/_ISSSYmB0020).

8.4.2 Patient population

In this study 10 COPD patients (six male/four female) were included. All patients were categorised by the GOLD guidelines as GOLD stage III with a mean ± SD FEV1 of 34.8 ± 7.7% predicted. The mean ± SD age of the patients was 65.1 ± 3.3 years with a mean ± SD height of 170 ± 7 cm and weight of 93 ± 5 kg.

8.4.3 Study design

This was a double-blind, placebo-controlled crossover study designed to investigate a number of topics. A first aim was to demonstrate how functional respiratory imaging parameters such as changes in airway volumes and CFD-determined resistance can assess changes induced by a combination product compared to placebo. Subsequently these changes could be compared to other lung function parameters. Furthermore a comparison could be made between the combination product and placebo. A final aim of the study was to analyse whether the different outcome parameters could distinguish between placebo and active product. The latter was possible considering the double-blind design of the study.

At baseline (V1), patients received full lung-function testing and low-dose inspiratory and expiratory HRCT scans. A low-dose computed tomography (CT) scan reduces the radiation by lowering the current and increasing the pitch compared to a normal thoracic CT. Due to the natural contrast between air and the surrounding airway tissue, a significant reduction, up to six-fold, in the radiation dose can be obtained [2]. The lung function tests yielded the following parameters: FEV1, FEV1/FVC and peak expiratory flow (PEF) from the spirometry; and airway resistance (Raw), specific airway resistance (sRaw), functional residual capacity (FRC) and total lung capacity (TLC) from body plethysmography. After the initial tests and scans the patients were randomised to receive either placebo or budesonide/formoterol combination (Symbicort®, AstraZeneca, Södertälje, Sweden). In this study a combination product (ICS/LABA) was used as suggested by the GOLD guidelines for the treatment of COPD GOLD stage III patients. The lung function and imaging tests were repeated 4 h after the administration of the product or placebo (V2). Patients returned to the hospital 1 week later, and the lung function tests were repeated pre-dose (V3). To limit radiation dose, no baseline HRCT scan was taken at this point. Subsequently patients received either the combination product or placebo. Again, 4 h after the administration of the formulation, both lung function and imaging tests were performed (V4). To limit the radiation dose given to the patient as much as possible a dose-reduction protocol was applied. The natural contrast between the intraluminal air and the surrounding tissue allows for a significant reduction in dose without compromising image quality. The scanner used was a General Electric VCT Lightspeed scanner (GE Healthcare, Chalfont St Giles, UK) with 64 detector rows. The HRCT settings were as follows: tube voltage, 120 kV; tube current, between 10 mAs (low-weight patients) and 100 mAs (high-weight patients); noise factor, 28; collimation, 0.625 mm; rotation time, 0.6 s; and pitch factor, 1.375. The field of view was indicated by the CT technician based

on the scout image and was positioned closely around the thorax to optimise in-plane image resolution which was around 0.5 mm. The resulting radiation dose was in the order of 1 – 2 mSv per scan. Images were reconstructed to a slice thickness of 0.6 mm to attain near cubic voxels. Respiratory gating was used to ensure the proper lung volume. CT examinations were performed blindly.

8.4.4 Image post-processing

Post-processing of the HRCT images included segmentation of the airway tree structure and CFD flow simulations. Segmentation can be defined as the grouping of voxels that belong to an anatomical structure (e.g. tracheobronchial tree, lung). This group of voxels or mask can subsequently be used to create a patient specific three-dimensional model of the anatomical structure under consideration. For this study the focus was placed on the tracheobronchial tree, with HU ranging from -1024 to -824 [11], and in particular the smaller airways starting from the segmental level (generation 2 – 4). Using state-of-the-art imaging equipment it is possible to distinguish, in the HRCT images, airways with a diameter as low as 1 mm. Smaller airways cannot be further detected since the in-plane resolution of the scanner (512x512) is typically not sufficient to distinguish between the intraluminal and the alveolar air. Consequently the analysis was performed on all airways starting from generation 2 – 4 down to the smallest detectable airways. The DICOM (Digital Imaging and Communications in Medicine) images obtained in this clinical study at the different measurement instances were assessed using the commercially available, US Food and Drug Administration approved, software package Mimics (Materialise, Leuven, Belgium). The tracheobronchial tree was subsequently segmented using a semi-automatic approach where the central airways up to around generation 4 – 5 are automatically generated and the smaller branches are added manually. A total of three airway tree models were obtained per patient: the model from V1 was based on pre-bronchodilation images, the airway constructed at V2 was either after administration of placebo or the combination, and the model based on V4 was again either after administration of placebo or the combination depending on what was used in V2. After segmentation, all models of the same patient were superimposed using a least-squares method. Subsequently all models were trimmed such that the branches extended equally far and a comparison could be made between the different geometries excluding the variability induced by the manual segmentation. The main outcome parameter of the segmentation procedures is the distal airway volume (iVaw) (Figure 8.1). In addition to the changes in volume, the changes in resistance were determined using CFD (iRaw). CFD is a computer method that provides flow characteristics throughout the entire reconstructed airway model. Flow simulations were performed using Fluent v6.3 (Ansys Inc, Lebanon, NH, USA), which solved the Reynolds-averaged Navier–Stokes (RANS) equations. Steady flow was considered at 30 L/min. More details on the flow simulation principles can be found in De Backer et al. [10]. The CT and CFD analysts were blinded with respect to the randomisation to avoid any bias.

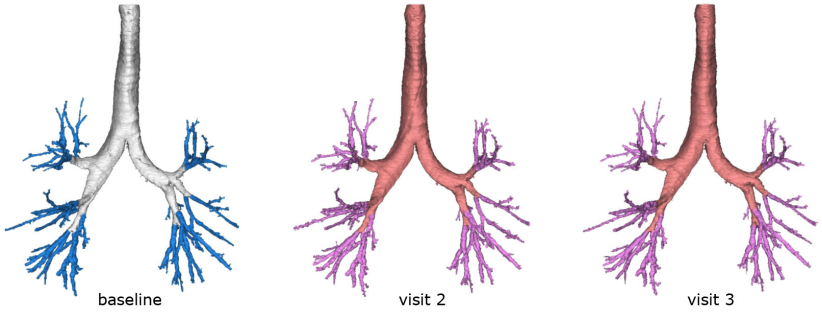

Figure 8.1: HRCT-based airway models indicating distal airway branches (iVaw) at baseline and visits 2 and 3

8.4.5 Statistics

Differences were assessed using the Wilcoxon matched-pairs test. Sample size calculations were performed using t-test for dependent samples. A p-value < 0.05 was considered to be statistically significant. Results are presented as mean $\pm$ SD.

8.5 Results

iVaw significantly increased (p = 0.011) in patients 4 h after they received budesonide/formoterol in combination (Table 8.1). The distal airway volumes increased from 9.6 $\pm$ 4.67 cm^3 to 10.14 $\pm$ 4.81 cm^3. The airway resistance decreased from 0.051 $\pm$ 0.021 kPas/L to 0.043 $\pm$ 0.019 kPas/L.

Figure 8.2 illustrates changes in distal airway volumes after the administration of the placebo and the combination product. No lung function parameter showed a significant change. The FEV1 did increase slightly from 34.8 $\pm$ 7.69%p to 35.9 $\pm$ 7.89%p but not significantly (p = 0.34). The sRaw decreased from 5 $\pm$ 2.87 kPas to 4.65 $\pm$ 2.29 kPas but again not significantly (p = 0.14). Although both iRaw and sRaw declined, there was no correlation between the parameters (r = 0.45, not significant). A decreasing trend in FRC was observed after administration of budesonide/formoterol indicating a reduction in hyperinflation.

The bronchodilating effect, defined as an increase in iVaw and a decrease in iRaw, seems higher in a limited number of patients (n = 7); this effect seems not to be systematic. This appears more clearly in the functional imaging parameters (Table 8.2).

A sample size calculation revealed that in order to have a well-powered study (power goal of 90%) with iVaw as primary outcome parameter, a total of 16 patients would be required. When using iRaw, 34 patients were needed. Were FEV1 used as the primary end-point, the number of required patients would go up to 93. The least sensitive parameter in this regard is the PEF, with a total of 217 patients required to

	Budesonide/Formoterol		
	pre	post	p
iVaw [cm^3]	9.60 ± 4.67	10.14 ± 4.81	0.011*
iRaw [kPas/L]	0.05 ± 0.02	0.04 ± 0.02	0.047*
FEV1 [L]	0.95 ± 0.33	0.98 ± 0.33	0.34
FEV1 [% pred]	34.80 ± 7.69	35.90 ± 7.89	0.34
FEV1/VC [%]	34.32 ± 6.99	34.72 ± 6.67	0.51
PEF [L/s]	3.00 ± 1.26	3.12 ± 1.22	0.71
Raw [kPas/L]	1.00 ± 0.50	0.92 ± 0.45	0.20
sRaw [kPas]	5.00 ± 2.87	4.65 ± 2.29	0.14
FRC [% pred]	155.90 ± 35.6	151.00 ± 32.44	0.056
TLC [% pred]	115.80 ± 21.64	114.20 ± 19.03	0.13

* indicates statistical significance; ° indicates a trend

Table 8.1: Comparison of lung function and imaging parameters before and after the administration of budesonide/formoterol

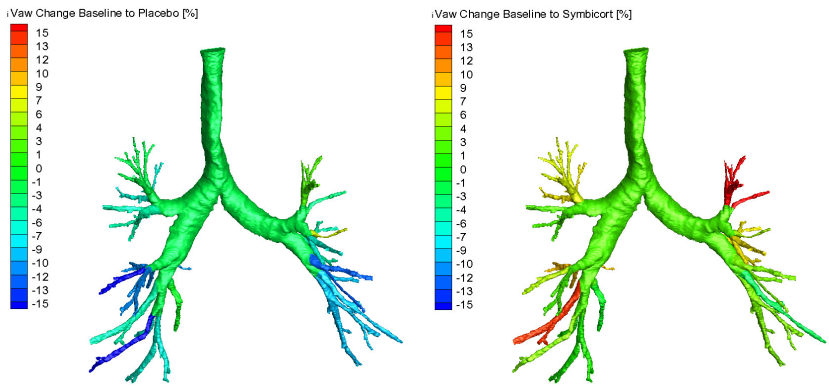

Figure 8.2: Illustration of distal airway volume changes [%] after administration of placebo (left) or combination product (right)

Patient	ΔiVaw%	ΔiRaw%
01	14.11 ± 9.07	-27.09 ± 21.74
02	2.79 ± 7.89	8.24 ± 49.17
03	-4.55 ± 3.88	24.83 ± 53.04
04	6.21 ± 5.03	-11.67 ± 36.77
05	-2.53 ± 14.82	51.02 ± 118.36
06	19.52 ± 27.85	-34.71 ± 43.05
07	17.40 ± 26.14	-19.57 ± 40.66
08	5.36 ± 10.87	-9.21 ± 37.27
09	35.38 ± 134.81	-6.48 ± 39.89
10	13.24 ± 10.82	-38.45 ± 20.81

Table 8.2: Average changes and standard deviations in iVaw (distal airway volume) and iRaw (airway resistance determined by computational fluid dynamics) for all patients after administration of budesonide/formoterol indicating the level of inhomogeneity in bronchodilation

attain statistically significant results.

When considering the effect of placebo a significant decline in iVaw (p = 0.025) and PEF (p = 0.025) was observed (Table 8.3). A downward trend was depicted by FEV1 (p = 0.09). CFD-based resistance increased significantly (p = 0.005); bodyplethysmography showed a significant increase in sRaw (p = 0.026) and an upward trend in Raw (p = 0.07). Figure 8.3 illustrates the individual changes in iVaw and iRaw after the administration of the combination product and placebo.

	Placebo		
	pre	post	p
iVaw [cm^3]	9.60 ± 4.67	9.16 ± 4.37	0.025*
iRaw [kPas/L]	0.05 ± 0.02	0.057 ± 0.031	0.047*
FEV1 [L]	0.96 ± 0.31	0.93 ± 0.33	0.07°
FEV1 [% pred]	34.9 ± 6.71	33.70 ± 7.24	0.09°
FEV1/VC [%]	33.68 ± 7.36	33.89 ± 6.80	0.74
PEF [L/s]	3.07 ± 0.95	2.77 ± 1.03	0.025*
Raw [kPas/L]	0.94 ± 0.46	1.01 ± 0.43	0.07°
sRaw [kPas]	4.89 ± 2.72	5.33 ± 2.48	0.026*
FRC [% pred]	151.30 ± 32.46	155.10 ± 30.95	0.15
TLC [% pred]	114.10 ± 19.3	116.00 ± 18.25	0.058

* indicates statistical significance; ° indicates a trend

Table 8.3: Comparison of lung function and imaging parameters before and after the administration of the placebo

A significant difference between placebo and the budesonide/formoterol com-

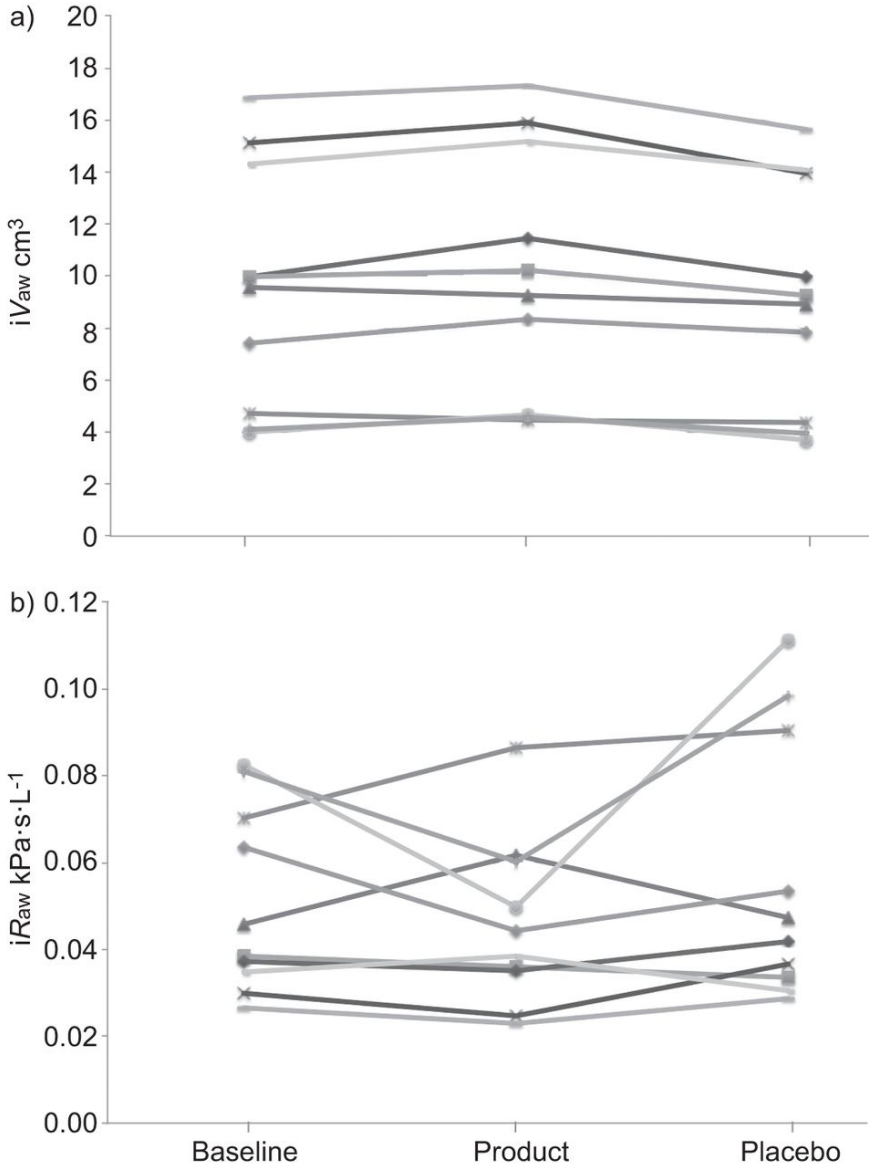

Figure 8.3: Individual changes in a) iVaw (distal airway volume) and b) iRaw (airway resistance determined by computational fluid dynamics) after administration of combination product and placebo

bination was observed in two lung function parameters: PEF (p = 0.027) and FEV1 (p = 0.037). The sRaw also indicated a significant difference (p = 0.036), as did TLC and FRC. The image-based peripheral airway volumes showed a highly significant difference between placebo and the active combination (p = 0.0005) (Table 8.4).

change [%]	Budesonide/Formoterol	Placebo	p
iVaw	+6.48 ± 7.46	-4.29 ± 4.45	0.0005*
iRaw	-7.02 ± 23.72	9.04 ± 18.37	0.005*
FEV1	+3.56 ± 10.49	-3.63 ± 6.10	0.037*
FEV1/VC	+1.53 ± 5.81	+1.02 ± 6.45	0.87
PEF	+4.47 ± 20.20	-10.26 ± 12.89	0.027*
Raw	-7.17 ± 23.62	+10.43 ± 14.75	0.09°
sRaw	-9.03 ± 25.01	+12.84 ± 14.24	0.036*
FRC % pred	-4.9 ± 7.06	+3.8 ± 7.67	0.017*
TLC % pred	-1.6 ± 3.03	+1.9 ± 2.77	0.015*

* indicates statistical significance; ° indicates a trend

Table 8.4: Comparison between the changes in lung function and imaging parameters induced by the combination product and placebo

Before unblinding, a prediction was made regarding the visit at which the active product was administered. The hypothesis was that after this visit the values must improve, where an improvement is defined as an increase in iVaw, FEV1, FEV1/FVC and PEF and a decline in iRaw, sRaw and Raw. Results showed that the FEV1 correctly predicted the visit at which budesonide/formoterol was administered in seven out of 10 cases (Table 8.5). The FEV1/FVC was correct in only five out of 10 patients. Both PEF and Raw predicted eight out of 10 correctly and the sRaw nine out of 10. The only parameters that in all cases adequately predicted the visit at which the active compound was administered were iVaw and iRaw (Table 8.6 and 8.7).

8.6 Discussion

In this study we demonstrated that in severe COPD patients, after inhalation of fixed combinations, changes in image-based three-dimensional airway geometry can be detected that are not reflected in the spirometric data. The three-dimensional images clearly provide the possibility to assess the airway tree and the subsequent changes comprehensively. The traditional two-dimensional approach is typically limited to a slice-by-slice assessment.

The severity of the disease is predominantly defined by FEV1, which is judged to be not completely reversible, and in fact barely reversible in stable stage III COPD patients [2, 14]. Demonstrating an improvement is therefore inherently almost impossible and a COPD medication is then assessed based on its ability to slow down the decline in FEV1 [8]. The current study results confirmed this

Patient	ΔFEV1 V2	ΔFEV1 V3	prediction	unblind
01	-0.069	0.081	V3	V3
02	-0.02	0	V3	V2$^{\neq}$
03	-0.02	0.041	V3	V3
04	0.029	-0.1	V2	V2
05	-0.099	-0.11	V2	V2
06	-0.041	0.19	V3	V3
07	0.02	0.01	V2	V2
08	-0.041	-0.05	V2	V3$^{\neq}$
09	-0.021	0.03	V3	V2$^{\neq}$
10	0.09	0.02	V2	V2

$^{\neq}$ indicates uncorrect prediction

Table 8.5: Predictive value of the change in FEV1 to determine the visit where combination product was administered

Patient	ΔiVaw V2	ΔiVaw V3	prediction	unblind
01	-0.25	14.45	V3	V3
02	2.19	-7.32	V2	V2
03	-6.87	-3.11	V3	V3
04	5.16	-7.87	V2	V2
05	-4.59	-6.88	V2	V2
06	-7.27	17.23	V3	V3
07	11.87	-3.34	V2	V2
08	-1.56	6.09	V3	V3
09	2.55	-7.25	V2	V2
10	12.97	5.74	V2	V2

$^{\neq}$ indicates uncorrect prediction

Table 8.6: Predictive value of the change in iVaw to determine the visit where combination product was administered

Patient	ΔiRaw V2	ΔiRaw V3	prediction	unblind
01	-0.98	-19.46	V3	V3
02	-0.86	23.10	V2	V2
03	59.41	12.47	V3	V3
04	-18.94	34.23	V2	V2
05	35.18	41.80	V2	V2
06	-43.74	49.05	V3	V3
07	-32.42	29.69	V2	V2
08	9.95	-16.25	V3	V3
09	-14.94	11.34	V2	V2
10	-42.81	-18.93	V2	V2

$^{\neq}$ indicates uncorrect prediction

Table 8.7: Predictive value of the change in iRaw to determine the visit where combination product was administered

hypothesis, as only a minor, insignificant change in FEV1 is observed when patients are treated with budesonide/formoterol. At least a trend towards decline in FEV1 is seen in the placebo group. Airway volumes obtained using body plethysmography appear to be more sensitive and depict a declining trend in FRC in line with recent studies. The only parameters that describe a small but nonetheless significant improvement in the treated group and a significant decline in the placebo group are the iVaw and the iRaw.

The decline in iRaw goes along with a decline (although not statistically significant) in the Raw measured with body plethysmography. The absolute value of the Raw is much higher than the iRaw because iRaw does not take into account the resistance of the upper airway and the equipment and illustrates the relative importance of upper airway resistance.

Furthermore, from this study it can be seen that when a COPD GOLD stage III patient doesn't receive active bronchodilating medication a relatively rapid decline in airway diameter and function occurs even after some hours, indicating also the role of the fixed combinations in maintaining airway patency in daily life. Therefore a highly significant difference is observed when comparing the treated and placebo groups.

The clinical relevance of these changes is the topic of ongoing research. In the current study the main question was to assess how different outcome parameters would describe changes induced by the inhalation product. It would appear valuable to first have outcome parameters that accurately describe changes in airway structure and function induced by a product. In a second phase, the clinical relevance of these changes could be investigated by correlating them to, for example, patient-reported outcome parameters (PROs). After all, if a parameter is not sensitive enough to reliably pick up changes in the system following a treatment, what would be the value of correlating this parameter with PROs? Should a correlation exist, this

would still not mean that the product caused this change in PRO. Of course it is important to assess these PROs, as diminishing respiratory symptoms should be one of the goals of treating COPD. As we can see that some patients have a more pronounced response to budesonide/formoterol than others, it is interesting to know whether they also report less dyspnoea.

The double-blind protocol in this study offered an interesting possibility to assess how well the different parameters could distinguish between the placebo visit and the visit where the active product was administered. The image-based parameters appeared to be the only parameters that correctly identified the respective visits for all patients. The FEV1/FVC ratio performed the worst, followed by the FEV1.

Even though this trial was performed in a limited number of patients, the placebo-controlled, crossover design ensured a good power of this pilot study. Based on these results it could be hypothesised that imaging, or at least a combination of lung function tests and imaging, is better suited to describe the mode of action of a product. The sample size calculations that were based on these data and performed post hoc indicated that imaging parameters could significantly reduce the number of patients in clinical trials by providing more sensitive information on the mode of action of a product. This opens the possibility of using this method at an early clinical stage to compare different compounds to each other or to placebo. Also dose–response based on imaging parameters in a limited number of patients could yield a more compelling picture versus the FEV1 response to different doses in very large clinical trials where results are often ambiguous.

In previous large-scale studies using FEV1 as an end-point, it can be observed that inhaled therapy with the recommended fixed combinations improves FEV1 in absolute terms only to a limited extent and that the decline in FEV1 is not altered. But at the same time other end-points such as quality of life or even, in larger populations, mortality, show at least a trend to improvement [3, 8, 9, 26]. This suggests that FEV1 may underscore real changes in airway structure induced by inhalation of combination therapies.

At present fixed combinations are most frequently and often uniquely used in severe stage III COPD patients and are considered to be mainly symptomatic treatments with the aim to improve daily life symptoms and exacerbations, but not, or to a limited extent, the progression of the disease. We therefore chose a combination product in this study to see whether the widely used (mainly for symptomatic improvement) fixed combinations do have an influence on the airway geometry in severe stage III COPD patients. The aim was not only to understand and to see the sensitivity of the FEV1 but also to better understand the discrepancies between some PROs and FEV1 with the fixed combinations. Therefore insight both into the mode of action and also into the clinical relevance of the fixed combination inhalation therapy mostly used and recommended could be obtained. For this aim, a small-scale study seemed to be indicated given that the mentioned discrepancies between PROs and FEV1 were already demonstrated in previous large-scale and long-term studies (Tristan, Torch, Euroscope, Uplift).

Treatment is mainly targeted at reducing the work of breathing in COPD

patients. From physiological and anatomical studies [6, 27] it is known that the majority of the airway resistance is situated in the first 4 – 6 generations. It is therefore not unreasonable to assume that airway dilation in this region results in a clinical improvement in the patient's condition. It would be worthwhile to assess the respiratory structure and function in a broader range of disease severity levels in a larger set of patients. One could for instance take lung function tests and HRCT images during an episode of exacerbation and after recovery. This would allow for a correlation between imaging parameters, lung function and patient-reported outcome parameters.

Even though the functional respiratory imaging appears to provide sensitive and valuable information, the technique also has its limitations. Segmentation still involves some manual processing of the images, potentially introducing a level of variability. Airways smaller than 1 – 2 mm are not visible with the current state-of-the-art CT scanners and therefore cannot be segmented. The cost and the use of ionising radiation currently prevents the implementation of the method in very large phase-III trials and as a standard test in clinical routine for all patients. It appears that this method is best suited to determine product efficacy in early clinical phases and to assess treatment of the more severe patients in a clinical routine setting. As such the method could complement other novel pulmonary function tests such as multi-breath nitrogen washout and forced oscillation which are targeted at obtaining more information about the smaller airways. These methods are in general less expensive and provide information about the tissue and the smaller airways. However they do not provide regional information and are sometimes labour intensive. Therefore a proper combination of imaging and lung function tests could result in an efficient, comprehensive set of tools to treat patients with respiratory diseases.

References

[1] Christopher Adams and Van V. Brantner. Spending on new drug development. *SSRN eLibrary*, March 2008.

[2] S Appleton, P Poole, B Smith, A Veale, T J Lasserson, and M M Chan. Long-acting beta2-agonists for poorly reversible chronic obstructive pulmonary disease. *Cochrane database of systematic reviews (Online)*, (3):CD001104, 2006. PMID: 16855959.

[3] Geraldine Bale, Pablo Martínez-Camblor, P. Sherwood Burge, and Joan B. Soriano. Long-term mortality follow-up of the ISOLDE participants: Causes of death during 13 years after trial completion. *Respiratory Medicine*, 102(10):1468–1472, October 2008.

[4] P S Burge. Randomised, double blind, placebo controlled study of fluticasone propionate in patients with moderate to severe chronic obstructive pulmonary disease: the ISOLDE trial. *BMJ*, 320(7245):1297–1303, May 2000.

[5] P Calverley, P Burge, S Spencer, J Anderson, and P Jones. Bronchodilator reversibility testing in chronic obstructive pulmonary disease. *Thorax*, 58(8):659–664, August 2003. PMID: 12885978 PMCID: PMC1746778.

[6] P. M. A. Calverley and N. G. Koulouris. Flow limitation and dynamic hyperinflation: Key concepts in modern respiratory physiology. *European Respiratory Journal*, 25(1):186–199, January 2005.

[7] Peter Calverley, Romain Pauwels, Jørgen Vestbo, Paul Jones, Neil Pride, Amund Gulsvik, Julie Anderson, and Claire Maden. Combined salmeterol and fluticasone in the treatment of chronic obstructive pulmonary disease: a randomised controlled trial. *The Lancet*, 361(9356):449–456, February 2003.

[8] Peter M. A. Calverley, Julie A. Anderson, Bartolome Celli, Gary T. Ferguson, Christine Jenkins, Paul W. Jones, Julie C. Yates, and Jørgen Vestbo. Salmeterol and fluticasone propionate and survival in chronic obstructive pulmonary disease. *New England Journal of Medicine*, 356(8):775–789, 2007.

[9] Peter MA Calverley, Klaus F Rabe, Udo-Michael Goehring, Søren Kristiansen, Leonardo M Fabbri, and Fernando J Martinez. Roflumilast in symptomatic chronic obstructive pulmonary disease: two randomised clinical trials. *The Lancet*, 374(9691):685–694, August.

[10] Jan W. De Backer, Wim G. Vos, Samir C. Vinchurkar, Rita Claes, Anton Drollmann, Denis Wulfrank, Paul M. Parizel, Paul Germonpré, and Wilfried De Backer. Validation of computational fluid dynamics in CT-Based airway models with SPECT/CT. *Radiology*, 257(3):854–862, December 2010.

[11] J.W. De Backer, W.G. Vos, A. Devolder, S.L. Verhulst, P. Germonpré, F.L. Wuyts, P.M. Parizel, and W. De Backer. Computational fluid dynamics can detect changes in airway resistance in asthmatics after acute bronchodilation. *Journal of Biomechanics*, 41(1):106–113, 2008.

[12] J.W. De Backer, W.G. Vos, C.D. Gorlé, P. Germonpré, B. Partoens, F.L.Wuyts, P.M. Parizel, and W. De Backer. Flow analyses in the lower airways: Patient-specific model and boundary conditions. *Medical Engineering & Physics*, 30(7):872–879, September 2008.

[13] Alejandro A. Diaz, Clarissa Valim, Tsuneo Yamashiro, Raúl San José Estépar, James C. Ross, Shin Matsuoka, Brian Bartholmai, Hiroto Hatabu, Edwin K. Silverman, and George R. Washko. Airway count and emphysema assessed by chest CT imaging predicts clinical outcome in smokers. *Chest*, 138(4):880–887, October 2010.

[14] James F Donohue. Minimal clinically important differences in COPD lung function. *COPD*, 2(1):111–124, March 2005. PMID: 17136971.

[15] Akane Haruna, Shigeo Muro, Yasutaka Nakano, Tadashi Ohara, Yuma Hoshino, Emiko Ogawa, Toyohiro Hirai, Akio Niimi, Koichi Nishimura, Kazuo Chin, and Michiaki Mishima. CT scan findings of emphysema predict mortality in COPD. *Chest*, 138(3):635–640, September 2010.

[16] John R. Hurst, Jørgen Vestbo, Antonio Anzueto, Nicholas Locantore, Hana Müllerova, Ruth Tal-Singer, Bruce Miller, David A. Lomas, Alvar Agusti, William MacNee, Peter Calverley, Stephen Rennard, Emiel F. M. Wouters, and Jadwiga A. Wedzicha. Susceptibility to exacerbation in chronic obstructive pulmonary disease. *New England Journal of Medicine*, 363(12):1128–1138, 2010.

[17] P. W. Jones and T. K. Bosh. Quality of life changes in COPD patients treated with salmeterol. *American Journal of Respiratory and Critical Care Medicine*, 155(4):1283–1289, April 1997.

[18] Paul W Jones. COPD: functional status, health status and primary care. *Primary Care Respiratory Journal*, 20(3):227, 2011.

[19] Paul W. Jones, Julie A. Anderson, Peter MA Calverley, Bartolome R. Celli, Gary T. Ferguson, Christine Jenkins, Julie C. Yates, Jørgen Vestbo, Michael D. Spencer, and The TORCH Investigators. Health status in the TORCH study of COPD: treatment efficacy and other determinants of change. *Respiratory Research*, 12(1):71, May 2011.

[20] P.W. Jones, F.H. Quirk, and C.M. Baveystock. The st george's respiratory questionnaire. *Respiratory Medicine*, 85, Supplement 2(0):25–31, September 1991.

[21] Ching-long Lin, M.H. Tawhai, G. Mclennan, and E.A. Hoffman. Computational fluid dynamics. *Engineering in Medicine and Biology Magazine, IEEE*, 28(3):25 –33, June 2009.

[22] Grant Mair, John Maclay, Joy J. Miller, David McAllister, Martin Connell, John T. Murchison, and William MacNee. Airway dimensions in COPD: relationships with clinical variables. *Respiratory Medicine*, 104(11):1683–1690, November 2010.

[23] David M. Mannino. COPD epidemiology, prevalence, morbidity and mortality, and disease heterogeneity. *Chest*, 121(5 suppl):121S–126S, May 2002.

[24] Romain A. Pauwels, A. Sonia Buist, Peter M. A. Calverley, Christine R. Jenkins, and Suzanne S. Hurd. Global strategy for the diagnosis, management, and prevention of chronic obstructive pulmonary disease NHLBI/WHO global initiative for chronic obstructive lung disease (GOLD) workshop summary. *American Journal of Respiratory and Critical Care Medicine*, 163(5):1256–1276, April 2001.

[25] D. P. Tashkin, B. Celli, M. Decramer, D. Liu, D. Burkhart, C. Cassino, and S. Kesten. Bronchodilator responsiveness in patients with COPD. *European Respiratory Journal*, 31(4):742–750, April 2008.

[26] Donald P. Tashkin, Bartolome Celli, Stephen Senn, Deborah Burkhart, Steven Kesten, Shailendra Menjoge, and Marc Decramer. A 4-Year trial of tiotropium in chronic obstructive pulmonary disease. *New England Journal of Medicine*, 359(15):1543–1554, October 2008.

[27] X.L. Yang, Yang Liu, and H.Y. Luo. Respiratory flow in obstructed airways. *Journal of Biomechanics*, 39(15):2743–2751, 2006.

9

Novel functional respiratory imaging of changes in small airways of patients treated with extrafine beclomethasone/formoterol

Respiration 2013; Online Ahead of Print: doi:10.1159/000347120

Wim Vos, Jan De Backer, Gianluigi Poli, Annick De Volder, Liesbet Ghys, Cedric Van Holsbeke, Samir Vinchurkar, Lieve De Backer and Wilfried De Backer

9.1 Abstract

Background: Inhaled formulations using extrafine particles of long-acting-β2-agonists and corticosteroids were developed to optimize asthma treatment. Findings that these combinations reach and treat smaller airways more effectively are predominantly based on general, non-specific outcomes with little information on regional characteristics.
Objectives: This study aims to assess long-term effects of extrafine beclomethasone/formoterol on small airways of asthmatic patients using novel functional respiratory imaging methods.
Methods: 24, stable, asthma patients were subdivided into three groups (steroid-naive, n = 7; partially-controlled, n = 6; well-controlled, n = 11). Current treatment was switched to a fixed combination of extrafine beclomethasone/formoterol

(Foster®, Chiesi Pharmaceuticals, Italy). Patients underwent lung function evaluation and high resolution thorax computerized tomography scan. Local airway resistance was obtained from computational fluid dynamics.
Results: After 6 months, the entire population showed improvement in pre-bronchodilation imaging parameters including, small airway volume (p = 0.0007), resistance (p = 0.011) and asthma control score (p = 0.016). Changes in small airway volume correlated with changes in asthma control score (p = 0.004). Forced expiratory volume in 1 s (p = 0.044) and exhaled nitric oxide (p = 0.040) also improved. Functional respiratory imaging provided more detail and clinical relevance compared to lung function tests, especially in the well-controlled group where only functional respiratory imaging parameters showed significant improvement, while the correlation with asthma control score remained.
Conclusions Extrafine beclomethasone/formoterol results in significant reduction of small airways obstruction, detectable by functional respiratory imaging. Changes in imaging parameters correlated significantly with clinically relevant improvements. This indicates that functional respiratory imaging is a useful tool for sensitive assessment of changes in the respiratory system after asthma treatment.

9.2 Contributions of the author

The contributions of the author to this study are similar to the contributions in chapter 8. While chapter 8 quantifies the acute effects of medication in chronic obstructive lung disease, this study looks at long-term effects in an asthma population.

9.3 Introduction

The prevalence of asthma continues to rise, stimulating an ongoing effort in the development of new inhaled medications to optimize the treatment of asthmatic patients. A number of studies have supported the benefit of combining a long-acting β2-agonist (LABA) with inhaled corticosteroids (ICS) [4, 21]. While the LABA induces smooth muscle relaxation, and hence reduced airway constriction, the ICS is predominantly used to control the airway disease and therefore reduces the number and frequency of exacerbations [5]. Combination products are typically administered using either dry powder inhalers (DPIs), or metered dose inhalers (MDIs). The shift from environmentally unfriendly chlorofluorocarbons (CFC) to hydrofluoroalkane (HFA) propellants allows the development of HFA solution formulations. These are optimized to either achieve particle deposition patterns similar to established CFC-based drug formulations (aerosol diameter size for MDIs being 3 – 4 µm), thus facilitating the transition to new environment-friendly pMDIs in the clinical setting, or to achieve extrafine drug particles able to penetrate deeper into the airways (aerosol diameter size 1 – 2 µm) [1]. Initial findings demonstrated that a combination of extrafine beclomethasone/formoterol (BDP/F) improved lung function with similar efficacy compared to other non-extrafine fixed

combinations. This finding is not surprising considering that spirometric tests (i.e. forced expiratory volume in 1 second (FEV1) and peak expiratory flow (PEF)) performed in these studies did not provide comprehensive evaluation of the entire bronchial tree as they lack sufficient resolution to describe subtle changes in the small airways [22, 23]. This has prompted the need for developing new, image based [3, 6], techniques capable of detecting functional changes occurring in the more distal part of the lung following the administration of drugs able to reach and treat small airways [2, 12, 14].

Novel functional respiratory imaging (FRI) methods using computational fluid dynamics (CFD) provide new opportunities to gain insights into the mode of action of newly developed inhalation compounds targeting small airways. By converting patient specific high resolution computed tomography (HRCT) images to detailed three-dimensional computer models of the airways, CFD allows description of flow properties and aerosol behavior in the smaller airways (diameter 1 – 2 mm). By repeating measurements after an intervention, this approach yields a personalized assessment of changes in airway volume and CFD-based resistance. The method has been used in previous studies to assess morphological and flow features of large [9] and small [8] airways. A recent validation study [10] by our group demonstrated very good agreement between the HRCT/CFD method and imaging methods such as single photon emission computed tomography (SPECT). In other studies we showed that FRI could be used to assess the acute bronchodilating effects of a LABA in asthma [7] and COPD [11].

However, a trial evaluating the long-term effects of asthma medications on the imaging parameters described above is still lacking. Therefore, this trial aims to assess whether FRI can be used to describe changes occurring in the small airways of asthmatic patients following a 6 month treatment period with BDP/F (which is able to target the distal airways). Steroid-naive patients, as well as subjects already treated with non-extrafine fixed combinations, were enrolled in this study. This allowed the assessment of whether introduction of an extrafine treatment can induce additional changes in the small airways in steroid-naive and patients previously treated with non-extrafine combination therapies.

9.4 Material and Methods

9.4.1 Patient Selection

This study involved 24 stable asthmatic patients, as defined by the GINA guidelines (Global strategy for asthma management and prevention). Patients were subdivided into three different groups according to their treatment phenotype. The first group comprised steroid-naive asthmatics (n = 7). The remaining 17 patients were already under treatment with a daily beclomethasone-equivalent dose of 500 to 1000 µg at inclusion and were divided in two groups according to their level of asthma control as measured by the asthma control test (ACT) [19]: 6 were partially controlled and 11 well-controlled (n = 11). All patients gave their informed consent and the study

has been approved by the Ethics Committee of the Antwerp University Hospital.

9.4.2 Study Medication

Enrolled patients were switched from their current treatment (SABA, LABA,or ICS/LABA fixed combinations) to a fixed combination of extrafine HFA solution of beclomethasone/formoterol (BDP/F, Foster®, Chiesi Pharmaceuticals, Italy) 100/6 µg, 2 inhalations twice daily, delivered via a pMDI device. The study medication has a smaller mean mass aerodynamic diameter (MMAD = 1.3 – 1.4 µm) compared to medications that patients were receiving before inclusion (MMAD = 2.5 – 4 µm).

9.4.3 Lung function tests and FRI

All patients underwent full lung function evaluation and HRCT scan of the thorax at inclusion and after 6 months of treatment with the study medication. To assess only the long term effects of the compound on pre-bronchodilation airway geometry and not the acute bronchodilator effect, all tests were performed in the morning, before the patients took their medication and following an appropriate wash-out period for short and long acting bronchodilators (>12 h and >24 h, respectively).

Lung function tests included spirometry, full body plethysmography, exhaled nitric oxide (eNO), blood gases, and ACT questionnaire. The following parameters were considered for this study:

- FEV1
- Tiffeneau ratio (FEV1/forced volume vital capacity (FVC))
- Specific airway resistance (sRaw)
- eNO
- ACT score

HRCT scans were taken on a GE LightSpeed VCT scanner using a dose reduction protocol (120 kV, 10 – 100 mAs; noise factor 28; collimation 0.625 mm; rotation time 0.6 s and pitch factor 1.375) resulting in an effective dose of 1 – 2 mSv per HRCT scan. Scan resolution was 0.5 m^2 and slice increment was 0.6 mm. Scans were taken during a breath hold at two different lung levels, i.e. functional residual capacity (FRC) and total lung capacity (TLC). The arms of the patients were raised above their heads. To ensure the correct lung volume, HRCT scans were respiratory volume-gated during the moment of scanning using a pneumotach flow signal.

Subsequently, HRCT images were imported into Mimics, a commercial, FDA approved, medical image processing software package (Materialise, Leuven, Belgium, Food and Drug Administration, K073468; CE certificate, BE 05/1191 CE01). This software package converts HRCT images into patient specific, three-dimensional computer models of the lung lobes and the airway tree. By segmenting

lung lobes at FRC and TLC, the internal airflow distribution could be derived from the relative volume change. The airway tree, i.e. intraluminal air, was evaluated at TLC level and could be segmented down to bronchi with a diameter of about 1 – 2 mm. Beyond this point the HRCT resolution is insufficient to distinguish alveolar and intraluminal air. A typical airway model includes 5 – 10 generations, depending mainly on the disease state of the individual patient. Distal airway volumes (iVaw) could be assessed at individual airways or in different regions. Figure 9.1 shows a division of a segmented airway model in central airways (gray) and distal airways (red, starting at the segmental level). From previous studies it is known that BDP/F reaches both large and small airways [9], therefore in this study we focused predominantly on the small airway region.

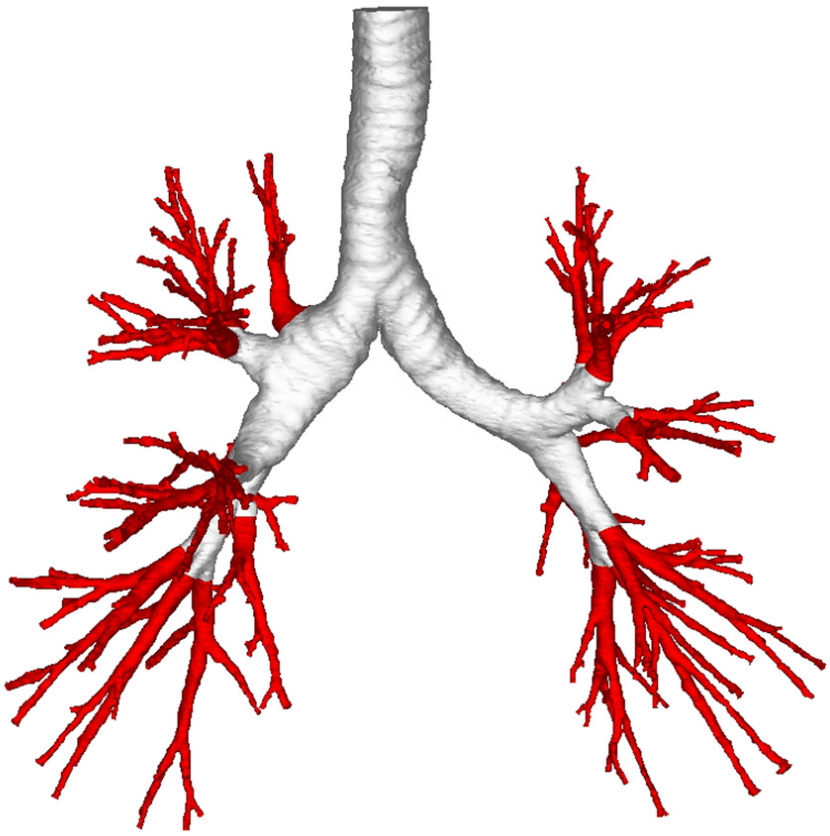

Figure 9.1: Frontal view of three-dimensional reconstruction of airway structure from HRCT images showing central (gray) and distal (red) airways. The main focus in this study was on the distal (red) airways.

The smoothed airway models were subsequently trimmed perpendicular to the centerlines at the trachea and the terminal bronchi to obtain a model that is suitable for flow simulation. Next, these models were exported to a meshing software package (TGrid 5.0, Ansys Inc, Lebanon, USA) where they were divided into discrete tetrahedral elements. After proper mesh convergence analysis, mesh size for this study was set to 4 million elements. Based on the resulting computational mesh, flow properties were obtained throughout the entire flow domain by means of Reynolds averaged Navier-Stokes (RANS) computational fluid dynamics (CFD) (Fluent 6.3.26, Ansys Inc, Lebanon, USA). A steady, normal inspiratory flow of 25 L/min was simulated for all patients to mimic the flow properties at tidal breathing. The outflow to each lobe was adjusted iteratively for each patient to match the internal flow rate distribution obtained from the HRCT scans. Measures of resistance (iRaw) at TLC in individual airways or different regions, corresponding to the volume measurements, were obtained from CFD calculations. Resistance was defined as the total pressure drop over an airway divided by the flow rate through that airway.

9.4.4 Statistical analysis

Statistical analysis was performed using Statistica 9.1 (StatSoft, Tulsa, USA). Changes in individual parameters after 6 months of treatment with the study medication were evaluated using Wilcoxon matched pairs analysis. Correlations between the changes in different parameters were evaluated using Spearman correlations. Differences between the three groups of patients were assessed using Mann-Whitney U test. Sample size calculations were performed using t-test for dependent samples. All statistical tests were considered significant when $p < 0.05$.

9.5 Results

9.5.1 Total study population

A total of 24 asthmatic subjects (all Caucasian, 16 females, 52.8 $\pm$ 11.9 years) were analyzed in this study. Medications used by patients before enrollment are listed in Table 9.1. The majority of patients were treated with ICS/LABA combinations delivered as fixed combinations (n = 17), while 2 patients were treated with LABA only. Reliever therapy consisted of the use of short-acting β2-agonists (n = 5) or fixed combination of short-acting β2-agonists and muscarinic antagonists (n = 2) and short-acting muscarinic antagonists (n = 1).

Considering the entire population, a significant difference was found in all parameters except FVC, FEV1/FVC and sRaw after 6 months of treatment with the study medication (Table 9.2). A significant improvement was observed in asthma control with an increase in the ACT score from 19.79 $\pm$ 4.46 at baseline to 21.67 $\pm$ 4.55 at the end of treatment, (p = 0.016). FEV1 increased from 96.3 $\pm$ 15.72% of predicted normal values to 100.1 $\pm$ 16.8%, (p = 0.044). Sig-

nificant changes were recorded also in imaging parameters with airway volume (iVaw) increasing from 8.36 $\pm$ 4.71 cm^3 to 9.64 $\pm$ 5.19 cm^3, (p = 0.0007) and CFD-based airway resistance (iRaw), decreasing from 0.082 $\pm$ 0.084 kPas/L to 0.050 $\pm$ 0.030 kPas/L, (p = 0.01), with a maximal increase in iVaw of 11.7% of the baseline value.

Figure 9.2 shows that changes in iVaw and iRaw occurred predominantly in the smaller, more distal airways while changes in larger airways were less pronounced. In addition, changes in iVaw significantly correlated with changes in ACT score (R = 0.49, p = 0.015) (Figure 9.3). At the end of treatment a significant decrease was detected in eNO (p = 0.040), which showed a 38% reduction versus baseline.

Nr	Group	ICS	LABA	LABA + ICS	SABA	SAMA
01	WC	-	-	Seretide 50/500, 2x1/d	-	-
02	PC	-	-	Seretide 50/500, 2x1/d	Ventolin PRN	-
03	WC	-	-	Symbicort Turbohaler 4.5/160, 2x1/d	-	-
04	SN	-	-	-	Ventolin (aerosol): 5 mg/mL, 6 drops, 3x/d	Atrovent (aerosol) 0.5 mg/mL: 0.5 mg/d
05	PC	-	-	Symbicort Turbohaler 4.5/160, 2x2/d	-	-
06	SN	-	Oxis 4.5 µg, 2x2/d	-	-	-
07	WC	-	-	Seretide 50/250, 2x1/d	-	-
08	PC	-	-	Symbicort Turbohaler 4.5/160, 2x1/d	-	-
09	PC	-	-	Symbicort Turbohaler 4.5/160, 2x2/d	-	-
10	WC	-	-	Seretide 25/250, 2x1/d	Ventolin PRN	-
11	WC	-	-	Symbicort Turbohaler 4.5/160, 2x2/d	-	-
12	WC	-	-	Symbicort Turbohaler 4.5/160, 2x2/d	-	-
13	PC	-	-	Symbicort Turbohaler 4.5/160, 2x2/d	-	-
14	SN	-	Foradil 12 µg, 2x/d	-	Ventolin, PRN	-
15	SN	-	-	-	Ventolin, 100 µg, 3x2/d	-
16	PC	-	-	Seretide 25/250, 2x1/d	Duovent, PRN	-
17	SN	-	-	-	-	-
18	SN	-	-	-	-	-
19	WC	-	-	Symbicort Turbohaler 4.5/160, 2x2/d	-	-
20	WC	-	-	Symbicort Turbohaler 4.5/160, 2x1/d	-	-
21	WC	-	-	Symbicort Turbohaler 4.5/160, 2x1/d	-	-
22	WC	-	-	Symbicort Turbohaler 4.5/160, 2x1/d	-	-
23	WC	-	-	Symbicort Turbohaler 4.5/160, 2x1/d	-	-
24	SN	-	-	-	Duovent, PRN	-

Table 9.1: List of medications taken by enrolled patients before entering the study: WC=well controlled, PC=partially controlled, SN=steroid-naive, ICS=inhaled corticosteroid, LABA=long acting β2-agonist, SABA=short-acting β2-agonist, SAMA=short-acting muscarinic antagonist, -=not applicable

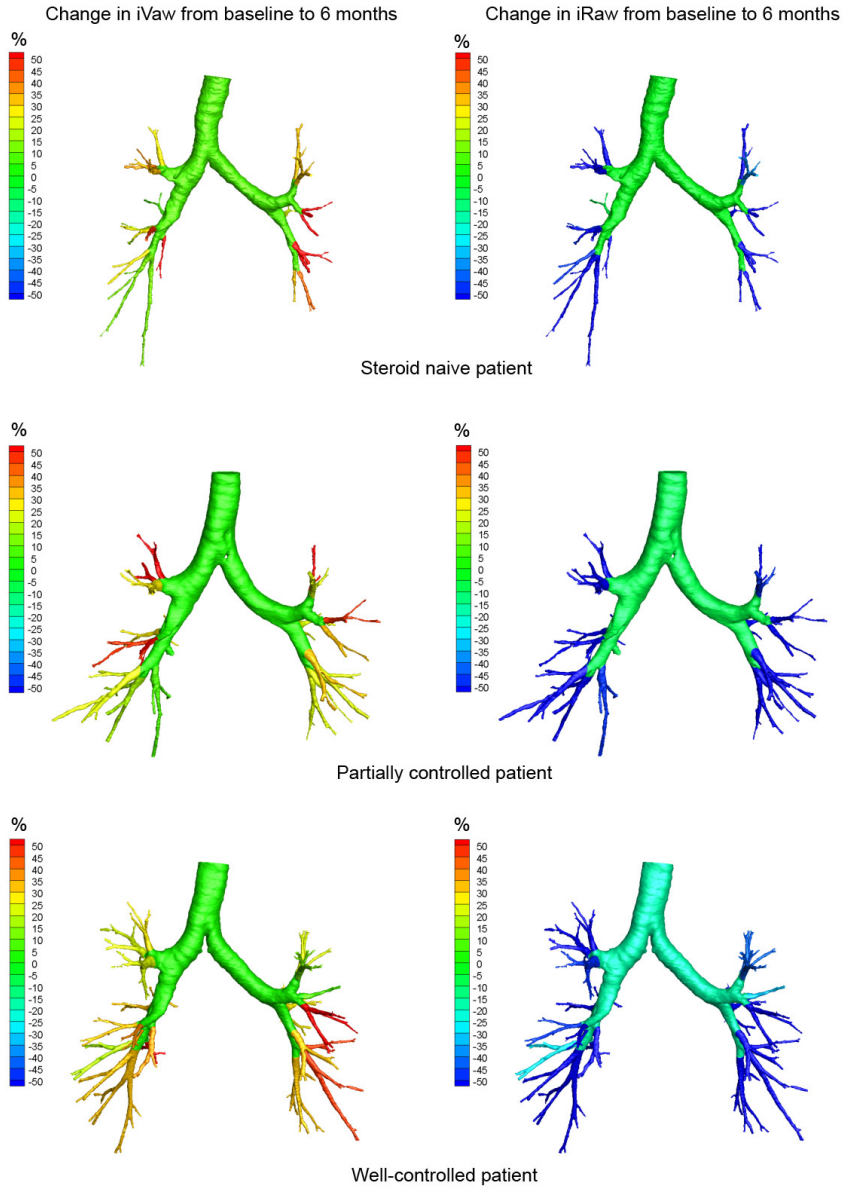

Figure 9.2: Changes in image based airway volume (iVaw, left) and CFD based airway resistance (iRaw, right) for steroid-naive (top), partially controlled (middle), and well-controlled (bottom) asthma patients.

	Baseline		6 months		
	Average	**SD**	**Average**	**SD**	**p-value**
Total			n = 24		
iVaw [cm^3]	8.36	4.71	9.64	5.19	0.0007*
iRaw [kPas/L]	0.082	0.084	0.05	0.03	0.011*
Δ ptot [Pa]	34.1	35	20.8	12.5	0.011*
FEV1 [%]	96.3	15.72	100.08	16.8	0.044*
FVC [L]	3.82	0.99	3.85	1.01	0.584
FEV1/FVC [%]	70.93	6.65	72.89	6.44	0.11
eNO [ppb]	44.07	54.78	27.48	29.47	0.040*
sRaw [kPas/L]	1.52	0.71	1.4	0.84	0.225
ACT score	19.79	4.46	21.67	4.55	0.016*
Steroid-naive			n = 7		
iVaw [cm^3]	7.24	4.23	9.14	6.57	0.043*
iRaw [kPas/L]	0.107	0.112	0.061	0.039	0.237
Δ ptot [Pa]	44.6	46.7	25.4	16.3	0.237
FEV1 [%]	93.34	17.47	99.29	19.65	0.176
FVC [L]	3.78	1.06	3.79	1.18	1
FEV1/FVC [%]	69.54	7.32	73.69	7.04	0.128
eNO [ppb]	61.47	75.81	30.54	26.08	0.31
sRaw [kPas/L]	1.68	0.88	1.55	1.07	0.735
ACT score	15.29	5.02	19.29	6.85	0.018*
Partially controlled			n = 6		
iVaw [cm^3]	8.53	4.37	9.86	4.42	0.116
iRaw [kPas/L]	0.09	0.11	0.047	0.033	0.173
Δ ptot [Pa]	37.5	45.8	19.6	13.8	0.173
FEV1 [%]	88.23	18.45	91.23	18.09	0.116
FVC [L]	3.54	0.71	3.61	0.73	0.5
FEV1/FVC [%]	72.82	8.64	73.51	8.71	0.753
eNO [ppb]	26.4	19.64	22.58	13.67	0.463
sRaw [kPas/L]	1.37	0.5	1.26	0.58	0.402
ACT score	20.33	3.14	21.67	2.8	0.463
Well controlled			n = 11		
iVaw [cm^3]	8.99	5.42	9.84	5.11	0.041*
iRaw [kPas/L]	0.061	0.035	0.044	0.023	0.062
Δ ptot [Pa]	25.4	14.6	18.3	9.6	0.062
FEV1 [%]	102.58	11.25	105.41	13.23	0.374
FVC [L]	4	1.12	4.02	1.08	0.859
FEV1/FVC [%]	70.78	5.35	72.04	5.12	0.657
eNO [ppb]	42.64	53.48	28.2	38.39	0.091
sRaw [kPas/L]	1.49	0.72	1.39	0.86	0.266
ACT score	22.36	2.01	23.18	2.99	0.214

*Table 9.2: Changes in imaging and lung function parameters after 6 months of treatment with extrafine beclomethasone/formoterol. * = $p < 0.05$*

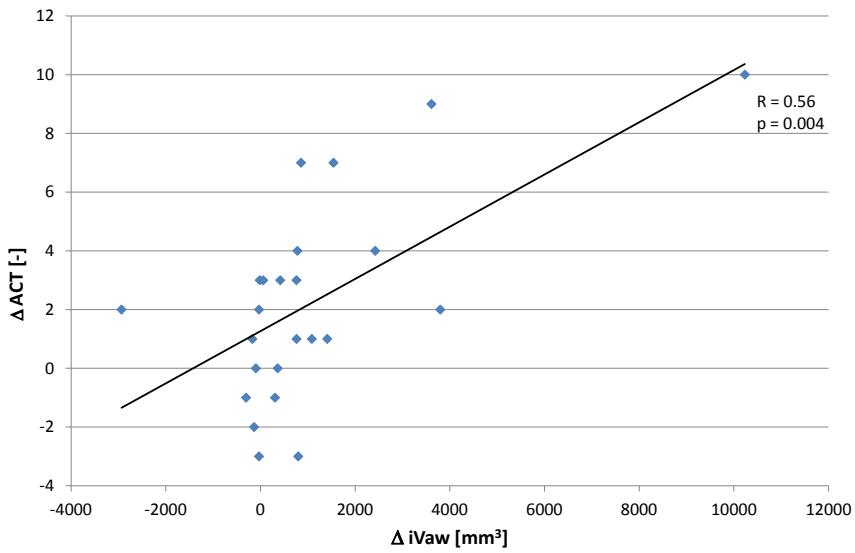

Figure 9.3: Correlation between changes in image-based airway volume (iVaw) and change in asthma symptom score (ACT) for all patients.

9.5.2 Steroid-naive patients

For the steroid-naive group, which included seven asthmatic patients (baseline FEV1 = 93.3% of predicted normal value), treatment did not result in significant changes in lung function parameters as measured by spirometry or body plethysmography (Table 9.2). However, FRI analysis showed a significant improvement in iVaw from 7.24 $\pm$ 4.23 cm^3 to 9.14 $\pm$ 6.57 cm^3 (p = 0.043) and an improvement, although not significant, in iRaw from 0.107 $\pm$ 0.112 kPas/L to 0.061 $\pm$ 0.039 kPas/L. A non-significant trend was observed also for eNO, which decreased by 50% by the end of the study. Treatment of steroid-naive patients with extrafine BDP/F resulted in significant improvement of asthma control, as shown by the increase in ACT score from 15.29 $\pm$ 5.02 to 19.29 $\pm$ 6.85, (p = 0.018).

9.5.3 Partially controlled patients

In the group of partially controlled patients (n = 6) no parameter changed significantly and no correlations were found between any parameters and the ACT score (Table 9.2).

9.5.4 Well-controlled patients

The group of well-controlled patients included 11 asthmatics with a baseline ACT score of 22.4 and FEV1 value of 102%. All patients included in this group were previously treated with ICS/LABA fixed combinations (Table 9.1) and switching to the study medication maintained the same high level of asthma control and good lung function. However, FRI showed significant improvement of iVaw from 8.99 $\pm$ 5.42 cm^3 to 9.84 $\pm$ 5.11 cm^3, (p = 0.041) and a clear trend in reduction of iRaw from 0.061 $\pm$ 0.035 kPas/L to 0.044 $\pm$ 0.023 kPas/L, (p = 0.062). As observed in the entire population, changes in iVaw correlated with changes in ACT score (R = 0.72, p = 0.012, Figure 9.4). No correlation was observed between changes in FEV1 and ACT score. Furthermore, sample size calculation indicated that a total of 68 patients would be needed to attain a significant difference with a power goal of 90% if FEV1 is used as an outcome parameter in a controlled (baseline versus intervention) study in well controlled mild asthmatics. On the other hand, when using the average change in iVaw or iRaw as outcome parameter the required sample size is reduced to 25.

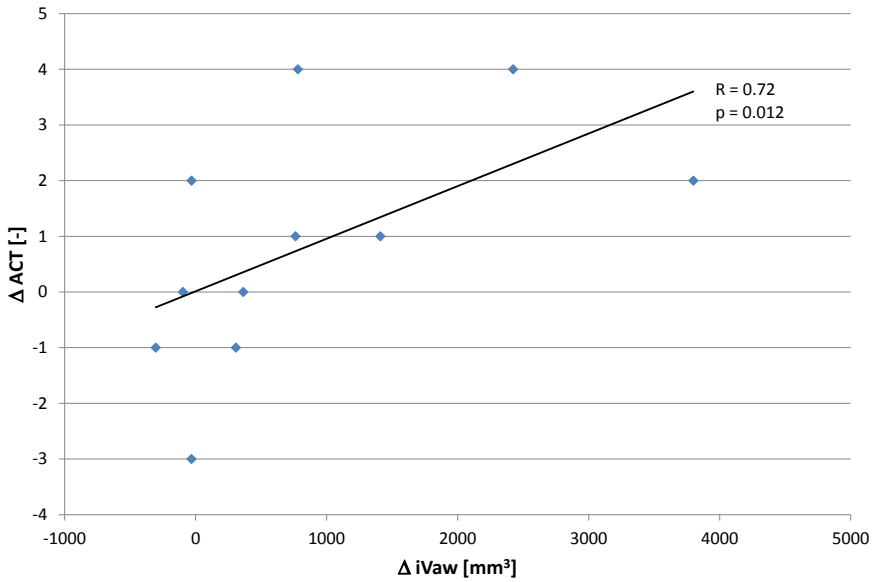

Figure 9.4: Correlation between changes in image-based airway volume (iVaw) and asthma symptom score (ACT) for well-controlled patients.

9.6 Discussion

The aim of this study was to assess whether long-term treatment with extrafine BDP/F can induce detectable changes in the distal airways of asthmatic patients, who are either steroid-naive or already under treatment with non-extrafine ICS/LABA fixed combinations. When considering the entire study population, the trial shows that 6 month therapy with extrafine BDP/F results in significant improvements in pre-bronchodilation imaging parameters such as small airway volume and CFD-based resistance. Notably, a significant correlation was found between changes in small airway volume and changes in asthma control score, suggesting that reaching and treating the small airways with extrafine BDP/F translates into clinical benefits for patients.

Changes in small airway parameters can be detected by FRI both in steroid-naive patients and in well-controlled patients previously treated with non-extrafine combinations. In asthmatic patients well-controlled with non-extrafine combinations, the switch to extrafine BDP/F leads to a significant improvement in pre-bronchodilator imaged airway volume, which occurred predominantly at the level of the small airways and was more sensitive than changes in FEV1. The observed improvement in asthma symptom scores again significantly correlated with the increase in imaged airway volume indicating that imaged airway volume is of clinical significance.

Overall these findings indicate that BDP/F extrafine formulation can target areas of the lungs left untreated by larger particle fixed combinations.

In a previous 6-month, randomized, controlled trial, extrafine BDP/F was compared to the combination of the same drugs (BDP+F) given as larger, non extrafine particles. The study showed that, for equivalent steroid dosages, there was no difference in the morning peak expiratory flow (PEF) between both preparations, but patients taking the extrafine particle combination did have significantly better asthma control as a consequence of the improved lung distribution that was previously demonstrated using Krypton ventilation scan [12, 13, 15]. In other investigations, the extrafine particle combination was always comparable to either fluticasone/salmeterol [17] or budesonide/formoterol [18] in terms of FEV1 and PEF improvements. These findings were not surprising considering that these spirometric tests did not provide comprehensive evaluation of the entire bronchial tree as they are unable to properly reflect small airway abnormalities.

There are two main reasons why this study could be considered innovative. Firstly the study focused on different 'treatment phenotypes' as it included steroid-naive, partially controlled and fully controlled patients. It did not include a typical run-in period where patients are taken off corticosteroids for a number of weeks. Secondly, this study employs a novel imaging method, combining HRCT imaging with flow simulations to investigate whether FRI could describe clinically relevant changes in well-controlled patients. This would demonstrate the true clinical significance and potential added value of using extrafine particle formulations.

In the current study, virtually all parameters indicated an improvement when

considering the complete population. This finding is in line with previous studies using this combination, which focused mainly on morning PEF [16, 18]. The current study expanded the knowledge by focusing on additional variables using multiple approaches such as exhaled breath analyses and in particular imaging. Also these parameters also suggested an additional beneficial clinical effect.

The imaging parameters showed the best correlation with the changes in asthma symptoms. The clinical relevance of FRI was further illustrated in the steroid-naive group where both ACT score and iVaw changed significantly, even though the sample size was limited. Also in the larger, well-controlled group the good correlation between changes in iVaw and ACT score supported the hypothesis that FRI yields clinically significant results.

Additional added value of imaging lies in the enhanced sensitivity to detect clinically relevant changes. Apparently when patients are well-controlled, FEV1 is not sensitive enough to describe additional subtle changes and additional improvement in that parameter is difficult to detect. Imaging parameters showed further consistent improvement in airway caliber and indicated where these changes mainly occurred. Previously only demonstrated indirectly [20], it is now possible to directly observe that a dilating effect is present in both the larger and smaller airways.

In a similar manner to FEV1, the ACT score appears to have limited predicting power to describe additional changes in well-controlled patients, especially considering the more subjective nature of patient reported outcome (PRO) parameters. A combination of classical lung function, PRO parameters, and FRI methods has the potential to enhance the description of the mode of action of new compounds. This could result in a reduction of the number of patients required in clinical trials as indicated by the power analysis. In addition, by performing studies in well-controlled patients it could potentially be possible to determine whether switching to a novel product has a beneficial effect on the number of exacerbations and possible decline in respiratory function.

Although this study is the largest clinical trial (n = 24) available using FRI, the power in the subgroups is still limited by the small sample size. In the partially controlled group (n = 6) especially, this could have had an influence on the final findings. Future research should consider equal subgroups with a sample size $n \geq 10$ per subgroup. The HRCT based airway models only include airways with diameters larger than 1 mm due to the limits of the scan resolution. This region, however, already includes 80 – 90% of the airway resistance [10]. Generations beyond the reconstructed parts are taken into account through the CFD boundary conditions that are derived from HRCT-based lobar expansion.

Based on the results from the current study it would be interesting to investigate the effect of the extrafine BDP/F combination in patients with irreversible airway disease. The increased sensitivity could also assist in the assessment of anti-inflammatory compounds where classical outcome parameters alone are likely not sufficient.

References

[1] D Acerbi, G Brambilla, and I Kottakis. Advances in asthma and COPD management: delivering CFC-free inhaled therapy using modulite technology. *Pulmonary pharmacology & therapeutics*, 20(3):290–303, January 2007.

[2] Jean Bousquet, Gianluigi Poli, Daniela Acerbi, Raffaella Monno, Steven Ramael, and Fabrice Nollevaux. Systemic exposure and implications for lung deposition with an extra-fine hydrofluoroalkane beclometasone dipropionate/-formoterol fixed combination. *Clinical pharmacokinetics*, 48(6):347–58, January 2009.

[3] Pierre-Y Brillet, Valérie Attali, Gaëlle Nachbaur, André Capderou, Marie-H Becquemin, Catherine Beigelman-Aubry, Catalin I Fetita, Thomas Similowski, Marc Zelter, and Philippe A Grenier. Multidetector row computed tomography to assess changes in airways linked to asthma control. *Respiration; international review of thoracic diseases*, 81(6):461–468, 2011. PMID: 21051856.

[4] Peter M A Calverley, Julie A Anderson, Bartolome Celli, Gary T Ferguson, Christine Jenkins, Paul W Jones, Julie C Yates, and Jø rgen Vestbo. Salmeterol and fluticasone propionate and survival in chronic obstructive pulmonary disease. *The New England journal of medicine*, 356(8):775–89, February 2007.

[5] Mario Cazzola and Ronald Dahl. Inhaled combination therapy with long-acting beta 2-agonists and corticosteroids in stable COPD. *Chest*, 126(1):220–37, July 2004.

[6] Silvestro Ennio D'Anna, Roberto Asnaghi, Gaetano Caramori, Lorenzo Appendini, Manfredi Rizzo, Carmelo Cavallaro, Giorgio Marino, Francesco Cappello, Bruno Balbi, and Antonino Di Stefano. High-resolution computed tomography quantitation of emphysema is correlated with selected lung function values in stable COPD. *Respiration; international review of thoracic diseases*, 83(5):383–390, 2012. PMID: 21832824.

[7] J W De Backer, W G Vos, A Devolder, S L Verhulst, P Germonpré, F L Wuyts, P M Parizel, and W De Backer. Computational fluid dynamics can detect changes in airway resistance in asthmatics after acute bronchodilation. *Journal of biomechanics*, 41(1):106–13, January 2008.

[8] J W De Backer, W G Vos, C D Gorlé, P Germonpré, B Partoens, F L Wuyts, P M Parizel, and W De Backer. Flow analyses in the lower airways: patient-specific model and boundary conditions. *Medical engineering & physics*, 30(7):872–9, September 2008.

[9] Jan W De Backer, Wim G Vos, Stijn L Verhulst, and Wilfried De Backer. Novel imaging techniques using computer methods for the evaluation of the

upper airway in patients with sleep-disordered breathing: a comprehensive review. *Sleep medicine reviews*, 12(6):437–47, December 2008.

[10] Jan W De Backer, Wim G Vos, Samir C Vinchurkar, Rita Claes, Anton Drollmann, Denis Wulfrank, Paul M Parizel, Paul Germonpré, and Wilfried De Backer. Validation of computational fluid dynamics in CT-based airway models with SPECT. *Radiology*, 257:854–862, 2010.

[11] L. A. De Backer, W. Vos, J. De Backer, C. Van Holsbeke, S. Vinchurkar, and W. De Backer. The acute effect of budesonide/formoterol in COPD: a multi-slice computed tomography and lung function study. *European Respiratory Journal*, 40(2):298–305, December 2011.

[12] Wilfried De Backer, Annick Devolder, Gianluigi Poli, Daniela Acerbi, Raffaella Monno, Christiane Herpich, Knut Sommerer, Thomas Meyer, and Fabrizia Mariotti. Lung deposition of BDP/formoterol HFA pMDI in healthy volunteers, asthmatic, and COPD patients. *Journal of aerosol medicine and pulmonary drug delivery*, 23(3):137–48, June 2010.

[13] Alfredo García Arieta. On the superiority of BDP/FF HFA pMDI fixed combination over the free combination of BDP CFC pMDI and FF DPI. *Respiratory medicine*, 103(12):1969–1970; author reply 1971–1972, December 2009. PMID: 19744845.

[14] Deborah A Gentile and David P Skoner. New asthma drugs: small molecule inhaled corticost... [curr opin pharmacol. 2010] - PubMed result. *Current opinion in pharmacology*, 10(3):260–5, June 2010.

[15] G Huchon, H Magnussen, A Chuchalin, L Dymek, F Bonnet Gonod, and J Bousquet. Lung function and asthma control with beclomethasone and formoterol in a single inhaler. *Respiratory medicine*, 103(1):41–9, January 2009.

[16] Pierluigi Paggiaro. New pharmacologic perspectives in pneumology: beclomethasone-formoterol extrafine. *The open respiratory medicine journal*, 3:38–42, January 2009.

[17] A Papi, P Paggiaro, G Nicolini, A M Vignola, and L M Fabbri. Beclomethasone/formoterol vs fluticasone/salmeterol inhaled combination in moderate to severe asthma. *Allergy*, 62(10):1182–8, October 2007.

[18] A Papi, P L Paggiaro, G Nicolini, A M Vignola, and L M Fabbri. Beclomethasone/formoterol versus budesonide/formoterol combination therapy in asthma. *The European respiratory journal : official journal of the European Society for Clinical Respiratory Physiology*, 29(4):682–9, April 2007.

[19] Michael Schatz, Christine A Sorkness, James T Li, Philip Marcus, John J Murray, Robert A Nathan, Mark Kosinski, Trudy B Pendergraft, and Priti

Jhingran. Asthma control test: reliability, validity, and responsiveness in patients not previously followed by asthma specialists. *The Journal of allergy and clinical immunology*, 117(3):549–56, March 2006.

[20] N Scichilone, S Battaglia, C Sorino, G Paglino, L Martino, A Paternò, R Santagata, M Spatafora, G Nicolini, and V Bellia. Effects of extra-fine inhaled beclomethasone/formoterol on both large and small airways in asthma. *Allergy*, 65(7):897–902, July 2010.

[21] Don D Sin, Malcolm Johnson, Wen Qi Gan, and S F Paul Man. Combination therapy of inhaled corticosteroids and long-acting beta2-adrenergics in management of patients with chronic obstructive pulmonary disease. *Current pharmaceutical design*, 10(28):3547–60, January 2004.

[22] Omar S Usmani. Unravelling the small airways: structure-function-treatment relationships in asthma and COPD. *Respiration; international review of thoracic diseases*, 84(1):1–3, 2012. PMID: 22759946.

[23] Sylvia Verbanck. Physiological measurement of the small airways. *Respiration; international review of thoracic diseases*, 84(3):177–188, 2012. PMID: 22948000.

Part IV

Novel applications

10

Particle deposition in airways of chronic respiratory patients exposed to an urban aerosol

Environmental Science & Technology 2012; 46(21): 12162-12169

Benjamin Horemans, Cedric Van Holsbeke, Wim Vos, Larysa Darchuk, Velibor Novakovic, Angel Conesa Fontan, Jan De Backer, Rene Ernest Vangrieken, Wilfried De Backer and Karolien De Wael

10.1 Abstract

Urban atmospheres in modern cities carry characteristic mixtures of particulate pollution which are potentially aggravating for chronic respiratory patients (CRP). Although air quality surveys can be detailed, the obtained information is not always useful to evaluate human health effects. This paper presents a novel approach to estimate particle deposition rates in airways of CRP, based on real air pollution data. By combining computational fluid dynamics with physical-chemical characteristics of particulate pollution, deposition rates are estimated for particles of different toxicological relevance, i.e. minerals, iron oxides, sea salts, ammonium salts and carbonaceous particles. Also, it enables some qualitative evaluation of the spatial, temporal and patient specific effects on the particle dose upon exposure to the urban atmosphere. Results show how heavy traffic conditions increases the deposition of anthropogenic particles in the trachea and lungs of respiratory

patients (here, +0.28 and +1.5 $\mu g \cdot h^{-1}$, respectively). In addition, local and synoptic meteorological conditions were found to have a strong effect on the overall dose. However, the pathology and age of the patient was found to be more crucial, with highest deposition rates for toxic particles in adults with a mild anomaly, followed by mild asthmatic children and adults with severe respiratory dysfunctions (7, 5 and 3 $\mu g \cdot h^{-1}$, respectively).

10.2 Contributions of the author

Together with dr. Horemans, the author of this thesis was the principal researcher in this study. The main challenge that was tackled here was the coupling of the particulate measurements to the simulations. The author converted the data from the micro-analytical physical-chemical analyses with respect to chemical composition, particle count and equivalent aerodynamic diameters to boundary conditions for the particulate simulations in the airways. This novel approach made it possible to assess deposition rates for selected chemical classes of particles.

10.3 Introduction

It is well known that health effects of air pollution and the associated increase in morbidity and mortality exert an enormous social and economic pressure on society. Especially airborne particles received considerable attention due to their chronic effects on human health. Scientific studies show how the presence of particles in the lungs causes inflammation of the local tissue, leading to an accelerated progression or exacerbation of asthma and chronic bronchitis, and can lead to cardiovascular disease [32]. Also, ultra-fine particles with aerodynamic diameters (AD) below 0.1 μm are known to be translocated from the respiratory epithelium to the blood circulation and subsequent secondary target organs such as heart, liver, brains and testis [18, 25, 39]. This causes adverse effects on the cardiovascular and central nervous system and poses a genetic risk to humans.

Although airway particle deposition affects the entire population, there are some groups which are more vulnerable than others. Dominici et al. [11] demonstrated how exposure of elderly (above 65 years of age) to fine particles (AD smaller than 2.5 μm) increases the risk for hospital admission related to cardiovascular and respiratory diseases. Children, at the other hand, have a significantly lower nasal filter efficiency [5] and are more rapidly inflamed by deposited particles in the tracheobronchial and alveolar regions [24]. Apart from elderly and children, chronic respiratory patients (CRP) suffering from asthma or a chronic obstructive pulmonary disorder (COPD) are more sensitive to particulate pollution. High particle concentrations and black carbon (BC) levels were associated with an increased fraction of exhaled nitric oxide in asthma patients [23], while chronic exposure to airborne particles during childhood is hypothesized to initiate the development of a COPD at later age [17]. Moreover, ultra-fine particles, transition metals and BC are

known to cause oxidative stress which may enhance pro-inflammatory effects in the airways of COPD patients that are already inflamed by their disease [28].

Mechanisms of particle induced inflammations are often linked to specific particle constituents. In their review on the health effects of particulate pollution, Pope and Dockery [32] underlined the need to study the role of physical-chemical effects of particles. This uncertainty reflects in the European legislation [14], which currently does not implement protective measures related to ultra-fine particles and specific toxic components due to insufficient scientific evidence [13]. The target values which are currently in use refer to total particle mass (AD < 10 and 2.5 μm) and do not necessarily restrict the particle dose (total airway deposition) nor the exposure to toxicological relevant particles.

The particle dose could be estimated theoretically by simulating the size-dependent deposition processes in human airways. Experimental results support the accurate predictions of various models, which numerically solve the behavior of air suspended particles at airway bifurcations or the tracheobronchial area as a whole [8, 31, 46]. Although powerful, the mathematical approach largely depends on the definition of the airway model, which may be casts or computer models obtained from morphometric analysis of the lungs [4, 29]. Recently, combination of computational fluid dynamics (CFD) with airway models obtained from high resolution computed tomography (CT) scans proved to be a valuable tool for simulating particle deposition in the airways of targeted patients [10]. This enables to evaluate the particle dose for a population which is more sensitive to particulate air pollution, such as CRP. Moreover, combined with size dependent information on the chemical composition of an urban aerosol, one can evaluate the toxicological relevance of air pollution exposure.

Here we demonstrate how the composition of individual particles, obtained with micro-analytical techniques, can be combined with patient specific simulations of particle deposition in the airways. This multi-disciplinary – though exploratory – study gives a quantitative description of particle deposition in airways of CRP exposed to an urban aerosol. Results are evaluated by considering the toxicological relevance of the urban pollution and the effects of local traffic conditions.

10.4 Materials and methods

10.4.1 Air quality survey

Three residential areas were selected to study the air quality near various traffic conditions in the urban environment of Antwerp, Belgium (Figure 10.1). The residential area at the left river bank is only a few hundred meters from the connection of the ring way with major highways E17 and E34, which channels all traffic from and towards the west. The second residential area is located in the southern suburbs of the city, which accommodates two major highways directing most traffic from and towards the south. One of them runs underneath the suburban residential area (E19) and the other at more than 2 km distance in southwestern direction (A12).

Traffic nearby the residential area in the city center is mainly limited by narrow streets, often with one-way direction. Considering the leading southwesterly winds (Figure 10.1), the area at the left river bank is supposed to be affected by continuous emissions of the nearby highway, especially as compared to the other areas. Therefore, this site will be later referenced as a heavy traffic environment while the others are considered as moderate traffic sites.

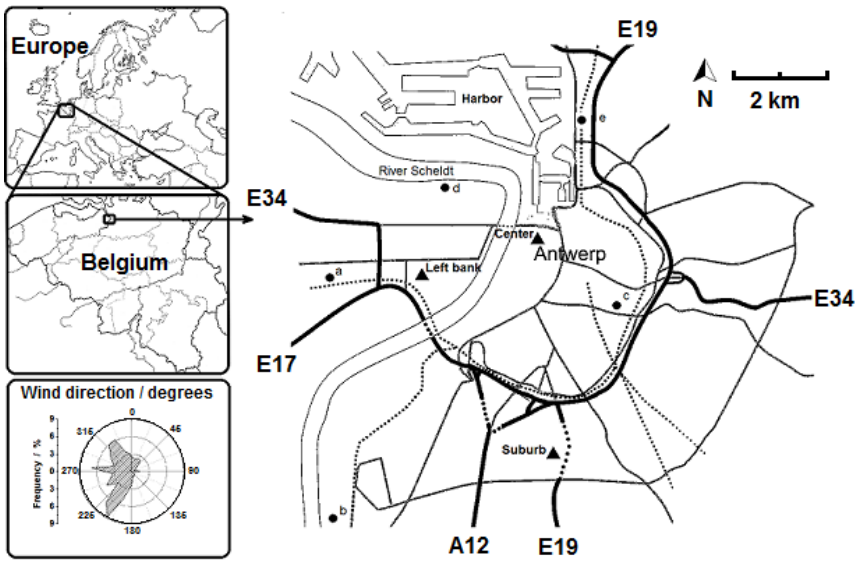

Figure 10.1: Schematic map indicating ▲ studied residential areas and • consulted network stations.

In each of the residential areas, three sampling stations were installed within 600 m distance from each other. Samples were collected concurrently at left bank and center stations from 12th until 18th of July 2011 and at left bank and suburb stations from 20th until 27th of July 2011. Fine particles (< 2.5 µm AD) were collected daily on Teflon membrane filters, using a Harvard-type MS&T sampler and a vacuum pump operating at 10 $L \cdot min^{-1}$ (Air Diagnostics and Engineering Inc., Harrison, ME, USA). Concentrations of BC were monitored every minute with micro-aethalometers (AE51, Magee Scientific, Berkeley, CA, USA) at one of the three stations per area. Each week, two sets of aerosol samples were collected with a berner cascade impactor for gravimetric and micro-analysis. When operated at 30 $L \cdot min^{-1}$, the berner impactor collects particles in 8 size fractions with a 50 % collection efficiency for particles of 0.0625, 0.125, 0.25, 0.5, 1, 2, 4 and 8 µm AD (stages 1–8, respectively). Particles above 16 µm AD are retained at the inlet of the cascade system. Additionally, air quality and meteorological data were consulted from several stations (a–e) in the measurement network of the Flemish environmental agency (VMM; see Figure 10.1).

10.4.2 Chemical analysis

Filter samples were allowed to equilibrate at stable atmospheric conditions (20 $\pm$ 1 °C and 50 $\pm$ 5 % relative humidity) before determining its mass on an electronic micro balance (MT5, Mettler Toledo, Columbus, OH, USA). The total particle mass was obtained by simply subtracting the mass of the filter. The bulk elemental composition of sampled aerosols was analyzed directly on the filters with energy-dispersive X-ray fluorescence spectrometry (Epsilon-5, PANalytical, Almelo, The Netherlands), according to an in-house developed method [40]. Finally, filters were sonicated for 15 min in ultra-pure water and the leachate was analyzed by ion chromatography with conductivity detection (DX-120, Dionex, Sunnyvale, CA, USA), as described elsewhere [19, 20]. The contribution of soil-dust to the collected fine particles was estimated from the Al, Si, Ca, Fe and Ti concentrations (obtained with EDXRF), as given by the soil dust equation of the Improve program [22]. Sodium and ammonium nitrates and sulfates were differentiated by simple assumptions on the preservation of mass and charge. The basic idea was that ammonium nitrate is only present if there is a stoichiometric excess of ammonium over sulfate [37], while any remaining nitrate was attributed to aged sea salt ($NaNO_3$). The amount of water associated with hygroscopic salts during gravimetric analysis was estimated with the aerosol inorganic model III [9, 12].

The molecular composition of 300 individual particles was analyzed manually on each of the stages 3–8 of the berner cascade impactor (cfr. air quality survey) with an InVia micro-Raman spectrometer, following protocols described elsewhere [33]. The elemental composition was analyzed automatically with electron-probe micro-analysis with energy-dispersive X-ray detection (200-300 per stage), for which the procedures were also extensively described in literature [35, 36]. Average particle diameters were calculated as dp = $(d_1 \times d_2^2)^{1/3}$, where d_1 and d_2 are the maximum and minimum Ferret's diameter obtained from the electron image. X-ray spectra for individual particles (1400–1800 per site) were evaluated by non-linear least-squares fitting with the AXIL code [43], and the elemental composition (m/M %) was calculated with a home-made quantification method [34]. A recently developed tool [3] allowed for automatic classification of particles into five chemical classes, depending on their elemental composition: minerals, iron oxides, sea salts (aged sea salts included), ammonium salts and carbonaceous particles. About 85–90 % of the measured particles could be classified into one of these groups. Since the molecular and elemental composition analysis was only made on stages 3–8 of the berner impactor (due to instrumental limitations), the obtained size distributions for each particle type were censored to the left (dp $>$ 0.3 μm).

10.4.3 Airway models

The three-dimensional geometry of the airways of asthma and COPD patients were obtained from a clinical database. These geometries were retrieved using the CT scan settings and segmentation algorithms described by De Backer et al. [10]. Institutional review board approval was obtained and a written informed consent

was signed by all patients.

The selection was made to cover the whole range of pathologies at different stages: one mild asthmatic adult and two mild asthmatic adults that were scaled to represent children (without airway deformations and with similar inhalation profiles as for healthy adults and children), one early stage COPD patient (with some airway deformations and slightly reduced flow), one persistent asthma patient (with an abnormal extrathoracic region) and a late stage COPD patient (restricted flow and high airway deformations in the whole lung). The pediatric lung models were obtained by projecting representative adult asthma models on airway models of pediatric cystic fibrosis patients such that the tracheobronchial airways were in good agreement for airway lengths and volumes. This was necessary since we have no scans of children with asthma and the fact that using cystic fibrosis patients is not representative for the population. All patients received a low dose CT scan of the extrathoracic region during slow inspiration (to prevent closure of the epiglottis) and two low dose CT scans of the tracheobronchial region, one during breath hold after normal expiration maneuver, i.e. functional residual capacity (FRC), and the other during breath hold at total lung capacity (TLC). During the scan, breathing maneuvers were controlled by a pneumotach, providing a real-time breathing signal. The lobar lung-volumes were reconstructed at both FRC and TLC lung levels of all patients. The lobar expansion from FRC to TLC (relative to the total increase in lung volume) was considered as a measure for the internal distribution of inhaled air. Combined with the inhalation profile (obtained with a pneumotach after the scans), the internal lobar airflow distribution was determined as a function of time.

10.4.4 Particle deposition rates

CFD calculations were performed for each airway model in order to assess local particle deposition patterns. A combined extrathoracic and tracheobronchial airway model was subdivided into 6 million tetrahedral elements for which the partial differential equations governing turbulent fluid flow were solved. For this evaluation of particle deposition, the approach of Vinchurkar et al. [45] was used. Kinetic-Energy Transport was chosen as the large eddy simulation subgrid model. The pressure-velocity coupling was performed using the SIMPLE scheme and second order schemes were chosen for the spatial discretization. The transient flow was calculated with a time step of 0.005 s. The particles were tracked with the fluid time step using Runge-Kutta scheme and Saffman Lift Force was taken unto account. The simulated particle sizes were those collected with the berner impactor. The patient specific inhalation flow profiles at the mouth and the calculated average internal flow distribution for each lobe at the terminal bronchi were used as boundary conditions for the flow simulations. This proprietary methodology (EU 09161455.2, US 61/182,493) was previously reported by De Backer et al. [10].

The contribution of each chemical class to the total mass of particles in a given AD size range (stage of the cascade impactor) was necessary to discriminate between the different compounds in the CFD simulations. Total particle mass was estimated from the AD and abundance of every aerosol type by assuming spherical

particles of unit density. In the CFD simulation, discrete particles with given AD were injected from the mouth over the full span of the inhalation cycle. Regional deposition of each particle type was assessed in the mouth, upper airway (from nasopharynx to larynx), trachea and lung (all airway generations after the trachea) segments of airways with a cross section down to 1 mm. Furthermore, exhaled fractions for all the particle diameters were taken into account by extrapolating the data from Usmani et al. [41] and the International Commission on Radiological Protection [1]. The calculated concentrations were converted to deposition rates in units of mass per hour, by scaling with patient specific inhalation profiles with 1/3 inhalation and 2/3 exhalation per breathing cycle.

10.5 Results

10.5.1 Urban particulate pollution

During the study, the average mass of fine air suspended particles was 9 ± 1 and 8 ± 1 $\mu g \cdot m^{-3}$ at the heavy traffic and moderate traffic sites, respectively (Figure 10.2). A paired sample t-test did not assume any significant difference between the averages of this mass-based metric ($p = 0.325$). In order to study the size-distribution of total particle mass, additional sampling was made with a cascade impactor on the last day of the campaign (Figure 10.3). At both sites, the mass median diameter (MMD) in the considered size range (0.0625–16 µm AD) was about 0.7 µm, with 80–90 % of the mass accounted by the fine fraction. However, the level of particles with an AD below 0.3 µm at the moderate traffic site was significantly lower as compared to the heavy traffic site, while the accumulation mode (0.3–2.5 µm AD) at this site was broadened and shifted to smaller particles (Figure 10.3).

About 60–90 % of the fine particle mass was explained by chemical analysis, however, it is to be noted that the BC mass at the heavy traffic site could be slightly overestimated due to repeated instrumental failure (cfr. composition on July 13th; see Figure 10.2). About 24 % of the mass could be attributed to ammonium salts (mostly ammonium sulfate), followed by BC (17 %), sea salts (11 %) and minerals (4 %). The mass fraction which was not accounted by chemical analysis could be attributed to organic carbon, which is typically twice the amount of BC, depending on its source [6, 30]. Micro-analysis on individual particles revealed a similar chemical composition. The most dominant particle types identified with EPMA were carbonaceous (11–25 % of the investigated particles per site), sodium nitrate (15–25 %) and mineral particles (18–19 %). Since the abundance of ammonium salts was relatively low in the studied particle size range (as compared to bulk composition), they were assumed to be mainly associated with particles with an AD below 0.25 µm. Raman analysis showed how the mineral fraction was mainly composed of silicates (24–64 %), among which quartz and Na,K-feldspathoids, calcite (22–43 %) and gypsum (9–26 %). Additionally, different types of iron oxides were spotted, such as magnetite, hematite and wüstite, as well as some iron

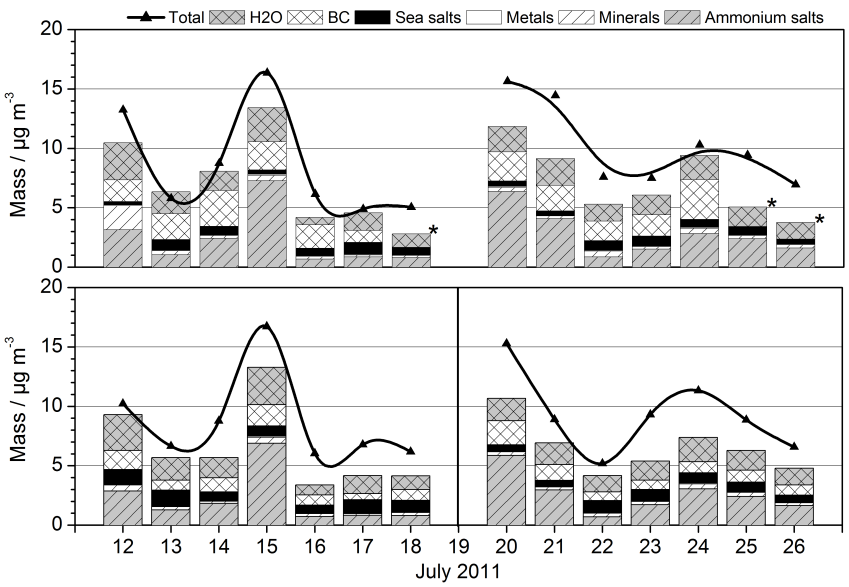

*Figure 10.2: Average mass and bulk composition of fine air suspended particles at the heavy (top) and moderate (bottom) traffic sites. * Missing BC data. Lines are drawn with the use of a b-spline algorithm.*

hydroxides, together amounting to about 5 % of the total analyzed particles per site. No direct differences were observed between the abundance of these particles among the various sites, however, the size distribution of the main particle classes did show some slight variations.

10.5.2 Particle deposition rates

The median deposition rate of all particle types in the airways of CRP was found to be maximally in the upper airway (22 %) and lung (62 %) segments of the model (Table 10.1). At a heavy traffic environment, deposition rates in the mouth and upper airways was found to be significantly lower compared to a moderate traffic environment, while the rate in the lungs was significantly higher (Table 10.1). These differences result from an increased fraction of sub-micrometer particles at the environment with heavy traffic (Figure 10.4) and illustrate how particle deposition is highly dependent on the size distribution of the inhaled aerosol.

Since the presence of a certain aerosol specie can alter the total particle size distribution, it also significantly affects the received particle dose upon inhalation. In order to describe particle deposition in clinically relevant terms, particle types identified with EPMA were grouped according to their toxicity. Carbonaceous and iron-rich particles are generally acknowledged to induce cytotoxic effects [16, 27, 42], but also crystalline silicates can cause oxidative stress due to the

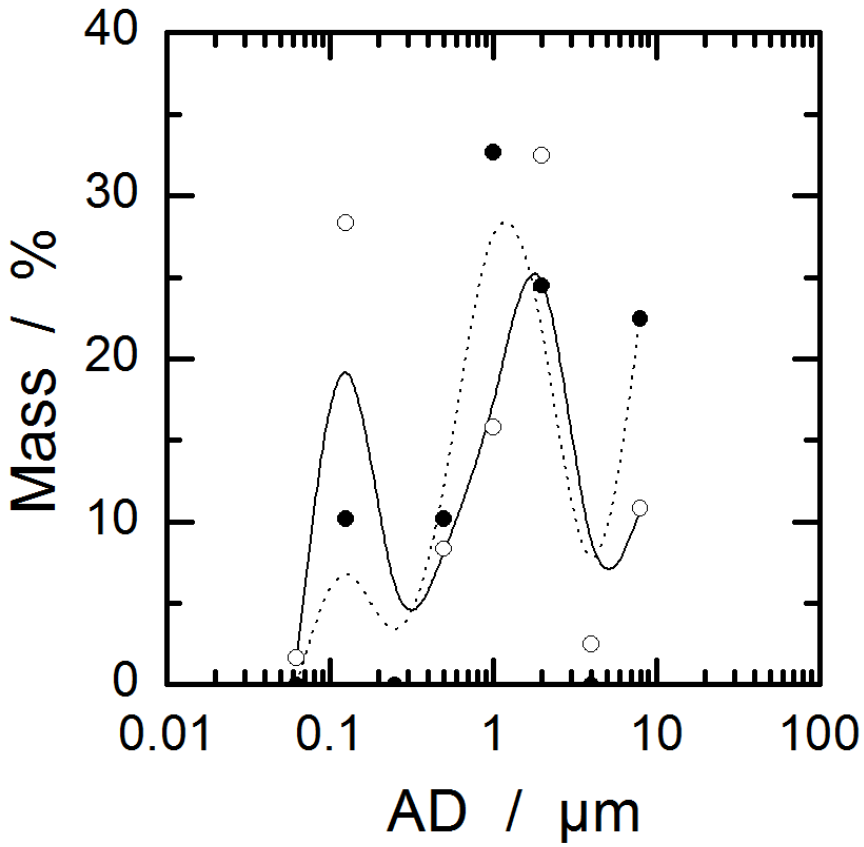

Figure 10.3: Size-distribution of particle mass at the –○– heavy and ··•··moderate traffic site. Lines are drawn with the use of a b-spline algorithm.

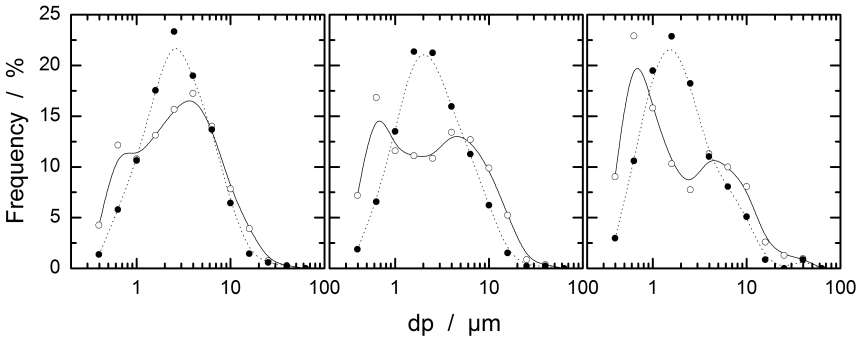

Figure 10.4: Size distribution of all (left), toxic (middle) and anthropogenic (right) particles on 15th of July at the –○– heavy and ··•·· moderate traffic site. Lines are drawn with the use of a b-spline algorithm.

Particle type[a]	Airway segment	Median (range), $\mu g \cdot h^{-1}$		p[b]
		Heavy traffic	Moderate traffic	
All	Mouth	0.20 (0.0 – 0.41)	0.21 (0.0 – 0.69)	**0.012**
	Upper airways	1.9 (0.41 – 6.7)	2.4 (0.40 – 8.4)	**0.004**
	Trachea	1.5 (0.16 – 3.2)	1.5 (0.15 – 3.6)	0.347
	Lung	7.8 (2.0 – 13)	7.2 (1.8 - 13)	**0.006**
Toxic	Mouth	0.16 (0.0 – 0.42)	0.20 (0.0 – 0.68)	**0.012**
	Upper airways	1.6 (0.29 – 4.8)	3.0 (0.35 – 7.2)	**0.002**
	Trachea	1.0 (0.11 – 2.3)	1.1 (0.12 – 2.9)	**0.015**
	Lung	4.8 (1.4 – 8.0)	4.9 (1.4 – 9.1)	0.308
Anthropogenic	Mouth	0.04 (0.0 – 0.21)	0.01 (0.0 – 0.15)	0.424
	Upper airways	0.44 (0.06 – 2.4)	0.15 (0.02 – 1.5)	0.347
	Trachea	0.25 (0.02 – 1.1)	0.09 (0.01 – 0.70)	0.136
	Lung	1.1 (0.26 – 3.8)	0.46 (0.09 – 2.2)	0.071

[a]All: Carbonaceous, iron-rich, minerals, ammonium salts and sea salts; Toxic: Carbonaceous, iron-rich and minerals; Anthropogenic: Carbonaceous and iron-rich (refer to text)
[b]Significance (bold: $p < 0.05$) of a Wilcoxon signed rank test; H_0: no median difference (n = 12)

Table 10.1: Particle deposition rates in the airways of chronic respiratory patients by segment

presence of ferric ions which are complexed with silanol groups at the surface [15]. Therefore, the carbonaceous, iron-rich and mineral particle fractions (the latter containing 60–85 % of pure or mixed aluminum silicates) were classified as being toxic to humans, while the health effects of sea salts and ammonium salts could be neglected at typical atmospheric concentrations [7].

Size distributions for toxic particles at the moderate and heavy traffic environment are given in Figure 10.4. Compared to the distribution of all particles, the maximum of the toxic particle distribution at the moderate traffic site shifted only slightly from 2.7 to 2.0 μm. However, at the heavy traffic environment one can see how the fraction of sub-micrometer and coarse (AD > 10 μm) particles gained importance over intermediate sizes (1–10 μm). Therefore, the increment of toxic particles deposited in the mouth and upper airways at a moderate traffic environment (+0.4 and +1.4 $\mu g \cdot h^{-1}$ over the heavy traffic environment, respectively) is even higher as found for total particle deposition, though no significant difference could be observed for the deposition in the lung segment (Table 10.1). Since particles of natural origin do not represent the fraction of aerosols due to manmade pollution, they are not useful in comparing the effects of anthropogenic emissions on particle deposition rates. Since mineral particles were dominantly present, they significantly alter the total size distribution and hence deposition rates for the particle group defined as toxic. Anthropogenic toxic particles (carbonaceous and iron-rich) were represented by a strong sub-micrometer mode at the heavy traffic site (Figure 10.4). Therefore, deposition rates for all airway segments at this site were higher than the moderate traffic site. Although statistical tests proofed these elevated deposition rates to be non-significant for all airway segments ($p < 0.05$), the probability value for the lung segment was found at the borderline of the significance level (Table 10.1).

10.6 Discussion

The daily average mass of fine air suspended particles was significantly correlated with average wind speeds (Pearson coefficient $r = -0.588$; $p < 0.05$), as well as with NO_2 and SO_2 concentrations ($r = 0.866$ and 0.530, respectively; $p < 0.05$). This shows how strong wind speeds from south-westerly directions (Figure 10.1) introduce fresh air and allow for the quick dispersal of local NO_2 and SO_2 emissions. On days with low wind speeds, these gases accumulate and produce particulate nitrate and sulfate in the urban air [38]. This local effect was superimposed on synoptic meteorology, which determines the particulate pollution load by sending marine or continental polluted air masses to Antwerp. Backward air mass trajectories indeed showed how elevated levels of total fine particle mass were associated with air masses which traveled largely over land in the last 24 hours before arrival ($r = 0.645$, $p < 0.01$).

From the total mass of fine particles and the MMD for particles ranging from 0.0625 to 16 μm AD one would conclude that the particulate pollution load was hardly affected by local traffic conditions. Also the bulk chemical composition was

comparable among sites, with fairly equal amounts of each component contributing to the urban aerosol. Although these estimators did not suggest any difference between sites, particles smaller than 0.3 μm AD were found to be elevated at the heavy traffic site (Figure 10.3). This indicates the closeness of an air pollution source, such as the neighboring highway. At the moderate traffic site (southern suburbs), these particles were found to be coagulated to bigger sizes, as shown by the shift in the accumulation mode (Figure 10.3). Micro-analysis of individual particles also revealed some differences in the size distribution of main aerosol types. Therefore, inhalation of airborne particles at the heavy and moderate traffic sites could result in a different total particle dose, since slight shifts in the main size modes of each aerosol type could definitely affect its deposition efficiency in human airways.

Simulated median particle deposition rates in the lung segment of CRP are shown in Table 10.2, as if they were breathing the air at the heavy and moderate traffic sites during two days of the air quality survey. Differences in the particle doses received at the moderate and heavy traffic site did not manifest through deposition rates of all particles, nor for toxic particles. The median deposition rate of anthropogenic particles at the heavy traffic site was about 0.5–1 $\mu g \cdot h^{-1}$ higher than at the moderate traffic site. Although the results of an air quality study did not necessarily assumed any significant difference in the mass or bulk composition of fine particles among sites, deposition rates for anthropogenic particles (silicate-rich minerals not included) were about 1.5–2.5 times higher at the heavy traffic site. Nevertheless, from Table 10.2 it can be seen that the differences between the two days were higher than between sites. This demonstrates how daily variation of air quality, as determined by local and synoptic meteorological conditions, is more relevant for the quality of air we breathe compared to the area (i.e. traffic condition) in which we live. Results clearly show that anthropogenic activity (presumably traffic) has an incremental effect on top of the background particulate air pollution. Interpretation of this result in clinical terms may be ambiguous, because differences in the deposition rates were not significant among sites when minerals were included.

The results also showed significantly different deposition rates between patients. For example, the total particle deposition rate in the lungs of the six CRP at the heavy traffic site on the 15th of July ranged from 3.1 to 13.2 $\mu g \cdot h^{-1}$. Therefore, patients were divided in three groups of differing pathological severity and age: severe/adult, mild/child and mild/adult. Deposition rates were highest for adults with a mild asthma or early stage COPD, and decreased for mild pediatric asthma patients and adults with a severe asthma or late stage COPD (Table 10.3). These differences were statistically significant for deposition of all particles as well as for toxic and anthropogenic particles ($p < 0.012$ according to a Wilcoxon signed rank test). These results show that adults with a mild respiratory dysfunction collect more particles as compared to mild pediatric asthma patients. This could be the result of differences in the airway geometry and inhalation profile of each patient. The airways of children are generally smaller, so they breath less air during each hour. Moreover, due to the smaller airway dimensions, particles are more easily

Particle type[a]	Date	Median (range), $\mu g \cdot h^{-1}$		p[b]
		Heavy traffic	Moderate traffic	
All	15/7	9.5 (3.1 – 13)	9.0 (3.1 – 13)	0.753
	25/7	5.8 (2.0 – 8.4)	5.0 (1.8 – 7.5)	0.917
Toxic	15/7	5.5 (1.8 – 8.0)	5.8 (2.2 – 9.1)	0.753
	25/7	4.0 (1.4 – 5.9)	3.5 (1.4 – 5.9)	0.917
Anthropogenic	15/7	2.6 (0.88 – 3.8)	1.5 (0.51 – 2.2)	**0.028**
	25/7	0.79 (0.26 – 1.1)	0.30 (0.09 – 0.42)	**0.028**

[a]All: Carbonaceous, iron-rich, minerals, ammonium salts and sea salts; Toxic: Carbonaceous, iron-rich and minerals; Anthropogenic: Carbonaceous and iron-rich (refer to text)
[b]Significance (bold: $p < 0.05$) of a Wilcoxon signed rank test; H_0: no median difference (n = 6)

Table 10.2: Particle deposition rates in the lungs of chronic respiratory patients by date

removed in the upper airways or trachea and do not penetrate as deep as they do in adult lungs. Similarly, although severe CRP are believed to be a sensitive population for air pollution, particle deposition was found to be lowest for adults with a severe respiratory dysfunction. These patients have, in general, airway deformations such as local narrowing and bends, which leads to enhanced deposition in the upper airways and trachea. In addition, they have a restricted airflow and thus a smaller air volume per inhalation cycle. Hence, people which are sensitive to air pollution due to a respiratory dysfunction protect themselves from particulate pollution by having a reduced airflow. Nevertheless, for each patient group the dose of anthropogenic particles at the heavy traffic site was about double of the dose that is received when inhaling the air at the moderate traffic environment.

In conclusion, the combination of CFD with physical-chemical characteristics of particulate pollution was found to be useful to calculate particle deposition in the airways of patients upon exposure to the urban atmosphere. The novelty of this simulation approach is the use of chemical information on individual airborne particles, which enables to study deposition rates for selected classes such as minerals or carbonaceous particles. In this way, one could focus for example on toxic particles only, for which the deposition rates are not influenced by abundant and rather coarse particle types without any toxicological relevance. As debates on particulate matter are mostly held on a local scale, it is important to understand that location (within the range of an urban environment) is less important in comparison with pathology and synoptic meteorological conditions. Of course, the only way to protect people's health is to keep particulate pollution within limits, especially in heavy traffic environments.

As this is a proof of concept study describing a novel approach, there are several limitations which should be underlined. First of all, the aerosol characteristics used in this study were obtained from airborne particle samples collected

Particle type[a]	Pathology/age	Median (range), $\mu g \cdot h^{-1}$		p[b]
		Heavy traffic	Moderate traffic	
All	Severe/adult	3.9 (2.0 – 7.5)	3.6 (1.8 – 7.1)	0.465
	Mild/child	7.6 (5.5 – 9.9)	6.9 (4.7 – 9.6)	0.465
	Mild/adult	11 (8.2 – 13)	10 (7.4 – 13)	0.465
Toxic	Severe/adult	2.6 (1.4 – 4.6)	2.5 (1.4 – 4.6)	1.000
	Mild/child	4.7 (3.8 – 6.0)	4.6 (3.0 – 6.4)	1.000
	Mild/adult	6.8 (5.7 – 8.0)	7.4 (5.8 – 9.1)	0.465
Anthropogenic	Severe/adult	0.78 (0.26 – 2.1)	0.38 (0.09 – 1.2)	0.068
	Mild/child	1.6 (0.75 – 2.8)	0.81 (0.28 – 1.6)	0.068
	Mild/adult	2.4 (1.1 – 3.8)	1.3 (0.87 – 2.2)	0.068

[a]All: Carbonaceous, iron-rich, minerals, ammonium salts and sea salts; Toxic: Carbonaceous, iron-rich and minerals; Anthropogenic: Carbonaceous and iron-rich (refer to text)
[b]Significance (bold: $p < 0.05$) of a Wilcoxon signed rank test; H_0: no median difference (n = 4)

Table 10.3: Particle deposition rates in the lungs of chronic respiratory patients by pathology and age

during only two days. Since it is obvious that the particulate pollution load largely determines the calculated deposition rates, the quantitative figures on particle doses could not be considered representative for the studied area. Nevertheless, since the concentration and composition of particles were rather typical for most medium sized cities [2, 20, 21, 26, 44], the qualitative evaluation remains valid for most situations encountered in urban environments. Secondly, the simulations were only performed in a small amount of patients. Extrapolating these results to a whole population is therefore dangerous. However, we believe that the concept of using real geometries obtained from CT scans instead of statistical models make the results more representative. The models were chosen in a way that they represent typical airway geometries for a certain group of CRP. Nevertheless, some limitations remain (1) Most people are nasal breathers, though mouth breathing was modelled since no nasal geometries were available; (2) The pediatric models were scaled down adult models, which means that it is possible that they slightly deviate from airway geometries found for this population; (3) The used CFD methodology was previously validated with SPECT/CT by De Backer et al. [10], but did not include the particle diameters that were simulated here; (4) In order to express particle dose in units of micro gram per hour, particles of well-defined AD were assumed to be spherical with unit density. Although shape effects could be important for the behavior of particles in human airways, it is thought that this approach is more accurate than defining the density for individual particles with a mixed composition.

Considering these limitations, it should be emphasized that this study is only a preliminary step in the assessment of the deposition rates of toxic particles in

human airways. Decisive conclusions regarding the potential health risks due to air pollution exposure require extended research, which combines more elaborated simulations of airway particle deposition with more extensive chemical analysis of the urban aerosol. In this regard, the present results must be treated with care when supporting the general debate on air quality and urban infrastructure.

10.7 Acknowledgement

The authors are grateful for the financial support of n.v. Vooruitzicht. Furthermore, co-workers at the environmental analysis research group are acknowledged for their help in the fieldwork.

10.8 Supporting Information Available

Size distributions of the major aerosol classes and a summary of the air quality and meteorology data of the VMM recorded during the survey.

References

[1] Human respiratory tract model for radiological protection. a report of a task group of the international commission on radiological protection. *Annals of the ICRP*, 24(1-3):1–482, 1994.

[2] Willemien Anaf, Benjamin Horemans, Teresa Madeira, M. Carvalho, Karolien De Wael, and René Van Grieken. Effects of a constructional intervention on airborne and deposited particulate matter in the portuguese national tile museum, lisbon. *Environ. Sci. Pollut. R.*, DOI: 10.1007/s11356-012-1086-7:1–9, 2012.

[3] Willemien Anaf, Benjamin Horemans, René Van Grieken, and Karolien De Wael. Chemical boundary condition algorithm for the classification of aerosol particles using computer controlled electron probe micro analysis. *Talanta*, page In press, 2012.

[4] B. Asgharian, M.G. Ménache, and F.J. Miller. Modeling age-related particle deposition in humans. *J. Aerosol Med.*, 17(3):213–223, 2004.

[5] M.H. Becquemin, D.L. Swift, A. Bouchikhi, M. Roy, and A. Teillac. Particle deposition and resistance in the noses of adults and children. *Eur. Respir. J.*, 4(6):694–702, 1991.

[6] László Bencs, Khaiwal Ravindra, Johan de Hoog, Zoya Spolnik, Nico Bleux, Patrick Berghmans, Felix Deutsch, Edward Roekens, and René Van Grieken. Appraisal of measurement methods, chemical composition and sources of fine atmospheric particles over six different areas of northern belgium. *Environ. Pollut.*, 158(11):3421 – 3430, 2010.

[7] Paul J A Borm, Frank Kelly, Nino Künzli, Roel P F Schins, and Kenneth Donaldson. Oxidant generation by particulate matter: from biologically effective dose to a promising, novel metric. *Occup. Environ. Med.*, 64(2):73–74, 2007.

[8] David Broday. Deposition of ultrafine particles at carinal ridges of the upper bronchial airways. *Aerosol Sci. Tech.*, 38(10):991–1000, 2004.

[9] Simon L. Clegg, Peter Brimblecombe, and Anthony S. Wexler. Thermodynamic model of the system h^{+}-nh_4^{+}-na^{+}-so_4^{2-}-no_3^{-}-cl^{-}-h_2o at 298.15 k. *J. Phys. Chem. A*, 102(12):2155–2171, 1998.

[10] Jan W. De Backer, Wim G. Vos, Samir C. Vinchurkar, Rita Claes, Anton Drollmann, Denis Wulfrank, Paul M. Parizel, Paul Germonpré, and Wilfried De Backer. Validation of computational fluid dynamics in ct-based airway models with spect/ct. *Radiology*, 257(3):854–862, 2010.

[11] Francesca Dominici, Roger D. Peng, Michelle L. Bell, Luu Pham, Aidan McDermott, Scott L. Zeger, and Jonathan M. Samet. Fine particulate air pollution and hospital admission for cardiovascular and respiratory diseases. *J. Am. Med. Assoc.*, 295(10):1127–1134, 2006.

[12] E-AIM. http://www.aim.env.uea.ac.uk/aim/aim.php, extended aim thermodynamic aerosol model. last access: 21th may 2012, 2012.

[13] EU. Second position paper by the cafe working group on particulate matter, December 2004.

[14] EU. Directive 2008/50/ec of the european parliament and the council of 21 may 2008 relating to ambient air quality and cleaner air for europe, 2008.

[15] A.J. Ghio, T.P. Kennedy, R.M. Schapira, A.L. Crumbliss, and J.R. Hoidal. Hypothesis: is lung disease after silicate inhalation caused by oxidant generation? *Lancet*, 336(8721):967 – 969, 1990.

[16] Peter S Gilmour, Axel Ziesenis, E.Rona Morrison, Mark A Vickers, Ellen M Drost, Isobel Ford, Erwin Karg, Claudia Mossa, Andreas Schroeppel, George A Ferron, Joachim Heyder, Michael Greaves, William MacNee, and Kenneth Donaldson. Pulmonary and systemic effects of short-term inhalation exposure to ultrafine carbon black particles. *Toxicol. Appl. Pharm.*, 195(1):35 – 44, 2004.

[17] Jonathan Grigg. Particulate matter exposure in children. *Proc. Am. Thor. Soc.*, 6(7):564–569, 2009.

[18] Maureen R. Gwinn and Val Vallyathan. Nanoparticles: health effects–pros and cons. *Environ. Health Persp.*, 114(12):1818–1825, 08 2006.

[19] B. Horemans, A. Worobiec, A. Buczynska, K. Van Meel, and R. Van Grieken. Airborne particulate matter and btex in office environments. *J. Environ. Monit.*, 10(7):867–876, 2008.

[20] Benjamin Horemans, Carolina Cardell, László Bencs, Velichka Kontozova-Deutsch, Karolien De Wael, and René Van Grieken. Evaluation of airborne particles at the alhambra monument in granada, spain. *Microchem. J.*, 99:429–438, 2011.

[21] Benjamin Horemans and René Van Grieken. Speciation and diurnal variation of thoracic, fine thoracic and sub micrometer airborne particulate matter at naturally ventilated office environments. *Atmos. Environ.*, 44(12):1497–1505, 2010.

[22] IMPROVE. http://vista.cira.colostate.edu/improve/tools.htm, standard aerosol-type equations. last excess: 21th may, 2012.

[23] Karen L. Jansen, Timothy V. Larson, Jane Q. Koenig, Therese F. Mar, Carrie Fields, Jim Stewart, and Morton Lippmann. Associations between health effects and particulate matter and black carbon in subjects with respiratory disease. *Environ. Health Persp.*, 113(12):1741–1746, 08 2005.

[24] Stefan Karrasch, Gunter Eder, Ines Bolle, Oliver Eickelberg, Akira Tsuda, and Holger Schulz. Pulmonary particle deposition is dependent on the stage of postnatal lung development. *Am. J. Resp. Crit. Care*, 181:A2190, 2010.

[25] Wolfgang G. Kreyling, Manuela Semmler-Behnke, and Winfried Möller. Ultrafine particle-lung interactions: does size matter? *J. Aerosol Med.*, 19(1):74–83, 2006.

[26] Barbara Krupińska, Anna Worobiec, Giuliana Gatto Rotondo, Velibor Novaković, Velichka Kontozova, Chul-Un Ro, René Van Grieken, and Karolien De Wael. Assessment of the air quality (no2, so2, o3 and particulate matter) in the plantin-moretus museum/print room in antwerp, belgium, in different seasons of the year. *Microchem. J.*, 102(0):49–53, 2012.

[27] John C. Lay, Kirby L. Zeman, Andrew J. Ghio, and William D. Bennett. Effects of inhaled iron oxide particles on alveolar epithelial permeability in normal subjects. *Inhal. Toxicol.*, 13(12):1065–1078, 2001.

[28] W. MacNee and K. Donaldson. Mechanism of lung injury caused by pm10 and ultrafine particles with special reference to copd. *Eur. Respir. J.*, 21(40 suppl):47s–51s, 2003.

[29] T. Martonen, Kristin Isaacs, and Dongming Hwang. Three-dimensional simulations of airways within human lungs. *Cell Biochem. Biophys.*, 42:223–249, 2005.

[30] T. Novakov, S. Menon, T. W. Kirchstetter, D. Koch, and J. E. Hansen. Aerosol organic carbon to black carbon ratios: Analysis of published data and implications for climate forcing. *J. Geophys. Res.*, 110(D21):D21205, 2005.

[31] Michael J. Oldham. Computational fluid dynamic predictions and experimental results for particle deposition in an airway model. *Aerosol Sci. Tech.*, 32(1):61–71, 2000.

[32] C. A. Pope and D. W. Dockery. Health effects of fine particulate air pollution: lines that connect. *J. Air Waste Ma.*, 56(6):709–742, 2006.

[33] S. S. Potgieter Vermaak and R. Van Grieken. Preliminary evaluation of micro-raman spectrometry for the characterization of individual aerosol particles. *Appl. Spectrosc.*, 60(1):39–47, 2006.

[34] C. U. Ro, J. Osan, I. Szaloki, J. de Hoog, A. Worobiec, and R. Van Grieken. A monte carlo program for quantitative electron-induced x-ray analysis of individual particles. *Anal. Chem.*, 75(4):851–859, 2003.

[35] C. U. Ro, J. Osan, I. Szaloki, K. Y. Oh, H. Kim, and R. Van Grieken. Determination of chemical species in individual aerosol particles using ultrathin window epma. *Environ. Sci. Technol.*, 34(14):3023–3030, 2000.

[36] C. U. Ro, J. Osan, and R. E. Van Grieken. Determination of low-z elements in individual environmental particles using windowless epma. *Anal. Chem.*, 71(8):1521–1528, 1999.

[37] J. H. Seinfeld. *Atmospheric chemistry and physics of air pollution*. John Wiley & Sons, New York, U.S.A., 1986.

[38] John H. Seinfeld. *Atmospheric chemistry and physics of air pollution*. Wiley, New York, 1986.

[39] Christopher M. Somers, Brian E. McCarry, Farideh Malek, and James S. Quinn. Reduction of particulate air pollution lowers the risk of heritable mutations in mice. *Science*, 304(5673):1008–1010, 2004.

[40] Z. Spolnik, K. Belikov, K. Van Meel, E. Adriaenssens, F. De Roeck, and R. Van Grieken. Optimization of measurement conditions of an energy dispersive x-ray fluorescence spectrometer with high-energy polarized beam excitation for analysis of aerosol filters. *Appl. Spectrosc.*, 59(12):1465–1469, 2005.

[41] O. S. Usmani, M. F. Biddiscombe, and P. J. Barnes. Regional lung deposition and bronchodilator response as a function of beta2-agonist particle size. *Am. J. Resp. Crit. Care*, 172(12):1497–504, 2005.

[42] Athanasios Valavanidis, Konstantinos Fiotakis, and Thomais Vlachogianni. Airborne particulate matter and human health: Toxicological assessment and importance of size and composition of particles for oxidative damage and carcinogenic mechanisms. *J. Environ. Sci. Heal. C*, 26(4):339–362, 2008.

[43] B. Vekemans, K. Janssens, L. Vincze, F. Adams, and P. Van Espen. Analysis of x-ray spectra by iterative least-squares (axil) - new developments. *X-Ray Spectrom.*, 23(6):278–285, 1994.

[44] Jordy Vercauteren, Christina Matheeussen, Eric Wauters, Edward Roekens, René van Grieken, Agnieszka Krata, Yaroslava Makarovska, Willy Maenhaut, Xuguang Chi, and Benny Geypens. Chemkar pm10: An extensive look at the local differences in chemical composition of pm10 in flanders, belgium. *Atmos. Environ.*, 45(1):108–116, 2011.

[45] Samir Vinchurkar, Lieve De Backer, Wim Vos, Cedric Van Holsbeke, Jan De Backer, and Wilfried De Backer. A case series on lung deposition analysis of inhaled medication using functional imaging based computational fluid dynamics in asthmatic patients: effect of upper airway morphology and comparison with in vivo data. *Inhal. Toxicol.*, 24(2):81–88, 2012.

[46] Yue Zhou and Yung-Sung Cheng. Particle deposition in a cast of human tracheobronchial airways. *Aerosol Sci. Tech.*, 39(6):492–500, 2005.

11

Functional respiratory imaging as a tool to personalize respiratory treatment in subjects with unilateral diaphragmatic paralysis

Respiratory care; in press

Cedric Van Holsbeke, Glenn Leemans, Wim Vos, Jan De Backer, Samir Vinchurkar, Michel Geldof, Pascal Verdonck, Paul Parizel, Paul Van Schil and Wilfried De Backer

11.1 Abstract

In two subjects with a unilateral diaphragmatic paralysis and complaints of dyspnea, a completely different treatment approach was chosen despite similar anatomical and physiological abnormalities. These decisions were supported by the results generated by Functional Respiratory Imaging (FRI). FRI was able to generate functional information with respect to lobar ventilation and local drug deposition. In one subject, it was found that some lobes were poorly ventilated and drug deposition simulation showed that some regions were undertreated. This subject underwent a diaphragm plication to restore the ventilation. In the other subject, it was found that all lobes were still ventilated. A conservative approach with regular follow-up was chosen to wait for spontaneous recovery of the diaphragmatic function. Both

subjects improved subjectively and objectively. These cases demonstrate how novel medical imaging techniques such as FRI can be used to personalize respiratory treatment in subjects with unilateral diaphragmatic paralysis.

11.2 Contributions of the author

The author of this thesis was the principal technical researcher in this study. The knowhow that was obtained in the previous chapters was used to bring the technique to the clinical practice. The main challenge here was to combine the different techniques from the previous chapters and to use them for clinical decision making. To make this possible, the author worked in close cooperation with pulmonologists, thoracic surgeons, radiologists and physiotherapists.

11.3 Introduction

In the last decade, personalised medicine has received special attention for its potential of individually tailored treatment, based on genetic or other information on an individual's health status. Following a statement of the European Society of Radiology, medical imaging plays a critical role in all aspects of personalised medicine [6].

New medical imaging techniques are capable of combining medical images with the quantification of certain biological processes in organs in order to detect diseases at the earliest possible time, to personalize diagnosis and to individualize medical or surgical treatment. Functional Respiratory Imaging (FRI) is a clinically validated computational technique that adds functional data to respiratory anatomical images [3]. Starting from low dose high resolution computed tomography (HRCT) scans, three-dimensional models of airways and lung models are extracted and computational fluid dynamics calculations are performed. A detailed description of the FRI methodology can be found in De Backer et al [3]. One of the design features of FRI is that local analyses can be performed while pulmonary function tests (PFT) are based on a black box approach where the information of the whole respiratory system is incorporated into single numbers. This results in an increased sensitivity of FRI as compared to PFT [4, 11].

In this report the clinical value of FRI to personalize and deliver the most optimal treatment is demonstrated in two subjects with an idiopathic unilateral paralysis of the diaphragm.

11.4 Case report

11.4.1 Study subject 1

A 57-year-old male subject (102 kg, 175 cm) with a known unilateral diaphragmatic paralysis since 1.5 years was referred to the hospital with recent complaints

of increasing dyspnea and orthopnea. Medical history revealed a condition of asthma. On clinical examination diminished vesicular breath sounds at the right lung base were present. The previous practitioner prescribed the subject four doses of salmeterol 25 µg - fluticason 250 µg (Seritide, GlaxoSmithKline) and fluticason 250 µg (Flixotide, GlaxoSmithKline) per day to control asthma exacerbation. PFT showed a highly reduced lung function (see Table 11.1) with both restrictive and obstructive elements. HRCT confirmed unilateral paralysis of the right diaphragm in combination with hypoventilation-induced atelectasis in the right middle (RML) and right lower lobe (RLL).

	Subject 1		Subject 2	
Parameter	Initial visit	Postoperative	Initial visit	After 6 months
VC [% predicted]	52	61	75	86
FEV1 [% predicted]	48	57	71	82
Tiffeneau index [%]	70	71	94	94
RV [% predicted]	113	96	69	95
FRC [% predicted]	77	77	67	94
TLC [% predicted]	71	71	71	87
Raw [kPas/L]	0.670	0.419	0.330	0.209
sRaw [kPas]	2.029	1.310	0.969	0.810

Table 11.1: Pulmonary function tests subject 1 & 2. VC: vital capacity; FEV1: forced expiratory volume in 1 second; Tiffeneau index: FEV1/VC; RV: residual volume; FRC: functional residual capacity, TLC: total lung capacity; Raw: airway resistance; sRaw: specific airway resistance

To investigate how much ventilation was still distributed to the RML and RLL, FRI was performed. The lobar expansion from functional residual capacity (FRC) to total lung capacity (TLC) was considered as a measure for the lobar ventilation as this represents the internal airflow lobar distribution (IALD) as defined in Equation 11.1.

$$IALD_{lobe}[\%] = 100\frac{V_{TLC_{lobe}} - V_{FRC_{lobe}}}{V_{TLC_{lungs}} - V_{FRC_{lungs}}} \tag{11.1}$$

In this equation, $IALD_{lobe}$ is the internal airflow lobar distribution to a specific lobe, $V_{TLC_{lobe}}$ is the volume of that lobe at TLC, $V_{FRC_{lobe}}$ is the volume of that lobe at FRC, $V_{TLC_{lungs}}$ is the total volume of all the lobes at TLC and $V_{FRC_{lungs}}$ is the total volume of all the lobes at FRC. Moreover, computational fluid dynamics calculations provided measures of local deposition of inhalation medication [3]. In this way, it was possible to assess to which zones the drug was delivered.

FRI analysis showed a poor ventilation of the RLL and no ventilation of the RML (Figure 11.1). In addition, very low levels of drug deposition were found in these lobes (Figure 11.2) when performing particle simulations using the compound

data of Tarsin and Stein et al [9, 10]. The poor drug deposition results found by FRI explain why a combination of several inhalation compounds were needed to treat the asthma, as these zones were probably pharmacological undertreated. Furthermore, a long-term non-ventilatory status of the RML could set the stage for repeated episodes of infection accounting for a vicious cycle of recurring bouts of inflammation that may result in a non-functional lobe [1].

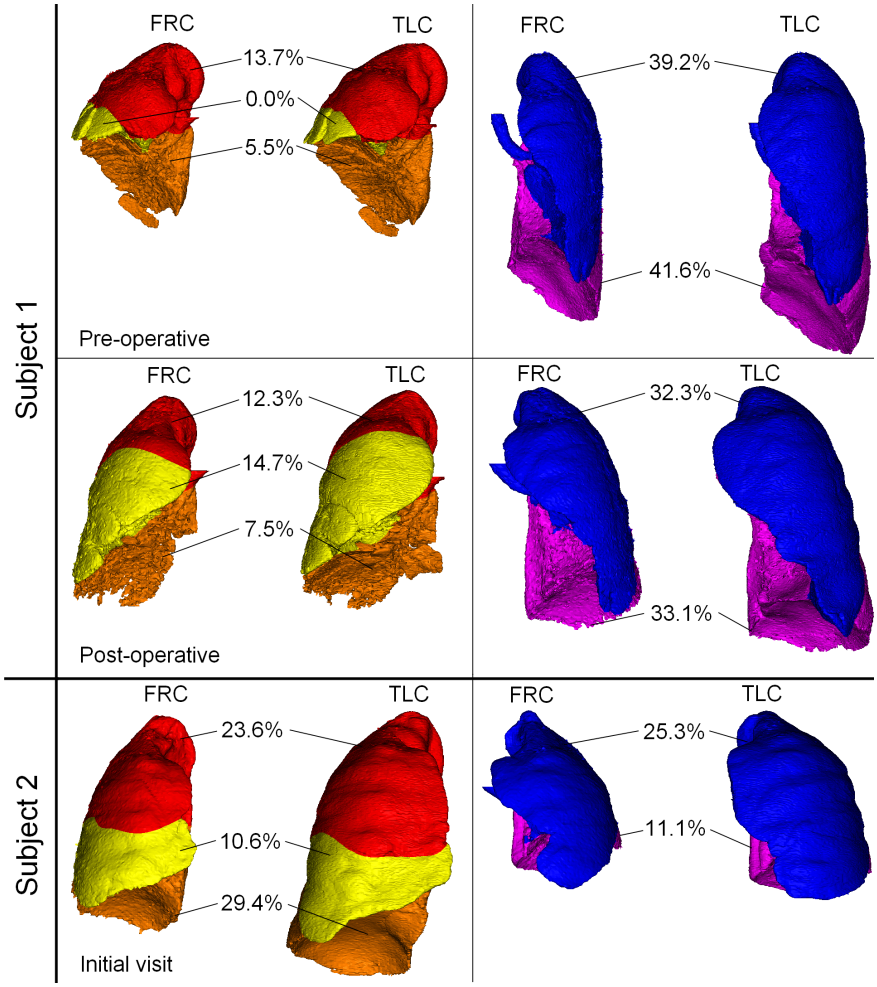

Figure 11.1: The internal airflow lobar distribution of the right upper lobe (red), right middle lobe (yellow), right lower lobe (orange), left upper lobe (blue) and left lower lobe (magenta) of subject 1 & 2. FRC: functional residual capacity, TLC: total lung capacity

In recent review Groth and Andrade [7] concluded that diaphragm plication seems a promising surgical technique to improve ventilation in subjects with di-

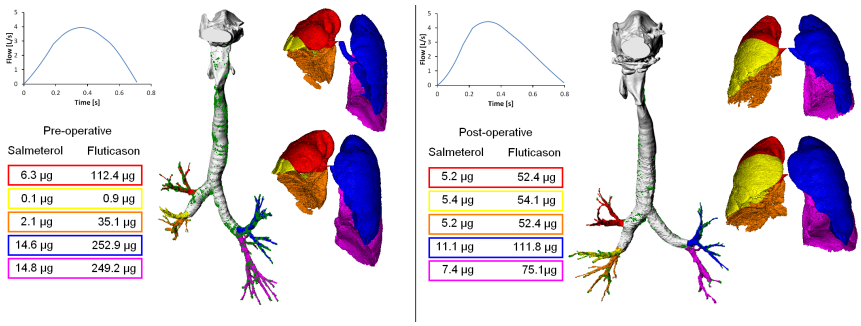

Figure 11.2: A visualisation of drug deposition simulations of subject 1. The green dots are the locations where the particles deposit. It is shown how much salmeterol and fluticason deposits in the right upper lobe (red), right middle lobe (yellow), right lower lobe (orange), left upper lobe (blue) and left lower lobe (magenta) in the pre- and post-operative situation.

aphragm paralysis. Therefore, a diaphragm plication was performed to place the paralyzed diaphragm in a position of maximum inspiration to relieve compression on the lung parenchyma and to allow its re-expansion.

Six weeks postoperatively, dyspnea was subjectively better. This was confirmed by an improvement in PFT (Table 11.1) and FRI, where the RML and RLL were much better ventilated than preoperatively (Figure 11.1). FRI also showed an improved drug deposition in these regions (Figure 11.2). It can be observed that the amount of active compound reaching RML and RLL increased from 38.2 µg (using salmeterol - fluticason) to 117.1 µg (using only salmeterol). This was clinically confirmed as the subject's asthma was kept stable using only four doses salmeterol 25 µg - fluticason 250 µg per day and as the obstructive components of the PFT improved despite the reduced medication.

11.4.2 Study subject 2

A 57-year-old male subject (92 kg, 181 cm) with a known unilateral diaphragmatic paralysis since eleven months presented at follow-up with recent complaints of increasing dyspnea and orthopnea. Clinical examination showed diminished vesicular breath sounds at the left lung base. The subject did not use any inhalation medication. PFT showed a significantly reduced lung function (Table 11.1) of restrictive nature. HRCT confirmed the unilateral paralysis of the left diaphragm and associated atelectasis of the left lower lobe was observed.

Subject 2 underwent the same FRI analysis as subject 1. This showed that all lobar regions were ventilated (Figure 11.1). Taken into account these FRI results, the physician considered a further conservative approach with regular follow-up since spontaneous recovery of the diaphragmatic function has been reported [5]. After 6 months, the breathlessness was completely resolved and total lung capacity was significantly improved (Table 11.1). No new FRI analysis was performed as

the physician found this unnecessary from a clinical point of view.

11.5 Discussion

Unilateral diaphragmatic paralysis is characterized by the loss of muscle contractility with progressive muscular atrophy that leads to an elevated position of the affected diaphragm. Treatment depends mainly on the cause of the paralysis, anatomical and physiological impairment (e.g. atelectasis) and the severity of symptoms. A conservative approach, with or without pharmacotherapy, may be considered since spontaneous recovery of the diaphragm can occur when clinical symptoms are minimal or tolerable and physiological impairment is absent [5]. In those subjects with anatomical and physiological impairment with persisting symptoms despite optimal therapy, surgical correction is indicated. Plication of the diaphragm in a series of 13 subjects with an unilateral impairment showed improvement in symptoms, lung function and quality of life that was maintained during 4–7 years [2]. Despite the promising results on both short-term and long-term outcomes, precise selection of suitable subjects is necessary [2, 8].

This case report demonstrates the potential of FRI as a new functional imaging technique in respiratory medicine to choose the right treatment plan in subjects with an idiopathic unilateral diaphragmatic paralysis. In both subjects, radiological examination revealed the appearance of atelectasis in the lower lobes. Atelectasis is commonly seen in combination with compression of the lung parenchyma, which affects compliance, therefore diminishing the regional ventilation of certain parts of the lung. Traditional clinical techniques are however not able to quantify these effects.

Although both subjects had the same anatomical and physiological abnormalities on HRCT, FRI showed a clear difference in regional ventilation. In our first case there was no lobar expansion of RML and a minor expansion of RLL. However all lobar regions in study subject two were ventilated. In other words, FRI was able to identify functional differences in these two subjects with apparently the same clinical and radiological findings.

Secondly, FRI was able to calculate local deposition of inhalation medication. In subject one, FRI showed that inhalation therapy was not reaching all zones. As a result, the proposed pharmacotherapy was probably inefficient in treating the obstructive symptoms.

Based on the clinical and radiological results, both subjects could be scheduled for surgery since they presented with anatomical and physiological abnormalities and still experienced symptoms despite optimal treatment. On the one hand, FRI analysis in subject two revealed that there was still regional ventilation in the left lower lobe even though atelectasis was present. Therefore a conservative approach with regular follow-up was chosen and spontaneous recovery of the diaphragm occurred after 6 months. On the other hand, taking into account the FRI results of subject one, we could conclude that surgery in subject one was the correct decision. Finally, this report demonstrates also that FRI was able to quantify the regional

functional redistribution of airflow to the right lung after the diaphragm plication, and this even without major clinical changes in classical lung function tests.

In conclusion, this case report demonstrates the clinical value of FRI as a tool to personalize medical treatment. In the future, this new functional imaging technique may result in a more precise diagnosis and treatment in a rapidly growing number of respiratory patients.

References

[1] Robert J. Albo and Orville F. Grimes. The middle lobe syndrome: A clinical study. *CHEST Journal*, 50(5):509–518, November 1966.

[2] Sezai Celik, Muharrem Celik, Bulent Aydemir, Cemalettin Tunckaya, Tamer Okay, and Ilgaz Dogusoy. Long-term results of diaphragmatic plication in adults with unilateral diaphragm paralysis. *Journal of Cardiothoracic Surgery*, 5(1):111, November 2010. PMID: 21078140.

[3] Jan W. De Backer, Wim G. Vos, Samir C. Vinchurkar, Rita Claes, Anton Drollmann, Denis Wulfrank, Paul M. Parizel, Paul Germonpré, and Wilfried De Backer. Validation of computational fluid dynamics in CT-based airway models with SPECT/CT. *Radiology*, 257(3):854–862, January 2010. PMID: 21084417.

[4] Lieve A. De Backer, Wim Vos, Jan De Backer, Cedric Van Holsbeke, Samir Vinchurkar, and Wilfried De Backer. The acute effect of budesonide/formoterol in COPD: a multi-slice computed tomography and lung function study. *European Respiratory Journal*, 40(2):298–305, January 2012. PMID: 22183484.

[5] Tarek A. Dernaika, Walid G. Younis, and Paul V. Carlile. Spontaneous recovery in idiopathic unilateral diaphragmatic paralysis. *Respiratory Care*, 53(3):351–354, January 2008. PMID: 18291052.

[6] European Society of Radiology. Medical imaging in personalised medicine: a white paper of the research committee of the european society of radiology (ESR). *Insights into Imaging*, 2(6):621–630, December 2011.

[7] Shawn S. Groth and Rafael S. Andrade. Diaphragm plication for eventration or paralysis: A review of the literature. *The Annals of Thoracic Surgery*, 89(6):S2146–S2150, June 2010.

[8] Simon M. Higgs, Afzal Hussain, Mark Jackson, Raymund J. Donnelly, and Richard G. Berrisford. Long term results of diaphragmatic plication for unilateral diaphragm paralysis. *European Journal of Cardio-Thoracic Surgery*, 21(2):294–297, January 2002.

[9] Stephen Stein. Estimating the number of droplets and drug particles emitted from MDIs. *AAPS PharmSciTech*, 9(1):112–115, March 2008.

[10] Walid Y. Tarsin, Stanley B. Pearson, Khaled H. Assi, and Henry Chrystyn. Emitted dose estimates from seretide® diskus® and symbicort® turbuhaler® following inhalation by severe asthmatics. *International Journal of Pharmaceutics*, 316(1–2):131–137, June 2006.

[11] Wim Vos, Jan De Backer, Gianluigi Poli, Annick De Volder, Liesbet Ghys, Cedric Van Holsbeke, Samir Vinchurkar, Lieve De Backer, and Wilfried De Backer. Novel functional imaging of changes in small airways of patients treated with extrafine Beclomethasone/Formoterol. *Respiration*, 2013.

12
Challenges in engineering

12.1 Introduction

While most work in biomedical engineering handles about the design of algorithms that are then tested in a few patient models, this works strives to create a technology that can be applied to large datasets. In this thesis, FRI is applied on 486 unique patient geometries and the results in the chapters are obtained by processing more than 75 TB of data. This is equivalent to 4500 piles of typed paper stacked as tall as the Eiffel Tower. The processing of this huge amount of patient specific data poses many challenges in engineering. Scalability in a clinical setting is mostly determined by repeatability and time-efficiency. In order get a technology that is of a high quality, consistent and fast, the amount of manual work has to be minimized by designing robust automation algorithms. In biomedical engineering, automation is very challenging as the anatomical variation within and in between subjects is very large, especially when dealing with diseased subjects. Besides automation, steps have to be taken to reduce the calculation time without losing precision by reducing the problem and only simulating the things that are needed to obtain the relevant results. In this chapter, some examples of challenges that were tackled to improve the scalability are described. In addition, some advanced algorithms that can be used in future studies but are not yet scalable enough are discussed.

12.2 Pre-processing and simulation

In the pre-processing and simulation phase, most work is put in the detection of user errors and optimization of the queuing and run time. Anatomical zones are

very difficult to map using computer algorithms due to the large inter and intra subject variation. That is why, in this thesis, anatomical zones are defined manually (although they are post-processed automatically). Every form of user interaction is however prone to errors and both automatic and manual control mechanisms are needed to ensure the quality. Several checks are built into the workflow that warn the user about unphysiological structures, unusual anatomical zones, missing data and mesh quality issues. Also, every step in the workflow is adapted for every different case. For example, when creating a volume mesh in SnappyHexMesh (OpenCFD Ltd., Bracknell, UK) like in chapters 4 and 6, one has to define a point inside the closed region that needs to be meshed. When the point is defined outside of the surface mesh of the airway, the bounding box surrounding the airway will be meshed which is not the desired behaviour when one wants to simulate the flow inside the airways. It is however not straightforward to automatically define a point inside the mesh as every airway object has different dimensions defined in different coordinate systems. An algorithm is designed to solve this problem.

In a first step, a point $\vec{P}$ is defined with the same coordinates as a point on the surface mesh and it is moved in a certain direction. To check if the chosen point $\vec{P}$ is inside the surface mesh, the solid angle of every planar face as seen from this origin point is calculated. The solid angle Ω subtended by a surface mesh S is defined as the surface area of a unit sphere covered by the surface's projection from a point $\vec{P}$ onto the sphere and is measured in steradians (sr). It can be calculated with equation 12.1.

$$\Omega = \iint_S \frac{\vec{r} \cdot \vec{N_{dS}}\, dS}{\|\vec{r}\|^3} \tag{12.1}$$

In equation 12.1, $\vec{r}$ is the vector position of a face with respect to point $\vec{P}$ with an (idealised) infinitesimal surface area dS and with $\vec{N_{dS}}$ representing the unit vector normal to dS. If the surface integral of all solid angles $d\Omega$ from all faces (Figure 12.1) to the point is equal to 4π sr, then the point is inside the closed surface S as the projections in all directions will cover the complete sphere. If it is equal to 0, then $\vec{P}$ is outside the mesh because the opposite normal vectors of the faces will cancel out the projections on the sphere. Depending on the result, the point can be moved in another direction and the algorithm can be repeated until a point is found inside the closed volume that needs to be meshed.

Several steps are taken to reduce the turnaround time of the simulations. A queuing mechanism is implemented to distribute the computational resources and software licenses in an optimal way. This system makes it possible to perform calculations while other tasks are waiting for input from a previous process. The insights gained from sensitivity analyses with respect to mesh, turbulence, time step, parallelization and particle convergence ensure fast and precise simulations.

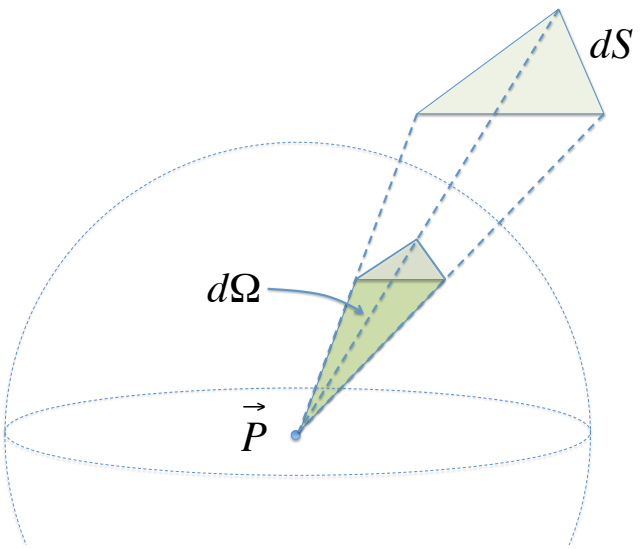

Figure 12.1: Solid angle

12.3 Post-processing

Quite some challenges in this thesis are in the phase of post-processing. The large amounts of data that are generated need to be converted in a form that allows human interpretation. It is important that the post-processing is completely automated and does not depend on graphical user interfaces, making it very cluster friendly. In sections 12.3.1 and 12.3.2, some morphometric measurement methods are described.

12.3.1 Surface area and volume

In most chapters, airway volumes are important outcome parameters. In chapter 7, the surface areas of the branches are needed to calculate the concentrations of inhaled antibiotics. To calculate the surface area and volume of a triangulated surface S, one has to assess these properties of every individual triangulated face.

The area of an individual triangle is simply calculated by multiplying the base by the height divided by two. This is done by extracting the points of that triangle and calculating the vectors from point 1 ($\vec{P_1}$) to point 2 ($\vec{P_2}$) and from point 1 to point 3 ($\vec{P_3}$) as $\vec{P_{1,2}}$ and $\vec{P_{1,3}}$. If these vectors would define a parallelogram, the area of that parallelogram would be defined by multiplying the base by the height which can also be written as equation 12.2.

$$\left\|\vec{P_{1,2}}\right\| \left\|\vec{P_{1,3}}\right\| sin\left(\theta\right) = \left\|\vec{P_{1,2}} \times \vec{P_{1,3}}\right\| \tag{12.2}$$

In equation 12.2, θ is defined as the angle between $\vec{P_{1,2}}$ and $\vec{P_{1,3}}$ (see Figure 12.2). The half of that area is then the area of the triangle dS.

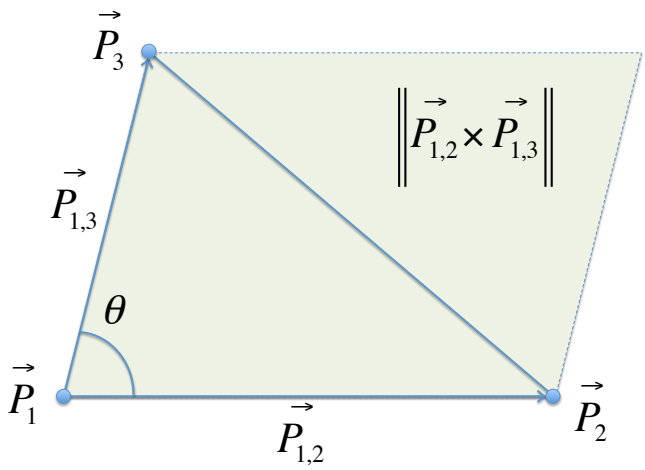

Figure 12.2: Area of a triangle

The volume under every triangle has to be defined for a certain direction. First, one has to construct the normal vector $\vec{N_{dS}}$ for the triangle from equation 12.3.

$$\vec{N_{dS}} = \vec{P_{1,2}} \times \vec{P_{1,3}} \tag{12.3}$$

If the direction is chosen to be the direction of the z axis, the z component of $\vec{N_{dS}}$, $\vec{P_1}$, $\vec{P_2}$ and $\vec{P_3}$ have to be extracted as N_{dSz}, P_{1z}, P_{2z} and P_{3z}. The z component of the triangle centroid is now calculated using equation 12.4.

$$C_z = \frac{P_{1z} + P_{2z} + P_{3z}}{3} \tag{12.4}$$

With this information, the projection of dS in the direction of the z axis on the $x - y$ plane can be calculated with equation 12.5.

$$dSz = dS \frac{N_{dSz}}{\left\| \vec{N_{dS}} \right\|} \tag{12.5}$$

Multiplying dSz with C_z is then the contribution dV of that triangle to the total volume as seen in Figure 12.3.

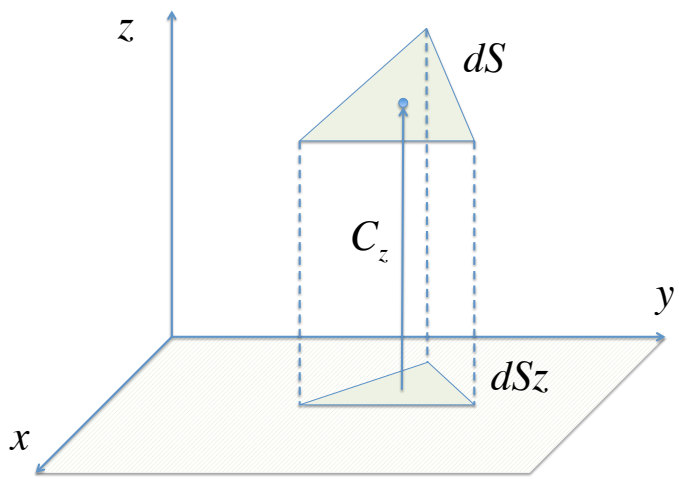

Figure 12.3: Volume under a triangle

Finally, the total surface area S_{surf} and volume V_{tot} are respectively given by the equations 12.6 and 12.7.

$$S_{surf} = \iint_S dS \tag{12.6}$$

$$V_{tot} = \iint_S dV \tag{12.7}$$

$$\tag{12.8}$$

12.3.2 Cross-sectional area

In chapters 3, 4 and 6 mean and minimal cross-sectional area's are used as outcome parameters. To get these values, cross-sectional areas have to be calculated at every

level in the airway. First, a centerline is generated using a proprietary algorithm. In a desired point $\vec{P}$ on that centerline, a plane with normal vector $\vec{N}$ is constructed perpendicular to this line. The plane is now given by equation 12.9.

$$N_x(x - P_x) + N_y(y - P_y) + N_z(z - P_z) = 0 \tag{12.9}$$

The triangulated mesh S consists out of points and the connections between them. For every point $\vec{P_1}$ in the triangulated mesh with a connection to a point $\vec{P_2}$, a vector $\vec{P_{1,2}}$ can be constructed. This vector can be parametrized by equation 12.10.

$$(x, y, z) = (P_{1x} + P_{2x}\lambda\,, P_{1y} + P_{2y}\lambda\,, P_{1z} + P_{2z}\lambda) \tag{12.10}$$

When substituting equation 12.10 into equation 12.9, and solving for the parameter λ, the coordinates of the intersection point can be constructed. These coplanar intersection points form a closed polyline (Figure 12.4). Assuming a Delaunay triangulated mesh, this closed polyline can be constructed by connecting the intersection points on the connections that have a mutual point in the mesh as visualised in Figure 12.5.

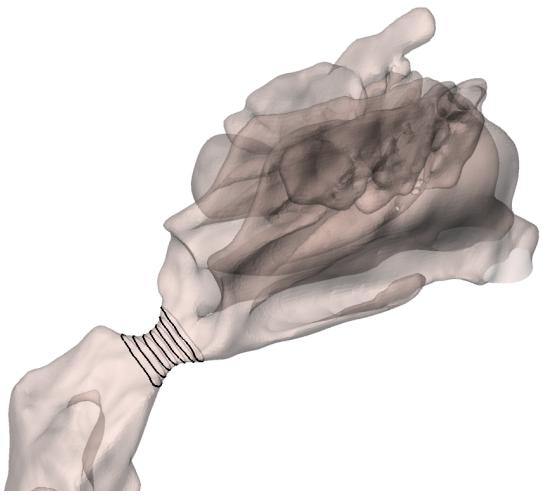

Figure 12.4: Closed polylines on an upper airway surface

If we now create a coordinate system (x', y') parallel to the plane, the cross-sectional area inside the polyline is defined by equation 12.11.

$$S_{cross} = \frac{1}{2}\sum_{i=0}^{n-1}(P_{ix'}P_{(i+1)y'} - P_{(i+1)x'}P_{iy'}) \tag{12.11}$$

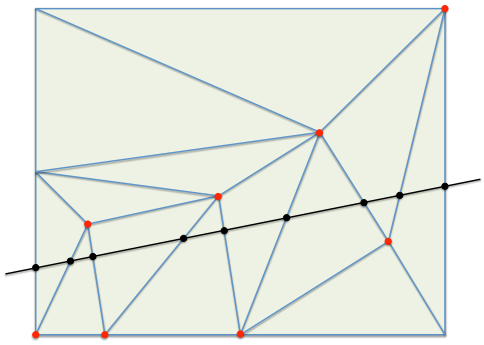

Figure 12.5: Connecting the intersection points: The coplanar intersection points are visualised by the black dots. The red dots represent the mutual points in the mesh

12.4 Advanced algorithms

Scalability is an important factor when creating a clinically relevant technology. However, this does not mean that additional research in more advanced algorithms is useless. As Moore's law is still valid nowadays, it is possible that technologies that require too much computer power to be incorporated in the FRI workflow are common practice in a few years. In section 12.4.1, a method to perform one-way coupled fluid structure interaction (FSI) simulations in airways is proposed. FSI adds some extra functional information by incorporating the movement of the airways during flow simulations. In section 12.4.2, it is described how the incorporation of realistic device boundary conditions can improve the simulations of nasal sprays.

12.4.1 One-way coupled fluid structure interaction

Modeling human breathing using FSI is a challenging topic due to the complex interactions between flow and structure. Flow is simulated in an airway model, the forces on the geometry are calculated and depending on the material properties a movement is induced. This movement has an effect on the flow, creating the need of a coupling between the flow and structure equations. Performing this in a subject-specific way is almost impossible as tissue properties and muscle interactions vary a lot inter- and intra-subject. However, one-way coupled FSI is possible when only the airway movement is known.

Imaging modalities such as high resolution computed tomography (HRCT) scans make it possible to make a detailed anatomical model of the subject's airways. A HRCT at functional residual capacity (FRC) and at total lung capacity (TLC)

gives the initial and the final geometry of a breathing cycle. Mapping the nodes of the TLC mesh to the nodes of the FRC mesh using a point set registration algorithm gives the transformation matrix of every node, resulting in a moving mesh that steers the flow. This mapping is performed using the nonrigid Coherent Point Drift Algorithm (CPD) [1]. In CPD, the alignment of two node sets is considered as a probability density estimation problem and the Gaussian mixture model centroids (representing the TLC node set) is fitted to the FRC node set by maximizing the likelihood.

In this example, lower airway models of a healthy subject are reconstructed until the first generation of segmental airways at both TLC and FRC. The FRC model is then mapped to the TLC model using CPD. The resulting transformation matrix is used to create models of 50 intermediate airway states. Correct meshes are generated for these models and computational fluid dynamics simulations are performed. Using a piecewise constant interpolation algorithm, the results of the previous mesh are transformed to the next mesh after which the calculations can continue. Examples are given in Figure 12.6.

The generation of these models is however not feasible with the original code. The main problem with the original CPD algorithm is that huge amounts of memory are required to perform the morphing. The largest memory hog is the construction of the affinity matrix, determining the similarity between points. For two points $\vec{P_1}$ and $\vec{P_2}$, the affinity is given by equation 12.12.

$$G_{1,2} = \exp\left(-\frac{1}{2\beta^2}\left\|\vec{P_1} - \vec{P_2}\right\|^2\right) \tag{12.12}$$

In equation 12.12, β defines the width (smoothness) of the Gaussian kernel. The memory usage of original algorithm that is used to construct the affinity matrix is heavily influenced by the dimension of the Euclidian space. When constructing this matrix with 64 bit double precision, the memory usage is defined by equation 12.13.

$$\text{Memory} = \left(2 \times \text{dimension} \times n_p^2 + 2 \times \text{dimension} \times n_p\right) \times 64 \text{ bits} \tag{12.13}$$

In equation 12.13, n_p is the amount of points in the mesh. The amount of memory needed to perform morphing on a coarse three-dimensional mesh consisting of 50000 points is 112 GB, making it very difficult to handle. A new algorithm is constructed for which the memory usage is less influenced by the Euclidian dimension and that is able to reduce the memory usage for the purposes in this thesis. When constructing the affinity matrix with 64 bit double precision using this algorithm, the memory usage is defined by equation 12.14.

$$\text{Memory} = \left(n_p^2 + 3 \times \text{dimension} \times n_p\right) \times 64 \text{ bits} \tag{12.14}$$

The amount of memory needed to perform morphing on a coarse three-dimensional mesh consisting of 50000 points is 19 GB, which is already more

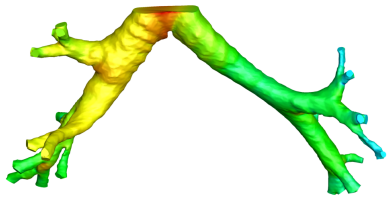

(a) FRC model

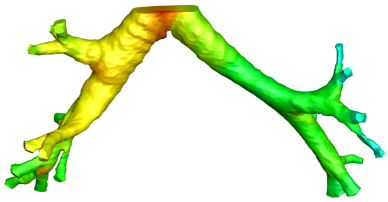

(b) 20% between FRC and TLC

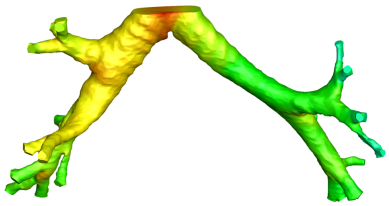

(c) 40% between FRC and TLC

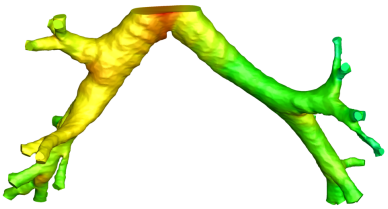

(d) 60% between FRC and TLC

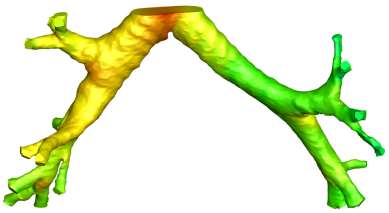

(e) 80% between FRC and TLC

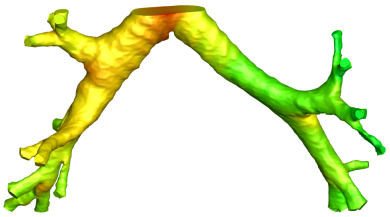

(f) TLC model

Figure 12.6: One-way coupled FSI simulation

in the range of a typical computer cluster node. The memory usage in function of the number of points in the mesh of both algorithms is given in figure 12.7. When one a has a cluster node with 23 GB of free memory, it is now possible to deal with 55556 instead of 22682 points.

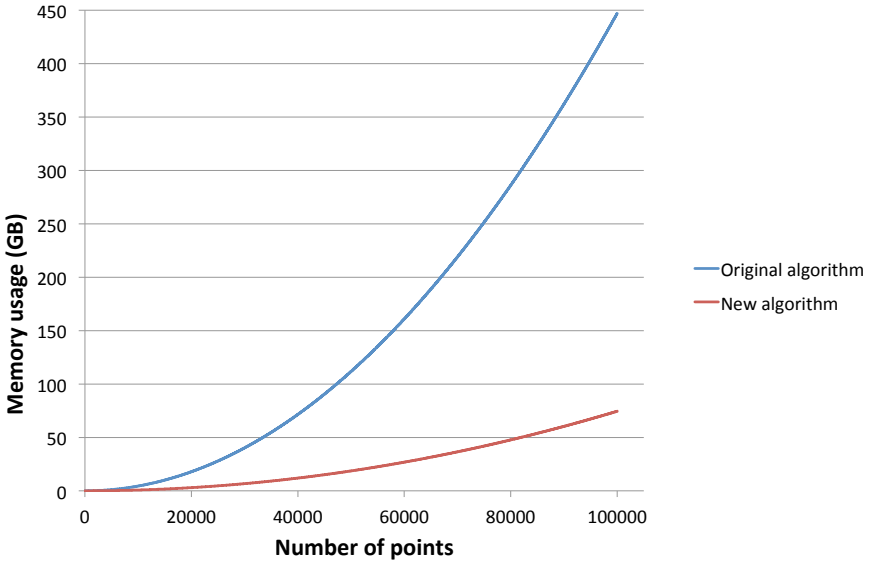

Figure 12.7: Memory usage when constructing the affinity matrix

At this moment, 24 hours of computer time and a few hours of manual work are needed to get the models. It is also not known if these simulations yield in clinically relevant results. One of the possible applications is in the field of phenotyping. When assessing the lobar resistances as a function of airway volume, the possibility exists that this can be related to a physiological phenomenon. When looking at Figure 12.8, it can be observed that the resistance towards the left lower lobe follows a different trend than the other lobes when inhaling. This heterogenous pattern can possibly be an indication for an underlying condition.

12.4.2 Realistic device boundary conditions

Metered-dose inhalers deliver a specific amount of medication to the patient by injecting a suspension of liquefied gas propellant and active compound into the oral or nasal cavity. When assessing aerosol deposition in the lungs after administration of a product in the oral cavity, the effect of the liquid propellant can be neglected since the aerosol cloud almost instantly takes the much higher momentum of the inhalation flow due to its small response time. However, when simulating breath hold conditions or nasal sprays with negligible inhalation flow, the momentum that

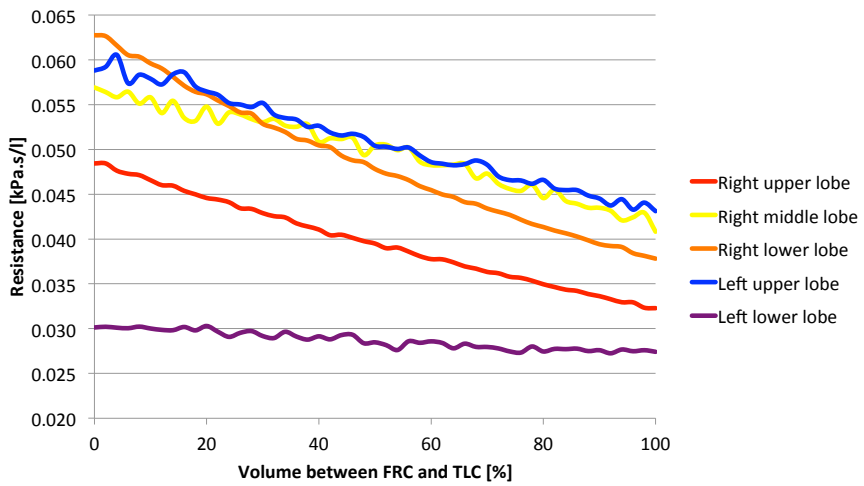

Figure 12.8: Lobar resistance as a function of volume

is transferred from the propellant to the particles will have a large influence on the deposition.

This situation is quite complex as different materials and the interactions between them need to be simulated. The results of a test case be seen in figures 12.9(a) and 12.9(b). In this case, a suspension of a liquid ethanol dilution and inert particles with a diameter of 4 µm are injected from a small orifice. The boundary condition at the left boundary is a zero total pressure, the boundary condition at the right boundary is a transient under pressure profile. Figure 12.9(a) shows the situation during the injection and figure 12.9(b) shows what happens 5 ms after the injection. The black dots represent the positions of the particles, the colour scale represents the concentration of ethanol where red is a high concentration and blue is a low concentration. It can be seen that during the injection, the particles are driven by the cloud of diluted alcohol and that dispersion occurs afterwards.

In order to use this approach in real cases, the properties of both propellant and compound exiting the device need to be assessed accurately. In the future, this system will be used in a study after it is investigated what level of complexity (evaporation, diffusion sources, ...) is needed to obtain accurate results.

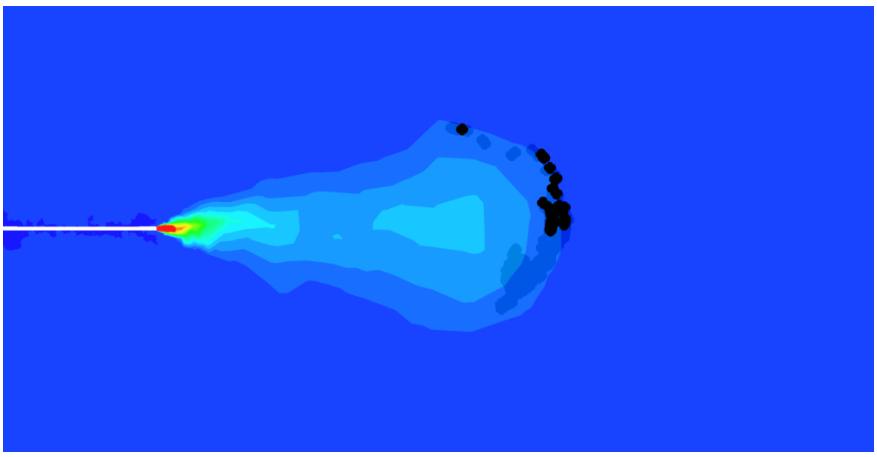

(a) During injection

(b) 5 ms after injection

Figure 12.9: Particles in an ethanol dilution

References

[1] A. Myronenko and Xubo Song. Point set registration: Coherent point drift. *IEEE Transactions on Pattern Analysis and Machine Intelligence*, 32(12):2262–2275, 2010.

13
Conclusion

This conclusion starts with an overview of the results that are obtained in this thesis.

It is shown that FRI is able to quantify the effects on upper airway morphology and functionality of mandibular repositioning in adult OSA patients. Furthermore, the treatment effects can be predicted from baseline measurements, making it possible to split the population in risk groups. This enables the physician to provide more effective patient treatment, which is especially useful in techniques with a low success rate. The results are in line with clinical literature but the biomechanical observations cannot be mapped directly to clinical outcome due to the lack of sleep data for this population. This issue is addressed in pediatric OSA patients where it is found that baseline measured FRI parameters are better correlates for OSA severity than clinical scores of upper airway patency. Preliminary data also show that there are differences in upper airway morphology in subjects who do not benefit from a treatment.

When looking at the behavior of inhalation medication, FRI is able to capture the importance of patient specific features, such as upper airway morphology, in having a significant impact on the effective lung dose and therefore the treatment efficacy. Furthermore, FRI analyses show that there is a large inter- and intra-subject variation in upper airway morphology and functionality. This states the importance of using as much subject specific information as possible when simulating particle deposition. FRI is also shown to be useful in optimizing treatment on a patient specific base. A high heterogeneity in concentration levels of inhaled antibiotics is observed in cystic fibrosis patients and this heterogeneity is connected to the disease severity. While some patients receive high concentrations of inhaled antibiotics in the whole lung, other patients receive low concentration in some, mostly the more diseased, lobes.

When looking at the effects of inhalation medication in small airway diseases, FRI is very sensitive in picking up changes in local airway morphology and functionality. In both asthma and COPD patients, FRI parameters are three to six-fold more sensitive in picking up drug-induced changes as compared to PFT. Even when compared to other state-of-the-art imaging techniques, FRI seems to be a more sensitive marker. In a very recent trial that is very similar to the study in chapter 8, oxygen-enhanced MRI is used to assess the acute effects of formoterol in COPD patients. There it is found that the effect size measured with the imaging technique is only around 30% higher than PFT [1]. This increased sensitivity can lead to smaller numbers of patients in clinical trials without losing power. Besides the increased sensitivity of FRI, an increased specificity is observed compared to the traditional techniques. Correlations were found between changes in FRI parameters and changes in patient feeling. This gives an indication that FRI has the possibility to measure changes in quality of life after treatment.

This increased sensitivity also opens the possibility for FRI in pilot studies and clinical practice. It is shown that FRI can help to understand the behaviour of airborne particles in the lungs. This study is the first study combining detailed physical-chemical analyses of particulate pollution with patient specific particle simulations. The main finding is that location within the range of an urban environment is less important in comparison with pathology and synoptic meteorological conditions when measuring lung doses of airborne particles. FRI can also help physicians in selecting the right treatment for the right person. In two patients with an idiopathic unilateral diaphragmatic paralysis, a different treatment approach was chosen despite both having similar anatomical and physiological abnormalities on radiological examination. FRI showed impairments in ventilation and drug delivery in one patient, while this was not the case in the other patient, resulting in a surgical and conservative approach respectively. These cases demonstrate the potential of FRI in personalizing respiratory treatment.

The question that most people will have is: Is FRI a better alternative to traditional techniques like PFT and AHI? The short answer is “no”. The long answer is “we don’t know yet”. While traditional techniques have their flaws, they have been validated in numerous long-term clinical trails and have been linked to comorbidities and mortality. Their inherent black box approach does not have to be a disadvantage as a lot of the subject’s physiology is taken into account, reducing the risk of defining a wrong region of interest. FRI is still in its early development phase and is at this moment no competitor for PFT and sleep scores. However, this thesis shows that FRI can have an added value in several domains.

The strengths of FRI are the regional information, quantified outcome, minimal invasiveness and multi-facet approach, resulting in a high sensitivity and specificity. These properties make it possible to use FRI in early clinical trials as a design tool rather than a mere analysis tool. A myriad of information about the efficiency of the intervention becomes available through FRI, allowing tailoring of the drug formulation or medical device to optimize the treatment. As a lot of clinical trials lead to inconclusive results on the general study population, FRI can be used to distinguish responders from non-responders. As fewer patients in fewer centres are

needed, the overall costs of clinical trials can be reduced. FRI is very well suited to reach go/no go decisions early in the development process of a device or drug. Using FRI in small-scale clinical phase IIa trials can significantly de-risk the very expensive phase III trials. Validated traditional tests can here be combined with FRI, where the latter is used as a tool to assess the mode of action. This means that the quantitative results will be reported, but no clinical conclusions will be connected to these results. In Figure 13.1, an example of such a workflow is given when dealing with inhalation medication.

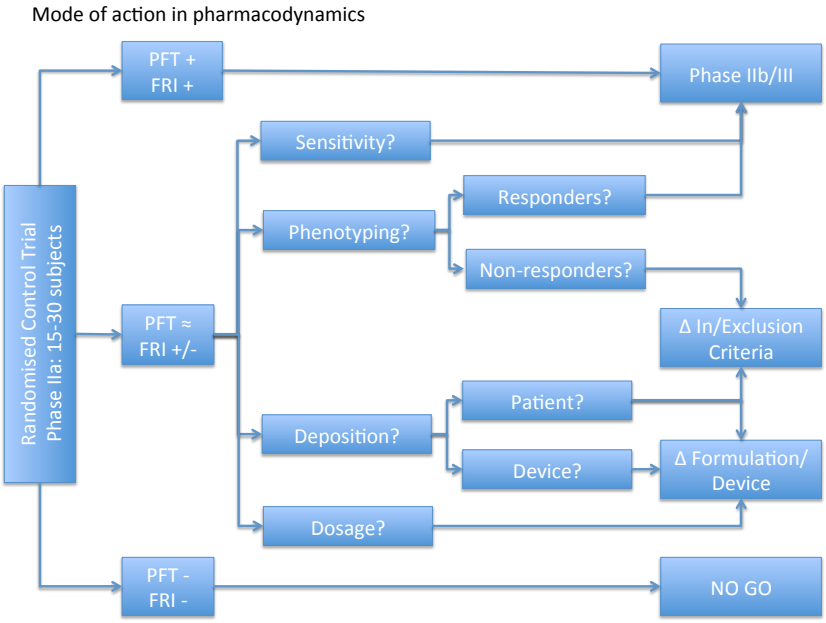

Figure 13.1: Workflow example for a phase IIa study in pharmacological development

Suppose that a study is performed to assess the efficacy of an inhalation medication in 15 – 30 subjects. There are now different possibilities:

- Both FRI and PFT give positive signals: This means that the compound is probably effective and that further phase IIb and phase III trials can be performed.

- Both FRI and PFT give negative signals: This means that the compound is probably not effective and that further phase IIb and phase III trials are not useful.

- FRI gives a signal (either positive or negative) and PFT is inconclusive:

- Sensitivity: If FRI gives a signal (preferably positive) and no specials reasons are found for the inconclusiveness of PFT, then probably the number of included patients was to low. Phase IIb and phase III trails with more patients can be started.
- Phenotyping: FRI gives a signal in general, but some opposite signals are seen for some patients. FRI can now be used to distinguish responders from non-responders. If the general FRI signal is positive, this probably means that the chosen population is valid and further phase IIb and phase III studies can be performed to investigate the details. If the general FRI signal is negative, this probably means that the chosen population is not the correct one for this medication. The in- and exclusion criteria can be changed and the trial can be performed again.
- Deposition: It is found that the drug does not deposit in the targeted regions. If it is related to the phenotype of the patient, the in- and exclusion criteria can be changed and the trial can be performed again. If it is related to the device, the formulation or the device can be changed and the trial can be performed again.
- Dosage: The drug deposits in the targeted regions but the required dosage or concentration is not reached. The formulation or the device can be changed and the trial can be performed again.

FRI is also an interesting technology for niche markets with high unmet needs. People who undergo major surgery, such as lung transplantation, can profit from FRI as this technology allows very local follow-up analyses, possibly detecting signs of rejection in an early stage. Also people suffering from orphan diseases such as radiation pneumonitis, pulmonary alveolar proteinosis, cystic fibrosis, idiopathic pulmonary fibrosis and alpha-1 antitrypsin deficiency can benefit from the patient specific nature of FRI, as most of these diseases are difficult to standardize. Another problem with these rare diseases is that some of them are so rare that it is almost impossible to perform large-scale studies. Chances are real that traditional techniques are not sensitive enough to detect possible effects in these studies. This opens the possibility for FRI to become a surrogate endpoint for orphan diseases. This means that clinical conclusions can be connected to the FRI results. Another challenge that can be tackled using FRI is the question of bioequivalence. When a manufacturer wants to introduce a generic drug to the market, the behavior of that drug needs to be similar to the behavior of the original product. FRI can be used to assess the effective lung deposition of both compounds. Furthermore, the in vivo effect can be assessed in relatively small and short clinical trials using a crossover design. In this way, the characteristics of the device and formulation can be linked to therapeutic effect and it can be determined whether the two products induce similar effects. Personalized medicine is another domain where FRI can have an added value. As novel therapies are becoming more and more expensive while the budgets in healthcare are decreasing, regulatory authorities will demand superiority over the standard of care to justify the additional expenditure. Apart

from very novel breakthroughs, superiority can mostly only be demonstrated by selecting the appropriate patients. FRI allows these patient specific insights, making it possible to deliver the right treatment to the right patient.

FRI can also help to understand the health effects of air pollution in a multidisciplinary approach. Real air pollution measurements can be performed at different locations and under different conditions. The physical-chemical characterization of these data can be used as input data for FRI, which on his turn can generate input data for health-effect modelling algorithms. Combining this approach with clinical trials can result in a better understanding of the mechanics and clinical effects of air pollution.

FRI is still in its early development phase and further research is needed in order to expand its possibilities. A first research line that comes to mind is to search for correlations between drug deposition and effect size, making a link between the second and the third part of this thesis. A lot of attention will have to be given to correct characterization of the compound, the device and inhalation manoeuvre in order to perform correct patient specific simulations. In a later stage, these insights can be used to construct dose-response curves for a specific medication.

It would also be interesting to search for threshold values for changes in FRI parameters that indicate clinical significance. Is a 1% decrease in airway resistance clinically significant? Or is 80% needed? Or does it depend on the patient? An approach that could be taken is to perform FRI analyses on the same patients in two extreme states of their disease. For example, patients with extreme airway deformation during exacerbation and with more normalized airways after recovery could be analyzed. Or severe sleep apnea patients before and after successful treatment could be compared. The broad spectrum of both FRI parameters and patient reported outcomes could make it possible to determine cut-off values for clinical relevance.

A last line of research for the near future is the power of FRI in phenotyping patients. Traditional clinical tests are used to classify patients by disease severity. Due to the insensitive nature of these techniques, the possibility exists that patients are wrongly categorized, perhaps resulting in patients not receiving the optimal treatment. Ideally, a phenotyping study would start with a set of healthy volunteers for whom FRI parameters such as airway shape, resistance, compliance, vasculature, emphysema and inflation are locally measured at different lung levels. In this way standard values and their variations over a breathing cycle are known. Afterward, sets of patients that are classified with the traditional method can be analyzed in a similar manner and can be compared to the healthy population. This makes it possible to detect overlaps, gaps and shifts in the normal classification methods.

These insights will undoubtedly lead to new research questions, making FRI a very exciting technique with endless possibilities.

Despite the fact that quite some challenges in engineering are tackled (Chapter 12), the readers of this thesis will notice that the research approach is more from a clinical than from an engineering point of view. While a lot of research in biomedical engineering is targeted towards the creation of very complicated mathematical models in idealised geometries or small cross-sectional patient datasets, the author

of this thesis strives to design simple, clinically relevant and scalable models that are easy to understand and that can be used in a normal clinical setting in large longitudinal studies. Although both top-down and bottom-up approaches have their advantages and disadvantages, one should not forget that biomedical engineering is not only about the algorithm but about the patient. If a model is able to help a patient, then it is a useful model. If adding some complexity to the model leads to a better quality of life for the patient, then it is a better model. This thesis shows that engineering and medicine do not have to clash. The author believes that multidisciplinary teams consisting of doctors, engineers and (life) scientists are the future of medicine and hopes that this thesis is a good step forward in that direction.

References

[1] A. R Morgan, G. J. Parker, C. Roberts, G. A Buonaccorsi, N. Maguire, P. L Hubbard, D. Singh, J. Vestbo, L. Bjermer, J. Jögi, L. H Nordenmark, Z. Taib, J. Sarv, P. Bruijnzeel, and J. C Waterton. LATE-BREAKING ABSTRACT: evaluating dynamic oxygen-enhanced MRI biomarkers of lung function: Sensitivity to conventional COPD treatment. Barcelona, September 2013.

Appendices

A
Computational fluid dynamics

A.1 The Generic Scalar Transport Equation

The most fundamental law of physics is the law of conservation. A differential equation expresses such a conservation principle where each term in this equation represents a physical mechanism through which the conserved quantity evolves. There are three mechanisms that the terms in a differential equation usually describe [11, 16]:

- The accumulation or transient process accounts for the temporal rate of change of a given quantity within an infinitesimal volume.
- The convection process accounts for the transport of the quantity due to any existing velocity field. Convection occurs at the macro level and it is the source of nonlinearity in the Navier-Stokes equations.
- The diffusion process describes the transport of the quantity due to the presence of any gradients of that quantity. This happens at the molecular level. By itself, diffusion is a linear process provided the diffusion coefficient is a constant.

In certain cases, there are terms that cannot be cast into the transient, convective, and diffusive terms. These are then lumped into what is a called a source term. For example, the gravitational effects, the pressure gradient and any other body forces are part of the source term in the Navier-Stokes equations.

The universality of the three mechanisms discussed above makes it possible to construct a general differential equation that describes the conservation principle

of a quantity. Note that the placement of the terms comes from the fundamental principles of deriving the conservation equations, i.e. transient and convective terms should balance diffusive and source terms. For generality, we shall pick a dummy physical quantity and call it ϕ. The generic scalar transport equation is now given as equation A.1 [11, 16].

$$\underbrace{\frac{\partial \rho\phi}{\partial t}}_{\text{Transient term}} + \underbrace{\nabla\cdot(\rho U\phi)}_{\text{Convection term}} = \underbrace{\nabla\cdot(\Gamma\nabla\phi)}_{\text{Diffusion term}} + \underbrace{S_\phi}_{\text{Source term}} \tag{A.1}$$

In this equation, ρ is the density, t the time, U the velocity vector and Γ the diffusion coefficient. The del operator is given by ∇. The recognition that all the relevant differential equations for heat and mass transfer, fluid flow, turbulence, and related phenomena can be thought of as particular cases of the generic scalar transport equation is an important time-saving step. As a consequence, we need to concern ourselves with the numerical solution of only equation A.1. Even in the construction of a computer program, it is sufficient to write a general sequence of instructions for solving equation A.1, which can be repeatedly used for different meanings of ϕ along with appropriate expressions for Γ, S and with appropriate initial and boundary conditions [11].

A.2 The Navier-Stokes Equations

The Navier-Stokes equations are the basic governing equations for a viscous, heat conducting fluid and are based on the three fundamental conservation laws [13]:

- The mass of a fluid is conserved (continuity): section A.2.1
- The linear momentum is conserved: the rate of change of momentum equals the sum of the forces on a fluid particle (Newton's second law): section A.2.2
- The energy is conserved: the rate of change of energy is equal to the sum of the rate of heat addition to and the rate of work done on a fluid particle (first law of thermodynamics): section A.2.3

The resulting continuity equation, momentum equation and energy equation are mostly referred as the Navier-Stokes equations. These equations are specialized forms of equation A.1.

A.2.1 Continuity equation

The procedure for casting any particular differential equation into the generic scalar transport equation is to manipulate it until, for the chosen dependent variable, the unsteady term and the convection and diffusion terms conform to the standard form [11]. To obtain the continuity equation (for compressible flows) set $\phi = 1$.

Since diffusion is not present and in the absence of sources set the diffusion coefficient and the source term to zero to obtain equation A.2 [1, 5, 13]. This equation mathematically expresses that the sum of the time rate of change of mass inside the control volume and the net mass flow over the boundaries of the control volume equals zero [2].

$$\frac{\partial \rho}{\partial t} + \nabla.\left(\rho U\right) = 0 \tag{A.2}$$

The right hand side can be replaced by a term source S_C. This is any mass added to the continuous phase and any user-defined sources [7].

A.2.2 Momentum equation

The momentum equation is completely based on Newton's second law, given by equation A.3.

$$\sum_{i=0}^{n} F = m.a \tag{A.3}$$

The momentum equation can be written as equation A.4. The mass times the acceleration is expressed on the left-hand side of the equation while the right-hand side describes all the possible surface and body forces that can act on an object [2].

$$\frac{\partial\left(\rho U\right)}{\partial t} + \nabla.\left(\rho U U\right) \quad = -\nabla p + \nabla.\left(\tau\right) + S_M \tag{A.4}$$

As the most common body force is the gravitational force, the source term (S_M) can be replaced by the sum of the gravitational body force (ρg) and external body forces (F). F also contains other model-dependent source terms such as porous-media and user-defined sources [7].

To define the viscous stress tensor τ in a more understandable way, we will transform equation A.4 in its Cartesian form, given as equation A.5 [1, 13].

$$\begin{aligned}
\frac{\partial\left(\rho u_x\right)}{\partial t} + \nabla.\left(\rho u_x U\right) &= \tfrac{\partial(-p+\tau_{xx})}{\partial x} + \tfrac{\partial \tau_{yx}}{\partial y} + \tfrac{\partial \tau_{zx}}{\partial z} + S_{Mx} \\
\frac{\partial\left(\rho u_y\right)}{\partial t} + \nabla.\left(\rho u_y U\right) &= \tfrac{\partial \tau_{xy}}{\partial x} + \tfrac{\partial(-p+\tau_{yy})}{\partial y} + \tfrac{\partial \tau_{zy}}{\partial z} + S_{My} \\
\frac{\partial\left(\rho u_z\right)}{\partial t} + \nabla.\left(\rho u_z U\right) &= \tfrac{\partial \tau_{xz}}{\partial x} + \tfrac{\partial \tau_{yz}}{\partial y} + \tfrac{\partial(-p+\tau_{zz})}{\partial z} + S_{Mz}
\end{aligned} \tag{A.5}$$

For a Newtonian fluid, assuming Stokes Law for mono-atomic gases, the components of the viscous stress tensors τ_{ij} are now given by equation A.6 [12]. In these equations, μ is the dynamic viscosity.

$$
\begin{aligned}
\tau_{xx} &= \tfrac{2}{3}\mu\left(2\tfrac{\partial u_x}{\partial x} - \tfrac{\partial u_y}{\partial y} - \tfrac{\partial u_z}{\partial z}\right) \\
\tau_{yy} &= \tfrac{2}{3}\mu\left(2\tfrac{\partial u_y}{\partial y} - \tfrac{\partial u_x}{\partial x} - \tfrac{\partial u_z}{\partial z}\right) \\
\tau_{zz} &= \tfrac{2}{3}\mu\left(2\tfrac{\partial u_z}{\partial z} - \tfrac{\partial u_x}{\partial x} - \tfrac{\partial u_y}{\partial y}\right) \\
\tau_{xy} &= \tau_{yx} = \mu\left(\tfrac{\partial u_x}{\partial y} + \tfrac{\partial u_y}{\partial x}\right) \\
\tau_{xz} &= \tau_{zx} = \mu\left(\tfrac{\partial u_z}{\partial x} + \tfrac{\partial u_x}{\partial z}\right) \\
\tau_{yz} &= \tau_{zy} = \mu\left(\tfrac{\partial u_y}{\partial z} + \tfrac{\partial u_z}{\partial y}\right)
\end{aligned}
\tag{A.6}
$$

A.2.3 Energy equation

The energy equation is the mathematical expression that energy cannot be created nor destroyed but it can change form. The left-hand side of this equation expresses the rate of change of energy inside a fluid element while the right-hand side is the sum of the net flux of heat into the element and the rate of work done on the element due to surface and body forces [2]. The energy equation is given as equation A.7 [13].

$$
\begin{aligned}
\frac{\partial(\rho E)}{\partial t} + \nabla.(\rho E U) = \; & -\nabla.(pU) + \Big[\tfrac{\partial(u_x\tau_{xx})}{\partial x} + \tfrac{\partial(u_x\tau_{xy})}{\partial y} \\
& + \tfrac{\partial(u_x\tau_{xz})}{\partial z} + \tfrac{\partial(u_y\tau_{xy})}{\partial x} + \tfrac{\partial(u_y\tau_{yy})}{\partial y} \\
& + \tfrac{\partial(u_y\tau_{zy})}{\partial z} + \tfrac{\partial(u_z\tau_{xz})}{\partial x} + \tfrac{\partial(u_z\tau_{yz})}{\partial y} \\
& + \tfrac{\partial(u_z\tau_{zz})}{\partial z}\Big] + \nabla.(k_H\nabla T) + S_E
\end{aligned}
\tag{A.7}
$$

In this equation, E is the total energy, T the temperature and k_H the heat conduction coefficient. The source term S_E includes the heat of chemical reaction and any other volumetric heat sources that have been defined [7].

A.3 Discrete phase

When one wants to assess the behaviour of a discrete element in a flow (for example the modelling of particle transport), not only the flow equations from section A.2, but also the additional governing transport equation A.8 describing the discrete phase trajectory need to be solved [7].

$$
\frac{dv_i}{dt} = \underbrace{F_D}_{\text{Drag force}}(u_i - v_i) + \underbrace{g_i(1-\alpha)}_{\text{Gravity force}} + \underbrace{F_x}_{\text{Additional acceleration forces}}
\tag{A.8}
$$

In this equation, v_i and u_i are the components of the particle and local fluid velocity, respectively, g_i denotes gravity and α is the density ratio ρ/ρ_p where ρ_p is the density of the discrete phase. The drag force F_D is a function of the relative velocity between the continuous and discrete phase and is given by f/τ_p where f is the drag factor and τ_p is the response time for the particles. The additional acceleration forces F_x can include forces generated by pressure gradients, thermophoretics, rotating reference frames, brownian motions, lift and user defined sources.

Additional equations with respect to heat and mass transfer can be solved in addition to equation A.8 to model heating, evaporation and coagulation, but these are out of the scope of this thesis.

Equation A.8 can be used to calculate the discrete phase patterns based on the results of the equations in section A.2. One can decide that the solution is then complete (1-way coupling), or that feedback to the continuous phase is needed (2-way coupling). In the latter approach, the continuous phase is impacted by the discrete phase (and vice versa), yielding in additional source terms in the Navier-Stokes equations. Calculations of both phases need to be alternated until a converged coupled solution is achieved.

A.4 Computational fluid dynamics

Computational fluid dynamics is a computer simulation technique that allows to determine the behavior of a flow [6]. In this method, flow is described by the Navier-Stokes equations and is numerically solved on a computational grid (the mesh). This method makes it possible for the system of mathematical equations to be solved iteratively. The result is that flow features such as speed, pressure and density are known everywhere in the model.

The numerical technique that is mostly used in CFD nowadays, is the finite volume method (FVM), but several other methods exist. The difference between the methods are associated with the way in which the flow variables are approximated and with the discretization processes. In outline, the numerical methods that form the basis of the solver perform the following steps [13]:

- An approximation of the unknown flow variables by means of simple functions
- A discretization by substitution of the approximations into the governing flow equations and subsequent mathematical manipulations
- A solution of the algebraic equations

The key step of the finite volume method is the integration of the transport equations over a three-dimensional control volume. To perform a CFD calculation in a computational domain, the domain is divided into a number of smaller, non-overlapping sub-domains: a grid (or mesh) of control volumes (or cells). After

setting the appropriate boundary conditions and fluid properties, a FVM calculation can be run. In this numerical technique, the steps given above are implemented in the following manner [13]:

- A formal integration of the governing equations of fluid flow, described in section A.2, over all the finite control volumes of the computational domain. The resulting statements express the exact conservation of relevant properties for each finite size cell. This clear relationship between the numerical algorithm and the underlying physical conservation principle forms one of the main attractions of the finite volume method

- A discretization process involving the substitution of a variety of approximations for the terms in the integrated equation that are representing flow processes such as convection, diffusion and sources. This converts the integral equations into a system of algebraic equations

- A solution of the algebraic equations by an iterative method

When analyzing the FVM technique, it can be noticed that the accuracy of a CFD solution is governed by the number of cells in the grid. In general, the larger the number of cells, the better the solution accuracy.

CFD programs contain discretization techniques suitable for the treatment of the key transport phenomena, convection and diffusion as well as for the source terms and the rate of change with respect to time. The underlying physical phenomena are complex and non-linear so an iterative solution approach is required [13].

A.4.1 Laminar flow

Flows in the laminar regime are completely described by the equations that are developed in section A.2. In simple cases, these equations can be solved analytically. More complex flows can be calculated numerically with CFD techniques such as the finite volume method without additional approximations [13]. To see whether a flow is laminar or not, the Reynolds number, which is given by equation A.9, has to be calculated [14].

$$Re = \frac{\rho U d_h}{\mu} \tag{A.9}$$

In this equation, d_h is the hydraulic diameter, defined as 4 times the cross-sectional area, divided by the wetted perimeter. The Reynolds number of a flow gives a measure of the relative importance of inertial forces and viscous forces. In experiments on fluid systems it is observed that at values below the so-called critical Reynolds number Re_{crit}, the flow is smooth and adjacent layers of fluid slide past each other in an orderly fashion. If the applied boundary conditions do not change with time, the flow is steady. This regime is called laminar flow [13].

At higher Reynolds numbers, flows are observed to become turbulent. Even with constant boundary conditions applied, a chaotic and random state of motion develops in which the velocity and pressure change continuously with time within substantial regions of flow [13]. In this case, the inertial forces are dominant with respect to the viscous forces [2].

The transition from laminar to turbulent flow occurs at Re_{crit}. In all systems, this Re_{crit} value is different and depends on the irregularity and the compliance of the wall. Irregular geometry can trigger early transition to turbulent flow [2]. Typically, for pipe flows, laminar flow occurs in regions where Re $<$ 2000 and turbulent flow is present in circumstances under which Re $>$ 4000. The range of 2000 $<$ Re $<$ 4000 is known as the transition range [14].

A.4.2 Turbulent flow

Turbulent flows are characterized by three-dimensional, time-dependent, random fluctuations of velocity. These fluctuations cause a mixing of transported quantities such as momentum and energy [2]. Turbulence is characterized by the presence of a large range of excited length and time scales. The irregular nature of turbulence stands in contrast to laminar motion [15].

Turbulence can be solved without any modelling. However, despite the performance of modern supercomputers, a direct simulation of turbulence by the time-dependent Navier-Stokes equations, called direct numerical simulation (DNS), is only possible for rather simple flow cases at low Reynolds numbers. The restrictions of DNS become quite obvious when recalling that the number of grid points needed for sufficient spatial resolution scales as $Re^{9/4}$ and the computational time as Re^3 [4]. For complex cases, turbulence has to be approximated by a model.

Due to the complexity of turbulent flow and difficulties in its understanding and physical interpretation, it is difficult to introduce a unique conceptual model. However, there are certain characteristics and properties associated with turbulence, which have been shown experimentally and numerically, that are used commonly in describing turbulent flows [9].

Turbulence modelling is, together with grid generation and algorithm development, one of three key elements in computational fluid dynamics. However, far less precision has been achieved in turbulence modelling compared to the other key elements. This is not really surprising since this is an approximation of an extremely complicated phenomenon [15]. Several turbulence models are discussed in sections A.4.2.1 and A.4.2.2.

A.4.2.1 Reynolds Averaged Navier-Stokes equations

To make the explanation of the Reynolds Averaged Navier-Stokes (RANS) equations easier, the Navier-Stokes equations described in section A.2 are simplified to represent an adiabatic, incompressible flow with constant dynamic viscosity [1, 12, 13]. The Navier-Stokes equations are now given by the continuity (equation A.10) and momentum (equation A.11) equations:

$$\nabla.U = 0 \tag{A.10}$$

$$\rho\left(\frac{\partial U}{\partial t} + U.\nabla U\right) = -\nabla p + \mu\nabla^2 U + S_M \tag{A.11}$$

To derive the RANS equations for this case, equations A.10 and A.11 are rewritten in another form as equations A.12 and A.13 [10, 15].

$$\frac{\partial u_i}{\partial x_i} = 0 \tag{A.12}$$

$$\rho\frac{\partial u_i}{\partial t} + \rho\frac{\partial\left(u_i u_j\right)}{\partial x_j} = -\frac{\partial p}{\partial x_i} + \frac{\partial}{\partial x_j}\left[\mu\left(\frac{\partial u_i}{\partial x_j} + \frac{\partial u_j}{\partial x_i}\right)\right] + S_M \tag{A.13}$$

The RANS equations govern the transport of the averaged flow quantities, with the whole range of the scales of turbulence being modelled. A turbulent flow may be defined as a flow which contains self-sustaining fluctuations of flow properties imposed on the main flow [9]. The flow quantities can thus be expressed as the sum of an average quantity and a fluctuation as given by the Reynolds decomposition in equations A.14 and A.15 [2].

$$u_i = \overline{u_i} + u_i' \tag{A.14}$$

$$p = \overline{p} + p' \tag{A.15}$$

Time averaging equations A.12 and A.13 by using equations A.14 and A.15 yields to equations A.16 and A.17.

$$\frac{\partial \overline{u_i}}{\partial x_i} = 0 \tag{A.16}$$

$$\rho\frac{\partial \overline{u_i}}{\partial t} + \rho\frac{\partial\left(\overline{u}_i\overline{u}_j\right)}{\partial x_j} = -\frac{\partial \overline{p}}{\partial x_i} + \frac{\partial}{\partial x_j}\left[\mu\left(\frac{\partial \overline{u_i}}{\partial x_j} + \frac{\partial \overline{u_j}}{\partial x_i}\right) - \rho\overline{u_j' u_i'}\right] + S_M \tag{A.17}$$

Equations A.16 and A.17 are usually referred to as the Reynolds Averaged Navier-Stokes equations. The quantity $-\rho\overline{u_j' u_i'}$ is known as the Reynolds-stress tensor [15]. This tensor has to be modelled in order to close the system of equations. Some additional equations are introduced to solve for the turbulent viscosity [2].

By far the most popular turbulence models utilized today for flow and heat transfer calculations are the low-Reynolds number two-equation eddy viscosity models. The $k-\epsilon$ and $k-\omega$ models are the most utilized as these models often offer a good balance between complexity and accuracy [8]. They belong to the

so-called first-order closures and are mostly based on the eddy-viscosity hypothesis of Boussinesq [4]. The turbulence viscosity is solved trough the introduction of a scalar for the turbulent kinetic energy (k) and the turbulent dissipation rate (ϵ) or the specific dissipation rate (ω) [2].

The standard $k - \epsilon$ model is a semi-empirical model that assumes a fully turbulent flow and negligible molecular viscosity. It is semi-empirical because only the value of k is derived from the exact equation, ϵ is obtained using physical reasoning. Improved models exist in the form of the realizable $k - \epsilon$ model and the RNG $k - \epsilon$ model [2].

The standard $k - \omega$ model is a fully empirical model that does not assume a fully turbulent flow. The low Reynolds number $k - \omega$ can even obtain an accurate laminar solution when the turbulent viscosity approaches zero [3, 15]. An improved model exist in the form of the SST $k - \omega$ model. New features make this model more accurate for a wider class of flows [2].

Since all scales of turbulence must be modelled in the RANS equations, a model which is capable of predicting turbulence over a wide range of flow conditions and geometries does not exist [9].

A.4.2.2 Filtered Navier-Stokes equations

The filtered Navier-Stokes are obtained by filtering the time-dependent Navier-Stokes equations in a way that certain eddies, whose scales are smaller than the filter width or grid spacing used in the computational grid, are filtered out. In this way, only the dynamics of the large eddies are governed. This is called the large eddy simulation (LES) approach [2].

LES provides a compromise between DNS, where all scales of turbulence are computed directly from the Navier-Stokes equations, and RANS equations, where all scales of turbulence are modelled. In this approach, the filtered Navier-Stokes equation is solved for the large-scale motion, while the small scales are computed from a turbulence model, known as the subgridscale model [9]. This is a good approach because the larger eddies can not be modelled well as they are highly dependent on the geometry of the computational domain and the boundary conditions, they are mostly anisotropic. Small eddies are better suited for modelling as they are mostly isotropic [2].

After the application of the filtering process, the incompressible Navier-Stokes equations are given by equation A.18 and A.19 [9].

$$\frac{\partial \overline{u_i}}{\partial x_i} = 0 \tag{A.18}$$

$$\begin{aligned} \rho\frac{\partial \overline{u_i}}{\partial t} + \rho\frac{\partial\left(\overline{u}_i\overline{u}_j\right)}{\partial x_j} &= -\frac{\partial \overline{p}}{\partial x_i} + \frac{\partial}{\partial x_j}\left[\mu\left(\frac{\partial \overline{u_i}}{\partial x_j} + \frac{\partial \overline{u_j}}{\partial x_i}\right)\right] \\ &\quad -\frac{\partial \tau_{ij}}{\partial x_j} + S_M \end{aligned} \tag{A.19}$$

Where τ_{ij} is the subgrid scale stress tensor which represents the effect of small

scales. The subgrid scale stress tensor is given by equation A.20 [9].

$$\tau_{ij} = \rho\overline{u_i u_j} - \rho\overline{u}_i\overline{u}_j \tag{A.20}$$

Since the small-scale eddies are more or less universal and homogeneous, it is postulated that the subgrid scale model would be applicable to a wide range of flow regimes and conditions [9]. The use of the subgrid scale model allows to use a coarser grid and a smaller time-step compared DNS. However, the requirements are still much higher than needed for RANS simulations [2]. Typically, LES takes 5 to 10 % of the computing time compared to DNS [9]. Subgridscale models that are frequently used are the Smagorinsky-Lilly subgrid scale model and the Wall-adapting local eddy-viscosity model [2].

A.5 Conclusion

In this chapter, the numerical technique used in most CFD software packets is described. It is explained what a laminar and a turbulent flow is and when there is a transition between these types of flow. In the end, a summary of different turbulence models is given.

References

[1] John D. Anderson. *Computational Fluid Dynamics*. McGraw-Hill Science/Engineering/Math, 1st edition, February 1995.

[2] J.W. De Backer. *Functional imaging using Computational Fluid Dynamics for the Assessment and Treatment of Respiratory Diseases*. PhD thesis, University of Antwerp, June 2008.

[3] J.W. De Backer, O.M. Vanderveken, W.G. Vos, A. Devolder, S.L. Verhulst, J.A. Verbraecken, P.M. Parizel, M.J. Braem, P.H. Van de Heyning, and W.A. De Backer. Functional imaging using computational fluid dynamics to predict treatment success of mandibular advancement devices in sleep-disordered breathing. *Journal of Biomechanics*, 40(16):3708–3714, 2007.

[4] J. Blazek. *Computational Fluid Dynamics: Principles and Applications*. Elsevier Science, 1st edition, June 2001.

[5] Tuncer Cebeci, Jian P. Shao, Fassi Kafyeke, and Eric Laurendeau. *Computational Fluid Dynamics for Engineers: From Panel to Navier-Stokes Methods with Computer Programs*. Springer, 1st edition, June 2005.

[6] Ludovic de Rochefort, Laurence Vial, Redouane Fodil, Xavier Maitre, Bruno Louis, Daniel Isabey, Georges Caillibotte, Marc Thiriet, Jacques Bittoun, Emmanuel Durand, and Gabriela Sbirlea-Apiou. In vitro validation of computational fluid dynamic simulation in human proximal airways with hyperpolarized 3He magnetic resonance phase-contrast velocimetry. *J Appl Physiol*, 102(5):2012–2023, May 2007.

[7] Fluent Inc. *Fluent 6.3 User's Guide*. Fluent Inc., Centerra Resource Park, 10 Cavendish Court, Lebanon, NH 03766, September 2006.

[8] Vijay K. Garg and Ali A. Ameri. Two-equation turbulence models for prediction of heat transfer on a transonic turbine blade. *International Journal of Heat and Fluid Flow*, 22(6):593–602, December 2001.

[9] Klaus A. Hoffmann and Steve T. Chiang. *Computational Fluid Dynamics*, volume 3. Engineering Education System, Wichita, Kansas, 67208-1078, USA, 4th edition, August 2000.

[10] Soo-Jin Jeong, Woo-Seung Kim, and Sang-Jin Sung. Numerical investigation on the flow characteristics and aerodynamic force of the upper airway of patient with obstructive sleep apnea using computational fluid dynamics. *Medical Engineering & Physics*, 29(6):637–651, July 2007.

[11] Suhas Patankar. *Numerical Heat Transfer and Fluid Flow*. Taylor & Francis, 1 edition, 1980.

[12] John C. Tannehill, Dale Arden Anderson, and Richard H. Pletcher. *Computational Fluid Mechanics and Heat Transfer*. Taylor & Francis, 2nd edition, 1997.

[13] H. Versteeg and W. Malalasekra. *An Introduction to Computational Fluid Dynamics: The Finite Volume Method*. Prentice Hall, August 1995.

[14] Lee Waite and Jerry Fine. *Applied Biofluid Mechanics*. McGraw-Hill Professional, 1 edition, May 2007.

[15] David C. Wilcox. *Turbulence Modeling for CFD*. Dcw Industries, Incorporated, 5354 Palm Drive, La Canada, California 91011, 1st edition, November 1994.

[16] Ynot. An easy way to remember the navier stokes equations, August 2008.